OVERCOMING CHALLENGES OF FUNDAMENTAL ELECTROCHEMICAL KINETIC STUDIES UNDER DILUTE-REAGENT CONDITIONS

by

Kindle Shea Williams

M.S. Chemical Engineering Practice, Massachusetts Institute of Technology, 2018
B.S. Chemical Engineering with Majors in Chemical Engineering and Chemistry, University of Alabama, 2016

Submitted to the Department of Chemical Engineering
in partial fulfillment of the requirements for the degree of

Doctor of Philosophy in Chemical Engineering
at the
MASSACHUSETTS INSTITUTE OF TECHNOLOGY
May 2022

Author.....
Kindle Shea Williams
Department of Chemical Engineering
March 4, 2022

Certified by .....
Karthish Manthiram
Visiting Professor
Thesis Supervisor

Certified by .....
William H. Green Jr.
Hoyt C. Hottel Professor in Chemical Engineering
Thesis Supervisor

Accepted by .....
Patrick S. Doyle
Robert T. Haslam (1911) Professor of Chemical Engineering
Chairman, Committee for Graduate Students

OVERCOMING CHALLENGES OF FUNDAMENTAL ELECTROCHEMICAL KINETIC STUDIES UNDER DILUTE-REAGENT CONDITIONS

by

Kindle Shea Williams

Submitted to the Department of Chemical Engineering on March 4, 2022
in partial fulfillment of the requirements for the degree of
Doctor of Philosophy in Chemical Engineering

ABSTRACT

Electrochemical reactions show promise for decarbonizing the chemical industry through distributed, local chemical synthesis; replacement of hazardous, atom-inefficient, and emissions-heavy precursors and processes with benign reagents and electrical potential; the storage of intermittent renewable energy in chemical bonds; and the direct conversion of CO_2 into value-added chemicals. Before electrochemical technologies can be deployed, however, they must go through many stages of development. Different electrochemistries have different needs prior to deployment. In this thesis, we focus on lab-scale, fundamental kinetic studies of select electrochemistries – particularly those chemistries for which dilution or mixing phenomena are of practical concern.

We first discuss electrochemical CO_2 reduction – a chemistry that is very well studied in the lab environment, but has yet to reach deployment stage. In particular, we address the questions: what happens if we do not have access to a pure CO_2 gas feed? Is electrochemical CO_2 reduction tolerant to common CO_2 impurities such as N_2 and O_2? Through mechanistic study, we demonstrate that neither the rate nor the mechanism of CO_2 reduction is affected by the presence of O_2, but that the cathodic co-reduction of O_2 at relevant potentials represents a parasitic current – an energetic trade-off for tolerance to feed impurity which should be considered in technoeconomic analyses of CO_2 reduction systems.

Next, we consider mixtures not in the gas phase but in the liquid phase: blended aqueous-nonaqueous electrolytes. Such mixtures are often used to bring organic substrates into contact with water as a co-reactant, for example in O-atom transfer chemistries. We describe and measure complexities of working in such systems, such as solvent components that behave nonideally and ill-defined potential scales. We report the first measurement of the water dependence of nonaqueous alkaline hydrogen evolution, accounting for such nonidealities. In doing so, we propose molecular explanations for water's nonideal behavior and hypothesize many roles water can play in blended electrolytes. Finally, we use such a blended electrolyte to develop an approach to benzylic C-H oxidation for the production of commodity chemicals.

We hope this work represents a useful step toward the understanding and deployment of these relevant electrochemical systems.

Thesis supervisor: Karthish Manthiram
Title: Visiting Professor

Thesis supervisor: William H. Green Jr.
Title: Hoyt Hottel Professor of Chemical Engineering

Dedicated to my family,
who set me on my path in this world
and who will certainly be more proud
than the rest of the planet is
about this particular contribution
to the human endeavor.

I love you the mosterest!

ACKNOWLEDGEMENTS

I tend not to go into new experiences with too many expectations. But I'm certain if I had entered my PhD with expectations, they would have been defied. The main thing I learned – and that I learned quickly – is that the people are what makes this all worth it. I thought of keeping this brief and surface-level, so as not to forget anyone, but that could not have done justice to the village that raised this PhD. MIT Acknowledgement length guidelines be darned.

First, to my mentor on this journey: Karthish. I knew when I came to MIT, and I know now, that I made the right decision. Thank you for your vision, your flexibility, your willingness to ask for feedback and to grow and learn with us. Thank you for encouraging us to "make a bold hypothesis." Thank you for supporting me and being there to listen when times were really hard. Thank you for teaching me, through example, to call my parents more often. Thank you for believing in me more than I have believed in myself. Thank you for the chance to build something new and exciting. Things weren't always smooth, especially with your move, but the dream lives on. I hope (and I expect) the legacy we built together will carry on into your work at Caltech. I wish for you all the fullness and blessings that life has to offer. Can't wait to come visit sometime!

Next, to my committee, Profs. Bill Green and Bilge Yildiz: thank you for your input on this work, from science to safety to my professional development. I made it my goal to assemble a committee not just of good scientists but also of good people – folks who care about their mentees. You have proven that through your reliable kindness and good humor. Thank you for putting up with my (at times convoluted, desperate) attempts to schedule meetings. Bill, thank you in particular for stepping up as my formal advisor when Karthish left for Caltech.

I looked forward to building a new lab in grad school – more than almost anything else, I dreamed of having co-workers I really enjoyed hanging out with – and boy, did I hit the jackpot. To the OG's, Nik, Zack, and Nate Dogg, I have so appreciated your companionship throughout these 6 years. I was intimidated by all of your intellects coming out of our coursework, but I quickly found 3 caring and passionate friends who were willing to teach patiently and work together as a team, highlighting each other's strengths. You all have stretched me in unexpected ways. Thank you. To Nik, thank you for this wonderful living, flourishing entity that is our friendship. You always did have a green thumb. We complement one another very well – we may yet get to start some venture together, just like we practiced. Time will tell. To Zack, I always appreciated your easygoing humor and loved hearing you call my name as you entered the lab. Looking forward to seeing you just down the coast in a few months. And to Nate Dogg, thank you for being a great roommate and steady friend – I'll start making my Miami travel plans soon. To those who came after, you kept this experiment wonderful! Joy, you have been a reliable leader in the group, an abundantly kind person, and the best, most fearless question-asker I know – thank you. You will make a great professor one day. Joseph, I can always count on you for some soft-spoken sarcasm and a laugh – but on a serious note, thank you for all the work you have done to make our lab and the ChemE department a better place. Minju, your hard work and dedication has always impressed me – and your adaptability during this present time is commendable. Thank you for your jokes and the good conversations. Adi, your deep love for learning and teaching has been evident since I met you. Thank you for teaching us so much during your time with the group, and for nerd-sniping us from time to time. Katie, I feel like we have a special connection that it's hard to put into words. Thank you for your work taking over the safety officer position (for a time), and thank you for always being down for real talk. Trent, thank you for your contributions to the HER/HOR work – you were so quick to dive into literature and experiments alike, and you would have been the perfect person to take over the project for good if fate hadn't set the lab on a different path. Fang-Yu, thank you

for your hard work and self-sufficiency in the lab – it was a joy to help out when I got the chance. Simar, thank you for your enthusiasm and for always having the camera at the ready. Sayandeep, thank you for your long conversations and your youthful spirit – you brought much laughter to the group. To all the postdocs who have joined our ranks over the years – Hee Jo, Glen, Kyoungsuk, Dengtao, Ruquan, Minghui, and Shuliang – thank you for being teachers and partners on this journey. To the UROPs who worked with us – Michal, Sierra, Jess, Alex, Kelly, Olu, Ygor, Tess (hopefully I caught everyone!) – thank you for contributing to this effort, and I hope your time in the lab was a good learning experience and felt safe. In particular, thanks a ton to Jess, the talented and eager undergraduate student I was fortunate to mentor in 2019-2020. Your willingness to go try experiments in lab resulted in a lot more pre-COVID data than I even fully appreciated until there was time to sit and look at it all. The xylene chapter features your work throughout. Thank you for putting up with what I'm sure was a sometimes jarring level of disorganization on my end, as I navigated some of the hardest parts of my PhD journey. Hope everything is well for you. And to those who have just joined or are soon to do so – Thu, Channing, Chenyu – I look forward to getting to know you from afar (and hopefully from a-near at some point)! May your experience of the Manthiram lab be as rewarding as the one I got to have.

During the last few years, I was also fortunate to be funded by and interact with the Center for Molecular Electrocatalysis (CME). I particularly want to thank Jason Bates for early correspondence about high measured water orders; Travis Marshall-Roth and Deiaa Harraz of the Surendranath lab for good conversations on the MIT side; Catherine Wise and Rishi Agarwal of the Mayer lab for help with RHE measurements; and Jim Mayer, Shannon Stahl, and Morris Bullock for fruitful scientific conversations.

Friends from outside the lab also made this thesis possible – even fun at times. Thank you to my entire cohort at MIT ChemE for making the first year especially a rewarding (if exhausting) endeavor. Sharon, thanks for being an awesome first-year roommate and a great friend. I have enjoyed being a goober with you. Suzane, thank you for allowing me to be the 3rd Barton Bella with you and CJ – sorry we are leaving so soon after your return to the States. Kevin, thank you for the laughter, advice, musings on life, and overall one of the most rewarding friendships I've been a part of. We'll always have Clingman's Dome – you, me, and CJ. Here's to many more adventures in the future. To the whole Snow crew (OG's CJ, Mark, AJ, Justin, and Steph, and honorary members Matt, Sharon, Suzane, and Amanda): thank you for teaching me to ski, watching many movies, playing many games, and making sure first year wasn't all-work, no-play (and instead, it was all-work, all-play, no-sleep).

I got to be a part of so many exciting development and service opportunities during my time at MIT, and the folks I met truly defined the experience. Thank you for the whole Fall 2017 Practice School crew (CJ, Nate, Supra, AJ, Albert, Thomas, and Kate) for making our travels and tribulations a true joy, despite the floodwaters. Thanks also to our mentors, Bob and Brian – Brian in particular, for staying in touch and helping with many a rec letter since. Sorry I haven't pulled my weight on those apps, Brian. Thank you to my fabulous co-TA Katharine for an amazing and laughter-filled experience teaching EChem. Thank you to the many talented and committed past and present members of GSAB, for your collective commitment to advocating for students in the department – it was an honor to serve with you. Thank you to my mentees- and buddies-turned-friends from throughout the years: Nadia, Lexi, Jenna, K'yal, Matt, Grace, and Yuan. Especially big thanks to MY original buddy Sahag for flexibility and for showing me the "good life" in Boston (i.e. spending the department's money with reckless abandon), and to my 1st-year mentor Sam for kind guidance through that precarious time. Thank you to the extremely hard-working GSU organizers who have built this movement and taught me so much about labor and organizing. I wish I could have put more time into our

work, but I'm hopeful that it will all come to fruition very soon. To the rest of the world, I say: Unionize! Thank you to the Sidney Pacific house government for making SP one of the greatest places to live and serve. Even though I had to hide away in my lab or in my room in later years to finish this very thesis, know that your efforts were highly appreciated. Special thanks to my Outreach co-Chair Mohammad; Adela and Claire who came after us; and Penny and Belén who preceded and succeeded me, respectively, in the role of Bikes Chair. Also thanks to SPEC 2018-19 (Sami, Olivia, Karthik, Zack, and AJ), SPEC 2019-20 (Lucio, Matt, Lynda, Webster, and James), and SPEC 2020-21 (Geeticka, Belén, Chris, Brandon, and Michael) for leading the charge. Thanks to Andrea for your great deskwork, lovely conversations, fun movie nights, and true friendship. My thanks also go out to folks who participated in the inaugural MIT Science Policy Review, specifically Anthony as EIC and Martin as the lead author on my paper – it was a joy to edit for you. Martin, thank you for teaching me so much about halocarbons! Thanks also to everyone involved in LEAC and Green Labs. I also enjoyed the chance to participate in the Harvard Energy Journal Club – thank you all for welcoming me with open arms and teaching me so much. Many thanks also to my teammates in the many intramural sports that MIT ChemE has to offer. In particular: thanks to David, William, and our other soccer captains throughout the years for many seasons of fun, and 2 championships along the way; thank you to Dan, Andy, Sarah, Pedro, and everyone else in the hockey leagues for helping me find my true calling as a goalkeeper; thank you to Ani for teaching me (and so many others) to play cricket, and the whole team for many fun seasons and championships; thank you to Cynthia, Albert, and other Kan Jammers for teaching me to properly throw a Frisbee; thank you to Kevin Greenman for being my cornhole partner, sharing the 2021 Rock Award, and organizing COVID IMs; and shout-out also to all the generations of GSC-X who have done the same. Also, thanks to the casual squash crew (CJ, Kevin, Zack, Nathan, Karthik, Sam, and Kevin Fox) for teaching me and for the many fun times. (Racket up!!)

My time at MIT was not without physical and mental stress – but fortunately, we have professionals for help with that! I want to thank my Physical Therapist, Dr. Jocelyn Mach, for helping me recover from a knee injury in my 2nd year and teaching me so much about this great gift that is my own body. Thanks also to my PCPs – Dr. Egan for being so caring and explaining things in a way that a scientist can appreciate, and Dr. Ounis-Skali for seeing my post-quals physical distress, correctly identifying the issue, and referring me to MH&C. Thank you very much to Dr. Hsi for the past 4 years of therapy. I will miss our check-ins – don't worry, I'll send a postcard. And I'll make sure to get enough sleep in the next steps! Thank you also to the entire thesis group – those who have gone before (Zach, Diviya, Orhan, Gustavo, Bianca) and those who have still to defend (Haley, Alex, Mahreen, Fiona, Marv, Molly, Hannah). Congrats who those who have made it out already. We all will in due time!

My time at MIT was also made considerably more smooth by the incredibly talented and hard-working admins – in particular, many thanks to Barb for not only your help but also your conversations and friendship; to Gwen for being simultaneously one of the most kind and efficient people I've ever met; and to Helen for all that you have done for the group, especially through the chaos of the pandemic. Many thanks also to the folks from MIT Facilities and EHS who have solved many a crisis through the years and have been great people to hang out with besides; Gerry, Chris, and Brian in particular, as well as Jen for all your Green Labs work pre-COVID. Thanks also to ChemE HQ, the Student Office, and the ChemE computer staff for all of your support through the years.

In these years there was also life also apart from MIT. In particular I want to thank the community at First Church in Cambridge for the many opportunities to serve and grow alongside you, whether through landscaping, house work, sanctuary work, or the study of reparations. You are doing good work in the community. Peace be with you all.

To those who kept in touch from Alabama, I really appreciate your thoughtfulness and patience with me. Shuwen, I was glad you got to visit, and I'm so happy MIT was your next step. You truly amaze me with your caring heart and deep intellect. Lynda, thanks for hanging out – it has been nice to see you and Matthew in Boston, even if we couldn't connect very often due to COVID. Joe, it was great to visit the chocolate factory when you visited, and thank you for the advice from SRNL. Lauren, I was glad you were able to visit once – I'd like to return the favor in Ann Arbor soon. Darn this pandemic. Anyway, I want to make sure you know I have very often repeated your quote: "I don't work best under pressure – I work *exclusively* under pressure." I still have the book you sent, and I intend to read it once I defend this silly thesis of mine. Be on the lookout for me soon! And to those I have since lost touch with, but who supported me on the first part of this journey, thank you. Sam, I'm sorry I wasn't there in the way you needed. And Alex, I will always be grateful for what we had. I hope you are both building the most wonderful lives, even if I can't be in them in the same way anymore. Always happy to reconnect and start fresh. You know where to find me.

And to everyone from White House who has stayed in touch, you all hold very special places in my heart. Ashton and Krista, words can't describe how grateful I am that our friendship has continued through these years. I was so glad to get to participate in your weddings, and see you start families. Looks like I'm next?? I'll keep you posted. Shelby, thank you for the unexpected calls and the hilarious, impassioned conversations that ensued – I want you to know I was very often thinking of you too, even if I didn't say so. Saleen and Po, thank you for your texts – I hope you are both doing well. Luke, thank you for pulling together the Shakespeare Saturdays crew during COVID – I am so proud of what you are doing at WHHS! John, thank you for staying in touch and always being you. I wish you much strength for your own thesis journey, and I hope the world grows ever kinder toward you.

To all of my professors, and to my past mentors from other lives – Dr. Woski, Joe, Prof. Dumesic, Maddie, Dr. Sharpe, Mrs. Batson, so many of my teachers and coaches from high school and prior – thank you for pouring your teaching and guidance into me. I hope you can see that this thesis is also the product of your work and care.

Also, if I could offer one un-acknowledgement, it would be to the COVID-19 pandemic. No thanks to you, pandemic. 0/10. Wishing health and safety for all who read this, and comfort for those who have lost loved ones. Thank you to the health care workers, public health workers, and all other overworked, underpaid essential workers who sacrificed so much to help us through this time. You too had a role in this thesis.

This may seem silly, but one of the constants in my life for the past 12 years has been Nerdfighteria. I want to thank John W. for introducing me to John & Hank Green back in high school, and John and Hank for creating such good community and such enriching content. Nerdcon 2017 was a blast, even if I'm awkward and don't know how to make friends. Thank you for shaping how I see the world, and for keeping me company during late nights in the lab through your podcasts. DFTBA.

To Caroline, the person who played basically the biggest role in my life for the past 4 years, thank you so much for everything. We are continuously building this wonderful life together, and I can't wait to see what comes next. Thanks also to your family for being so generous and accepting me on road trips and virtual game nights alike.

Lastly, I want to thank my family – both my extended Williams & Shea families, especially those who paid visits and who I was able to visit in CT these past few years – but mostly my parents. I know you haven't always understood what was going on in this wild world of academia, but thank you for supporting me the whole way. Everything I am today, I can be because of the foundation you set for me. I will always be grateful.

TABLE OF CONTENTS

LIST OF FIGURES

LIST OF TABLES

List of Abbreviations and Acronyms

A_j	area of peak j
a_j	activity of species j
ACN	acetonitrile
AE	alkaline electrolyzer
aq.	aqueous
c_j	concentration of species j
CA	chronoamperometry
CO_2R(R)	carbon dioxide reduction (reaction)
CPET	coupled proton-electron transfer
CV	cyclic voltammetry
D_j	diffusivity of species j
DMSO	dimethyl sulfoxide
ECSA	electrochemically active surface area
E^0	standard reduction potential
E_a^j	activation energy index j
ET	electron transfer
EtOH	ethanol
F	Faraday's constant
Fc	ferrocene
FE	Faradaic efficiency
FEP	fluorinated ethylene propylene
FID	flame ionization detector
FT-IR	Fourier transform – infrared (spectroscopy)
FTO	fluorine-doped tin oxide
G^j	Gibbs free energy of index j
GC	gas chromatograph
GDE	gas diffusion electrode
H_j	Henry's law coefficient for species j
h	Planck constant
HER	hydrogen evolution reaction
HOR	hydrogen oxidation reaction
HS	headspace
H_{UPD}	hydrogen underpotential deposition
I_j	intensity of peak j OR total current toward j
i	current density
IPA	isopropyl alcohol
K_j	equilibrium constant with index j
k_j	rate constant with index j
k_B	Boltzmann constant
KIE	kinetic isotope effect
LSV	linear sweep voltammetry
MD	molecular dynamics

Me_{10}-Fc	decamethyl ferrocene
MIR	manual IR-drop (Ohmic drop) correction
MPL	microporous layer
m_T	Tafel slope
n	number of electrons
NMR	nuclear magnetic resonance
NP	nanoparticle
OAT	oxygen-atom transfer
OCV	open circuit voltage
OER	oxygen evolution reaction
ORR	oxygen reduction reaction
P_j	partial pressure of species j
PEEK	polyether ether ketone
PEIS	potentiometric electrochemical impedance spectroscopy
PEM(E)	proton exchange membrane (electrolyzer)
PET	polyethylene terephthalate
PSRK	predictive Soave-Redlich-Kwong
PT	proton transfer
PTFE	polytetrafluoroethylene
q	number of electrons transferred during a rate-determining step
R	ideal gas constant
r_j	reaction rate for reaction index j
RDE	rotating disk electrode
RDS	rate-determining step
Re	Reynolds number
RHE	reversible hydrogen electrode
Sc	Schmidt number
SHE	standard hydrogen electrode
SOE	solid oxide electrolyzer
STP	standard temperature & pressure
SWV	square wave voltammetry
T	temperature
$TBABF_4$	tetrabutylammonium tetrafluoroborate
TBAOH	tetrabutylammonium hydroxide
TCD	thermal conductivity detector
TRL	technology readiness level
TS	Tafel slope
TST	transition state theory
tBuOOH	*tert*-butyl hydroperoxide
U	total applied voltage; interchangeable with V, E
x_j	liquid mole fraction of species j
XAS	X-ray absorption spectroscopy

β	symmetry factor
γ_j	activity coefficient of species j
Δ	denoting a change in some variable
δ_j	diffusion boundary layer thickness for species j
θ_j	surface coverage of species j
μ_j	chemical potential of species j
ν_j	stoichiometric coefficient of species j
Π	product operator
Σ	summation operator
σ	Hammett parameter for a substituent
φ	electric potential
^{0}	denoting a standard or reference state
‡	denoting a transition state

List of Appendices

1 INTRODUCTION

1.1 Electrochemistry as a tool for decarbonization

Climate change is a defining challenge of the present generation. As of 2016, annual anthropogenic greenhouse gas emissions total 49.4 gigatonnes CO_2 equivalent.[1] Of this, 73.2% is attributable to total energy use; 24.2% specifically to energy use in industry; and 5.2% to direct process emissions from the production of chemicals such as ammonia and cement. Since CO_2 emissions are the largest contributions to these numbers, there is presently an ongoing push to decarbonize the energy sector through the use of renewable electricity generation – via the likes of solar, wind, hydropower, and (debatably renewable) nuclear power. However, in order to reach global climate goals, there is an urgent need to not only incorporate renewables into the energy sector, but also to address problems of renewable energy storage, sustainable manufacturing, and process electrification. A powerful tool in our kit which can address many of these issues is electrochemistry.[2]

At its core, the subject of electrochemistry is not so different from the subject of chemistry itself – the primary focus is on the behavior of electrons, and controlling where those electrons go as bonds are made and broken, and as oxidation states change. The difference is that, in contrast to chemical redox, an electrochemical system allows for the decoupling of reduction and oxidation into two distinct half-reactions that can be tuned independently from one another and also spatially separated from one another. Because electrons can pass through an external circuit connected to the interfaces at which charge transfer occurs, the driving force for a redox reaction can be supplied or harnessed as a voltage. This powerful thermodynamic handle offers many benefits, from enabling chemistries which would be otherwise impossible, to quicker responsiveness – allowing for easy ramp up/ramp down of reaction rates – to modularizability, allowing for the production of small-scale devices and highly distributed, decentralized implementation.[3]

There are several examples of electrochemical technologies or reactions that have contributed to decarbonization, and many more show promise for doing so in the future. One is the battery, and the lithium-ion battery in particular, which is a compact form of energy storage allowing for the off-grid electrical operation of small devices and appliances as well as vehicles.[4,5] Beyond the battery paradigm of storing energy in devices which can be cycled, we can also think about storing energy in chemical bonds, which leads us to electrosynthetic applications such as water splitting, CO_2 reduction, N_2 reduction, and organic electrosynthesis.[6,7] By splitting water to produce hydrogen, we can avoid the CO_2 emissions inherent in steam methane reforming, the state-of-the-art in industrial hydrogen production.[8] By reducing CO_2, we can reverse combustion and directly close the carbon cycle.[9] By reducing N_2 electrochemically, we can synthesize the valuable molecule ammonia at low temperatures and pressures, allowing for distributed fertilizer production.[10,11] And through the use of voltage, specific transformations such as the partial oxidation of small hydrocarbons as well as selective functionalization steps in pharmaceutical manufacturing pathways has been shown to be possible.[7] In this respect, electrosynthesis can be thought of both as a tool for renewable energy storage, and as an approach to sustainable manufacturing.

1.2 Current state of electrochemical technology development

Of course, different electrochemical technologies have been researched and developed to varying extents. On one hand, the state-of-the-art industrial processes for the production of chlorine, the refining of metals such as aluminum and magnesium, the separation of transition metals such as copper from aqueous solutions, and even the production of adiponitrile (a precursor to nylon-6,6) are all electrochemical.[12] On the other hand, electrochemical processes such as nitrogen reduction[13,14] and the partial oxidation of methane[15–19] are still in relatively early research stages, dealing with questions of reproducibility, low observed rates, and active catalyst discovery. Here we will make note of the present development level for electrochemical reactions highlighted in this thesis.[20]

1.2.1 Hydrogen evolution

First reported in the year 1789,[21] the splitting of water to produce hydrogen and oxygen is one of the simplest and most foundational electrosyntheses. The half-reactions involved can be written as follows (acidic form, pH 0):

HER: $2H_3O^+(aq) + 2e^- \rightleftharpoons H_2(aq) + 2H_2O(l)$ $E^0 = 0$ V vs. SHE

OER: $2H_2O(l) \rightleftharpoons O_2(aq) + 4H^+(aq) + 4e^-$ $E^0 = 1.23$ V vs. SHE

An abundance of reports on water splitting – over 20,000 articles – have been published in recent years. As a result, water splitting is one of the most highly developed electrosyntheses, with electrolysis units now commercially available. There are three major types of water splitting devices that have been developed: the proton exchange membrane electrolyzer (PEME), which is acidic and uses a hydrated membrane as the electrolyte; the alkaline electrolyzer (AE), which uses an alkaline liquid electrolyte; and the solid oxide electrolyzer (SOE), which conducts oxide ions through a solid oxide electrolyte and is operated at high temperatures. Of these, the PEME is the most developed, followed by the AE – although there is optimism that alkaline electrolysis, in promoting the more kinetically difficult half-reaction of OER at the expense of HER, will overtake PEME in commercial viability in the long-term. The selectivity of the reactions, their mechanisms, and even the design of systems for high-rate electrolysis, are well developed. Much research conducted in water splitting today aims to develop catalysts with catalytic activities and stabilities comparable to or better than expensive noble-metal-based materials such as Pt, while simultaneously being less expensive and more earth-abundant.[22–25] Simultaneously, alongside increasing interest in alkaline electrolyzers, there has been increasing research interest in electrolyte effects and solvent dynamics during HER, which is the more difficult half-reaction under alkaline conditions.[26–38]

While water-splitting technologies are highly developed in these contexts, even to the point that multiple large-scale electrolysis projects have been announced, it should be noted that our understanding of water reduction in particular is limited mostly to the context of aqueous electrolytes. Limited efforts have been dedicated to the study and development of water-splitting reactions in nonaqueous contexts,[39,40] or in the context of blended aqueous-nonaqueous electrolytes.[41,42]

1.2.2 CO_2 reduction

The electrochemical reduction of CO_2 consists of many different half-reactions, all following the general form:[20]

CO_2RR: $xCO_2 + n(H^+ + e^-) \rightleftharpoons C_xH_yO_z + mH_2O$ $E^0 = -0.47$~0.17 V vs. SHE

This reaction is again written in acidic form, at pH 0 – although CO_2 reduction is largely carried out at near-neutral pH's.

First reported in 1870,[43] electrochemical CO_2 reduction has seen a renewed wave of interest in the new millennium, as the deleterious effects of increasing levels of CO_2 in the atmosphere on global ecosystems have become more apparent. Products of CO_2 electrolysis on most metals have been fully reported,[9] and those showing the highest activity for products – namely Sn (for making formate), Ag/Au (for making CO), and Cu (for making CH_4 and multi-carbon products) – have been studied in great depth, through experiment, spectroscopy, and simulation. Alloying and nanostructuring of these materials, particularly Cu, has been a major subject of research.[44] In addition, certain highly-selective molecular catalysts – usually producing CO – have also garnered considerable interest.[45] In the meantime, as with HER, work in CO_2 reduction has also recently begun to address solvent effects, electrolyte salt effects, and the impact of local pH on reaction rate and selectivity.[46–51]

By now, several publications have demonstrated reasonably high-rate, durable, and selective systems for CO_2 electrolysis.[44,52] However, CO_2 reduction systems in general have a considerably lower technology readiness level (TRL) than water splitting systems. Commercially, there exist a handful of early-stage companies, as well as smaller divisions within large companies, aiming to deploy CO_2 reduction technologies; their success as measured through profitability remains to be seen.[53–55]

One practical aspect of CO_2 electrolysis which had been investigated only sparingly prior to this thesis work was the behavior of CO_2 reduction reactions at lower pressures of CO_2,[56] and/or in gas mixtures containing contaminants.[57,58] This is surprising, as one factor in determining the feasibility of CO_2 reduction is the cost of obtaining the CO_2 itself,[59,60] which can be decreased substantially by decreasing CO_2 feed purity.[61,62] Knowing exactly what impurities a CO_2 electrolysis system can tolerate, and how this impacts technoeconomic considerations, is a useful goal.

1.2.3 Partial oxidation of small organic molecules

Finally, we will briefly consider a class of transformations within organic electrosynthesis: the partial oxidation of small organics. The foremost example of such a chemistry is the partial oxidation of methane to produce methanol. This transformation is particularly attractive given that (a) methane, being a gas at STP, is more difficult to transport and handle than methanol, which is a liquid at STP, and (b) methane is particularly inexpensive in modern times as a result of the advent of hydraulic fracturing, whereas methanol is a valuable synthetic precursor.

However, as of this writing, the partial oxidation of methane to produce methanol at appreciable rates is still largely a dream.[15–19]

Expanding scope to include organics slightly heavier than methane, there is a small but growing body of literature focusing on electrochemical reactions for oxygen-atom transfer (OAT) to organics. Early work on O-atom transfer by researchers such as Dennis Johnson[63–69] and Richard Holm[70] in the 1980's and 1990's laid the groundwork for much modern OER catalysis as well as our own group's use of metal oxide nanoparticles to achieve O-atom transfer to epoxidize olefins[71] and make lactones from cyclic ketones.[72] Other groups such as those of Lutz Ackermann and Phil Baran are conducting work in electrochemical C-H activation (mostly sp^2 activation on aryl rings)[7,73,74] and partial oxidation of organics for pharmaceutical applications,[75–79] respectively. In addition, the electrochemical hydrogenation and oxidation of biomass-derived molecules is also a growing area of interest.[80]

In general, most reactions involving organic substrates are less developed than HER and the CO_2 reduction reactions, and there is more "green space" to not only explore catalysts but to ask which reactions are possible in the first place.

1.2.4 Identifying barriers to technology development

As may be observed from these brief overviews, a much-simplified representation of the workflow in electrocatalysis research and development might be: (1) first identify a half-reaction which can take place, then (2) study the impact of electrode material on that reaction, then (3) understand how electrolyte-side variables impact the reaction, given a particular electrode material, after which point (4) the engineering of the system can be tweaked and the technology can eventually be deployed. Aqueous acidic HER in particular has progressed through these stages toward commercialization, and CO_2 reduction is following behind, albeit at a somewhat considerable distance. Meanwhile, organic electro-oxidation reactions are less developed as a rule, with considerable room for additional reaction identification.

The question is: where might a Ph.D. thesis fit into this landscape? That is to say, where are the opportunities to conduct fundamental research for these applied contexts? Across the board, these chemistries require testing under more complex cases of deployment. Specifically for this thesis, we have identified 3 distinct opportunities to address barriers to technology development on these fronts:

1. Study HER in nonaqueous contexts in which the reaction may serve as a counter for an organic electro-oxidation.
2. Study the impact of gas feed impurities on electrochemical CO_2 reduction.
3. Develop novel partial oxidation reaction(s).

1.3 Brief description of work in this thesis

The primary focus of this thesis is to push the boundaries of practical understanding for these key chemistries, with a specific focus on the effects of mixtures on "ideal," well-documented reaction rates and mechanisms. In a sense, where chemistries have previously been described, we are applying them in a "messy" system that better reflects current research needs and real-world conditions. Figure 1-1 illustrates the two major themes of this work: developing a molecular-level understanding of electrochemical reactions in the context of 1) gas-phase diluents/contaminants, and 2) blended electrolytes.

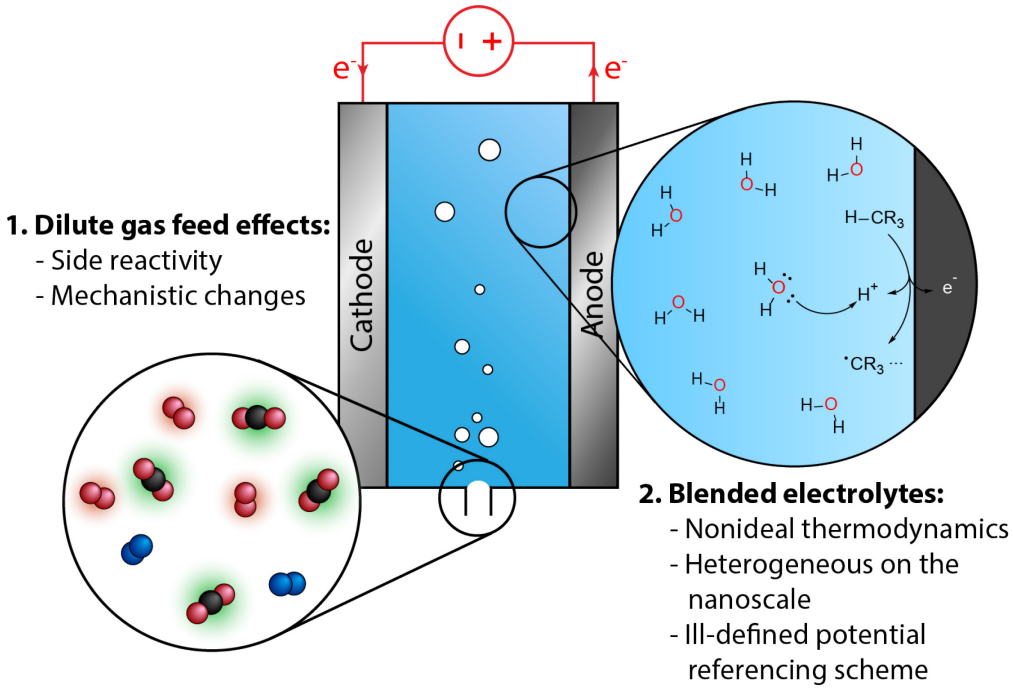

Figure 1-1. Overview of this thesis work, focusing on the development of mechanistic understanding of electrochemical reactions in the context of (1) dilute gas feed effects and (2) blended electrolytes.

Following this introduction, Chapter 2 is an exploration of the impact of gas feed impurities on electrochemical CO_2 reduction. In particular, we examine the impact of dilution with nitrogen and oxygen on CO_2 reduction on a planar gold foil catalyst. The motivation for doing so is that these gases are commonly found in practically-accessible CO_2 sources, ranging from flue gas

to air itself. We sought to understand the trade-off between CO_2 feed purity and reactor performance. In doing so, we discovered that neither the rate nor the mechanism of CO_2 reduction on Au is greatly impacted by the presence of oxygen. However, because O_2 is easily reduced at CO_2 reduction conditions, any O_2 present is reduced at a rate that is limited only by the diffusion of O_2 to the catalyst surface. Since electrons contributing to O_2 reduction are unable to contribute to CO_2 reduction, the reduction of O_2 can be considered parasitic current – a loss of efficiency during the reaction. This insight enables technoeconomic analyses of CO_2 reduction systems to consider the impact of feed purity on cost. In addition, our mechanistic investigation of CO_2 reduction contributed to a growing body of literature characterizing the reaction on Au, offering support for a chemical rate-determining step and opening the door to investigations of the impact of the bicarbonate ion on CO_2 reduction catalysis.

Chapters 3 & 4 focus on reactions taking place in blended aqueous-nonaqueous electrolytes. In Chapter 3, we explore the fundamentals of thermodynamic nonideality in blended solvents and how our understanding of this nonideality may impact mechanistic analysis. Using HER as a case study, we demonstrate that explicit accounting for water activity is necessary in order to yield meaningful water-dependence data for reactions in which water is a reactant. We present a methodology for quantifying nonidealities, and speculate on the many roles of water in a blended aqueous-nonaqueous electrolyte system. For instance, in the HER system where the measured water dependence is found to be ~3rd-order, we demonstrate that this may be attributable to multiple effects, from water's participation as a reactant, to acting as a proton/hydroxide shuttle, to displacing bulky surface adsorbates, to changes in both equilibrium potential and felt potential, to differences between solvation of reactants and transition states. We aim to provide perspective that is currently lacking in the scientific literature: an in-depth molecular-level discussion of thermodynamic nonideality which can be directly tied to bulk experimental measurements. In addition, we extend the relevance of the activity discussion to more complicated O-atom transfer chemistries such as cyclooctene epoxidation and cyclohexanone lactonization.

In Chapter 4, we build on the methodologies discussed in Chapter 3 to characterize a newly-reported electrochemical O-atom transfer chemistry: direct benzylic C-H activation. Using p-xylene as a model substrate, we characterize the product distribution from the reaction at various potentials and investigate pathways to forming more deeply oxidized products. We conduct a mechanistic analysis for the reaction, highlighting once again an unexpectedly high-order dependence of the reaction rate on electrolyte water content. In addition, we highlight the

impact of electrode material on C-H activation activity, noting in particular that carbon-based electrodes perform well, and the incorporation of metal catalyst materials does not positively impact reaction rate – a puzzling conclusion, to be sure, but one which implies that this reaction can be carried out without the use of expensive precious-metal-based materials. Future development of this reaction scheme may allow for the partial oxidation of xylene to more cleanly synthesize products such as terephthalic acid, which is used in the production of PET plastic and is currently made in a harsh, corrosive environment conducive to the undesired co-generation of CO_2.

Finally, in Chapter 5, we present conclusions and an outlook for these areas of research moving forward. Among other impacts, work from this thesis will hopefully aid in informing technoeconomic analyses for the deployment of CO_2 reduction units, spawn interesting next steps toward deconvoluting the roles of water in blended solvent environments via the study of H_2 and alcohol oxidation as well as the use of techniques such as soft X-ray spectroscopy and MD simulations for probing the structure of water, and enable new synthetic pathways requiring selective C-H activation.

2 IMPACT OF GAS FEED IMPURITIES ON ELECTROCHEMICAL CO_2 REDUCTION

The material in this chapter is adapted from Williams, K., Corbin, N., Zeng, J., Lazouski, N., Yang, D.-T., Manthiram, K. Protecting effect of mass transport during electrochemical reduction of oxygenated carbon dioxide feedstocks. *Sustainable Energy & Fuels* 2019, **3**, 1225-1232.[81] Reproduced with permission from the Royal Society of Chemistry.

2.1 Abstract

Electrochemical CO_2 reduction is a promising path toward mitigating carbon emissions while also monetizing waste gas through chemicals production and storage of surplus renewable energy. However, deploying such a technology for use on industrial CO_2 sources requires an understanding of the effects that gas feed impurities have upon CO_2 reduction reaction (CO_2RR). In this work, we elucidate the impact of molecular oxygen on the network of reactions occurring in a CO_2 reduction system. Our findings indicate that for a planar, polycrystalline Au electrode in an aqueous environment, oxygen reduction current is limited by the transport characteristics specific to the cell geometry and solvent; as a result, mass transport confers a protective effect by mitigating the otherwise thermodynamically and kinetically favorable reduction of oxygen. The presence of oxygen does not appear to have a significant impact on either CO_2RR or hydrogen evolution partial currents, indicating that the mechanisms of reduction reactions involving oxygen are independent of CO_2RR and hydrogen evolution. Further, an electrochemical kinetic analysis indicates many feasible candidates for the rate-determining step of CO_2RR; there is no indication that the CO_2RR mechanism at P_{CO2} = 0.5 atm is altered by the presence of oxygen, as the Tafel slopes (59 mV/dec) and reaction orders with respect to bicarbonate (0), CO_2 (~1.5), and protons (0 from lack of KIE) are consistent between systems with P_{O2} = 0 atm and those with P_{O2} = 0.5 atm. While this is

promising for the robustness of CO_2RR to oxygen impurities in gas feeds, the ultimate design trade-off when utilizing CO_2 sources containing oxygen is between the cost of separation processes and the corresponding cost of power inefficiency as a result of electrons lost to oxygen reduction. This represents a first step in understanding kinetic and transport considerations in the design of gas-impurity-tolerant CO_2 reduction systems.

2.2 Motivating the study of CO_2 reduction with oxygenated CO_2 feedstocks

With the rise of concern regarding carbon dioxide (CO_2) emissions, CO_2 valorization as a means of energy storage or chemicals production is an attractive pursuit. While round-trip efficiencies for energy storage technologies such as lithium ion batteries and pumped hydro power are greater than those for CO_2 electroreduction to fuels,[82] the generation of energy-dense chemicals allows for flexibility of energy recovery strategy as well as for product utilization in synthetic organic applications. CO_2 reduction reactions (CO_2RR) have been employed to reach products ranging from carbon monoxide (CO) and formate to more deeply-reduced products such as ethylene, methanol, and ethanol.[9,83,84] Generating such products from point-sources of CO_2 may prove to be an attractive means of both curtailing and monetizing CO_2 emissions in the future.

A major limitation of existing studies of CO_2 electroreduction, however, is that almost all experiments conducted to date have utilized gas feeds of 99.9% or purer CO_2. Those investigations which have focused on dilute streams of CO_2 have so far mostly done so in the context of low-conversion molecular catalysts and inert gas impurities such as nitrogen (N_2).[56] If CO_2 reduction is ever to be practically employed, it may not be feasible – logistically or economically – to expect end-users of CO_2 reduction technology to supply feedstocks of high CO_2 purity. Some estimates have indicated that the purification of CO_2 from air (which currently contains ~400 ppm or 0.04% CO_2)[85] would cost roughly $1000/metric ton CO_2 captured, while similar capture from the effluents of coal-fired power plants (containing 10-15% CO_2) would cost about $25-100/metric ton CO_2.[61] A more promising study on the design of a system for direct CO_2 capture from air was able to decrease the cost of air capture to $94-232/ton CO_2.[62] However, even this cost may prove prohibitive for the commercialization of CO_2 reduction technology, as many technoeconomic analyses investigating CO_2 reduction viability rely on CO_2 capture costs being no more than $30-60/ton CO_2.[59,60] Therefore, it would

be valuable for developed CO_2 reduction technologies to exhibit some degree of tolerance to gas feed impurities.

Previous studies involving non-inert impurities in CO_2 reduction streams have focused on the effects of NO_x, SO_x, and O_2 on CO_2RR at Cu cathodes.[57,58] In these contexts, O_2 was treated either as a species with the propensity to interfere with other impurities (e.g. by oxidizing poisoning sulfide ions),[57] or as a catalyst oxidant.[58] Ex-situ catalyst characterization and changes in bulk product distribution were the primary metrics of the impurities' effects, whereas impacts on the electroreduction mechanisms occurring in the cell and the physical phenomena governing the feed impurities' behavior in these contexts were not explicitly treated. Thus, there is a need to build upon these efforts in order to ensure the catalysts being developed for CO_2 reduction today will be viable for implementation in the future.

In particular, an abundant and reactive impurity in most anticipated CO_2 feed streams is molecular oxygen (O_2). Oxygen-tolerant catalytic networks are increasingly being studied for hydrogen evolution; methods for minimizing O_2 competition include the development of bio-inspired catalytic pockets in order to exclude, photo-reduce, or otherwise steer molecular oxygen away from poisoning catalytic systems for proton reduction.[86] Platinum catalysts for the hydrogen evolution reaction (HER) seem to maintain current density to HER in the presence of 0.21 atm O_2;[86] however, the exact means by which this is possible have not been investigated. It is equally as important, if not more so, for the impact of O_2 on CO_2 reduction to be studied and mitigated, since O_2 may very well be a constituent of CO_2 reduction gas feeds.

The goal of the present work is to demonstrate the effects of the presence of oxygen on the network of reactions occurring during electrochemical CO_2 reduction on gold catalysts. Gold was chosen as a test catalyst due to its high activity toward CO_2 reduction and for ease of study due to its high selectivity toward only gas-phase products (CO and H_2).[9,84,87–91] Cultivating an understanding of oxygen's effect on such an electrocatalytic system will pave the way for the development of systems with tolerance toward a broader variety of gas-phase impurities characteristic of many CO_2 point sources, which may be required for industrially viable CO_2 reduction.

2.3 Methods for electrochemical CO_2 reduction

2.3.1 Electrochemical cell

A two-compartment cell design was used for CO_2 reduction experiments (Figure A-A1).[92] A full treatment of cell design and assembly can be found in Appendix A (A.1, A.6).

2.3.2 Catalyst, electrolyte, reference, and gas feed preparation

Gold foils were mechanically wet-polished using new 400-grit sandpaper for 3 minutes, sonicated in Milli-Q® water for 3-5 minutes, and dried with compressed nitrogen gas prior to insertion in the electrochemical cell. Unpolished platinum foil was used as the counter-electrode, and the two electrode compartments were separated by a Selemion™ AMV anion-exchange membrane. Sodium bicarbonate electrolytes were prepared by dissolving sodium carbonate into Milli-Q® water to yield solutions with carbonate molarities of ½ the desired bicarbonate molarity, followed by bubbling overnight using instrument-grade (99.99%) CO_2 to convert the carbonate to bicarbonate. A leak-free Ag/AgCl reference electrode was used, and was calibrated to a master Ag/AgCl reference in saturated KCl before each experiment. Gas feeds during experiments were mixed by combining research-grade (99.999%) CO_2, industrial-grade (99.7%) O_2, and house-supplied N_2 (the inert feed) in the appropriate ratios. Total gas flow was set to 10 sccm unless otherwise noted, and the pressure in the electrochemical cell remained at roughly 1 atm. Further details on materials and experiments can be found in Appendix A (A.6. Electrochemical Experiments).

2.3.3 Product characterization

While minor electroreduction products were detected through a combination of NMR spectroscopy and colorimetric assays (see Appendix A.7. Product Detection), the majority of confirmed products were detected through in-line gas chromatography (GC). An SRI MG #5 Model 8610C GC was set up to auto-sample gas effluent from the electrochemical cell during operation. Products were detected using both a flame ionization detector (FID) and a thermal conductivity detector (TCD). Full details of GC setup and calibration can be found in Appendix A (A.7. Product Detection). GC samples taken at t = 20, 30, and 40 minutes during each electrolysis experiment were averaged for the data reported herein. Oxygen reduction reaction (ORR) current densities for most experiments were calculated from the balance of current after accounting for all detected products. The validity of this approach is confirmed both by lack of

detectable liquid-phase products (A.7.2. Proton NMR for Liquid CO_2RR Products) and by FE closure to 100% in the absence of oxygen.

2.4 Results & Discussion

2.4.1 Oxygen's effect on reactions in a CO_2RR cell

Initial experiments were conducted holding the partial pressure of CO_2 constant at 0.5 atm, while the pressure of O_2 was varied between 0 and 0.5 atm using N_2 as the balance. The effect of the oxygen partial pressure on partial current densities toward CO_2RR, HER, and ORR was quantified. (Figure 2-1) Results of this experiment conducted at different voltages can be found in Appendix A (A.8).

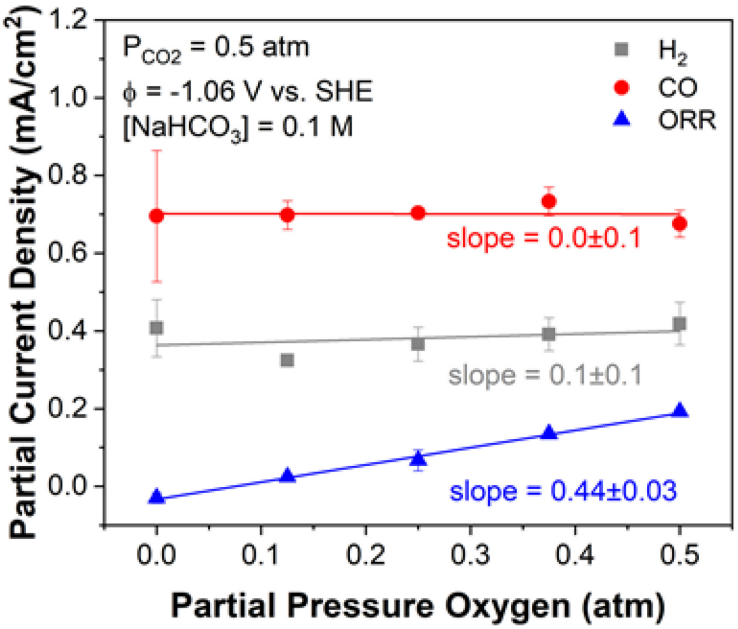

Figure 2-1. Oxygen's effect on partial current densities of HER (black), CO_2RR (red), and ORR (blue) in a cell flowing 0.5 atm CO_2 and various amounts of O_2, with N_2 as inert balance. Experiment was conducted at -1.06 V vs. SHE (-0.65 V vs. RHE) in 0.1 M $NaHCO_3$, with each point in duplicate.

As increasing amounts of oxygen were added to the gas feed, current toward ORR increased linearly while partial currents toward CO_2RR and HER remained roughly constant. This implies that ORR chemistry did not affect CO_2RR or HER catalysis. Further, it suggests the nature of the catalyst itself may have been unaffected by the presence of oxygen. It should be noted that there is somewhat larger uncertainty in the partial current measurements toward CO_2RR and HER, consistent with previous studies using foil electrodes.[93,94] This is because

foil preparation by polishing introduces surface irregularities that cannot be easily replicated from run to run. However, the uncertainties expressed in the error bars of this figure are noticeably small for the ORR data points. This is indicative that the quality of the foil preparation has no effect on ORR currents, and reinforces our confidence in the data.

At less reductive potentials and lower current densities, an apparent negative trend in both CO_2RR and HER current is observed (Figure A-A19). The fact that this trend is evident only at low overpotentials suggests either that oxygen interferes with these mechanisms in a distinct way at lower overpotentials, or that the effect of O_2 in the system is constant, but kept small on an absolute scale, therefore only showing up at low current densities.

To investigate why these trends hold true, the factors governing each reaction – namely, the kinetic versus transport control of ORR, as well as mechanistic aspects of CO_2RR and HER – were studied in the context of P_{CO2} = 0.5 atm.

2.4.2 ORR under CO_2 reduction conditions on gold

CO_2RR, HER, and ORR can be described through the following respective equilibria on gold at pH 7:[9,95]

CO_2RR: $CO_2(aq) + H_2O(l) + 2e^- \rightleftharpoons CO(aq) + 2OH^-(aq)$ E^0 = -0.52 V vs. SHE

HER: $2H_2O(l) + 2e^- \rightleftharpoons H_2(aq) + 2OH^-(aq)$ E^0 = -0.41 V vs. SHE

4e$^-$ ORR: $O_2(aq) + 2H_2O(l) + 4e^- \rightleftharpoons 4OH^-(aq)$ E^0 = 0.82 V vs. SHE

2e$^-$ ORR: $O_2(aq) + 2H_2O(l) + 2e^- \rightleftharpoons H_2O_2(l) + 2OH^-(aq)$ E^0 = 0.27 V vs. SHE

Thermodynamics would dictate that at CO_2 reduction conditions that allow for the formation of CO, reducing oxygen is extremely favorable. Since the equilibrium potential for CO_2 reduction is roughly -0.52 V vs. SHE in neutral media, the cathode must be held at more reductive potentials than -0.52 V vs. SHE in order to achieve significant CO_2 reduction currents. It is reasonable to imagine that at greater than 1.3 V of overpotential, the rate of ORR may not be strictly dictated by kinetics. However, it was prudent to confirm this experimentally.

In this vein, cyclic voltammograms taken at P_{CO2} = 0.5 atm were compared with and without a half-atmosphere of oxygen (Figure 2-2A). It can be observed that at around 0.25 V vs. SHE, the onset of ORR occurs. This reduction current density plateaus at -0.26 mA/cm^2 around -0.2 V vs. SHE. HER and CO_2RR onset, meanwhile, do not occur until the potential is swept down to almost -0.8 V vs. SHE. It is therefore concluded from this plot that ORR is transport-limited

at the CO_2RR potentials of interest. This explains the phenomenon wherein ORR current is not impacted by changes introduced to the catalyst surface by polishing – the current is limited by diffusion.

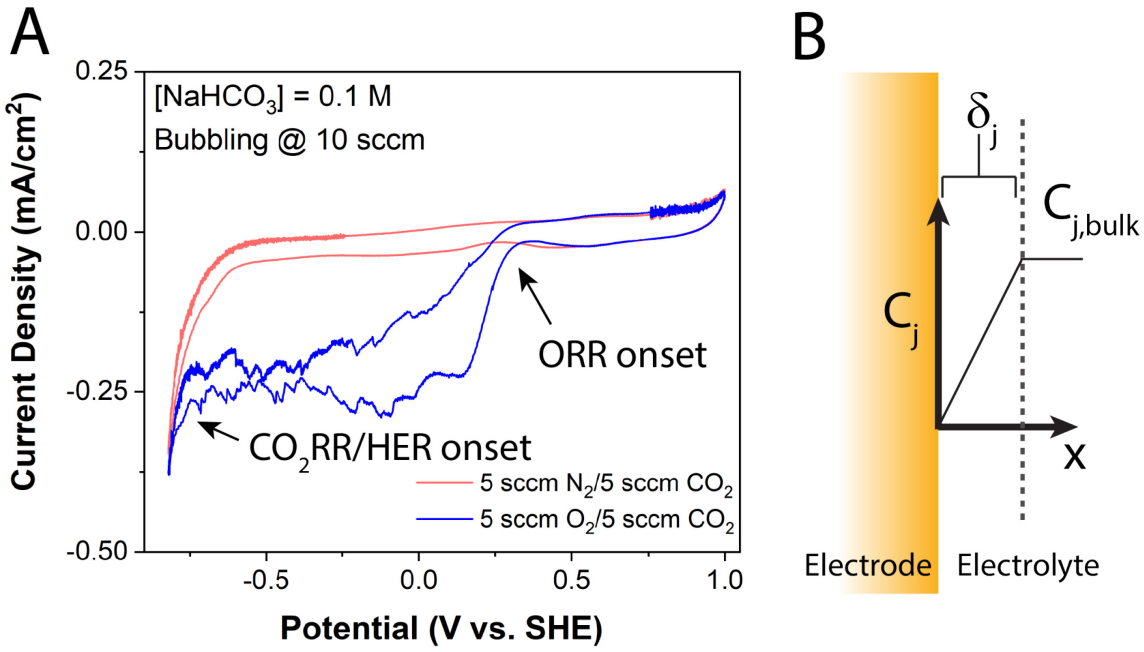

Figure 2-2. Transport limitations of ORR. (A) Modified CV scans (each is cycle #2 at a scan rate of 20 mV/sec) showing the onset and transport limitation of ORR at potentials less reductive than the CO_2RR operating regime. Relevant transport conditions were simulated by maintaining gas bubbling at 10 sccm. (B) Conceptual sketch of the stagnant mass-transport boundary layer model.

For a planar electrode, assuming a stagnant boundary layer model (Figure 2-2B), the formation of a linear species concentration profile at the catalyst surface leads to the expression:[96]

$$i_{lim,j} = -\frac{nFD_j c_{bulk,j}}{\delta_j} \qquad \text{(Eq. 1)}$$

where $i_{lim,j}$ represents the diffusion-limited current density for a reduction reaction involving species j, n is the number of electrons involved in the reduction, F is Faraday's constant, D_j is the diffusivity of species j, $c_{bulk,j}$ is the concentration of species j in the bulk of the solution (in turn dictated by Henry's law in the dilute limit), and δ_j is the mass transfer boundary layer thickness for species j. Because of the relative insolubility of oxygen in water – the Henry's law constant for O_2 is 0.0013 mol/kg·bar, compared to 0.034 mol/kg·bar for CO_2[97] – the relative transport-limited current density of oxygen compared to carbon dioxide in solution is quite low.

To understand more about the mass-transport boundary layer in the cell, its thickness was determined by measuring the diffusion-limited current density of the ferricyanide ion and back-calculating its mass-transport boundary layer thickness using Eq. 1.[98] A conversion was then applied to account for the difference in the diffusion coefficients of ferricyanide and gas-phase species such as CO_2 and O_2 (see Appendix A.6.5). For the transport of dissolved O_2 gas, the calculated boundary layer thickness was 200±7 μm. Using the values $n = 4$ (see below), $D_{O2} = 2.10\times10^{-5}$ cm^2/s,[99] and $C_{bulk,O2} = 0.65$ mM at 0.5 atm,[97] the resulting prediction for the ORR diffusion-limited current density is 0.26 ± 0.01 mA/cm^2, in remarkable agreement with our voltammogram.

In addition, it was necessary to confirm which type of ORR was occurring under CO_2 reduction conditions. Gold is a known peroxide-forming ORR catalyst,[100] more typically implicated in selective H_2O_2 formation under acidic conditions,[101,102] whereas within the bicarbonate mass transport boundary layer, conditions should be slightly basic (up to pH 9-10, depending on the current density drawn).[103] Long-term experiments passing over 50 C of charge were conducted in order to study the accumulation of ORR liquid-phase products; the colorimetric assay corresponding to the quantification of hydrogen peroxide in this electrolyte returned negative results, meaning that less than 10% of the oxygen being reduced is forming hydrogen peroxide (Appendix A.7.3). We can therefore posit not only that ORR is transport-limited at relevant testing potentials, but also that it is primarily forming water. As water is the chief component of the electrolyte, the ORR products are not expected to interfere with any other catalytic cycles occurring in the cell.

2.4.3 Changes to mechanism of CO_2 reduction

To follow up on these observations, it was pertinent to interrogate the effect that oxygen's presence in the CO_2 reduction environment had on the HER and CO_2RR mechanisms, especially in the low-current density regime. As the kinetics of HER were difficult to probe – a kinetically interpretable Tafel slope for HER was never attained, consistent with previous observations[89] – the focus of this investigation was on the mechanism of CO_2RR. Probing the effect of oxygen in this context necessitates not only the study of the CO_2 reduction mechanism under oxygenated conditions, but also the study of the same mechanism at dilute concentrations and with no oxygen present, as most investigations of CO_2 reduction to this point have been conducted at 1 atm of CO_2.[88,90,91,104] To this end, a mechanistic study of CO_2 reduction was conducted.

Kinetic data were captured through Tafel analysis, bicarbonate dependence, CO_2 dependence, and kinetic isotope effect (KIE) experiments. The results are displayed and discussed below (Figure 2-3).

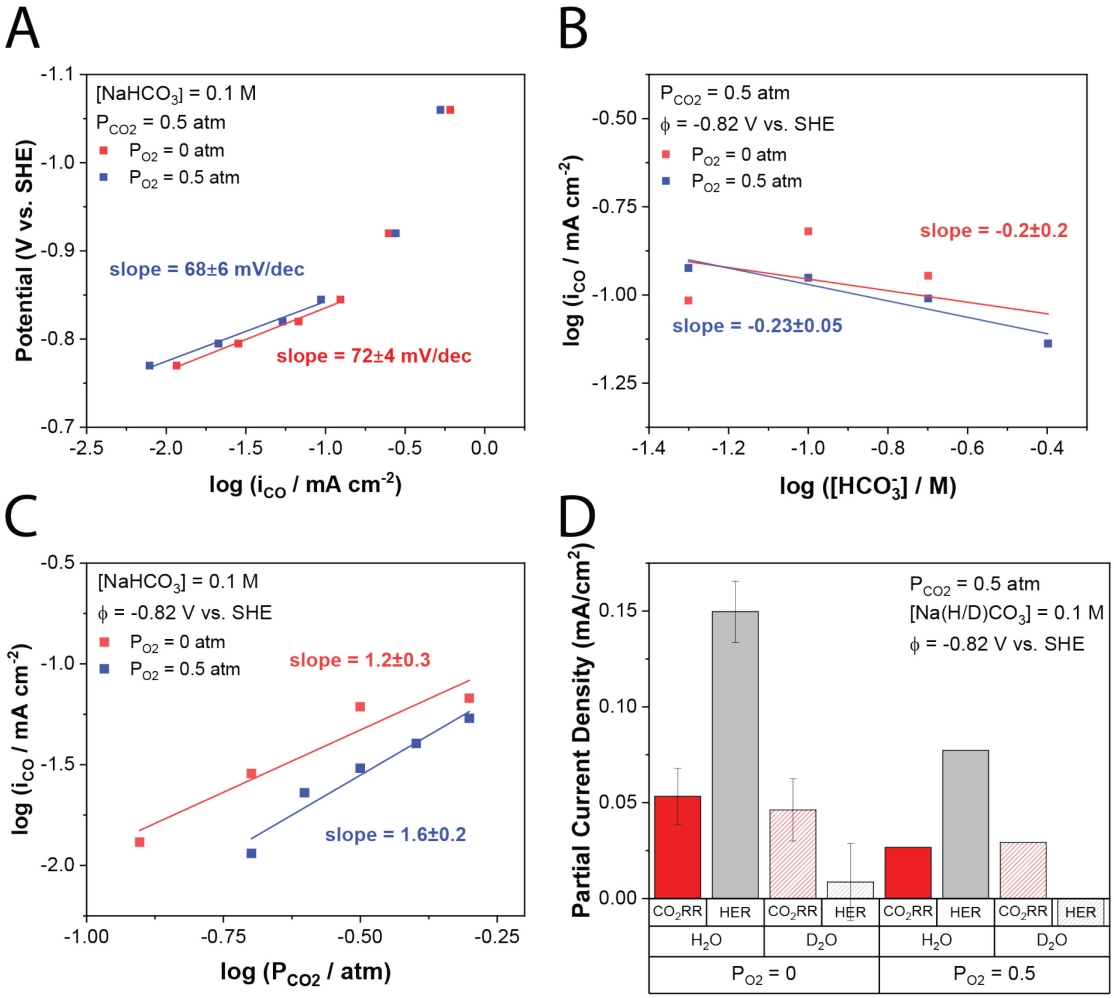

Figure 2-3. Summary of CO_2RR kinetic data on polycrystalline Au for P_{CO2} = 0.5 atm, both with and without 0.5 atm O_2. (A) Tafel slopes in 0.1 M $NaHCO_3$; (B) Bicarbonate dependence at -0.82 V vs. SHE; (C) P_{CO2} dependence at -0.82 V vs. SHE in 0.1 M $NaHCO_3$; and (D) Kinetic Isotope Effect for HER and CO_2RR at -0.82 V vs. SHE in 0.1 M $NaHCO_3$. Note that, consistent with the P_{O2} effect data, there is a slight decrease of CO_2RR and HER currents when oxygen is present.

2.4.3.1 Tafel slope

Tafel slopes were measured under 0.5 atm of CO_2 on Au, both with and without 0.5 atm O_2 (Figure 2-3A). The Tafel slope for CO_2RR under the testing conditions without oxygen is 72 ± 4 mV/dec, while in the presence of oxygen the slope is 68 ± 6 mV/dec. The results presented are consistent with a theoretical 59 mV/dec Tafel slope. The resulting data were interpreted as

being linear at potentials less reductive than -0.845 V vs. SHE. At potentials more reductive than this value, nonlinearities are observed which may be due to transport effects, mechanistic changes, or non-logarithmic kinetic response at high overpotentials.

The Tafel slope of 59 mV/dec indicates that a chemical step past the initial electron transfer to CO_2 is the rate-determining step (RDS) (see Appendix A.10). Subsequent experiments were designed to probe what this chemical step might be. Experiments were intended to probe purely the kinetics of the reaction and therefore were primarily conducted in the linear Tafel region – here selected as 300 mV overpotential, or -0.41 V vs. RHE in 0.1 M $NaHCO_3$ (-0.82 V vs. SHE).

2.4.3.2 Bicarbonate order dependence

One possibility for the RDS is the transfer of a proton from bicarbonate to the adsorbed CO_2 anion radical $\theta_{CO2-\cdot}$ to form θ_{COOH} (here θ is used to denote a surface adsorption site). The most straightforward way to test this RDS possibility is to conduct a bicarbonate order dependence test. This was done by varying the concentration of sodium bicarbonate in the electrolyte while holding the total solution ionic strength constant with sodium perchlorate. Perchlorate was regarded as an innocent bystander ion, while buffers such as phosphate were avoided due to their ability to poison the catalyst surface.[90] Further, the potential with respect to SHE rather than RHE was held constant, as this voltage is absolute in nature, and therefore represents the activity of the electron in the reaction – a factor which should be held constant when trying to probe the effects of a different reagent on the reaction rate. A full treatment of this topic can be found in Appendix A (A.10). These tests were performed at P_{CO2} = 0.5 atm both with and without oxygen (Figure 2-3B). In processing this data, note that we do not account for "salting-out" of CO_2, in contrast to the analysis reported in our 2019 publication; this is because CO_2 activity is constant in all of the bicarbonate tests (see Appendix A.6.2).

While most conceivable CO_2RR mechanisms consistent with the Tafel data might have either a zeroth- or first-order dependence on bicarbonate, the slope in the bicarbonate plot suggests that CO_2RR is negatively impacted by increased bicarbonate concentrations. The slope without O_2 is -0.2 ± 0.2, while the slope with O_2 is -0.23 ± 0.05. This trend is especially true as we approach the solubility limit of sodium bicarbonate at roughly 1.2 M (see Appendix A.6.2).[105] Results of the same experiment repeated with potassium bicarbonate, which is of a different purity than and nearly three times as soluble as the sodium salt, are shown in the Appendix (A.6.2). Because the potassium bicarbonate data yields a fairly clear zero-order dependence on

bicarbonate, it is anticipated that the negative slope in the sodium case is the result of a secondary effect and that the reaction order in bicarbonate is 0.

2.4.3.3 CO_2 order dependence

Experiments probing the effect of P_{CO2} in the inlet gas on CO_2RR current were conducted (Figure 2-3C). It should be noted that changes in P_{CO2} corresponded to bulk electrolyte pH changes; however, since bicarbonate order was found to be 0, this was regarded as having no convoluting effect on the CO_2 order dependence measurement. With slopes of 1.2 ± 0.3 and 1.6 ± 0.2 respectively for the cases with and without oxygen, the reaction order with respect to CO_2 can neither be said to be 1 nor 2. In fact, it is possible that we are operating in a regime of mixed control, where the rates of different paths toward CO_2 reduction – one of which involves a solution-phase CO_2 accepting an oxygen atom from a surface-bound species – are comparable. From these experiments alone, we cannot entirely rule out the possibility that the activity of CO_2 in solution may have a superlinear effect on current densities toward CO_2 reduction, although the slope here could also be due to changes in adsorbate coverage and other second-order effects.

2.4.3.4 Kinetic isotope effect

A proton involved in the RDS of CO_2RR need not come from the bicarbonate ion; protons are also plentiful in the water solvent. To examine the role of protons in the RDS, it is useful to note that a proton transfer occurring in an RDS is normally subject to a kinetic isotope effect; that is, because the proton is so light, and because its vibrational mode is the coordinate along which the reaction proceeds, affecting the frequency of vibration by swapping out an H for a D can elucidate the participation of the H in the reaction. Thus, experiments were conducted in which the H_2O solvent was replaced by D_2O, with proper accounting for additional required drying, membrane soaking, and bubbler replacement in order to minimize adventitious H_2O sources (Figure 2-3D) (Appendix A.6.3).

It was shown that at the testing conditions, the KIE is negligible (KIE = k_H/k_D = 1 within error) for CO_2 reduction, while for HER the value of the KIE is greater than 10. This is suggestive that while the KIE could be considerable in this experiment given the participation of a proton in the RDS, the KIE is not observed, and therefore it is unlikely that a proton transfer is involved. Notably, KIE experiments have been known to lead to false negative conclusions, but only in very specific and rare instances.[106]

2.4.3.5 Mechanistic interpretation of kinetic data

Notably, the kinetic data obtained here in the context of P_{CO2} = 0.5 atm differ from the outcomes presented in existing literature on CO_2RR mechanisms with P_{CO2} = 1 atm.[90,91] We therefore present a list of possible mechanisms, with a focus on those candidates which fit the Tafel slope data (Table 2-1). Derivations of rate laws and further discussion may be found in Appendix A (A.10).

Table 2-1. Postulated mechanisms of CO_2 reduction on gold under 0.5 atm CO_2.[90,104]

	RDS	Tafel Slope Form	Tafel Slope at 298 K, β = 0.5	Acidic Proton Order	P_{CO2} Order	KIE?
X.1	$CO_2 + \theta + e^- \rightleftharpoons \theta_{CO_2^{\bullet-}}$	$2.3RT/\beta F$	118	0	1	N
A.2	$\theta_{CO_2^{\bullet-}} + HCO_3^- \rightleftharpoons \theta_{COOH} + CO_3^{2-}$	$2.3RT/F$	59	1	1	Y
A.3	$\theta_{COOH} + e^- \rightleftharpoons \theta + CO + OH^-$	$2.3RT/(\beta+1)F$	39	0	1	N
B.2	$\theta_{CO_2^{\bullet-}} + H_2O \rightleftharpoons \theta_{COOH} + OH^-$	$2.3RT/F$	59	0	1	Y
B.3	$\theta_{COOH} + e^- \rightleftharpoons \theta + CO + OH^-$	$2.3RT/(\beta+1)F$	39	0	1	N
C.2*	$\theta_{CO_2^{\bullet-}} + [H^+] \rightleftharpoons \theta_{COOH}$	$2.3RT/F$	59		1	Y
C.3	$\theta_{COOH} + \theta \rightleftharpoons \theta_{CO} + \theta_{OH}$	$2.3RT/F$	59	0	1	N
C.4	$\theta_{CO} \rightleftharpoons \theta + CO$	$2.3RT/2F$	30	0	1	N
D.2	$\boldsymbol{\theta_{CO_2^{\bullet-}} + \theta \rightleftharpoons \theta_{CO} + \theta_{O^{\bullet-}}}$	$\boldsymbol{2.3RT/F}$	**59**	**0**	**1**	**N**
D.3	$\theta_{CO} \rightleftharpoons \theta + CO$	$2.3RT/2F$	30	0	1	N
E.2	$\boldsymbol{\theta_{CO_2^{\bullet-}} + CO_2 \rightleftharpoons \theta_{CO^+} + CO_3^{2-}}$	$\boldsymbol{2.3RT/F}$	**59**	**0**	**2**	**N**
E.3	$\theta_{CO^+} + e^- \rightleftharpoons \theta + CO$	$2.3RT/(\beta+1)F$	39	0	2	N
F.2*	$\theta_{CO_2^{\bullet-}} + [H^+] \rightleftharpoons \theta_{COOH}$	$2.3RT/F$	59		1	Y
F.3	$\theta_{COOH} \rightleftharpoons \theta_{CO^+} + OH^-$	$2.3RT/F$	59	0	1	N
F.4	$\theta_{CO^+} + e^- \rightleftharpoons \theta + CO$	$2.3RT/(\beta+1)F$	39	0	1	N
G.1†	$HCO_3^- + \theta + e^- \rightleftharpoons \theta_H + CO_3^{2-}$					
G.2	$\theta_{CO_2^{\bullet-}} + \theta_H \rightleftharpoons \theta_{COOH^-} + \theta$	$2.3RT/F$	59‡	0	1	Y
G.3	$\boldsymbol{\theta_{COOH^-} \rightleftharpoons \theta + CO + OH^-}$	$\boldsymbol{2.3RT/F}$	**59**‡	**0**	**1**	**N**
H.2	$\boldsymbol{\theta_{CO_2^{\bullet-}} + \gamma \rightleftharpoons \theta + \gamma_{CO_2^{\bullet-}}}$	$\boldsymbol{2.3RT/F}$	**59**	**0**	**1**	**N**
H.n◊	...					

Outcomes of experiments to probe the kinetics are listed next to each step in every postulated mechanism, under the circumstances that the step in question is the respective mechanism's rate-determining step (RDS). θ represents a catalytic active site on the Au electrode. β is the symmetry factor, interpreted as being 0.5. Bolded steps remain plausible RDS candidates after the kinetic investigation conducted here. *C.2 and F.2 are written such that any proton donor

could in principle serve as the proton source, including water and bicarbonate. [†]G.1 is a separate mechanistic step also involved in the HER pathway. [‡]Mechanism G requires the assumption that θ_H is dictated by equilibrium described by the Tafel step of HER. See derivation (A.10.7). [◊]H.n steps could in principle be almost anything, including previously listed mechanisms. H.2 is simply the rearrangement of $CO_2^{\bullet-}$ on the surface to generate an intermediate which then reacts to form products. It does not necessarily require that γ differs from θ.

In these mechanisms, CO_2RR is regarded as proceeding through inner-sphere transformations. While the list of mechanistic possibilities compiled here is not exhaustive, it encompasses many of the commonly reported mechanisms of CO_2 reduction to CO on Au, as well as a number of speculative possibilities.[104] In particular, excluded from this list are possibilities involving concerted proton-electron transfer (CPET). However, all mechanisms with CPET corresponding to initial CO_2 adsorption can also be collapsed down into the starting points represented by mechanistic steps C.2 and F.2, and therefore are also encompassed by this treatment.

The more commonly accepted intermediates for CO_2RR are implicated in mechanisms A and B. However, RDS candidates A.2 and B.2 are ruled out due to lack of bicarbonate dependence and KIE, respectively.

If we allow for the participation of surface sites or adsorbed species which are uncommon in the existing literature, then many RDS candidates remain (bolded options, Table 2-1). These include steps involving the formation of an Au-O bond, which we deem unlikely on the basis of gold's low oxophilicity; examples of this are θ_{COOH} dissociation into adsorbed CO and OH (mechanism C, excluded on the grounds of pH dependence) and the dissociation of adsorbed $CO_2^{\bullet-}$ into CO and an oxygen atom anion radical adsorbate (D.2). Mechanisms forming an Au-O bond can be avoided by instead invoking a cationic θ_{CO+} adsorbate species, which seems only to have been described in metal complexes rather than on surfaces;[107,108] this is exemplified in mechanisms which exhibit the participation of CO_2 in the RDS (E.2) and the dissociation of the θ_{COOH} intermediate into charged species (mechanism F, excluded on the grounds of pH dependence). Further, under certain mathematical assumptions and allowing for the θ_{COOH-} anion, the desorption of CO (G.3) is an RDS that is consistent with the data. A conformation change of adsorbed $CO_2^{\bullet-}$ (H.2) may also serve as the RDS.

Accumulation of surface intermediates involved in these mechanisms could be assessed by use of FT-IR in order to further narrow down the mechanistic possibilities or develop new, more

plausible hypotheses. For instance, a large IR band associated with θ_{CO} may indicate that this species has accumulated on the surface and is therefore the bottleneck in CO_2RR, supporting a CO desorption step as an RDS. The observation of such intermediates is currently a subject of debate.[89,91]

More relevant to the discussion of oxygen's effects, however, is the understanding of whether the mechanism of CO_2 reduction changes under oxygenated conditions in the electrochemical cell. The findings presented above suggest that so far, we have no reason to believe the mechanism of CO_2 reduction changes in the presence of oxygen. This is a promising result if we hope to develop oxygen-tolerant CO_2 reduction systems in the future.

2.4.4 Synthesizing the data into a picture of oxygen's interactions

Our understanding of the effect of ORR on the product distribution allows us to envision the interactions at the catalyst surface wherein the electrocatalytic steps involving CO_2 and HER are distinct from and unaffected by ORR intermediates and products (Figure 2-4). In this conception of the relevant catalytic interactions, while the mechanisms of none of the individual reactions can be isolated, the chemistries of CO_2RR and HER vs. ORR are nonetheless distinct from one another.

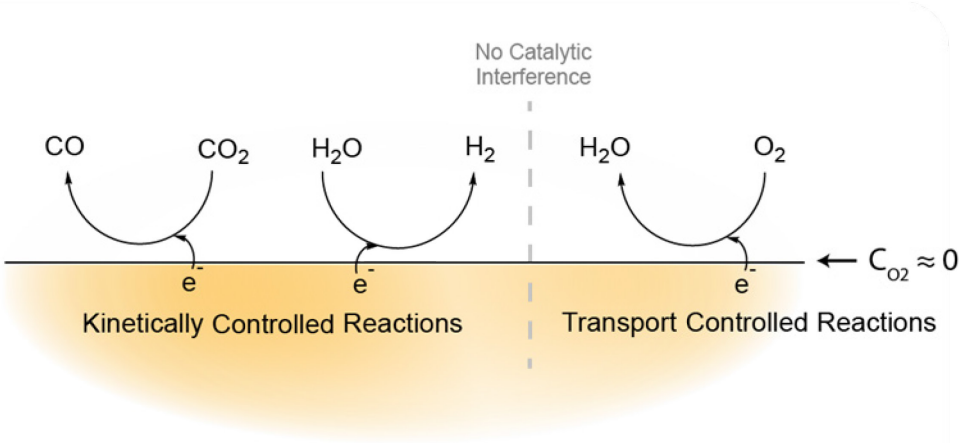

Figure 2-4. Interactions between CO_2RR, HER, and ORR during cathodic polarization on a bulk Au surface.

Because oxygen is less soluble than CO_2 in aqueous electrolyte, transport provides a protecting effect against ORR. However, that does not mean that ORR even in this context is entirely benign. It is important to note that for practical design purposes, a high-rate CO_2 reduction reactor may need to operate under configurations such as a gas diffusion electrode (GDE) or a

flowing-electrolyte design, wherein the length scales over which interfacial transport occurs are much smaller, and protecting effects of solubility are lessened. In such a scenario, the mechanistic analysis conducted here may not apply; further, power inefficiencies as a result of ORR may dominate economic considerations. Even in the context of the aqueous cell with a planar electrode reported here, assuming CO_2:O_2 ratios typical of flue gas streams from natural gas power plants (roughly 1.67:1),[109] and assuming activity and selectivity to CO_2 matching those reported here at -1.06 V vs. SHE, roughly 12% of applied power would be lost to ORR. In the case that this value in a practical system is smaller than the equivalent power loss required to purify a CO_2 stream of oxygen, direct reduction of a mixed O_2/CO_2 stream may be a viable design option. The strategy to accept loss of power in a CO_2 electrolyzer could be viewed as complementary to other techniques which have been suggested for thermochemically reducing dilute oxygen impurities in CO_2-rich feedstocks using methane.[110]

2.5 Conclusions

The presence of oxygen was shown to not have a significant impact on the current toward CO_2 reduction at high current densities, largely due to the suppression of ORR by the transport characteristics of a flooded aqueous electrolysis system. The presence of oxygen has not to this point been implicated in affecting the mechanism of CO_2 reduction. While these are promising results for CO_2 reduction system design and scale-up, it is likely that ORR could become an economic consideration, with the design trade-off being between cost of CO_2 separation and power inefficiencies introduced by the presence of oxygen.

Future work should be dedicated toward developing a better understanding of the RDS of CO_2RR on gold, as well as conducting similar studies on more oxophilic metals. Further, for power efficiency purposes, it may prove economical to invest effort toward the design of an inherently oxygen-tolerant CO_2RR system through modulating transport parameters at the electrode surface.

3 Accounting for Thermodynamic Nonidealities in Liquid-phase Electrocatalysis

Content of this chapter adapted from the recently-submitted publication: Williams, K., Limaye, A., Weiss, T., Chung, M., Manthiram, K. Accounting for species' thermodynamic activities changes mechanistic interpretations of electrochemical kinetic data. *ChemRxiv* 2022.[111]

3.1 Abstract

The thermodynamic activity of a reacting species, rather than the concentration of that species, generally determines the rate of a kinetically-limited reaction. In this work we demonstrate the need for the explicit accounting of reacting species' thermodynamic activities in solution, especially when conducting electrochemical kinetic tests. In hydrogen evolution in an alkaline acetonitrile-water blended electrolyte as well as previously-reported oxygen-atom transfer reactions (cyclooctene epoxidation and cyclohexanone lactonization), we demonstrate that accounting for species thermodynamic activity causes water-dependence measurements to yield different mechanistic interpretations than data which treats concentration as a proxy for activity. We hypothesize many ways in which water contributes to the reaction rate beyond direct participation in the reaction, offer initial molecular interpretations of the water activity-concentration relationship in the blended electrolyte, and discuss implications of these findings for better understanding solvent effects.

3.2 Introduction

Electrochemical reactions are some of the many tools at society's disposal for aiding in renewable energy storage, decarbonization of the chemical industry, modular/low-temperature and -pressure transformations, and selective chemical synthesis.[2] In the study of these reactions, attention has been paid to the design of both the electrode/catalyst material used to

facilitate charge transfer as well as the electrolyte – that is, the medium through which ionic conduction occurs between the anode and the cathode. In engineering liquid/solvated electrolytes, electrochemists are increasingly interested in solvent[47,112–114] and electrolyte salt[41,46,115,116] effects on reaction rates and mechanisms. Recent work has also demonstrated the usefulness of operating in mixed-solvent environments. For example, some O-atom transfer (OAT) reactions require contacting water – the O-atom source – with organic substrates, which are often relatively water-insoluble hydrocarbons.[71,72] An organic solvent is often used to bring these species into contact with one another in a single phase as an alternative to approaches involving two-phase[117–119] or segmented flow[120] setups. Acetonitrile is an example of such a solvent, often chosen due to its relative oxidative stability in the absence of a co-solvent.[121] The resulting electrolyte, consisting of organic solvent, water, salt, and any substrates of interest, we will here refer to as a "blended electrolyte" (or, in the absence of electrolyte salt, simply "blended solvent"). These electrolytes exhibit interesting intermolecular interactions and properties at the nanoscale, such as the clustering of water into so-called "nanoreactors."[41]

The literature is rich with investigations of the structure and properties of blended solvent systems outside the contexts of electrochemistry and catalysis. For instance, the proton-solvation properties of solutions consisting of water and amines,[122] nitriles, and alcohols[123] have been investigated. Techniques such as infrared (IR) spectroscopy,[124] nuclear magnetic resonance (NMR),[125] X-ray absorption spectroscopy (XAS),[126,127] and molecular dynamics (MD) simulation[125] have been applied to study the structure and bonding of components in blended solvents. Recently, much attention has been directed toward understanding blended electrolytes consisting of water and charged components such as ionic liquids,[128] as well as toward high-concentration salts in so-called "water-in-salt" electrolytes.[129] However, relatively little work in catalysis has been directed toward quantifying the impact of these structural changes brought about due to nonideal solvent mixtures – that is, solvent mixtures in which the activity coefficient of species of interest is not constant across the concentration range of interest (see 3.3. The relevance of species activities in rate laws).

Blended solvents have been employed in catalysis to varying extents based on application. In homogeneous catalysis, water/organic blended solvents have been used to illustrate solvent effects for acid-catalyzed biomass conversion.[130–132] Homogeneous hydrogen evolution reports utilizing transition metal complex catalysts have also implemented blended electrolytes consisting of organic solvents alongside organic acids acting as proton donors.[133,134] In general, research pertaining to hydrogen evolution (HER) and oxidation (HOR) has paid the most

explicit attention to the impact of water content and structure on heterogeneous catalysis, both in purely aqueous electrolytes, where interfacial water structure has become increasingly emphasized,[26–38,135,136] and in blended electrolytes.[41,42,137–139] Recent interest in decoupling the role of water as a proton source and as a solvent in heterogeneous HER and HOR has prompted novel investigations of the reactions in water/acetonitrile mixtures[33,42,137,140] as well as in water/carbonate-based electrolytes.[40] These works have utilized limited approaches to perform fundamental kinetic characterization on the reactions at hand that could decouple the many roles of water in these reactions; however, questions of thermodynamics with respect to potential scales and proper referencing techniques are increasingly being addressed.[141,142]

Outside of HER and HOR, electrochemical applications of blended electrolytes have focused less on the specific roles of water in reactions. Instead, reports have emphasized the impact of blended electrolyte composition on redox potentials for homogeneous complexes,[143] redox potentials for the various carbon dioxide reduction reactions (CO_2RR),[144] and effects of added acetonitrile in blended electrolytes for oxygen reduction (ORR)[145] and formic acid oxidation.[146] In addition, research efforts utilizing water as an O-atom source have also historically been conducted in blended electrolytes. While some of these works included explicit measurements of the dependence of reaction rate on water concentration,[71,72,147] no extensive treatment has been given in any of these works to the nonidealities of the electrolyte mixture.

In this work, we directly account for the nonideal thermodynamics of water in a blended electrolyte, and use this accounting to better understand measured dependences of heterogeneous electrocatalytic reaction rates on water. We conduct novel investigations on the water dependence of alkaline HER in acetonitrile, and also look back at previously-reported water dependences for electrocatalytic O-atom transfer chemistries. In addition, we discuss the structure and energetics of water in a simulated blended electrolyte, and offer a number of explanations for the many roles water plays in blended electrolyte electrocatalysis. While water is an interesting edge case when it comes to intermolecular interactions, many of these roles also pertain to nonaqueous co-solvents, lending to the broad applicability of these conclusions.

3.3 The relevance of species activities in rate laws

When studying electrochemical reactions, one useful goal might be to achieve mechanistic understanding of a reaction, often with an associated reaction rate expression. For an arbitrary reaction, a generic rate law can be written from Transition State Theory:

$$r = \frac{k}{\gamma_{\ddagger}} \prod_j a_j^{\nu_j} \quad \text{(Eq. 1)},$$

where r is the reaction rate, k is a reaction rate constant which subsumes details about temperature as well as energetics of the transition state, $\gamma_{\ddagger}$ is the activity coefficient of the transition state, and a_j represents the activity of species j with corresponding stoichiometric coefficient ν_j (see Appendix B for a full treatment of this rate formulation). That reaction rate laws should be formulated using species activities rather than species concentrations is well-established within the heterogeneous catalysis community, where explicit tracking of transition state nonidealities has been a subject of discussion.[148] The relationship between activity and concentration can be written as:

$$a_j = \frac{\gamma_j c_j}{c_{j,0}} \quad \text{(Eq. 2)},$$

where γ_j is the activity coefficient of species j, c_j is the concentration of species j, and $c_{j,0}$ is a reference concentration at which activity is typically set to be unity. Many researchers tend to apply the simplifying assumption that the activity coefficients γ_j are constant for a given species at all tested conditions – in other words, the reactants are assumed to behave ideally in solution. To assess the validity of this assumption, we can examine the anatomy of a previously measured activity-concentration relationship for a binary mixture.[149,150] (Figure 3-1)

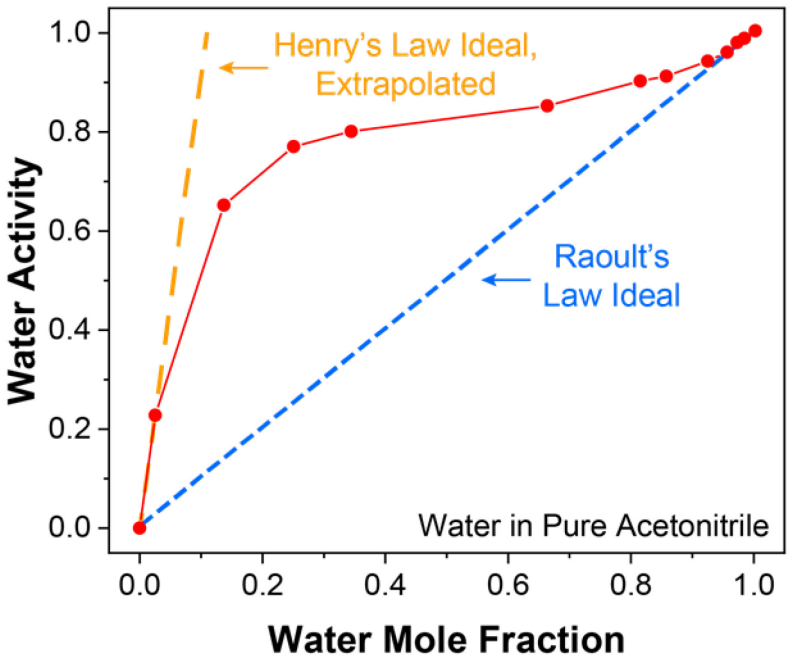

Figure 3-1. Illustrative concentration-activity relationship for a binary mixture of water and acetonitrile. The dashed orange and blue lines roughly indicate the Henry's Law (dilute water

reference) and Raoult's Law (pure water reference) ideal cases, respectively. Data extracted from Sirotkin et al.;[150] originally collected by Treiner et al.[149]

For this binary mixture of water and acetonitrile, we have noted the two distinct types of ideality using dashed lines. In the first type, the species of interest (here water) is assumed to be infinitely dilute in the solvent of interest, with each water molecule assumed not to interact to a great extent with other water molecules around it. In this formulation, we can refer to a species as being ideal with respect to Henry's law (orange dashed line). Here, concentration and activity can be related by:

$$a_j = \frac{c_j}{H_j} \quad \text{(Eq. 3)},$$

where H_j is the Henry's law constant for species j, and is the inverse slope of the dilute-j limit of the activity-concentration relationship, equivalent to $H_j = c_{j,0}/\gamma_j$. This formulation is often applied to dilute salts and dissolved gases in solution. On the other hand, the Raoult's law ideality formulation (blue dashed line) is one in which a saturated reference is used – a reference in which the species of interest is only engaging in self-interactions. For this formulation,

$$a_j = \frac{c_j}{c_{j,\infty}} \quad \text{(Eq. 4)}.$$

Where $c_{j,\infty}$ is a saturated reference state, equivalent to $x_j = 1$. This would imply that for a Raoult's law ideal mixture, $\gamma_j = 1$.

Examining the activity-concentration relationship for water and acetonitrile, it can be observed that an ideal formulation of either variety is only applicable across a very narrow range of concentrations. In a blended aqueous-nonaqueous system, we must consider the middle region, in which the relationship exhibits curvature. For most fully-miscible binary mixtures, the relationship will take this general shape: first upward, deviating positively from Raoult's law, then with decreasing slope, then curving upward to rejoin Raoult's law at high x_j. The positive deviation from Raoult's law across the middle of the plot indicates that species j is engaging in self-interactions that are more favorable than interactions with the other component of the mixture. Note that in these cases $\gamma_j > 1$. Water, being uniquely polar and strongly H-bonding, tends to have a large preference for self-interactions. As a result, the downward curvature at intermediate water concentrations leads to a very obvious "plateau" in activity. We hypothesize this is due to clustering of water at the nanoscale, though it appears discussion of the molecular origins of activity coefficient have been sparse in the literature.

Thus, in the case in which water and acetonitrile are the primary components of a blended electrolyte, it is necessary to apply a correction to measured data in which the composition of the electrolyte is changing. It should be noted that this conclusion generally applies to *any* electrolyte or reaction solution in which activity coefficients might reasonably be changing throughout a given set of tests.

3.4 Hydrogen evolution as a demonstration of the activity correction

In order to clearly illustrate the importance of the activity correction in a nonideal electrolyte mixture, we studied the water dependence in a blended electrolyte of one of the simplest, most well-studied electrocatalytic reactions: the hydrogen evolution reaction (HER). HER represents the cathodic half-reaction in oxidative electro-organic transformations such as oxygen-atom transfer chemistries[71,72] and is a foundational chemistry to understand in any solvent system under consideration for practical deployment. We elected to characterize HER on a Au rotating disk electrode (RDE) cathode using an electrolyte consisting of acetonitrile, water, 0.778 M $TBABF_4$, and 0.022 M tetrabutylammonium hydroxide (TBAOH). (Figure 3-2) Including base helped to ensure that water was the reactant rather than protons, and that there was no large pH swing in the working electrolyte throughout the course of the experiment. HER on Pt in this electrolyte was also studied, but was found to exhibit substantial shifts in Tafel slope at different values of water activity, suggesting (among other possibilities) an inconsistent reaction mechanism; those results may be found in Appendix B.

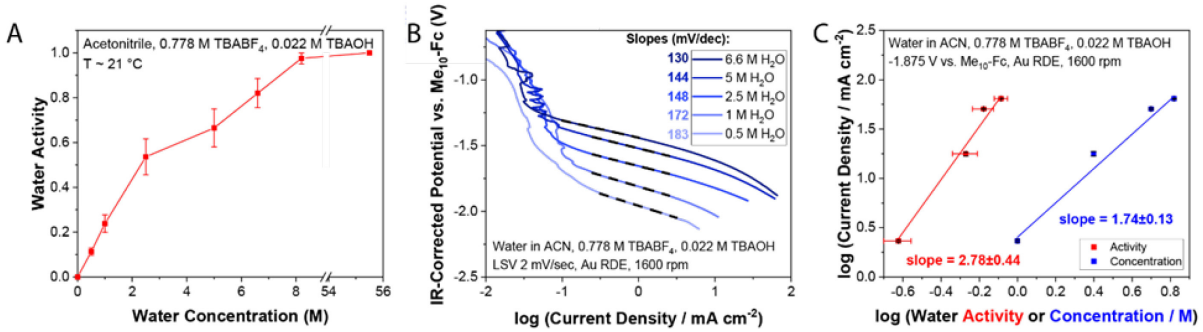

Figure 3-2. Data collected for the purpose of evaluating the mechanism of HER on Au in basic blended electrolyte. A) Concentration-activity relationship for water in acetonitrile with 0.778 M $TBABF_4$, 0.022 M TBAOH, measured using HS-GC-TCD. Error bars represent standard deviation from triplicate measurements. B) Tafel plots for HER at multiple concentrations of water in basic blended electrolyte (water in acetonitrile with 0.0778 M $TBABF_4$, 0.022 M TBAOH), collected on Au RDE under Ar atmosphere (deoxygenated electrolyte) by conducting linear sweep voltammograms at a sweep rate of 2 mV/sec from -0.5 V vs. Me_{10}-Fc

to roughly -2.0 V vs. Me_{10}-Fc. C) Water dependence of HER evaluated at a single potential, here -1.875 V vs. Me_{10}-Fc. X-error bars reflect errors in activity measurements, while y-error bars reflect measured error in Me_{10}-Fc calibrations. Further treatment of errors can be found in Appendix B.

Since the water dependence of HER in a blended electrolyte has never been reported, a new protocol was developed for this purpose. This protocol consisted of four main steps: 1) directly measuring water activity in the electrolytes of interest; 2) calibrating reference electrodes in those electrolytes; 3) performing linear sweep voltammograms in those electrolytes; and 4) combining all the data to yield a water dependence measurement for HER. Detailed experimental methods for each of these steps may be found in Appendix B.

In order to measure water activity, vapor-liquid equilibrium was invoked, which is to say: $\mu_{liquid} = \mu_{vapor}$, where μ represents species chemical potential. A headspace gas sampling protocol was established in which the vapor that had equilibrated over each electrolyte mixture could be sampled and characterized. (see Appendix B) This protocol was used to generate Figure 3-2A. It may be noted that the high concentration of the tetrabutylammonium salt, which is relatively hydrophobic, served to elevate water activity relative to that in a binary water-acetonitrile mixture at a given water mole fraction. (Figure 3-1) This is because unfavorable interactions in general increase species activity. The hydrophobicity of the salt also caused visual phase separation at c_{H2O} = 8.3 M, at which concentration the measured water activity was found to be within error of unity.

It may be noted that the activity measurements described above are bulk measurements, whereas heterogeneous electrocatalysis is an interfacial phenomenon. Why then should a bulk measured species activity value be applicable to reactions taking place at a surface? The surface environment is clearly quite different from the bulk, in ways ranging from specific surface interactions to features of the interfacial electric field.[151] The orientation and concentration of species in this region should also differ from that in the bulk. However, we emphasize that species activity measured in the bulk should be indicative of species activity at a surface in equilibrium with that bulk as long as there are no transport-induced limitations impeding the equilibrium between the bulk and surface, i.e. $\mu_{j,bulk} = \mu_{j,surf}$. Based on the definition of activity, this in turn means:

$$a_{j,bulk} = e^{(\mu_{j,bulk} - \mu_{j,0})/RT} = e^{(\mu_{j,surf} - \mu_{j,0})/RT} = a_{j,surf} \qquad \text{(Eq. 5)}$$

That is to say, regardless of any factors at an electrode surface that might affect species orientation and abundance – e.g., hydrophobicity, catalyst morphology, and polarization – bulk measured activity is equivalent to surface activity so long as surface fluxes are not so high that transport limitations cannot be neglected.

In order to establish a measure of electrochemical potential in each composition of the blended electrolyte, a leak-free Ag/AgCl pseudoreference electrode was calibrated versus decamethylferrocene (Me_{10}-Fc), an electron-transfer (ET) reference species whose redox potential demonstrates a high degree of solvent-independence.[152] It should be noted that the potential of an ET reference is distinct from a pH-dependent reference such as the reversible hydrogen electrode, RHE. Referencing against RHE would yield information about HER at a constant overpotential – a value that accounts for the thermodynamics of the proton transfer. Both the potential of an ET reference such as Me_{10}-Fc as well as that of a coupled proton-electron transfer (CPET) reference such as RHE can be measured in any arbitrary electrolyte.[141,153,154] Both referencing schemes are informative, especially in the context of one another – the difference between results referenced to the ET versus CPET can be attributed specifically to the thermodynamics of the proton transfer. For the purposes of this discussion, we will primarily examine the water dependence of HER at a constant potential versus an ET reference rather than at constant overpotential; results referenced to RHE as well as a further discussion of insights offered by those results can be found in Appendix B.

After obtaining the water activity-concentration relationship, as well as calibrating the reference electrode, HER experiments were conducted. Linear sweep voltammetry was performed using a polished, pre-oxidized Au disk in RDE configuration to generate Tafel plots (Figure 3-2B) as well as water dependence measurements (Figure 3-2C). (see Methods) It should be noted that while the RDE was spun at 1600 rpm for these measurements, similar tests were also conducted at 900 and 2500 rpm to demonstrate that transport limitations did not play a substantial role in the measurements (see Appendix B).

From the measured Tafel slopes of 130-183 mV/dec, we can conclude that the mechanism of HER on Au in the blended electrolyte media likely involves a rate-determining step with a cardinal Tafel slope value of 118 mV/dec, such as the Volmer step (initial electron transfer to a proton donor), the Heyrovsky step at high surface coverage (electron transfer to a solution-phase proton donor following adsorption of H*), or surface diffusion at moderate surface coverage (see Appendix B).[155,156] Of these, the Volmer is the most likely rate-determining step, as this aligns with previous reports on aqueous alkaline HER on Au.[157] The measured Tafel

slope decreases with increasing water content – or in other words, an increased presence of water leads to a larger current response to a given change in potential. It is possible that the difference in slopes is in some way related to the fact that the Tafel fits are performed at different potential ranges (see below for more details). Note that while the reported Tafel slopes were not fit using a Bayesian approach[158] due to persistent ORR background (see Appendix B), sensitivities to the fit range are reported in Appendix B.

With the assertion that the Volmer step is rate-limiting comes the physical picture of a single water molecule donating a proton which combines with an electron to form an adsorbed H-atom. However, working in the blended electrolyte environment allows us to ask: is this the only contribution water makes in this reaction, or are additional water molecules involved in facilitating the reaction? Figure 3-2C illustrates the dependence of HER on both water concentration (blue) as well as water activity (red) at a constant potential versus Me_{10}-Fc. To our knowledge, there is no precedent for the reporting of the water-dependence of HER in this manner. The line fit through the blue data with log(concentration) on the x-axis, which exhibits "saturation"-type curvature, exhibits a slope of 1.74±0.13, while the line fit to the red data with log(activity) on the x-axis gives a slope of 2.78±0.44. It is therefore clear regardless of the x-axis transformation that HER in an alkaline blended electrolyte on Au is dependent on water to a greater-than-1st degree. However, in analyzing the fit to the concentration-based data, one might reasonably propose mechanisms in which two distinct water molecules participate in the reaction – for instance, one as a reactant and one to coordinate the reacting molecule, or perhaps to shuttle a proton toward the electrode following a reaction. In processing the data with log(activity) on the x-axis, it becomes apparent that any simple proposed mechanistic picture involving distinct water molecules is insufficient to explain the reaction kinetics. A 2.78-order water dependence is quite high, and without the invocation of pre-equilibrated surface intermediates (which is incompatible with the assertion of a Volmer rate-determining step), it cannot be justified by the direct participation of ~2.78 water molecules in the reaction – they would all need to participate in a single elementary step. The activity-based data, then, has opened the door of mechanistic interpretation to additional complexity, which we can here begin to further examine.

3.5 The many roles of water

Water, despite its ubiquity in electrochemistry and (electro)catalysis, is an interesting edge case when it comes to intermolecular interactions. As mentioned previously, water has a strong

tendency toward self-interaction, making mixtures of water and other solvents highly nonideal. Moreover, water has several other interesting properties such as its small size, strong dipole, and Grotthuss-style diffusion mechanism for the transfer of protons and hydroxides.[41,159,160] These properties are especially amplified at an electrified interface.[151] As a result, there are many roles water can play in an electrocatalytic reaction. A non-exhaustive selection of such contributions is illustrated here. (Figure 3-3)

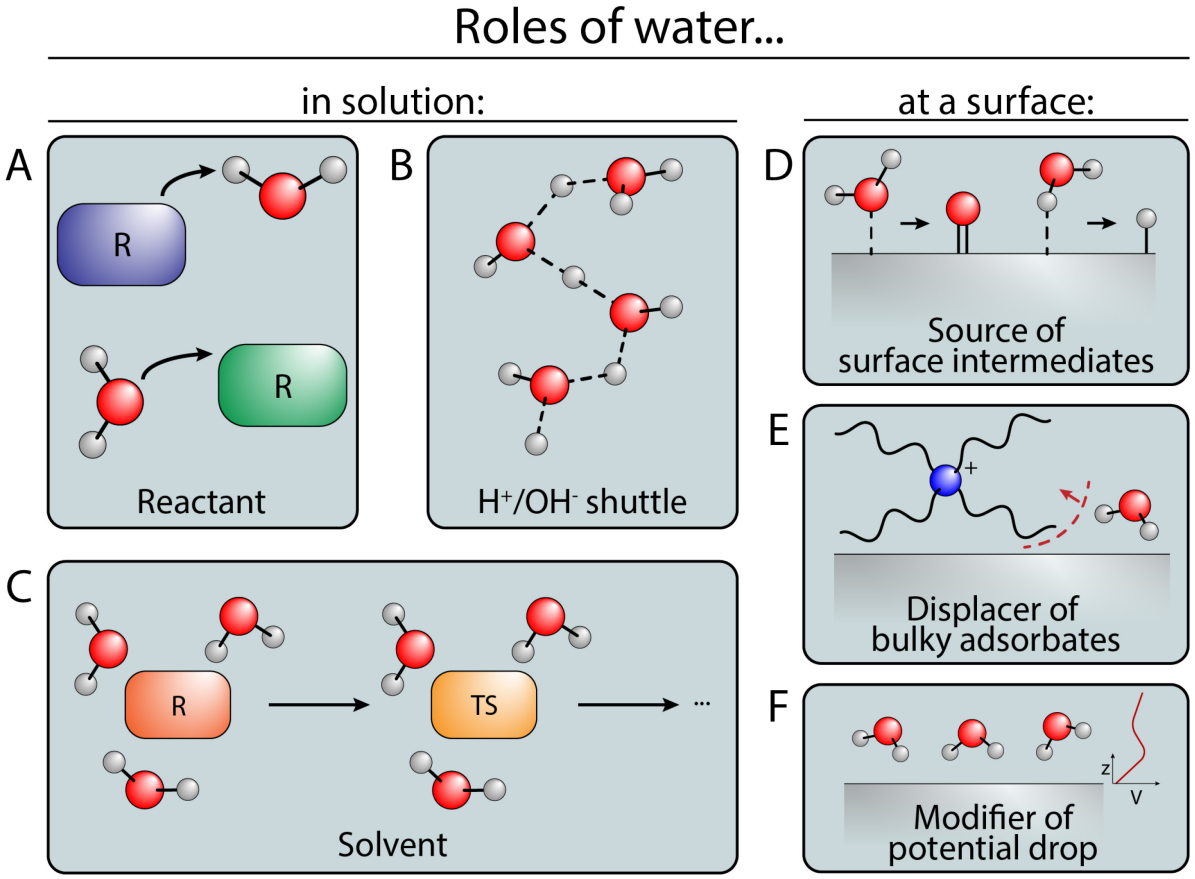

Figure 3-3. Schematics showing selected roles of water in an electrocatalytic reaction: A) as a reactant, B) a proton/hydroxide shuttle, C) a solvent, D) a source of surface intermediates, E) a displacer of bulky adsorbates such at the TBA^+ ion, and F) a modifier of the interfacial potential drop. Note that roles (A), (B), and (C) can also apply at interfaces.

Beyond direct participation as a reactant in solution phase (Figure 3-3A) and/or at a surface (Figure 3-3D), this scheme illustrates that water can also behave in many other ways. Water can act as a buffer, shuttling protons and hydroxide ions (Figure 3-3B); it can also modify the solvation of reacting species (Figure 3-3C). For instance, reactive intermediates' disruption of water H-bonding networks has been implicated in observed water orders of -3 in zeolite catalysis.[161] Water can also displace surface adsorbates such as TBA^+ and acetonitrile (Figure

3-3E)[41,162] – while itself blocking surface sites at the same time. In addition, we hypothesize that it can modify the shape and profile of the potential drop at an interface (Figure 3-3F), much as ions have been shown to do in the context of aqueous electrolytes.[48] On top of these effects, water can participate in specific electrostatic interactions at an interface.

When considering how to justify the 2.78-order water dependence, then, we are left with many possibilities. For instance, it would be reasonable to hypothesize that water participates both as a proton donor (Figure 3-3D) and as a hydroxide shuttle (Figure 3-3B) – or at least that some screening or diffusion of the resulting negative charge is required as the Volmer step proceeds. The question is, to what extent does hydroxide shuttling ability depend on water activity? We could equally easily postulate that outside of water's direct role as a surface reactant (Figure 3-3D), the only other way it acts is to displace surface adsorbates such as TBA^+ or acetonitrile; it is also possible that the transition state during the Volmer step is more stabilized by the presence of water as a solvent (Figure 3-3C), to the point that $\gamma_{\ddagger}$ is proportional to $a_{H2O}^{-1.78}$. Clearly, additional evidence is required in order to elucidate the origin of the 2.78 order dependence on water.

In addition to affecting the water order dependence, it is possible that the adsorbate displacement and potential-drop modification mechanisms illustrated in Figure 3-3E & F contribute to the observed increase in Tafel slopes at lower electrolyte water content. Moreover, the contributions of water as a solvent and proton shuttle (Figure 3-3B,C) leading to decreased Tafel slopes at higher concentrations are also in line with reports of higher concentrations of cations contributing to more facile water reduction.[157] Just as cations have been implicated in stabilizing the transition state for the Volmer step in alkaline aqueous media, so too can water fill this role for itself in the absence of strongly coordinating cations.

It is worth noting at this point that there is no reason to believe the combination of all these effects should yield an integer-order dependence of a reaction rate on a reactant, especially a reactant with as many roles as water. Moreover, although it is certainly the case that reactant species activity should be a relevant descriptor for reaction rate, there is similarly no reason to expect a linear relationship between log(rate) and log(reactant activity). This is because the different roles fulfilled by the reactant of interest are liable to change across a wide concentration range. For instance, trace water has been implicated in surface accumulation even in nominally nonaqueous electrolytes;[42] therefore, perhaps water's roles at a polarized interface are accentuated at low concentrations. On the other hand, maybe water only plays a traditional homogeneous solvating role for reacting species at much higher concentrations.

Because the prevalence of the contributions of any arbitrary solution component can shift as one traverses the selected range of concentrations, it stands to reason that, in general, order-dependence measurements may exhibit curvature even if the direct reaction mechanism itself is not changing.

When a dependence is observed to be linear, it is worth considering what this might mean for the mechanism in question. Such an observation could arise from very consistent contributions of the reactant of interest across the activity range of interest; however, it could also arise due to fortuitous cancellations of different effects as they concurrently become more and/or less relevant to the reaction rate. To fully understand an order-dependence study in this context, it is necessary to tease apart the various roles of the reactant of interest through electrolyte and catalyst design as well as through spectroscopic and modeling approaches.

Finally, we wish to reiterate that the linear-looking, 2.78-order slope achieved in Figure 3-2C is indicative of water order when the potential of the reaction is referenced versus Me_{10}-Fc, not a pH-dependent reference or gauge of overpotential such as RHE. When measured at a constant potential versus RHE (Figure A-B19), dependence of the rate on water content is still positive at most values of water activity, indicating that for the most part, the impact of water is not thermodynamic in nature. However, the slope specifically between the low-activity data points (0.5 M and 1 M water) does appear to be lower, suggesting that there may be more of a thermodynamic / equilibrium potential shift effect at these low values of water activity than at higher values of water activity.

3.6 Extension to other chemistries

In order to demonstrate the broad applicability of our approach with respect to chemistry, we have also conducted water activity measurements – again in acetonitrile-based blended electrolytes – for the analysis of two previously-reported oxygen-atom transfer chemistries: olefin epoxidation[71] and the lactonization of cyclic ketones[72] (Figure 3-4). Both of these chemistries have been shown to exhibit a nonzero rate dependence on water because water acts as the oxygen-atom source in these transformations. After measuring water activities in the exact electrolytes used for these two chemistries via headspace-gas chromatography-TCD (HS-GC-TCD) (Figure 3-4A,B), we shift the values on the x-axis of the water dependence plots to reflect water activity rather than water concentration. (Figure 3-4C,D)

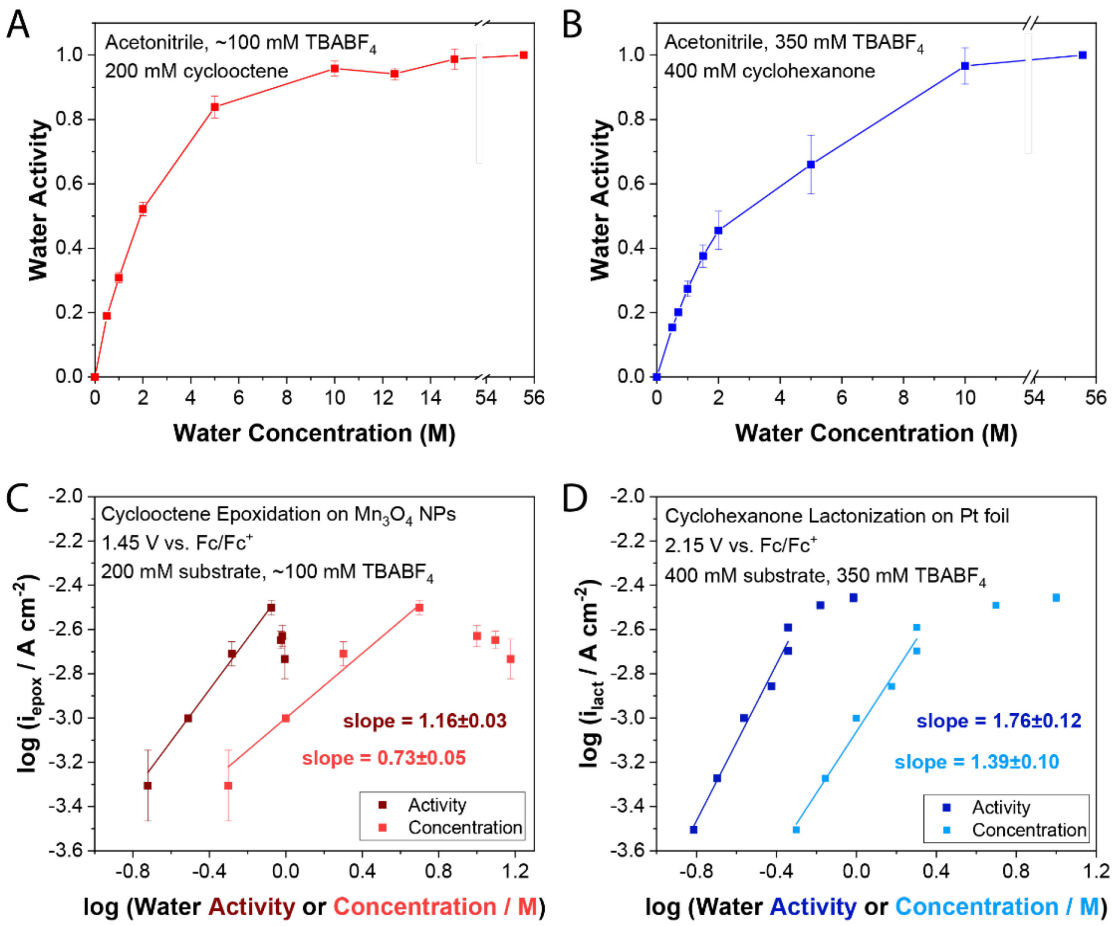

Figure 3-4. The effect of accounting for species activity for O-atom transfer chemistries in blended electrolytes. A) Water activity-concentration relationship in epoxidation electrolyte, consisting of acetonitrile, 100 mM $TBABF_4$, and 200 mM cyclooctene. B) Water activity-concentration relationship in lactonization electrolyte, consisting of acetonitrile, 350 mM $TBABF_4$, and 400 mM cyclohexanone. C) Water dependence data for cyclooctene epoxidation on Mn_3O_4 nanoparticles at +1.45 V vs. Fc, with concentration (light red) and activity (dark red) as descriptors for water availability, as shown in Jin et al.[71] D) Water dependence data for cyclohexanone lactonization on Pt at +2.15 V vs. Fc, with concentration (light blue) and activity (dark blue) as descriptors, as shown in Maalouf et al.[72] Note that in the case of (A) and (C), cyclooctene epoxidation, phase separation (seemingly of the substrate) was observed above ~10 M water.

It can be observed that the lighter-colored data in Figure 3-4C & D – plotted with water concentration as the operative variable – exhibit significantly different slopes when re-plotted as the darker-colored data in Figure 3-4C & D using water activity on the x-axis. These plots suggest that what was previously interpreted as "saturation" behavior – i.e., a waning dependence on water at higher concentrations – may be partially attributable to the curvature

of the water activity-concentration relationship above ~1 M. Some saturation behavior remains after correcting for activity coefficients of water, but as discussed previously, this is not necessarily due to a shift in the mechanism of each reaction in terms of the direct participation of water. Moreover, in the case of cyclohexanone lactonization on Pt, this correction suggests an altogether different interpretation of the mechanism – favoring a rate expression that is closer 2nd-order with respect to water rather than 1st-order. While this conclusion can be easily justified, it would not have been evident without the application of the activity-concentration correction.

Further, it should be noted that for these chemistries which also require an organic substrate, water content can have a substantial effect on substrate activity as well. We were able to perform limited tests on the effect of water content on substrate activity, with inconclusive results. (see Appendix B) It stands to reason, however, that the activity of hydrophobic substrates may increase with increasing water content – this is qualitatively borne out in the observed phase separation of the epoxidation electrolyte at high water content. Because the rate of cyclooctene epoxidation was shown to be proportional to $c_{cyclooctene}^{0.7}$, it is possible that the two order dependence measurements are interdependent on one another. In cases such as this, it is advisable to carefully measure the effects of one species' activity on another species' activity, and to design experiments such that one species' activity is held constant while the other is varied. This may require the formulation of electrolytes that contain different concentrations of a component whose activity is being held constant, which may seem counter-intuitive. For example, when conducting a water dependence experiment for cyclooctene epoxidation, it may be necessary to decrease the volume of cyclooctene added to the electrolyte as the water content increases, so that the activity of cyclooctene is the same at all tested conditions.

3.7 Toward a molecular picture of species activity

A desire for molecular understanding of how the water activity-concentration relationship arises in the blended acetonitrile-water system drove us to investigate this system using molecular dynamics simulations. (Figure 3-5) Molecular dynamics simulation systems composed of acetonitrile molecules,[163] tetrabutylammonium cations,[164] and tetrafluoroborate anions (force field parameters taken from Liu et al.[165]), and a variable number of water molecules (using the TIP3P force field with SHAKE constraints)[166] were constructed using the Packmol software.[167] (see Methods) It should be noted that the force field used in these

simulations has not been rigorously validated in the context of the blended electrolyte; as such, the simulation results should not be taken quantitatively, especially those at very low concentrations of water.

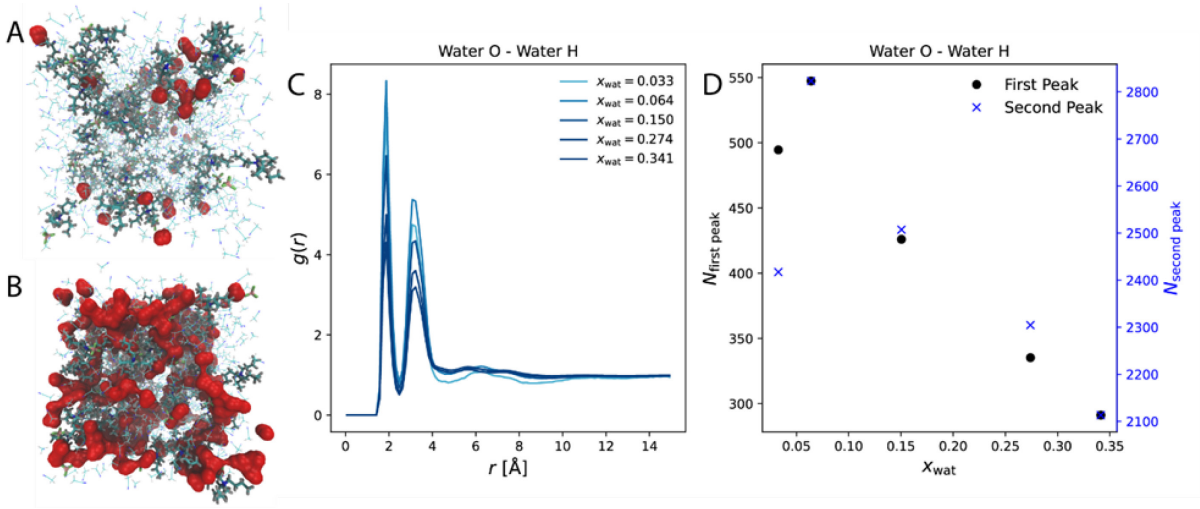

Figure 3-5. Results of molecular dynamics simulations of the acetonitrile-water blended electrolyte with 0.8 M $TBABF_4$. A) Snapshot of 0.5 M water condition; B) snapshot of 6.6 M water condition; C) radial distribution function showing relative abundance of water H-atoms as a function of radius from a central water O-atom; D) plot showing integrated areas of the first and second water peaks from (C) for each composition, versus electrolyte water mole fraction. In (A) and (B), water is shown as a red surface; TBA^+ and BF_4^- are shown in the licorice representation with carbon light blue, nitrogen blue, hydrogen gray, boron pink, and fluorine lime green; and acetonitrile in lines representation with the same color scheme.

Figure 3-5A & B are snapshots of the electrolyte box at low (0.5 M) and high (6.6 M) concentrations of water, respectively. Similar to previously reported simulations,[41] we observe relatively isolated water molecules at low concentrations and clusters or "nanodomains" at higher concentrations. The hydrophobic TBA^+ ions appear to carve out pockets where water is less concentrated, while water in the "nanodomains" becomes energetically similar to bulk water.

It is fairly straightforward to interpret the molecular pictures shown here to justify the concave-down trend in the activity curves (Figure 3-1, Figure 3-2A) in the dilute-water limit. At the lowest concentrations of water (Figure 3-5A), most water molecules are completely surrounded by acetonitrile and $TBABF_4$ – perhaps as little as 10-20% of water molecules are H-bonded to other water molecules. At this condition the chemical potential of any single water molecule is quite high, as it is engaging in less favorable interactions than it would be in a pure water phase.

As water is added into the system and we approach near-saturation conditions (Figure 3-5B), “wires” and even “domains” of water form in which water molecules are clustered with themselves. Under these conditions, the water molecules engage in more stabilizing interactions, and the chemical potential of any one water molecule is less than that of a water molecule in the dilute-water case. That is, the measured “energy per additional molecule” decreases as the concentration of water increases. This corresponds to a decrease in activity coefficient with increasing water concentration, and is borne out as a concave-down trend in the activity-concentration relationship. Notably, we can see from the radial distribution function showing water O – water H distances in Figure 3-5C, as well as the plot of the g(r) peak area values in Figure 3-5D, that water does have a propensity to cluster with other water molecules at all concentrations. The absolute abundance of water clusters increases with increasing concentration, as it is of course entropically disfavored for all water in the low-concentration limit to remain bound to itself. However, there is an enthalpic driving force that encourages excess water coordination, especially at the conditions of highest chemical potential per molecule of water.

A question that remains through this analysis, however, is whether certain sub-populations of water – such as dimers or tri+-mers – are more reactive than other sub-populations – for example, lone water molecules. While the probability of finding these populations gradually changes with water activity (Figure 3-5D), it is perhaps remarkable that despite all such reasoning, water activity remains the descriptor in the system that tends to linearize observed experimental trends.

While these results should be considered only preliminary, they are interesting enough to warrant validation in an experimental setup – which we strongly advocate. In the future, it would be interesting to take the further step of calculating activities directly from simulations as part of this validation, as well as to spectroscopically probe the structure of water in bulk blended electrolytes. In addition, due to the catalytic relevance of the surface, it is worth assessing the interfacial structure of water in the blended electrolyte – ideally under polarization – through both simulation as well as spectroscopy.

3.8 Conclusions

In this work, we emphasize the importance of directly measuring the thermodynamic activity of species relevant to electrocatalytic reactions in order to properly interpret electrochemical kinetic data. Headspace gas chromatography techniques have been used toward this end. Upon

applying a correction to account for the species activity coefficient in the solvent of interest, water dependence data for HER as well as previously studied O-atom transfer chemistries yields water orders that were previously obscured by changes in activity coefficient. However, these dependences do not necessarily exhibit linear slopes, nor slopes indicative of integer-order dependence, because of the many roles that water can play in the electrochemical system. Water mixtures are particularly prone to being affected by nonidealities, although any mixed system consisting of components that exhibit intermolecular interactions that strongly differ from self-interactions will also yield substantial nonidealities. Finally, we also speculate at the molecular origins of the water activity-concentration relationship in the blended electrolyte, for which validation of molecular simulations with experimental data is required. Principles discussed in this work are applicable to the deconvolution of system parameters in the future study of electrochemical active species dependence as well as solvent effects. Further, the relevance of these conclusions also extends to environments similar to blended electrolytes where local solvation deviates from that of a pure solvent, such as in zeolites and metal-organic frameworks.

3.9 Methods

3.9.1 Headspace-Gas Chromatography-TCD measurements for activity quantification

Each tested electrolyte composition was prepared in a 20-mL glass headspace vial under unaltered lab atmosphere, then capped and allowed to equilibrate at room temperature (~20-23 °C) for at least 12 hours. An Agilent automated headspace sampler then sampled from the electrolyte headspace, sending each sample through a DB 624-UI gas chromatography column that led to a thermal conductivity detector (TCD). The ideal gas law was assumed to hold for these headspace samples – a generally good assumption for air at STP. A pure water sample was taken in-between consecutive electrolyte samples. Using a Raoult's law referencing scheme in which the activity of pure water was defined as being equal to 1, the activity of water in each electrolyte was calculated as:

$$a_{H2O,sample} = \frac{A_{H2O,sample}}{A_{H2O,pure}} \quad \text{(Eq. M1).}$$

Triplicate measurements were conducted in this way to generate Figure 3-2A.

3.9.2 HER experiments: Au disk in RDE

The Au disk used in experiments was prepared[168] by consecutive polishes with 0.3 μm alumina on a vinyl pad (30 sec – 2 min) and 0.05 μm alumina MicroPolish on a microfiber pad (2 min), then sonicated twice in fresh 50:50 Milli-Q:acetone by volume (~2 min each). The disk was then electro-polished by inserting it into a rotator and cycling 200x between 0 and +1.800 V vs. a Pt wire counter electrode at a rate of 1 V/sec in an electrolyte of 0.1 M H_2SO_4. After a double-rinse with Milli-Q and drying with a Kimwipe, the electrode was ready for use. The RDE was inserted into a custom H-cell containing the working electrolyte, leak-free Ag/AgCl pseudo-reference electrode, as well as Pt wire counter electrode. The working compartment was sealed using a Pine Gas-Purged Bearing into which 20 sccm Ar gas was flowed to blanket the electrolyte and maintain an inert atmosphere. After reacting away the dissolved oxygen gas in solution, LSVs performed at a sweep rate of -2 mV/sec yielded the Tafel plots shown in Figure 3-2B. A cut through at a constant potential versus Me_{10}-Fc on Figure 3-2B, combined with the activity concentration relationship in Figure 3-2A, yielded the water dependence shown in Figure 3-2C.

3.9.3 Molecular dynamics simulations

The simulated MD systems were initially relaxed using conjugate gradient minimization, and then the system volume was relaxed over the course of a 1 ns NpT ensemble simulation using the Nose-Hoover thermostat and barostat, with an integration timestep of 1.0 fs. Upon volume relaxation, systems were prepared at the equilibrated densities, followed by a production NVT simulation of 1 ns using the Nose-Hoover thermostat, with a timestep of 1.5 fs. Densities of simulated electrolytes were found to be within 10% of experimental values.

4 Characterizing Direct Electrochemical Benzylic C-H Activation in a Blended Electrolyte

In this chapter, we extend the insights of Chapter 3 further to develop and study a method for partially oxidizing benzylic C-H bonds through direct electrochemical activation. This report contains current progress on reaction characterization, which will be supplemented with a small number of additional experiments prior to submission for publication in a peer-reviewed journal.

4.1 Background and motivation for electrochemical C-H activation

C-H activation, or the breaking of a carbon-hydrogen bond, is a desirable approach to achieving organic chemical transformations in as few steps as possible, with as little waste as possible.[169] However, because C-H bonds are ubiquitous in organic chemicals, activation of those bonds needs to be directed in some way in order to achieve reasonable selectivities. In addition, C-H activation is relatively difficult compared to O-H or N-H activation due to the low acidity of the C-H bond. In other words, heterolytic cleavage of a C-H to form C^- and H^+ is very unfavorable. On the other hand, C-H activation via homolytic cleavage – splitting C-H into $C^\cdot$ and $H^\cdot$ – is easier for C-H than for O-H or N-H, meaning thermodynamics impart a path toward selectivity in the homolytic case. Thus, routes to C-H functionalization often rely on coordination by a transition metal complex, or pathways that involve formation of a radical. This is one area of chemistry in which electrocatalysis has a chance to shine.

One quintessential aspiration of C-H activation is the conversion of methane to methanol. Practically, this is because methanol is not only a substantially more valuable chemical than methane in the era of hydraulic fracturing, but it is also much easier to transport, being a liquid at STP. However, the partial oxidation of methane has proven difficult. Methane's C-H bonds

exhibit the highest bond dissociation energy of any sp^3 C-H bond, and once the kinetic barrier to C-H activation has been crossed, it is often most favorable to over-oxidize CH_4 to CO or CO_2. Numerous works over the years have tried to oxidize methane to methanol, but achieving partial oxidation with any great degree of selectivity or high rates has been out-of-reach until relatively recently.[16,170] Instead, we can consider other C-H activation reactions as simpler starting points that may offer insights into approaches to more difficult C-H activation reactions.

A class of reaction that fits this description while also having practical applications is benzylic C-H activation – activation of a C-H bond adjacent to a phenyl ring. The simplest example of a benzylic substrate is toluene. For this work, we focus on p-xylene – a benzene with 2 methyl substituents para to one another. P-xylene is currently used largely as a feedstock for the production of terephthalic acid, which is itself a precursor to PET plastic. The conversion of p-xylene to terephthalic acid is brought about through the Amoco process, which is built around a thermochemical catalytic reactor.[171,172] In this reactor, p-xylene and O_2 gas are combined at ~200 °C and 15-30 bar, contacted in a solvent environment consisting of acetic acid, Co/Mn-based salts as catalysts for the C-H activation, and a Br^- source such as HBr that allows for radical propagation. The process achieves 98% conversion of p-xylene, with a terephthalic acid yield of 95%. However, the harsh, corrosive environment of the reaction requires thick-walled, highly engineered reaction vessels; the O_2 supplied at high pressures poses a safety hazard; and through the process, much of the acetic acid solvent is burned in the presence of the O_2, leading to the direct production of >1 mol of CO/CO_2 for every 4 mol p-xylene fed to the process. Thus, an alternative route with fewer direct emissions would be appealing.

The literature contains several examples of electrochemical benzylic C-H activation/partial oxidation, but the approaches to catalysis and sources of the O-atom that is ultimately incorporated into the product have varied widely. For instance, early reports of benzylic C-H activation tended to utilize homogeneous inorganic mediators for catalysis, containing active centers/ions such as Ce,[173–175] V,[176] Mn,[175,177] Co,[178,179] Rh,[180] Cu,[176,178,179] Bi,[181] and Se.[182] More recently, the use of organic mediators such as tBuOOH[183] and quinuclidine,[77] or even combined schemes using both metal and organic mediators such as Co/NHPI[184,185] for selective benzylic C-H oxidation has gained traction. Direct, unmediated C-H activation on carbon,[147,186,187] Pd,[188] and Pt[189] electrodes has also been reported. Across all of these reports, the molecules used as the O-atom source (or "oxidant") for the final product included methanol,[173,178,179,186,187] tBuOOH,[180,181] H_2O_2,[177] O_2,[77,176,185,188] and water.[147,174,175,183,189] The

emissions, hazards, and poor atom economy associated with certain of these oxidants, namely methanol, tBuOOH, and H_2O_2, make them less attractive as feeds to a C-H activation process. All told, we know of only a couple documented cases in which benzylic C-H bonds were activated directly – without the use of a mediator – at low temperatures, and where an abundant and benign oxidant such as O_2 or water was used as the O-atom source.[147,189] Of these examples, only one explicitly studied impacts of oxidant content upon the C-H activation reaction; however, nonidealities in the solution were not addressed, nor were partially oxidized products able to be isolated and characterized.[147]

In this chapter, we report findings that benzylic C-H bonds in substrates such as xylene can be activated directly, using water as the O-atom source, at a carbonaceous electrode, to produce primarily p-tolualdehyde. We characterize the response of the reaction rate to different perturbations in the system, such as system configuration, electrode material, potential, substrate concentration, water content, kinetic isotope effects, and pH. We propose a likely reaction pathway that involves a concerted proton-electron transfer from the substrate, invoking effects from Chapter 3 to explain a very high-order dependence of the reaction rate on water. In addition, we speculate on the role of the carbonaceous electrode material in this transformation, as it is surprisingly the case that somewhat low Tafel slopes are observed, despite the reaction being insensitive to electrode metals content.

4.2 Initial methods and characterization of product

4.2.1 Initial methods

To begin our investigations, we used a 1-compartment electrochemical cell, outfitted with a stir bar and outlet ports. The working electrode was chosen as MnO_x nanoparticles (NPs) on annealed Toray 060 carbon paper, in line with insights from prior works indicating the effectiveness of MnO_x NPs for O-atom transfer catalysis.[71] Pt foil was employed as the counter electrode. For the electrolyte, a blended electrolyte consisting of acetonitrile, varying amounts of water (5 M base case), $TBABF_4$ (0.1 M initially), and varying amounts of p-xylene (200 mM base case) was used. A leak-free aqueous Ag/AgCl pseudo-reference electrode calibrated to Fc and Me_{10}-Fc was used as the reference.

Products of the reaction were characterized primarily by NMR spectroscopy, by first diluting the electrolyte to a known volume, then preparing a sample with an internal standard of known concentration. Peak areas for products were compared to peak areas of the internal standard on

the basis of NMR calibration data from product standard solutions. (see Appendix C) Where applicable, gaseous products were detected in separate experiments through the use of in-line gas chromatography.

4.2.2 Possible products of benzylic C-H oxidation of xylene

Figure 4-1 depicts a variety of possible products that we anticipate making through the oxidation of p-xylene. Included are all combinations of oxidations at the benzylic positions, as well as representative sp^2 oxidation products from activation of C-H bonds directly on the aryl ring, and CO and CO_2, which represent over-oxidation products. The boxed species, 4-methylbenzyl alcohol (red), p-tolualdehyde (yellow), p-toluic acid (green), terephthalaldehyde (light blue), 4-carboxybenzoic acid (indigo), and terephthalic acid (violet) are species for which NMR standards were prepared. (see Appendix C)

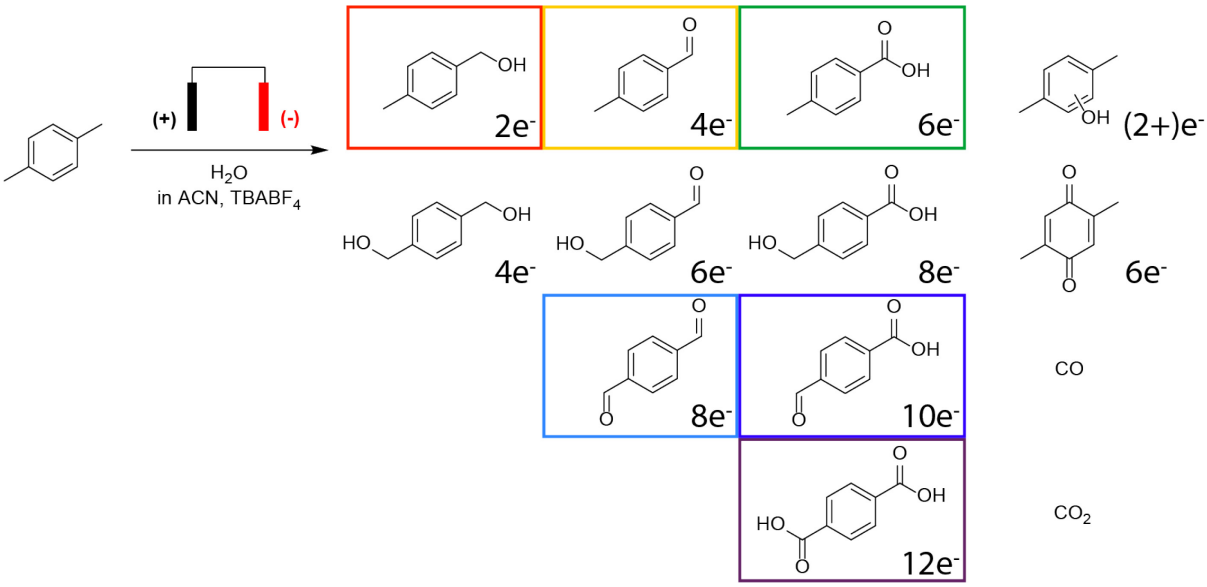

Figure 4-1. Anticipated products of electrochemical xylene oxidation in the presence of water. Numbers indicate the number of electrons required to produce each product. Boxed species were purchased and used in making NMR standards for electrolysis product analysis.

A few points should be noted here about the product distribution. First, the range of possible products is broad because it includes not only several degrees of oxidation at one benzylic carbon, but also combinations of oxidations at both benzylic positions. Certainly product analysis would be simpler and more straightforward for a substrate with fewer benzylic positions, such as toluene – but at the same time, the electron-donating p-methyl group makes oxidation of xylene easier than oxidation of toluene (see Section 4.9: Substrate scope & initial Hammett analysis). In addition, because oxidation at either one of the methyl groups has an

electron-withdrawing effect on the opposite methyl group, we anticipate that it is more thermodynamically difficult to achieve oxidation at both methyl groups than at just one. Because terephthalic acid is only sparingly soluble in acetonitrile and water in its acidic form, we relied on the formation of solids and subsequent alkaline treatment and NMR on those solids to indicate terephthalic acid formation – although again, because oxidation decreases propensity for deeper oxidation from a thermodynamic perspective, we did not expect initial tests to yield much if any terephthalic acid product. Finally, it should be noted that CO/CO_2 coming from the electrolyte doesn't necessarily come from the oxidation of xylene; it might instead be a product of acetonitrile breakdown. ^{13}C labeling experiments would be necessary to identify the source of any CO/CO_2. Even then, if these products could be ascribed to xylene oxidation, it would be necessary to identify other unlisted degradation products in the electrolyte in order to ascertain the number of electrons involved in the oxidation.

4.2.3 Observed products of benzylic C-H oxidation of xylene

Following electrolysis at roughly +1.4 V vs. Fc, passing a total of 30-50 coulombs, and subsequent product analysis in the 1-compartment cell, two major products were identified: 4-methylbenzyl alcohol ("alcohol") and p-tolualdehyde ("aldehyde"). The aldehyde was identified as the major product, accounting for ~20% of the anodic Faradaic efficiency, while the alcohol accounted for less – about 5-10% FE. (Figure 4-2)

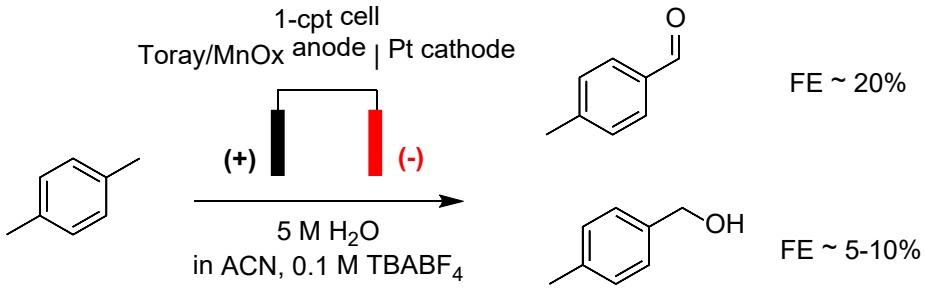

Figure 4-2. Major products from initial xylene oxidation experiments in the 1-compartment cell.

In addition to these main products, very small amounts of p-toluic acid and terephthalaldehyde were occasionally observed via NMR, with low FEs of ~1%. While the balance of FE was not fully studied in the 1-compartment configuration, minimal OER (FE <10%) was observed through subsequent experiments using in-line gas chromatography. Similarly, little to no CO/CO_2 were detected.

Through additional experiments using in-line gas chromatography, the counter reaction was confirmed to be HER with ~100% FE. (see Appendix C)

4.3 Impact of cell configuration

Part of the question of missing FEs at the anode can be answered through examining the impact of altered electrochemical cell configuration on the reaction. We experimented with insertion of a porous polyethylene-based separator (Daramic) to prevent movement of products between the anode and cathode compartments. When the cell was separated into 2 compartments in this way, the FE for alcohol product decreased substantially, to somewhere between 0-3%. In addition, the catholyte compartment was observed to be darker in color (yellow to brown) than the catholyte. It is difficult to explain the color changes observed in the catholyte – our hypothesis is that this can be caused by a small amount of cathodic polymerization of xylene and products. To explain the decrease in the amount of alcohol produced during the reaction in the 2-compartment cell, there are two most likely options: 1) alcohol is produced at the anode and is mostly further oxidized to aldehyde, although some can "escape"; and by inserting the separator, the less-oxidized alcohol is concentrated in the anolyte and prevented from escaping, and thus is further oxidized to the aldehyde. Or, option 2) the aldehyde is the main product directly from the anode, and this aldehyde can be partially reduced at the cathode back into the alcohol; so by inserting the separator, we are preventing the reduction of the product. This raises the possibility that back-reactions may decrease measured FEs over time.

A simple test of these hypotheses is to separately quantify the xylene oxidation products from the anode and cathode. More alcohol in anode compartment than the cathode compartment would indicate that the alcohol is produced at the anode and diffuses down its concentration gradient, over to the cathode side (option 1). More alcohol in the cathode compartment than anode compartment would indicate that the alcohol is produced by reduction of the aldehyde at the cathode, and diffuses down its concentration gradient, over to the anode side (option 2). Based on our experiments, it appears that option 1 (anodic co-production) is more likely, as the absolute concentration of alcohol is higher in the anolyte than in the catholyte. It is worth noting, however, that the relative concentration of the alcohol versus aldehyde is substantially higher in the catholyte than the anolyte. This result, then, does not preclude the possibility that both reactions (fast anodic alcohol oxidation and cathodic aldehyde reduction) are taking place with comparable rates, and this approach would not be sufficient to identify this. To further identify the sources of the products, two experiments could be run: 1) spike a typical product

amount of alcohol into the anode chamber and run the electrolysis. This will give a sense for the reaction rate of alcohol to aldehyde at the anode, which can then be used to back-calculate whether concentration of alcohol in the anolyte is sufficient to explain differences in rate toward aldehyde with vs. without the separator. 2) Spike some aldehyde into the catholyte chamber and apply a typical cathodic voltage reached during normal electrochemical operations, observing reduction reaction rate; compare these results to those achieved in (1). Initial experiments suggest that alcohol is oxidized to aldehyde at roughly the same rate as xylene is, and also that aldehyde can in fact be reduced to alcohol (as well as to xylene) at a Pt cathode. Notably, these former results may imply that the RDS of the xylene oxidation mechanism is either after formation of the alcohol, or that the RDS and alcohol oxidation steps take place at similar rates. As for the results showing aldehyde may be reduced: this merely motivates short-duration experiments in which products are prevented from reaching the cathode as much as possible so as to measure the results of direct oxidation.

Whether option 1 or 2 is closer to the truth determines how we calculate FE. For option 1, $FE = FE_{alc} + FE_{ald}$; for option 2, $FE = FE_{ald} + 2FE_{alc}$, to account for the fact that all alcohol generated was originally aldehyde, a product requiring twice the number of ET steps as xylene -> alcohol. For the purposes of the subsequent sections, we have calculated treating option 1 as valid when reporting separate FEs for aldehyde and alcohol, and when conducting kinetic analysis we have focused entirely on the major product p-tolualdehyde, excluding all other product partial currents. It should be noted, however, that due to the relatively low FEs measured for alcohol production in the 2-compartment setup – usually at least 10x less than the FE measured for aldehyde production – the method selected out of these two does not greatly impact analysis.

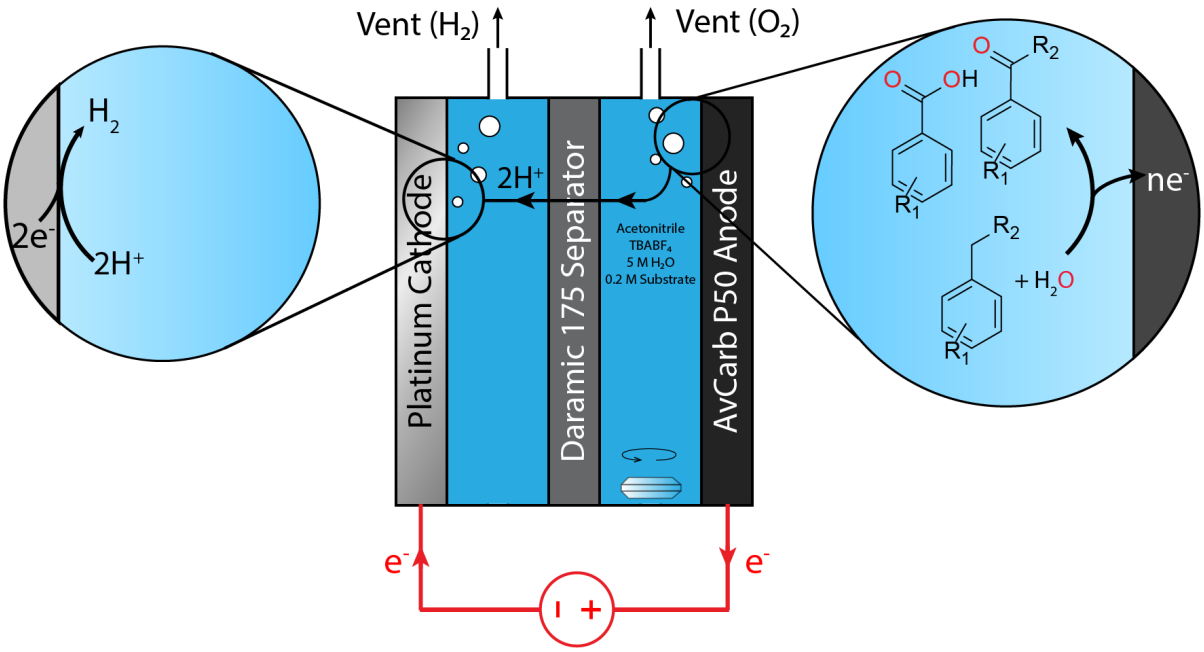

Figure 4-3. The 2-compartment cell setup used in most of the subsequent analysis. p-substituted toluenes (mostly p-xylene) are oxidized at the anode, protons travel across the cell, and hydrogen is evolved at the cathode.

4.4 Impact of charge passed

While still using the 1-compartment cell, we also made note that the FE for xylene oxidation decreased with increasing charge passed. (Figure 4-4) Increasing the number of coulombs passed in a single experiment from 5 to 50 C led to a decrease in aldehyde FE from ~25% to ~15%. The FE for alcohol production remained roughly constant. This also may be attributable to back-reaction of the aldehyde over time, or it could indicate the decreasing activity of the electrode for facilitating xylene oxidation. The impact of passing different amounts of charge on FE has not yet been studied in the 2-compartment cell, but could also aid in developing an understanding of the variety of reactions occurring at the cathode.

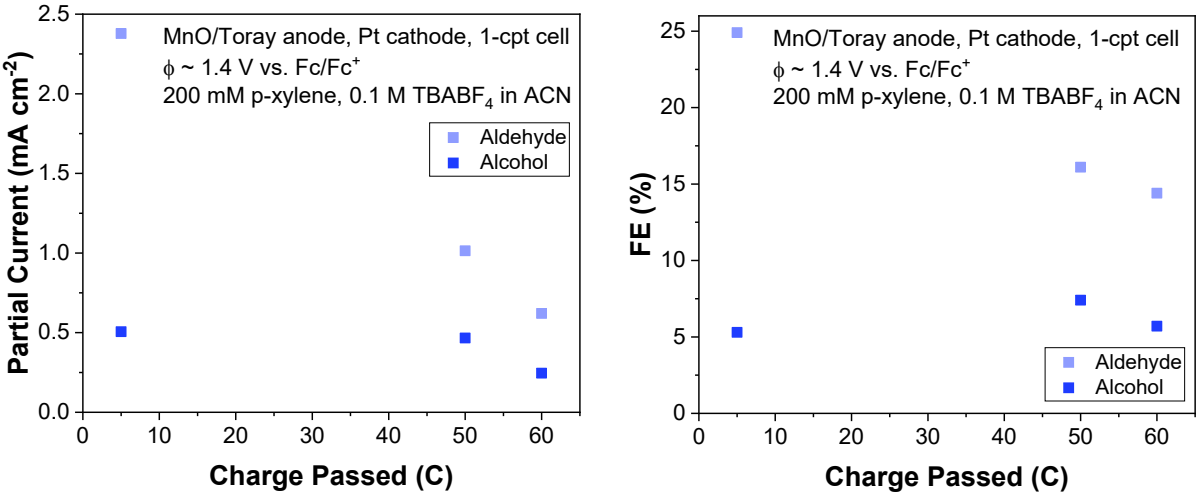

Figure 4-4. Impact of total charge passed on average partial current and average FE over the course of a xylene oxidation experiment.

4.5 Impact of catalyst materials

4.5.1 Metal- and metal-oxide-based catalysts

In order to understand the role of the catalyst, a variety of anode materials were tested for their abilities to facilitate xylene oxidation. We first investigated the effectiveness of various metal-oxide nanoparticles for xylene oxidation, deviating from MnO_x to investigate FeO_x, CoO_x, as well as Ir-decorated MnO_x, all supported on the same Toray 060 carbon paper, and all of which had previously demonstrated activity for O-atom transfer. In addition, we conducted xylene oxidation over a Pd foil due to molecular Pd catalysts' precedent for C-H activation activity, as well as a control experiment of xylene oxidation on bare carbon paper. (Figure 4-5)

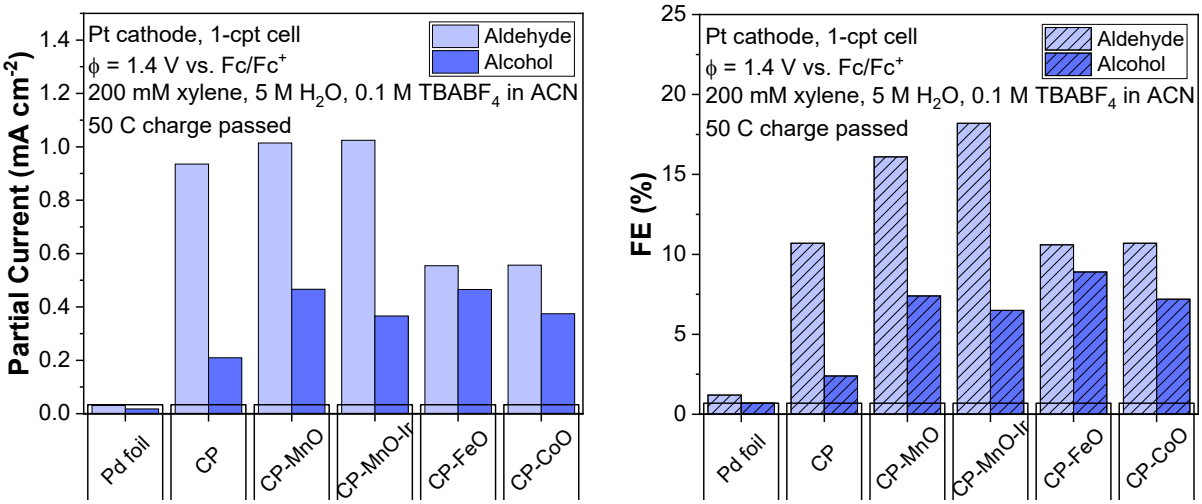

Figure 4-5. Partial currents and FEs for xylene oxidation on a variety of metal- and metal-oxide-based catalysts: Pd foil, bare Toray 060 carbon paper, MnO_x NPs on Toray 060, Ir-decorated MnO_x NPs on Toray 060, FeO_x NPs on Toray 060, and CoO_x NPs on Toray 060. Note the 1-compartment cell setup used in these tests.

Xylene oxidation currents and FEs were lower on the Pd foil than on any of the other experiments. While it is possible that lower currents could be attributed to lower electrochemically active surface area (ECSA) for a foil electrode versus a carbon-paper-based electrode, the decrease in FEs for xylene oxidation likely indicates that Pd is not a very good xylene oxidation catalyst. Comparing all of the metal oxide catalysts, we observe that perhaps the activity of the MnO_x NPs is better than that of the FeO_x and CoO_x; however, comparing especially partial current density measurements, the blank carbon paper control experiment would indicate that these variations are within the experimental noise. In fact, it appears that from a partial current perspective, there is very little difference between xylene oxidation on MnO_x NPs and the bare carbon paper support. Modest increases in FE for Mn-containing electrodes are suggestive, but not strong indicators that MnOx is serving as a good catalyst material.

4.5.2 Carbon- and inert-oxide-based electrodes

Since the bare Toray 060 showed considerable activity for xylene oxidation, we investigated the activities of other carbon papers as anodes in a 2-compartment cell setup. Using the MnOx on Toray 060 as a baseline, other materials investigated included: AvCarb P50 carbon paper; Freudenberg-H14 carbon paper; Sigracet BC carbon paper with microporous layer (MPL); and fluorine-doped tin oxide (FTO) – essentially, conductive glass. (Figure 4-6)

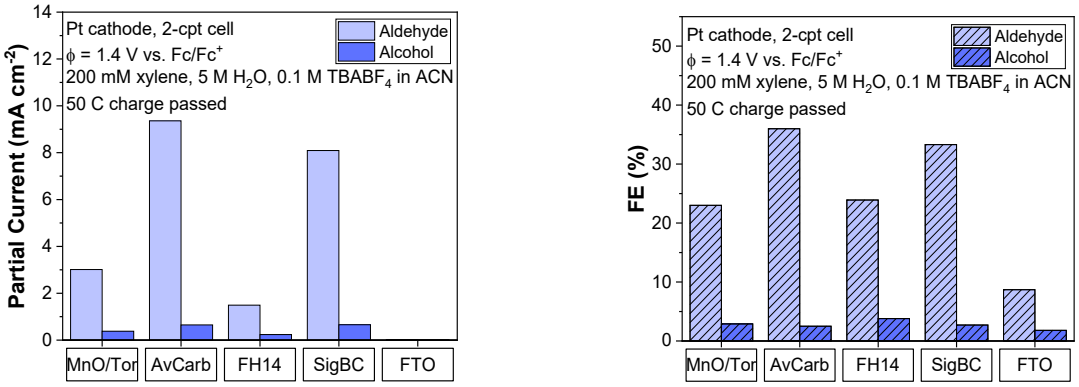

Figure 4-6. Partial currents and FEs for xylene oxidation on a variety of carbon- and glass-based electrodes: Toray 060 carbon paper, AvCarb P50 carbon paper, Freudenberg-H14 carbon paper, Sigracet BC carbon paper with MPL, and fluorine-doped tin oxide glass (FTO).

Differences between these supports were considerably larger than differences between different metal oxides on a given carbon support. FTO showed extremely low currents and xylene oxidation FEs of ~10%, and Freudenberg-H14 electrodes likewise exhibited a lower partial current density for xylene oxidation than Toray 060 carbon paper. However, other materials such as Sigracet BC and AvCarb P50 demonstrated increases in FE and partial current relative to Toray 060. The best-performing electrode out of those tested was found to be AvCarb P50, with a partial current density of almost 10 mA/cm^2 toward aldehyde production at the tested potential – an increase by nearly 4x over Toray. FEs toward xylene oxidation were nearly 40% in total on the AvCarb anode.

One interesting point to note is that in most of these tests, trends with respect to FE and partial current were consistent with one another; in other words, when a material or catalyst exhibited a higher FE than another material or catalyst, it also exhibited a higher partial current density toward xylene oxidation. There are at least two possible explanations for this: 1) there is a sort of autocatalytic property to the xylene oxidation reaction, wherein higher currents cause the reaction to proceed more easily. However, the more likely option is related to the nature of the measurements: 2) because a constant amount of charge is passed in each of these experiments, the duration of the experiment – and therefore the amount of time the electrolyte has to equilibrate – depends upon the rate of the reaction; as such, a longer experiment with lower total current density is also more likely to exhibit lower FEs from loss of oxidized product to the cathode, and subsequent reduction of that product. This mechanism assumes that product can be oxidized at the cathode; this is a phenomenon for which we have evidence. (see

Appendix C) This also raises the point that the results in Figure 4-6 and Figure 4-5 cannot be directly compared, since they were conducted in different cell setups. The 1-compartment cell used to generate Figure 4-5 skews results toward lower FE and partial current measurements, and tends to under-estimate differences between experiments. While we are confident that carbon material has a greater impact on xylene oxidation partial current and FE, a quantitative comparison could more accurately be made by conducting all relevant experiments in the same cell configuration.

The question arose: what could explain the effectiveness of certain carbon papers over one another, in contrast to the seeming lack of impact of the incorporation of metal oxides on those carbon papers – and what implications does this have for our molecular understanding of the catalysis taking place? In particular, carbon is normally viewed as an electrode material that does not strongly coordinate reacting species; in general, practitioners of electrocatalysis treat carbon-based electrodes as capable of achieving only outer-sphere transformations. To reconcile this, we can turn to the vanadium redox flow battery literature as an example. In vanadium redox flow batteries, carbon-based electrodes are often employed, and yet ongoing discussions in this literature suggest that electron-transfers and O-atom transfers taking place in these investigations may be inner-sphere, particularly at active sites containing oxygen functional groups.[190] This would suggest to us that it is in fact possible for carbon-based electrodes to facilitate inner-sphere electrochemistry. We therefore hypothesize that some mechanism may facilitate inner-sphere electrocatalysis for xylene oxidation on carbon electrodes – perhaps coordination to O-functional groups, or perhaps a mechanism unique to xylene, such as pi-stacking between the aryl ring of the substrate and graphitic portions of the carbon electrode. We began to investigate these hypotheses, and present initial results below.

4.5.2.1 Characterizing structural differences between carbon electrode materials

We probed the hypothesis that pi-stacking interactions between xylene and electrode could lead to inner-sphere catalysis, and therefore that variation in xylene oxidation activity between different carbonaceous electrodes could be explained by variation in the graphitic character of the electrode. To do this, we compared Raman spectra of 3 different carbon-based electrode materials exhibiting different activities for xylene oxidation: Freudenberg-H14 (least active), Toray 060 (more active), and AvCarb P50 (most active). (Figure 4-7)

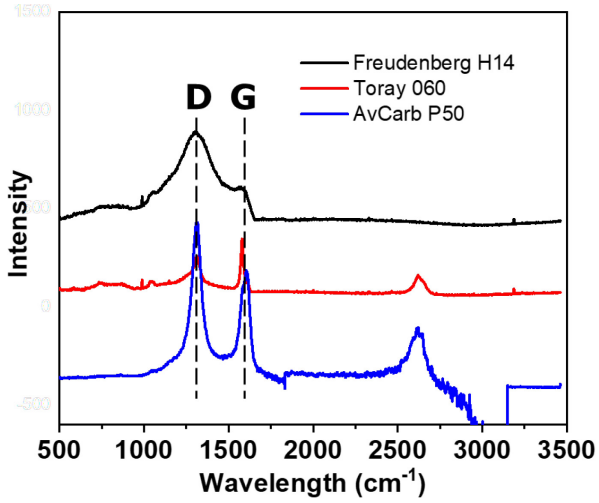

Figure 4-7. Raman spectra of 3 tested carbon-based materials: Freudenberg-H14 (black), Toray 060 (red), and AvCarb P50 (blue). Freudenberg and Toray Raman credit: Dengtao Yang.[191] AvCarb Raman credit: Kyoungsuk Jin. Thanks to the Anderson lab at MIT for the use of their instrument.

In these spectra, the D and G bands are labeled. The D peak at 1310 cm^{-1} can be assigned to C-C vibrations signaling "disorder," while the G peak at 1580 cm^{-1} is the E_{2g} sp^2 C=C stretching band indicating "graphitic" carbon.[192] If increased graphitic nature were associated with increased activity for xylene oxidation, we would expect that the ratio of the G peak to D peak (I_G/I_D) would be highest for the most active electrode materials, and vice versa. However, that does not seem to be the case; while the materials are active in the order AvCarb > Toray > Freudenberg, their I_G/I_D ratios are ordered Toray (~1.7) > AvCarb (~0.7) > Freudenberg (~0.2). It is possible that gathering these spectra at different times under different conditions makes it more difficult to directly compare them; as it stands from these results alone, however, there is no clear correlation between graphitic nature of carbon paper and activity for xylene oxidation.

As an additional test of the impact of graphitic carbon, we also tested xylene oxidation on two different AvCarb carbon felts – one designed to be graphitic, the other not. (Figure 4-8) While xylene oxidation proceeded more quickly on the graphitic felt than the non-graphitic felt, rates for the reaction on both of these felts were lower than on carbon paper. This may be partly due to the thickness of the carbon felts, which were roughly 5 mm in depth, and may have absorbed some of the oxidation products, preventing those products from being accounted for.

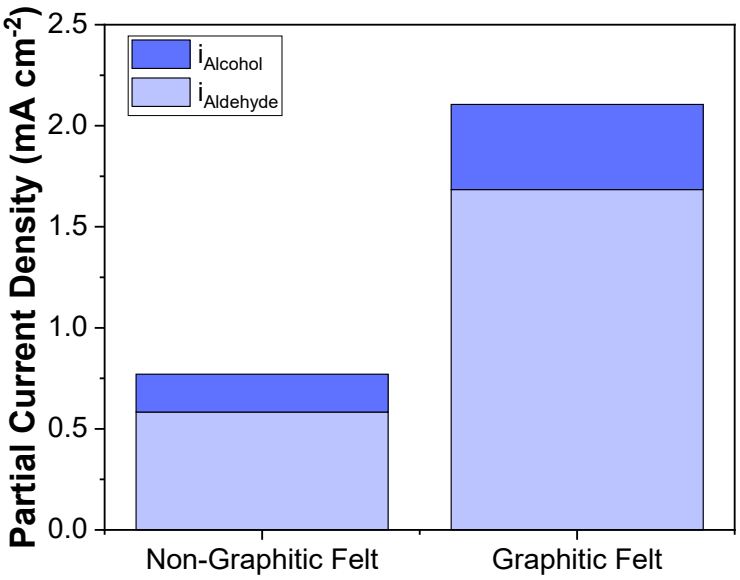

Figure 4-8. Partial currents toward xylene oxidation on the graphitic and non-graphitic AvCarb felts. Thanks to the Brushett lab at MIT for providing these felts.

Overall, it remains unclear whether the graphitic nature of a carbon electrode is related to its activity for xylene oxidation. Our limited tests are inconclusive in this regard.

4.5.2.2 Effect of carbon electrode oxidation on performance

In addition, we probed the hypothesis that O-functional groups on the carbon electrode may facilitate O-atom transfer to xylene, just as is the case for vanadium catalysis. In order to do this, we oxidized the AvCarb P50 carbon paper, using 2 approaches: 1) re-using a previously used anode, and 2) thermally oxidizing the anode in air at 600 °C for 1 hour prior to electrolysis. (Figure 4-9)

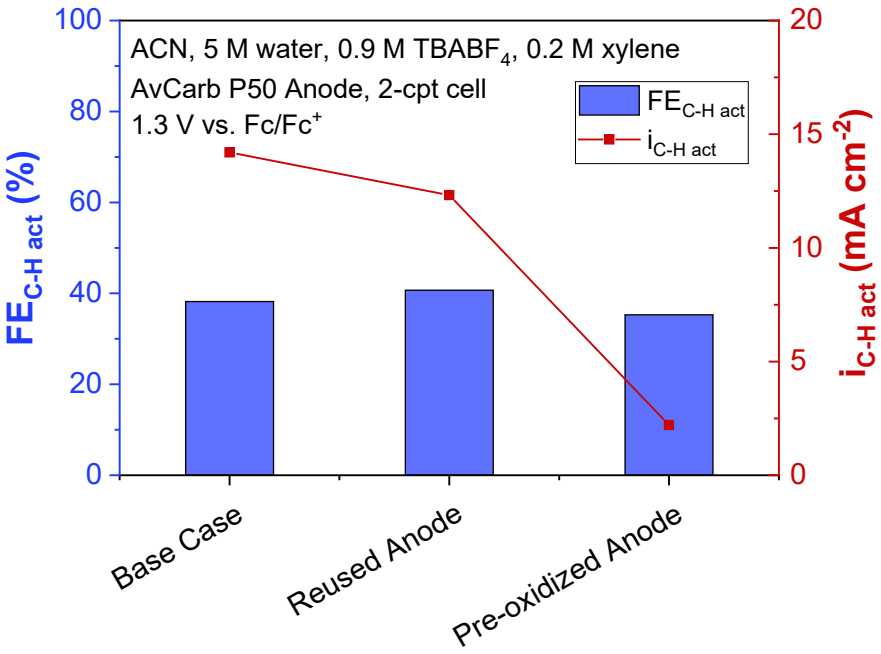

Figure 4-9. Effect of oxidation on FE and partial current toward xylene oxidation. Base case = no AvCarb P50 pre-treatment; reused anode = 2 experiments conducted one after the other using the same AvCarb P50 anode, with results from the second experiment shown; pre-oxidized anode = AvCarb P50 anode thermally oxidized in air at 600 °C for 1 hour prior to electrolysis.

Regardless of the scheme for pre-oxidation of the anode, the FE for xylene oxidation was roughly the same – about 35-40% in total. The total current on the different electrodes differed, however, meaning partial currents for xylene oxidation also differed. For this set of experiments, partial currents toward C-H activation were highest in the base case (i.e., no pre-oxidation), followed by the case with the reused anode, followed by the thermally oxidized anode, which had a partial xylene oxidation current only about 15% that of the base case.

While it is certainly the case that thermal oxidation does not have a straightforward effect on the activity of a carbon paper for electrocatalysis in general,[193] these results would imply that oxidation of the AvCarb anode does not positively impact xylene oxidation catalysis. Oxidation of a less-active carbon paper as a starting point may prove more interesting, but for the purposes of this work, the AvCarb electrode is not oxidized to enhance performance.

4.6 Transient changes during electrolysis & impact of solution ionic strength

Particularly with high-rate electrodes such as AvCarb P50, it was observed that experiments conducted in 0.1 M $TBABF_4$ electrolyte tended to run away in the first few minutes, with current increasing over time – sometimes to the point of potentiostat failure (automatic termination of the experiment). Through PEIS, it was determined that the resistance of the electrolyte decreased shortly after polarization, in a way that was reversible. In order to minimize the relative decrease in the resistance upon polarization, the ionic strength of the solution was increased by increasing the concentration of the $TBABF_4$ in the electrolyte to 0.885 M. This suppressed transient changes in current in the early part of experiments. (Figure 4-10)

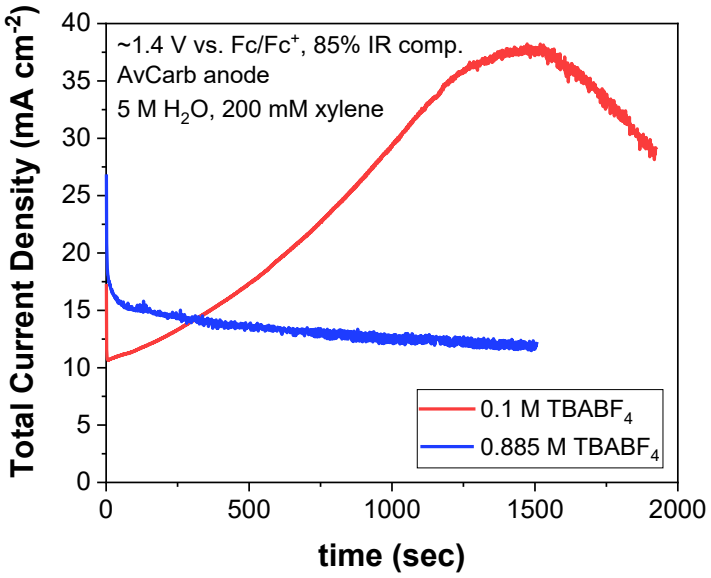

Figure 4-10. Effect of electrolyte salt concentration on the current profile during a constant-potential xylene oxidation experiment. Electrolytes were ACN with 5 M water, 200 mM xylene, and either 0.1 M $TBABF_4$ (red) or 0.885 M $TBABF_4$ (blue). Anode was AvCarb P50. IR compensation was set to 85% of the measured value.

The reason for this resistance decrease over time is unclear. It is likely that polarization leading to the production of protons and surface aggregation of more highly screening species such as water and BF_4^- ions serves to slightly decrease the Ohmic resistance right at the anode interface; however, we find it improbable that such an effect would be observed over the span of a few millimeters, the distance scale over which the reference electrode and working electrode are separated. This is a phenomenon which warrants further inquiry. Regardless, for the purposes of this thesis, the finding that transient changes could be suppressed by concentration of the

electrolyte salt was utilized; subsequent data mostly represent results from systems in which electrolyte $TBABF_4$ concentration was ~0.8-0.9 M.

4.7 Response of xylene oxidation to potential

Following finalization of the cell design, identification of AvCarb P50 as an electrode material, and establishment of a "standard" electrolyte, the xylene oxidation reaction was characterized on an AvCarb P50 electrode in a 2-compartment cell. To establish the response of different components of the electrolyte to potential, four electrolytes were prepared: 1) an acetonitrile blank with 0.885 M $TBABF_4$, 2) ACN + 0.885 M $TBABF_4$ + 200 mM xylene, 3) ACN + 0.885 M $TBABF_4$ + 5 M water, and finally, 4) ACN + 0.885 M $TBABF_4$ + 5 M water + 200 mM xylene, the "standard" electrolyte. CVs were conducted in order to observe the potential-dependent behavior of these electrolytes. (Figure 4-11)

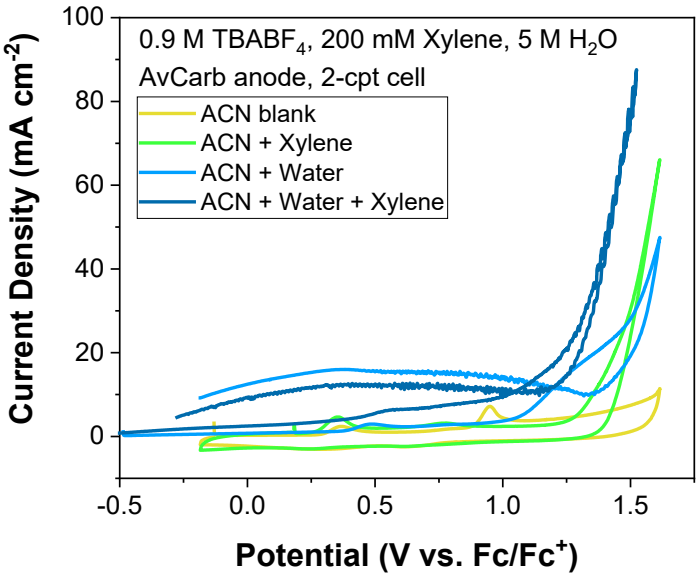

Figure 4-11. Cyclic voltammograms of different electrolytes to isolate the potential response of different reagents. Traces include: acetonitrile background (yellow), + xylene (green), + water with no xylene (light blue), and + water + xylene (dark blue).

We can make a number of observations from this set of CVs. First, since the ACN oxidation background (yellow) is relatively low across the potential range of interest, it is possible to observe from the light blue and green curves both the onset of water oxidation (and possible concurrent ACN oxidation in the presence of water), as well as xylene oxidation, independently of one another. From the green trace, we can see that xylene can be activated even in the absence of water, reaching a current density of 10 mA at around 1.3 V vs. Fc/Fc^+. From the light blue trace, we observe that the onset of current happens earlier for water oxidation,

reaching 10 mA around 1.2 V vs. Fc/Fc^+. However, this early onset seems to represent a slight "shoulder" in front of a steeper-onset wave that takes over around 1.4 V vs. Fc/Fc^+. Additionally, we see that the presence of water in the electrolyte in both the light and dark blue traces leads to the persistence of a background oxidative current on the reverse sweep, roughly 10 mA in magnitude. This background current persists to some extent on subsequent CVs as well. It is unclear exactly how this current arises; traditional CV analysis would suggest that this phenomenon of crossover indicates a reaction with an "ECE" mechanism – that is, an initial electrochemical step, followed by a chemical step, followed by another electrochemical step. If the first electron transfer happens at a high potential and the subsequent chemical step is slow and/or the final electrochemical step can also take place at lower potentials than the initial electron transfer, a new background current will persist as this final electron transfer takes place on the reverse sweep. It is possible that such a mechanism dominates for water oxidation in this context, or for acetonitrile oxidation in the presence of water. That said, it is also strange that this background current exhibits "arcing" behavior, first increasing slightly and then decreasing again below roughly 0.3 V vs. Fc/Fc^+. Regardless of the explanation for this phenomenon, it is clear from the CVs that traditional CV analysis alone will likely be unable to tell the full story of xylene oxidation. From a CV analysis perspective, the reason is that the traces lack peaks. The onset of water/solvent oxidation takes place a bit too close to the onset of xylene oxidation. Moreover, none of these processes are very simple; for instance, we do not know what xylene is being oxidized to, what other species participate in the reaction, and whether the water oxidation represents OER alone or also the activation of ACN. The reactions taking place cannot be fully decoupled from one another via CV. This means we need to conduct experiments during which we explicitly quantify the products of the various reactions taking place.

Figure 4-12 presents this potential-dependence data, as a result of batch experiments similar to those previously reported, passing 50 C for each experiment. By quantifying the products post-experiment, we can report an average FE over the course of the run. The peak FE was observed at 1.25 V vs. Fc, and was found to be roughly 50% toward xylene oxidation products. Similar FEs (40%) at substantially higher rates (~37 mA/cm^2) can be obtained by further increasing potential by 100 mV.

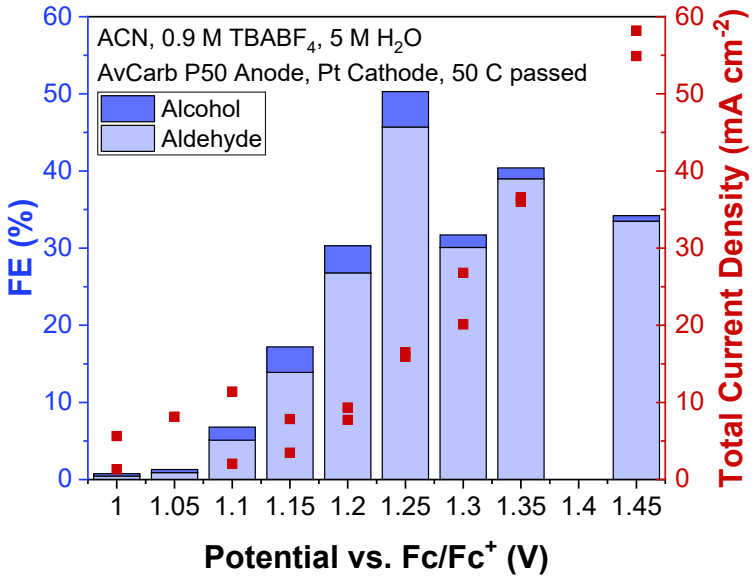

Figure 4-12. FEs (blue, left axis) and total current density (red, right axis) for xylene oxidation at several potentials. Potentials are "nominal potentials," not felt potentials after final 15% IR correction. Duplicates were run for each potential except 1.05 V, and all current densities are reported. Reported FEs are from first replicate only but are representative of duplicate data set as well.

4.8 Electrochemical kinetic tests to identify reaction mechanism

In order to move past understanding of the potential-dependent behavior of the reaction, toward a full mechanistic understanding, additional tests were needed. In this section we present the potential-dependence data in the form of a Tafel plot for p-tolualdehyde formation, as well as reporting data on substrate dependence, water dependence, kinetic isotope effect, and pH effects. We also highlight results of an explicitly aerobic experiment meant to intercept O_2 gas as an oxidant in the absence of water. Using all of these results together, we propose a mechanistic pathway toward xylene partial oxidation.

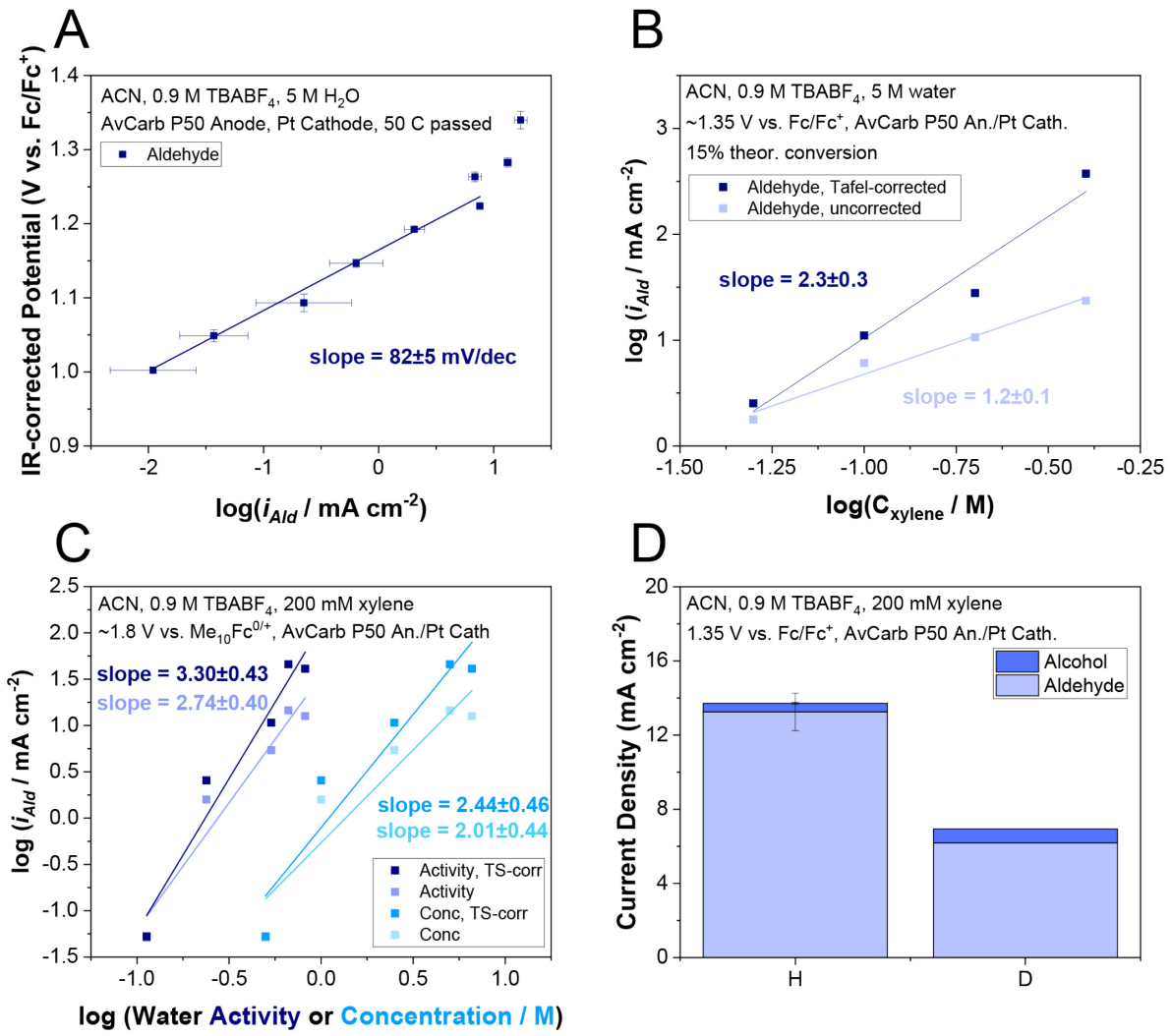

Figure 4-13. Electrochemical kinetic data for the reaction of xylene and water to produce p-tolualdehyde. (A) Tafel plot, (B) xylene dependence, (C) water dependence, and (D) kinetic isotope effect.

4.8.1 Tafel slope

By representing the potential dependence data in Figure 4-12 as a Tafel plot, we get Figure 4-13A. The Tafel slope, fit for data obtained between roughly 1 V and 1.25 V vs. Fc/Fc^+ (nominally), is 82±5 mV/dec. Reinforcing the discussion from Section 4.5, this is a relatively low Tafel slope – lower than the 120+ mV/dec that is normally associated with an outer-sphere electron transfer RDS – supporting the idea that some sort of inner-sphere catalysis may be taking place. We know that a cardinal Tafel slope value is not necessarily to be expected,[158] especially for a complicated reaction with a broad range of possible products. Moreover, if we do elect to interpret this slope expecting a cardinal value, it is difficult to draw any simple conclusion. Cardinal Tafel slope values in this range include 120 mV/dec and 60 mV/dec –

82±5 mV/dec is nearly equidistant from these, and the uncertainty in the data does not warrant interpretation as either 120 or 60. (see Appendix C) It is possible that under the conditions tested, the reaction is under mixed control between two different rate-determining steps – one involving an initial electron transfer from xylene, and another involving a subsequent chemical step. Deconvolution of these possibilities could be possible by probing the Tafel slope under a different set of conditions, such as at a different water concentration or different substrate concentration.

It should be noted that the seeming "autocatalytic" effect that may be attributable to a systematic error in data collection methodology also applies here – it may be the case that, if back-reaction of products occurs at the cathode, then lower currents (observed at lower potentials) result in longer experiments to pass the same amount of charge, and partial currents are deflated by loss of the product to back-reaction over time. This error would have the effect of decreasing the Tafel slope relative to its "true" value.

4.8.2 Xylene dependence

We measured the dependence of the reaction rate on xylene by altering the xylene concentration in the electrolyte and observing the corresponding C-H activation rate. (Figure 4-13B) In order to ensure that xylene depletion did not affect measurements, a constant theoretical conversion (conversion of xylene to aldehyde assumed 100%) of 15% was maintained, meaning different amounts of charge were passed for each experiment.

Because total current does vary with xylene concentration, it is important to try to anticipate total current prior to experiments and adjust the applied potential slightly so that the "felt potential" – the potential felt at the anode, which does not account for the final 15% of Ohmic resistance – is as consistent as possible between experiments. Since each data point is a batch-averaged partial current measurement, there is no other practical way to make data within a single measurement set comparable. As a result of this potential inconsistency, the raw measured xylene dependence of 1.2±0.1 changes drastically upon application of a correction which uses the measured local Tafel slope to back-correct measured currents. This approach (with local TS measured as 142 mV/dec) yields a xylene dependence of 2.3±0.3. This second-order dependence should be tested by subsequent iterative experiments with the goal of ensuring constant-potential operations so that no Tafel correction needs to be applied.

It should be noted that the analysis presented here assumes that xylene is dilute enough that concentration is a reasonable proxy for activity; seeming lack of curvature in the measured data supports this, but the assumption should be verified by xylene activity measurement.

4.8.3 Water dependence

In addition, the water dependence for the reaction was measured, this time employing an activity correction for water, which is known to behave nonideally across the concentration range of interest. By utilizing the water concentration-activity curve presented for a 0.8 M $TBABF_4$ ACN electrolyte in Chapter 3, the measured water dependence changes from 2.01-order with relatively strong "saturation" behavior (concentration case, light blue) to 2.74-order and more linear (activity case, purple). As for the meaning of these slopes, it is yet unclear – we can again refer to the many mechanisms for water's participation in electrocatalytic reactions, as illustrated in Figure 3-3. In addition to all of these possibilities, there is also a chance that water may not be the direct oxidant in the reaction, but rather that water forms peroxide or O_2 which then goes on to react with xylene. Regardless, we can say that the very high measured water order here is suggestive that the role(s) played by water in the C-H activation reaction are more similar to the role(s) played by water during HER in a blended electrolyte than they are to water's roles in other O-atom transfer reactions.

Again, because it is experimentally impossible to exactly hold "felt potential" vs. Me_{10}-Fc constant, a Tafel slope correction can and likely should be used in order to make better sense of the data at a constant potential. Applying this correction (with local TS measured as 142 mV/dec), the water dependence values change to 2.44-order and 3.30-order for concentration and activity, respectively. Importantly, because the total current varies so greatly with water content, this point about adjusting the applied potential to maintain a constant "felt potential" becomes even more relevant for the collection of this data set. As with the xylene dependence data, additional experiments are required in order to make this correction unnecessary.

The high measured water orders after all corrections are applied raise a final question which was also addressed in Chapter 3 – if the water dependence is this high, is it not possible that some portion of the water dependence arises from thermodynamic shifts in reaction equilibrium potential? In other words, perhaps this reaction should be analyzed on a pH-dependent scale such as RHE. Unfortunately, it is unlikely that we would be able to measure the equilibrium potential for C-H activation, in contrast to O-H or N-H activations, because of the relatively low exchange currents for C-H activation.[154] Utilizing an RHE scale, however, would imply

an assumption that the thermodynamics of protons matters to steps that impact the rate of the C-H activation reaction. By studying KIE and pH dependence below, we can begin to probe whether this is a valid assumption.

4.8.4 Kinetic isotope effect

We measured the kinetic isotope effect for xylene oxidation by running experiments with xylene-d10, a fully deuterated substrate. If cleavage of the C-H (C-D) bond is part of the rate-determining step of the reaction, then deuteration at this position should cause the reaction to proceed more slowly. This is a slight simplification, of course – as mentioned in Chapter 2, many variables change in subtle ways with the replacement of protons by deuterons, and there are cases in which CPET reactions have been shown to not exhibit KIE's (k_H/k_D) of much more than 1.[106] However, noting these caveats, we did observe a k_H/k_D of about 2 for xylene oxidation, suggesting that C-H cleavage may in fact be a feature of the RDS.

It should be noted that the product yield was determined through a different mechanism for the deuterated experiment (analyzed via GC-MS) than for the protonated experiment (analyzed via NMR), since the deuterated product does not feature NMR-active protons. As such, this measured KIE is only preliminary, and should be confirmed by a direct comparison using consistent quantification methods.

4.8.5 pH dependence

In addition, while we did not conduct a comprehensive pH dependence study, experiments were designed in which 0.09 M electrolyte salt was used. This salt was $TBABF_4$ in the base case, but was swapped with HBF_4 in an acidic experiment and TBAOH for an alkaline experiment, generating electrolytes with pH of roughly 1 and 13, respectively. (Figure 4-14)

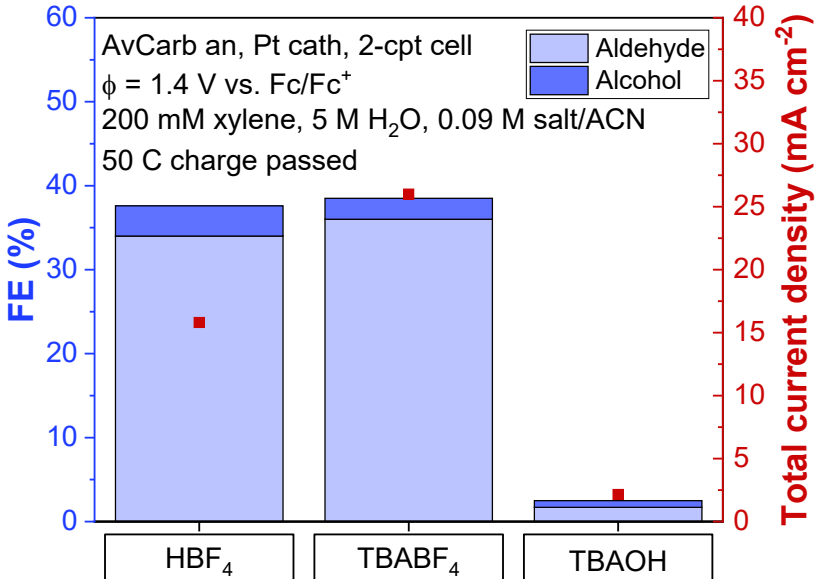

Figure 4-14. pH-dependence experiments for xylene oxidation, in 3 cases: 1) 0.09 M HBF_4 (acidic), 2) 0.09 M $TBABF_4$ (neutral, un-buffered), and 3) 0.09 M TBAOH (alkaline). FEs (blue) and total current density (red) are reported.

As is evident from the figure, the explicit addition of acid did not greatly impact the measured xylene oxidation FEs, although the total current density in the cell decreased by about 40% relative to "neutral" conditions. The relatively similar results under acidic and "neutral" conditions are to be expected, since the local pH at the polarized anode interface is acidic in the unbuffered case regardless of the bulk pH. In contrast, the experiment featuring 0.09 M TBAOH resulted in FEs of less than 5%, and a total current of only about 2 mA – a decrease by more than 90% from the neutral case.

Since these experiments are conducted at very low ionic strength, it is difficult to deconvolute pH effects from other impacts of altered electrolyte. Additional – although not directly comparable – experiments were carried out at a total ionic strength of 0.9 M, with $TBABF_4$ as the supporting electrolyte and either 0.1 M or 0.01 M TBAOH to make the bulk pH basic. In these cases, total current decreased less dramatically (36 mA/cm^2 neutral → 17.1 mA/cm^2 at "pH 12" → 22.1 mA/cm^2 at "pH 13"), and FEs did the same (aldehyde: 34% neutral → 26.7% at "pH 12" → 7.3% at "pH 13"). A variety of additional unidentified products were observed in the pH 13 case.

It is unclear what causes the decrease in FE with increasing pH; this runs counter to our intuition, assuming that a basic electrolyte more easily accepts protons released from xylene as the C-H bond is broken. It is possible that the kinetics of this transfer are somehow disfavored

in base, or that other oxidative reactions taking place simultaneously alongside C-H activation are more strongly favored in the basic environment. It is also possible that the alkaline electrolyte alters the carbonaceous anode in some way that is disadvantageous for xylene oxidation. Regardless, a neutral-to-acidic electrolyte seems preferable for this reaction, which is interestingly consistent with not only the industrial process for xylene oxidation,[171,172] but also with many research reports on benzylic C-H activation.[147,173–179,181,187,188]

4.8.6 Testing for alternative oxidants

As a final contribution to our mechanistic analysis, we sought to test the hypothesis that the contribution of water in the reaction does not have to be direct, but rather that water can first be oxidized to a stronger oxidant such as peroxide or O_2 gas, which can subsequently react with xylene.

4.8.6.1 Peroxide

A colorimetric assay designed to detect H_2O_2 was used on a representative electrolyte sample, and did not reveal a detectable amount of peroxide persistent in the solution following electrolysis. We did not, however, test the selective addition of peroxide to the reaction, so it remains possible that peroxide species are formed as short-lived intermediates during the experiment.

4.8.6.2 Oxygen

We conducted an experiment with no xylene while bubbling N_2 through the working electrolyte for gaseous product detection at an in-line gas chromatograph. Under these conditions, we were unable to detect any O_2 gas made as a product of water oxidation. This seems to indicate that O_2 is not generated during the experiment, but it is also possible that O_2 very quickly reacts under the conditions tested, so that no O_2 is detectable in the outlet. We therefore aimed to probe whether O_2 gas in the absence of water was capable of oxidizing xylene. To do this, we conducted a test in a dry ACN-based solvent without addition of water while bubbling O_2 gas. Under this condition, some xylene was indeed made – although the total current density was low, at 2.77 mA/cm^2, and the measured aldehyde FE was 14.7%. This represents a substantially smaller current toward xylene oxidation than in the case with 5 M water and no flowing O_2 (>10 mA toward aldehyde product). It is possible that the low solubility of O_2 gas in the electrolyte contributed to this. However, because extreme supersaturation (dissolution above $a_{O2} = 1$) of O_2 at the interface due to OER in experiments with water is unlikely – especially in the case that no O_2 escapes the system as a gaseous product – and because a diffusion-limited

current density for direct reaction of O_2 at such an electrode under these conditions is expected to be on the order of 10 mA (higher than the observed current), we hypothesize that the direct involvement of O_2 is at most a minor pathway toward xylene oxidation products, occurring at substantially lower rates than xylene oxidation in which water participates as the direct oxidant.

4.8.7 Proposed reaction pathway

With all of this mechanistic data in mind, we propose a reaction pathway toward synthesis of the alcohol and aldehyde products observed in this work. (Figure 4-15)

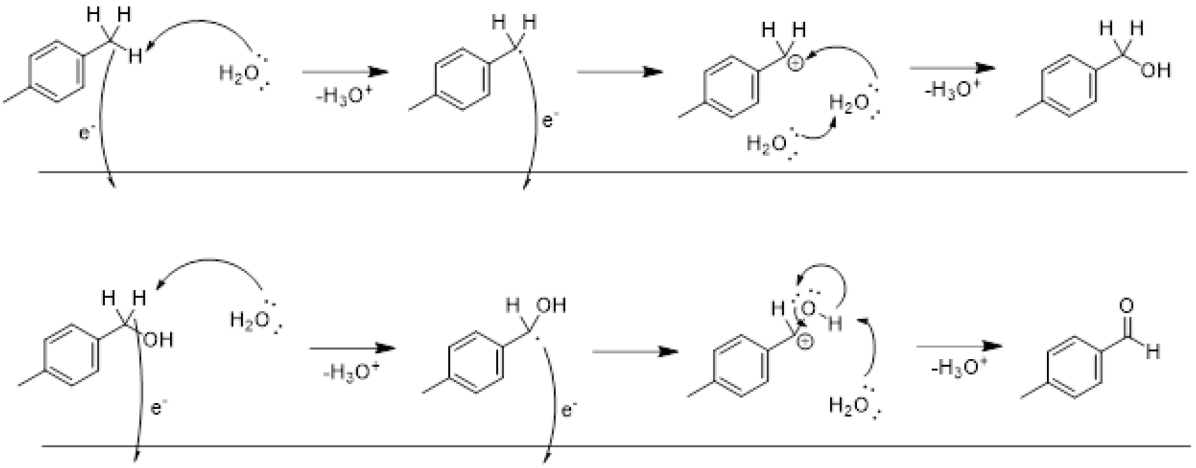

Figure 4-15. Proposed xylene oxidation reaction pathway, first generating 4-methylbenzyl alcohol (top row), followed by p-tolualdehyde (bottom row).

We invoke the participation of a single xylene molecule, hypothesizing that the initial step is a concerted proton and electron transfer to produce a xylene radical. Water can act as the base in this step, as one of its many roles. Because this initial activation is a CPET rather than a PT or ET step alone, much like in the case of HER in a blended electrolyte, the impact of water activity on the rate of the reaction is quite large in magnitude – although we have yet to selectively identify why this is the case.

Following this step, we hypothesize that an additional electron transfer to form a cation, followed by attack by water to form a C-O bond, can lead to formation of the alcohol. By largely repeating this sequence of events once more on the alcohol, we obtain the aldehyde product.

While it remains possible that water may functionalize the surface of the carbon paper electrode itself, we are not certain of this, since oxidation of the electrode seems to have no positive impacts on measured rates. In addition, while we have some sense that xylene and the various

reactive intermediates may be coordinated to the carbon surface, we have not drawn this explicitly. Coordination to the surface could be a reason why we observe very little alcohol product directly from the reaction – while this is a stable intermediate along the reaction pathway, perhaps it is oxidized further rather than detaching and diffusing into the bulk of the electrolyte.

We wish to emphasize that this is still a preliminary understanding of xylene oxidation, and that much of the steps depicted here – including essentially everything after the initial CPET – is difficult to experimentally probe. Future work to even better understand the mechanism of direct electrochemical xylene oxidation with water is warranted.

4.9 Substrate scope & initial Hammett analysis

We have also begun to explore the scope of substrates to which this C-H oxidation approach applies. In addition to studying 4-methylbenzyl alcohol and p-tolualdehyde as starting materials (the products reported throughout this chapter), a variety of other substrates including benzyl-substituted and para-substituted species has been tested. (Figure 4-16)

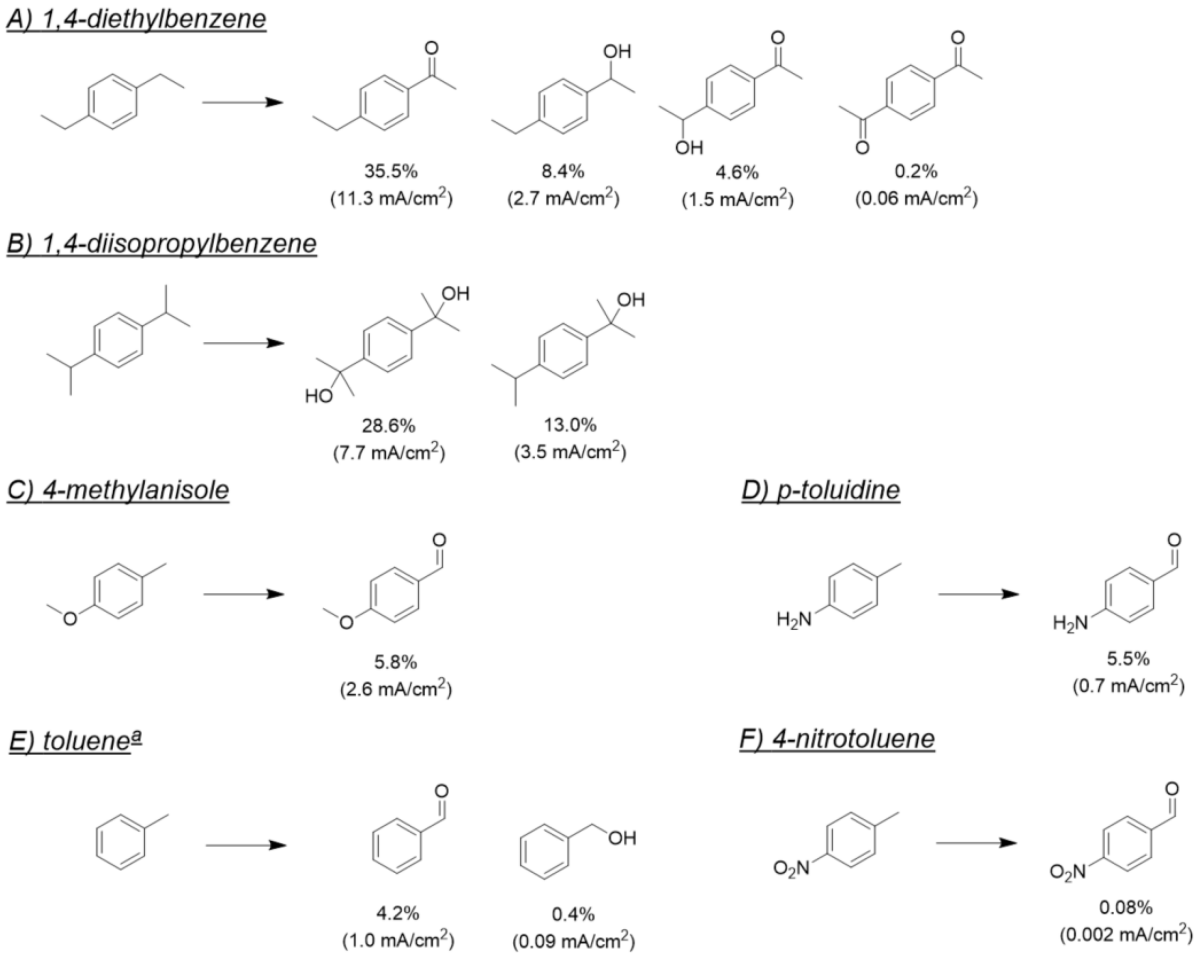

Figure 4-16. Products of benzylic C-H oxidation with a variety of substrates: A) 1,4-diethylbenzene, B) 1,4-diisopropylbenzene, C) 4-methylanisole, D) p-toluidine, E) toluene, and F) 4-nitrotoluene. Percentages reported are FE for the corresponding product, while current densities are the partial current densities for each product. Unless otherwise noted, each experiment was conducted at the standard conditions for xylene oxidation (AvCarb anode, 2-cpt cell, 1.35 V vs. Fc/Fc^+, 5 M water, 200 mM substrate). [a] Toluene oxidation carried out at 1.45 V vs. Fc/Fc^+ in order to achieve appreciable currents.

It can be observed that the most electron-rich substrates with the least heteroatoms – especially the benzylic-substituted xylenes – tend to be the most reactive. All told, the quantified FEs for C-H oxidation are 48.7% for 1,4-diethylbenzene and 41.6% for 1,4-diisopropylbenzene. Other electron-rich substrates such as 4-methylanisole and p-toluidine also exhibit low but measurable FEs for benzylic C-H oxidation, in the range of 5-6%. The issue with these substrates seems to be that the heteroatom imparts cross-reactivity, leading to the production of many unidentifiable products. In addition, we also tested relatively electron-poor substrates such as toluene and 4-nitrotoluene. Even increasing the oxidative potential by 0.1 V, the FE for

toluene oxidation was <5%. For 4-nitrotoluene at standard conditions, the FE for C-H activation was even lower, at 0.08%. As we might expect, the inductive effect of the p-substitution has an effect on reactivity for these substrates. However, the observed differences in C-H activation rate are larger than might be predicted from these inductive effects alone. To visualize this, we present a (very preliminary) Hammett analysis. (Figure 4-17)

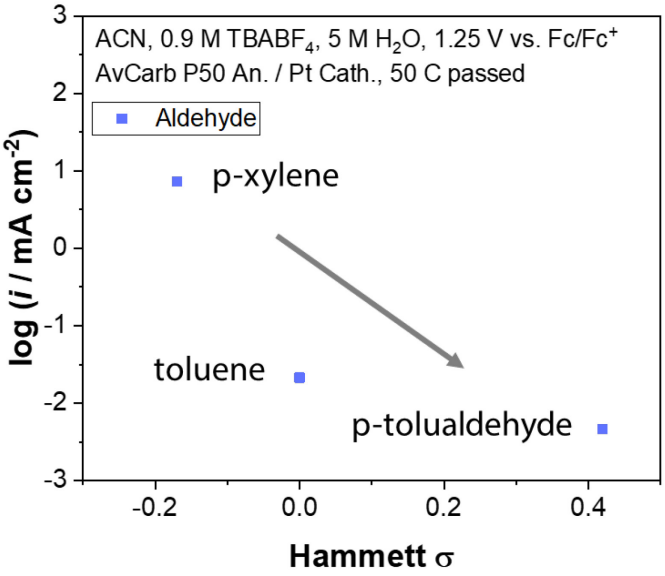

Figure 4-17. Hammett plot for benzylic C-H oxidation for the substrates p-xylene, toluene, and p-tolualdehyde, focusing specifically on current toward aldehyde products. Hammett parameter values from Hansch et al. 1991.[194]

For 3 selected species – p-xylene, toluene, and p-tolualdehyde – we have plotted the logarithm of the current density specifically toward the formation of the corresponding aldehyde product – p-tolualdehyde, benzaldehyde, and terephthalaldehyde, respectively – versus the Hammett parameter for each substrate.[194] The Hammett parameter is an empirical constant for a given substituent that indicates electronic effects – field-based and induction-based – that that substituent exerts on a certain position of a molecule. (Here we use σ_p, the para-parameter.) As indicated by the arrow, the trend we observe in these three substrates is generally in the expected direction; as the σ increases, meaning the para-substituent withdraws more electron-density from the benzylic site, so too does the oxidation rate decrease. However, it does so with a much steeper slope than is usually reported for Hammett analyses, particular between p-xylene and toluene. This is even despite the fact that the toluene experiment is carried out at a more oxidizing potential than the p-xylene experiment.

Hammett analysis, then, is insufficient in the case of our set of reactions. This is for many reasons: chief among them, the fact that each of these reactions exhibits a wide product

distribution that is not just limited to the products plotted here. The complexity of these reactions warrants further study prior to analysis of this sort.

4.10 Xylene oxidation in different solvents

Finally, xylene oxidation has been tested in methanol- and ethanol-based blended electrolytes, in addition to the electrolytes reported here based on acetonitrile. Due to experimental issues, we have not yet been able to reliably quantify the FEs for C-H activation in these electrolytes. However, from these initial investigations, it seems that ethanol is an equally effective solvent for xylene oxidation. On the other hand, it seems that methanol-based electrolytes perform rather poorly, whether due to oxidation or evaporation of the solvent during the experiment. Further investigation is required in order to optimize the solvent for this reaction. Such investigation will do well to bear in mind the concepts discussed in Chapter 3, controlling for species activity in the analysis.

4.11 Conclusions

Here we have presented an initial characterization of the direct benzylic C-H oxidation of xylene and related substrates on carbonaceous anodes. We move far beyond the current state of the literature, reporting not just the product distribution – primarily aldehyde with a small amount of alcohol – but also how those products are generated. We report the impact of changes to the cell configuration on this distribution. In addition, other variables investigated include: total charge passed, catalyst material, potential, substrate activity, water activity, kinetic isotope effect, pH, addition of O_2 oxidant, and benzylic as well as para-substitution of the substrate. Electrochemical kinetic data was combined to propose a mechanistic pathway for benzylic C-H oxidation that involves an initial CPET from xylene, with water acting as a key mediator for this process. Outstanding questions from this investigation include whether and how the benzylic substrate and intermediates chemically interact with the carbonaceous anode; exactly what roles water plays during the oxidation, including how the thermodynamics of C-H activation change with water content; why alkaline pH's lead to lower activities for C-H activation; how much product is formed as a result of reaction with O_2 produced as an intermediate; and identification of the major source of alcohol from the reaction, along with a full accounting for product back-reaction. In addition, future work in this area should aim to fully account for anodic FE, as well as closure of the mass balance on the substrate. We hope

that this work can serve as a basis for further investigation and development of this direct C-H activation approach, which does not require the use of metal catalysts.

5 CONCLUSIONS & OUTLOOK

5.1 Conclusions

This thesis work broadly aimed to address the challenges and complexities of conducting mechanistic analysis for electrochemical reactions under "messy," real-world conditions. Specifically, we focused on: 1) side-reactivity and mechanistic shifts when conducting CO_2 reduction with impure gas feeds, and 2) thermodynamic nonidealities in blended aqueous-nonaqueous electrolyte systems, through the lens of both the widely-studied hydrogen evolution reaction as well as a relatively novel electrochemistry, xylene oxidation.

In the case of CO_2 reduction on dilute and oxygen-containing CO_2 feedstocks, we demonstrated that the presence of O_2 gas in a CO_2 feed does not greatly impact the overall CO_2R rate on Au, nor the CO_2R mechanism on Au. O_2 does, however, quickly react at typical CO_2R potentials – and its rate at a flooded electrode is limited by O_2 transport to the electrode surface. ORR represents an efficiency loss in this system and is therefore viewed as parasitic current. We also presented a mechanistic analysis of CO_2R under both oxygenated and N_2-diluted conditions, providing evidence for a chemical (n = 1, q = 0) rate-determining step.

With our study of nonidealities in blended electrolytes, we demonstrated that accounting for species' thermodynamic activities is critical for accurate interpretation of electrochemical kinetic data. Through HER as a case study, we showed that water is a particularly important reacting species to which this accounting applies, as its strong self-interactions cause it to behave less ideally than many other solvents in mixtures. We reported the high dependence of Au-catalyzed water reduction on water activity (~3^{rd}-order), and proposed many roles that water can play in the reaction as an explanation for this high dependence. We speculated on the molecular origins of the relationship between concentration and activity, and extended the relevance of our arguments to O-atom transfer reactions that exhibit rate dependence on electrolyte water content, such as cyclooctene epoxidation and cyclohexanone lactonization.

Finally, we demonstrated direct benzylic C-H oxidation in the ACN-water blended electrolyte and conducted novel kinetic investigations on this chemistry, accounting for species nonidealities. We showed that direct oxidation of xylene to p-tolualdehyde with moderate selectivities (FE ~50%) is possible even (and especially) on metal-free carbonaceous

electrodes. We hypothesized that these electrodes engage in inner-sphere interactions with aromatic substrates. We also demonstrated a very high dependence of the xylene oxidation reaction rate on electrolyte water content, with a water order of ~3-4 measured. This result, coupled with the measured kinetic isotope effect for the reaction, suggested that high water dependence may be correlated with the predominance of CPET steps in a reaction mechanism. We also presented preliminary substrate scope results for this class of reaction.

5.2 Outlook

Much progress has already been made in further advancing the study and implementation of some of these chemistries; for others, however, there is much still to be done. Herein we will propose many future steps that naturally follow from this work.

5.2.1 CO_2 reduction with gas-phase contaminants and concentrated electrolytes

In the years since the publication of our study on oxygenated CO_2 feedstocks, there has been increased attention paid to CO_2R in the presence of contaminants. For instance, researchers have designed systems imbued with microporous polymers[195,196] and ionomers[197] which act to sieve O_2 in oxygenated feedstocks, preventing O_2 from reaching electrode surfaces and imparting CO_2R selectivity. Others have investigated the impact of different contaminants on CO_2R, such as NO_x.[198] Still others have continued to address questions of CO_2R at low CO_2 pressures, absent reactive impurities.[199,200] That said, there is still a disappointing lack of discussion of CO_2 feed purity requirements, or assumptions thereof, when analyzing the feasibility of CO_2R deployment. Among other goals, our study aimed to highlight that the choice to model and operate CO_2 electrolyzers with "pure" CO_2 feeds is just that – a choice. There is a good opportunity to develop technoeconomic models which can be explicit about this design decision, and can use results such as ours and those that have been published since in order to inform trade-offs in process performance caused by relative CO_2 feed purity.

Beyond addressing gas feed contamination, our work also contributed to ongoing conversations surrounding the mechanism of CO_2 reduction without contaminants.[90,91] Preliminary results from our work (Appendix) also revealed suppression of CO_2 reduction at high concentrations of bicarbonate, which was further elucidated as a poisoning effect by Zeng *et al*. out of our own lab.[201]

CO_2 reduction as a field is continuing to develop, and we anticipate that CO_2R systems will begin commercial deployment in the coming years. It may take a while, however, for CO_2R to

reach similar optimized performance as HER. Ongoing academic-level investigations into design considerations such as electrode flooding[202] and bipolar membranes[203] is representative of the distance CO_2R has yet to cover as a field of study. Looking further into the future, an even earlier-stage class of research in CO_2 utilization – namely, organic carboxylation – is also on the rise, and is beginning to show promise for eventual use in CO_2 upgrading.[204]

5.2.2 Deconvoluting roles of water in blended electrolytes

The proposal that water plays many distinct roles in blended electrolyte systems opens up the opportunity to deconvolute those roles from one another. Here we briefly describe some approaches to isolating water's various contributions to electrochemical reactions through sequential simplification of the reaction taking place in the blended electrolyte.

The first simplification that can be made is the removal of water as a direct reactant, but retention of its role as a Brønsted-Lowry base/acid. This can be achieved through the study of the impact of water content on proton-/H-atom-transfer reactions such as hydrogen oxidation or alcohol oxidation at the anode; or, at the cathode, low-rate acidic HER. These are all reactions which involve proton transfer to or from a reagent that is not water itself. However, water may be present in the reaction to coordinate a proton transfer or act as a buffer in the corresponding generation of a proton or hydroxide.

Next, the reaction could be further simplified by removing the proton-transfer aspect and focusing entirely on water's impact on ET-only reactions. We can tease out water's role in solvation by studying the impact of water content on ET reactions for species that are more or less affected by solvation – e.g. by comparing the ET behavior of a more solvent-agnostic species such as Me_{10}-Fc and that of a solvent-exposed redox species such as diquat or ethyl viologen. Water dependence of e.g. ethyl viologen redox at a constant potential vs. Me_{10}-Fc would give insight into water's solvating role and corresponding kinetic impacts, or lack thereof.

To begin to address surface-specific roles such as the displacement of adsorbates by water, one could turn to surface-sensitive spectroscopy to examine surface speciation. There is precedent for study of TBA^+ cations at surfaces;[49,205] however, these methodologies may be complicated by the nature of the blended electrolyte. In addition, one could also consider experimentally probing features of the interface such as potential drop by using some sort of tethered moiety at an electrode surface, and/or computationally probing the interface using molecular dynamics simulations.

Assuming one could identify a redox mediator with kinetics entirely unaffected by water content – or with affected but fully characterized kinetics w.r.t. water content – one could also use mediated electrocatalysis to entirely remove water's roles at the electrode surface by extending the ET reaction of interest into the bulk electrolyte.

5.2.3 Spectroscopy to characterize relationships between thermodynamics and electrolyte structure

In order to further develop our hypotheses surrounding the relationship between measurable thermodynamics (species activity) and the structure and intermolecular interactions of species in the blended electrolyte, we propose to spectroscopically probe the bulk and interfacial structure of water in these systems. This is possible through techniques such as soft X-ray absorbance spectroscopy, which can selectively probe O-atoms in solution.[206] Such measurements made in electron-yield mode can offer information specifically on surface-adjacent water molecules, even under slight polarization.

5.2.4 Extending conclusions from blended electrolyte work to new systems

One additional application of the activity-accounting techniques reported in the blended electrolyte work is in informing studies on solvent effects. Any study involving solvent screening or reporting a solvent effect should consider the impact of the solvent on the thermodynamics of the reactants – and if possible, measure this impact using headspace sampling or similar techniques.

5.2.5 Developing electrochemical xylene oxidation

The xylene oxidation reaction reported in this thesis is still in early stages of development. Further study on the role of the catalyst could help in the eventual development of an even more effective material that can achieve C-H activation at higher rates through inner-sphere interactions. In addition, a more complete product characterization including mass balance on the benzylic substrate and accounting for the full balance of anodic FE should be conducted.

5.2.6 Incorporating xylene oxidation into electrosynthetic schemes

Finally, because of developments on other electrochemistries, it is possible to consider combining many electrochemical steps along more complicated synthetic pathways. For instance, right now we are not aware of any direct electrochemical C-N functionalizations for unactivated hydrocarbons. If we consider starting from N_2, H_2O, and substituted toluenes,

however, we can devise a fully-electrochemical route toward C-N functionalization: first, employ a combined water-splitting and nitrogen reduction device to generate ammonia.[11] In parallel, use water to partially oxidize the toluene species to its corresponding aldehyde (this work). Finally, combine the aldehyde and ammonia in a recently-developed electrochemical reductive amination scheme to make benzylic C-N bonds.[207] A reach goal along this pathway is the eventual development of a chemistry that can transform CO_2 to aromatic species such as xylene, meaning that the full synthesis route would be fully sustainable, relying only on inputs of air, water, and electricity.

We hope that this thesis has contributed in some small way to the realization of a future in which sustainable syntheses such as these are practicable.

6 REFERENCES

(1) Ritchie, H.; Roser, M. CO2 and Greenhouse Gas Emissions https://ourworldindata.org/co2-and-other-greenhouse-gas-emissions (accessed Jan 22, 2022).

(2) Schiffer, Z. J.; Manthiram, K. Electrification and Decarbonization of the Chemical Industry. *Joule* **2017**, *1* (1), 10–14. https://doi.org/10.1016/j.joule.2017.07.008.

(3) Schiffer, Z. J.; Limaye, A. M.; Manthiram, K. Thermodynamic Discrimination between Energy Sources for Chemical Reactions. *Joule* **2021**, *5* (1), 135–148. https://doi.org/10.1016/j.joule.2020.12.014.

(4) Scrosati, B. History of Lithium Batteries. *J. Solid State Electrochem.* **2011**, *15* (7–8), 1623–1630. https://doi.org/10.1007/s10008-011-1386-8.

(5) Reddy, M. V.; Mauger, A.; Julien, C. M.; Paolella, A.; Zaghib, K. Brief History of Early Lithium-Battery Development. *Materials (Basel).* **2020**, *13*, 1884. https://doi.org/10.3390/ma13081884.

(6) Yan, Z.; Hitt, J. L.; Turner, J. A.; Mallouk, T. E. Renewable Electricity Storage Using Electrolysis. *Proc. Natl. Acad. Sci.* **2020**, *117* (23), 12558–12563. https://doi.org/10.1073/pnas.1821686116.

(7) Zhu, C.; Ang, N. W. J.; Meyer, T. H.; Qiu, Y.; Ackermann, L. Organic Electrochemistry: Molecular Syntheses with Potential. *ACS Cent. Sci.* **2021**, *7* (3), 415–431. https://doi.org/10.1021/acscentsci.0c01532.

(8) Acar, C.; Dincer, I. Review and Evaluation of Hydrogen Production Options for Better Environment. *J. Clean. Prod.* **2019**, *218*, 835–849. https://doi.org/10.1016/j.jclepro.2019.02.046.

(9) Hori, Y. Electrochemical CO_2 Reduction on Metal Electrodes. *Mod. Asp. Electrochem.* **2008**, *42*.

(10) Lazouski, N.; Schiffer, Z. J.; Williams, K.; Manthiram, K. Understanding Continuous Lithium-Mediated Electrochemical Nitrogen Reduction. *Joule* **2019**, *3* (4), 1127–1139. https://doi.org/10.1016/j.joule.2019.02.003.

(11) Lazouski, N.; Chung, M.; Williams, K.; Gala, M. L.; Manthiram, K. Non-Aqueous Gas Diffusion Electrodes for Rapid Ammonia Synthesis from Nitrogen and Water-Splitting-Derived Hydrogen. *Nat. Catal.* **2020**, *3* (5), 463–469. https://doi.org/10.1038/s41929-020-0455-8.

(12) Pletcher, D.; Walsh, F. C. *Industrial Electrochemistry*, 2nd Ed.; Springer, Dordrecht, 1993. https://doi.org/10.1007/978-94-011-2154-5.

(13) Suryanto, B. H. R.; Du, H. L.; Wang, D.; Chen, J.; Simonov, A. N.; MacFarlane, D. R. Challenges and Prospects in the Catalysis of Electroreduction of Nitrogen to Ammonia. *Nat. Catal.* **2019**, *2* (4), 290–296. https://doi.org/10.1038/s41929-019-0252-4.

(14) Andersen, S. Z.; Čolić, V.; Yang, S.; Schwalbe, J. A.; Nielander, A. C.; McEnaney, J.

M.; Enemark-Rasmussen, K.; Baker, J. G.; Singh, A. R.; Rohr, B. A.; et al. A Rigorous Electrochemical Ammonia Synthesis Protocol with Quantitative Isotope Measurements. *Nature* **2019**, *570* (7762), 504–508. https://doi.org/10.1038/s41586-019-1260-x.

(15) Jang, J.; Shen, K.; Morales-Guio, C. G. Electrochemical Direct Partial Oxidation of Methane to Methanol. *Joule* **2019**, *3* (11), 2589–2593. https://doi.org/10.1016/j.joule.2019.10.004.

(16) Kim, R. S.; Surendranath, Y. Electrochemical Reoxidation Enables Continuous Methane-to-Methanol Catalysis with Aqueous Pt Salts. *ACS Cent. Sci.* **2019**, *5* (7), 1179–1186. https://doi.org/10.1021/acscentsci.9b00273.

(17) Fornaciari, J. C.; Primc, D.; Kawashima, K.; Wygant, B. R.; Verma, S.; Spanu, L.; Mullins, C. B.; Bell, A. T.; Weber, A. Z. A Perspective on the Electrochemical Oxidation of Methane to Methanol in Membrane Electrode Assemblies. *ACS Energy Lett.* **2020**, *5* (9), 2954–2963. https://doi.org/10.1021/acsenergylett.0c01508.

(18) Prajapati, A.; Collins, B. A.; Goodpaster, J. D.; Singh, M. R. Fundamental Insight into Electrochemical Oxidation of Methane towards Methanol on Transition Metal Oxides. *Proc. Natl. Acad. Sci. U. S. A.* **2021**, *118* (8). https://doi.org/10.1073/pnas.2023233118.

(19) Arminio-Ravelo, J. A.; Escudero-Escribano, M. Strategies toward the Sustainable Electrochemical Oxidation of Methane to Methanol. *Curr. Opin. Green Sustain. Chem.* **2021**, *30*, 100489. https://doi.org/10.1016/j.cogsc.2021.100489.

(20) Martín, A. J.; Pérez-Ramírez, J. Heading to Distributed Electrocatalytic Conversion of Small Abundant Molecules into Fuels, Chemicals, and Fertilizers. *Joule* **2019**, *3* (11), 2602–2621. https://doi.org/10.1016/j.joule.2019.09.007.

(21) van Troostwijk, A. P.; Deiman, J. R. Sur Une Maniere de Décomposer l'Eau En Air Inflammable et En Air Vital. *Obs. Phys.* **1789**, *35*, 369.

(22) Zou, X.; Zhang, Y. Noble Metal-Free Hydrogen Evolution Catalysts for Water Splitting. *Chem. Soc. Rev.* **2015**, *44* (15), 5148–5180. https://doi.org/10.1039/c4cs00448e.

(23) Wu, H.; Feng, C.; Zhang, L.; Zhang, J.; Wilkinson, D. P. *Non-Noble Metal Electrocatalysts for the Hydrogen Evolution Reaction in Water Electrolysis*; Springer Singapore, 2021; Vol. 4. https://doi.org/10.1007/s41918-020-00086-z.

(24) Li, Y.; Zhou, L.; Guo, S. Noble Metal-Free Electrocatalytic Materials for Water Splitting in Alkaline Electrolyte. *EnergyChem* **2021**, *3* (2), 100053. https://doi.org/10.1016/j.enchem.2021.100053.

(25) Ďurovič, M.; Hnát, J.; Bouzek, K. Electrocatalysts for the Hydrogen Evolution Reaction in Alkaline and Neutral Media. A Comparative Review. *J. Power Sources* **2021**, *493* (March). https://doi.org/10.1016/j.jpowsour.2021.229708.

(26) Garcia-Araez, N.; Climent, V.; Feliu, J. Potential-Dependent Water Orientation on Pt(111), Pt(100), and Pt(110), as Inferred from Laser-Pulsed Experiments. Electrostatic and Chemical Effects. *J. Phys. Chem. C* **2009**, *113* (21), 9290–9304. https://doi.org/10.1021/jp900792q.

(27) Roman, T.; Groß, A. Structure of Water Layers on Hydrogen-Covered Pt Electrodes. *Catal. Today* **2013**, *202* (1), 183–190. https://doi.org/10.1016/j.cattod.2012.06.001.

(28) Rebollar, L.; Intikhab, S.; Snyder, J. D.; Tang, M. H. Kinetic Isotope Effects Quantify PH-Sensitive Water Dynamics at the Pt Electrode Interface. *J. Phys. Chem. Lett.* **2020**, 2308–2313. https://doi.org/10.1021/acs.jpclett.0c00185.

(29) Cheng, T.; Wang, L.; Merinov, B. V.; Goddard, W. A. Explanation of Dramatic PH-Dependence of Hydrogen Binding on Noble Metal Electrode: Greatly Weakened Water Adsorption at High PH. *J. Am. Chem. Soc.* **2018**, *140* (25), 7787–7790. https://doi.org/10.1021/jacs.8b04006.

(30) Sarabia, F. J.; Sebastián-Pascual, P.; Koper, M. T. M.; Climent, V.; Feliu, J. M. Effect of the Interfacial Water Structure on the Hydrogen Evolution Reaction on Pt(111) Modified with Different Nickel Hydroxide Coverages in Alkaline Media. *ACS Appl. Mater. Interfaces* **2019**, *11* (1), 613–623. https://doi.org/10.1021/acsami.8b15003.

(31) Ranninger, J.; Mayrhofer, K. J. J.; Berkes, B. B. The Crucial Role of Water in the Stability and Electrocatalytic Activity of Pt Electrodes. *J. Phys. Chem. C* **2021**, *125* (24), 13254–13263. https://doi.org/10.1021/acs.jpcc.1c02124.

(32) Lam, Y. C.; Soudackov, A. V.; Hammes-Schiffer, S. Kinetics of Proton Discharge on Metal Electrodes: Effects of Vibrational Nonadiabaticity and Solvent Dynamics. *J. Phys. Chem. Lett.* **2019**, *10* (18), 5312–5317. https://doi.org/10.1021/acs.jpclett.9b01984.

(33) Ledezma-Yanez, I.; Wallace, W. D. Z.; Sebastián-Pascual, P.; Climent, V.; Feliu, J. M.; Koper, M. T. M. Interfacial Water Reorganization as a PH-Dependent Descriptor of the Hydrogen Evolution Rate on Platinum Electrodes. *Nat. Energy* **2017**, *2* (4), 1–7. https://doi.org/10.1038/nenergy.2017.31.

(34) Dubouis, N.; Serva, A.; Salager, E.; Deschamps, M.; Salanne, M.; Grimaud, A. The Fate of Water at the Electrochemical Interfaces: Electrochemical Behavior of Free Water Versus Coordinating Water. *J. Phys. Chem. Lett.* **2018**, *9* (23), 6683–6688. https://doi.org/10.1021/acs.jpclett.8b03066.

(35) Yang, X.; Nash, J.; Oliveira, N.; Yan, Y.; Xu, B. Understanding the PH Dependence of Underpotential Deposited Hydrogen on Platinum. *Angew. Chemie - Int. Ed.* **2019**, *58* (49), 17718–17723. https://doi.org/10.1002/anie.201909697.

(36) Liu, E.; Li, J.; Jiao, L.; Doan, H. T. T.; Liu, Z.; Zhao, Z.; Huang, Y.; Abraham, K. M.; Mukerjee, S.; Jia, Q. Unifying the Hydrogen Evolution and Oxidation Reactions Kinetics in Base by Identifying the Catalytic Roles of Hydroxyl-Water-Cation Adducts. *J. Am. Chem. Soc.* **2019**, *141* (7), 3232–3239. https://doi.org/10.1021/jacs.8b13228.

(37) Liu, E.; Jiao, L.; Li, J.; Stracensky, T.; Sun, Q.; Mukerjee, S.; Jia, Q. Interfacial Water Shuffling the Intermediates of Hydrogen Oxidation and Evolution Reactions in Aqueous Media. *Energy Environ. Sci.* **2020**, *13* (9), 3064–3074. https://doi.org/10.1039/d0ee01754j.

(38) Rebollar, L.; Intikhab, S.; Snyder, J. D.; Tang, M. H. Determining the Viability of Hydroxide-Mediated Bifunctional HER/HOR Mechanisms through Single-Crystal Voltammetry and Microkinetic Modeling. *J. Electrochem. Soc.* **2018**, *165* (15), J3209–J3221. https://doi.org/10.1149/2.0271815jes.

(39) McCarthy, B. D.; Martin, D. J.; Rountree, E. S.; Ullman, A. C.; Dempsey, J. L. Electrochemical Reduction of Brønsted Acids by Glassy Carbon in Acetonitrile-Implications for Electrocatalytic Hydrogen Evolution. *Inorg. Chem.* **2014**, *53* (16), 8350–8361. https://doi.org/10.1021/ic500770k.

(40) Castelli, I. E.; Zorko, M.; Østergaard, T. M.; Martins, P. F. B. D.; Lopes, P. P.; Antonopoulos, B. K.; Maglia, F.; Markovic, N. M.; Strmcnik, D.; Rossmeisl, J. The Role of an Interface in Stabilizing Reaction Intermediates for Hydrogen Evolution in Aprotic

Electrolytes. *Chem. Sci.* **2020**. https://doi.org/10.1039/c9sc05768d.

(41) Dubouis, N.; Serva, A.; Berthin, R.; Jeanmairet, G.; Porcheron, B.; Salager, E.; Salanne, M.; Grimaud, A. Tuning Water Reduction through Controlled Nanoconfinement within an Organic Liquid Matrix. *Nat. Catal.* **2020**, *3*, 656–663. https://doi.org/https://doi.org/10.1038/s41929-020-0482-5.

(42) Ledezma-Yanez, I.; Koper, M. T. M. Influence of Water on the Hydrogen Evolution Reaction on a Gold Electrode in Acetonitrile Solution. *J. Electroanal. Chem.* **2017**, *793*, 18–24. https://doi.org/10.1016/j.jelechem.2016.08.018.

(43) Royer, M. E. Réduction de l'acide Carbonique En Acide Formique. *C. R. Hebd. Seances Acad. Sci.* **1870**, 731–732.

(44) Nitopi, S.; Bertheussen, E.; Scott, S. B.; Liu, X.; Engstfeld, A. K.; Horch, S.; Seger, B.; Stephens, I. E. L.; Chan, K.; Hahn, C.; et al. Progress and Perspectives of Electrochemical CO2 Reduction on Copper in Aqueous Electrolyte. *Chem. Rev.* **2019**, *119* (12), 7610–7672. https://doi.org/10.1021/acs.chemrev.8b00705.

(45) Corbin, N.; Zeng, J.; Williams, K.; Manthiram, K. Heterogeneous Molecular Catalysts for Electrocatalytic CO2 Reduction. *Nano Res.* **2019**, *12* (9), 2093–2125. https://doi.org/10.1007/s12274-019-2403-y.

(46) Ringe, S.; Clark, E. L.; Resasco, J.; Walton, A.; Seger, B.; Bell, A. T.; Chan, K. Understanding Cation Effects in Electrochemical CO2 Reduction. *Energy Environ. Sci.* **2019**, *12* (10), 3001–3014. https://doi.org/10.1039/c9ee01341e.

(47) König, M.; Vaes, J.; Klemm, E.; Pant, D. Solvents and Supporting Electrolytes in the Electrocatalytic Reduction of CO2. *iScience* **2019**, *19*, 135–160. https://doi.org/10.1016/j.isci.2019.07.014.

(48) Hussain, G.; Pérez-Martínez, L.; Le, J. B.; Papasizza, M.; Cabello, G.; Cheng, J.; Cuesta, A. How Cations Determine the Interfacial Potential Profile: Relevance for the CO2 Reduction Reaction. *Electrochim. Acta* **2019**, *327*. https://doi.org/10.1016/j.electacta.2019.135055.

(49) Li, J.; Li, X.; Gunathunge, C. M.; Waegele, M. M. Hydrogen Bonding Steers the Product Selectivity of Electrocatalytic CO Reduction. *Proc. Natl. Acad. Sci. U. S. A.* **2019**, *116* (19), 9220–9229. https://doi.org/10.1073/pnas.1900761116.

(50) Malkani, A. S.; Anibal, J.; Xu, B. Cation Effect on Interfacial CO2 Concentration in the Electrochemical CO2 Reduction Reaction. *ACS Catal.* **2020**, *in press*. https://doi.org/10.1021/acscatal.0c03553.

(51) Zhang, Z. Q.; Banerjee, S.; Thoi, V. S.; Shoji Hall, A. Reorganization of Interfacial Water by an Amphiphilic Cationic Surfactant Promotes CO2Reduction. *J. Phys. Chem. Lett.* **2020**, *11* (14), 5457–5463. https://doi.org/10.1021/acs.jpclett.0c01334.

(52) Dinh, C.; Burdyny, T.; Kibria, M. G.; Seifitokaldani, A.; Gabardo, C. M.; Arquer, F. P. G. de; Kiani, A.; Edwards, J. P.; De Luna, P.; Bushuyev, O. S.; et al. CO2 Electroreduction to Ethylene via Hydroxide-Mediated Catalysis at an Abrupt Reaction Interface. *Science (80-.).* **2018**, *360* (May), 783–787. https://doi.org/10.1126/science.aas9100.

(53) Küngas, R.; Blennow, P.; Heiredal-Clausen, T.; Holt, T.; Rass-Hansen, J.; Primdahl, S.; Hansen, J. B. ECOs - A Commercial CO2 Electrolysis System Developed by Haldor Topsoe. *ECS Meet. Abstr.* **2017**, *MA2017-03* (1), 118–118.

https://doi.org/10.1149/ma2017-03/1/118.

(54) Syngas - The Renewable Feed Gas https://www.sunfire.de/en/syngas (accessed Feb 4, 2022).

(55) twelve https://www.twelve.co/ (accessed Feb 4, 2022).

(56) Kumagai, H.; Nishikawa, T.; Koizumi, H.; Yatsu, T.; Sahara, G.; Yamazaki, Y.; Tamaki, Y.; Ishitani, O. Electrocatalytic Reduction of Low Concentration CO2. *Chem. Sci.* **2019**, Advance Article. https://doi.org/10.1039/C8SC04124E.

(57) Zhai, Y; Chiachiarelli, L; Sridhar, N. Effects of Gaseous Impurities on the Electrochemical Reduction of CO_2 on Copper Electrodes. *ECS Trans.* **2009**, *19* (14), 1–13. https://doi.org/10.1149/1.3220175.

(58) Engelbrecht, A.; Hämmerle, M.; Moos, R.; Fleischer, M.; Schmid, G. Improvement of the Selectivity of the Electrochemical Conversion of CO_2 to Hydrocarbons Using Cupreous Electrodes with in-Situ Oxidation by Oxygen. *Electrochim. Acta* **2017**, *224*, 642–648. https://doi.org/10.1016/j.electacta.2016.12.059.

(59) Verma, S.; Kim, B.; Jhong, H. M.; Ma, S. A Gross-Margin Model for Defining Technoeconomic Benchmarks in the Electroreduction of CO2. *ChemSusChem* **2016**, *9*, 1972–1979. https://doi.org/10.1002/cssc.201600394.

(60) Bushuyev, O. S.; Luna, P. De; Dinh, C. T.; Tao, L.; Saur, G.; Lagemaat, J. Van De; Kelley, S. O.; Sargent, E. H. What Should We Make with CO_2 and How Can We Make It ? *Joule* **2018**, *2*, 825–832. https://doi.org/10.1016/j.joule.2017.09.003.

(61) House, K. Z.; Baclig, A. C.; Ranjan, M.; van Nierop, E. A.; Wilcox, J.; Herzog, H. J. Economic and Energetic Analysis of Capturing CO_2 from Ambient Air. *Proc. Natl. Acad. Sci.* **2011**, *108* (51), 20428–20433. https://doi.org/10.1073/pnas.1012253108.

(62) Keith, D. W.; Holmes, G.; St. Angelo, D.; Heidel, K. A Process for Capturing CO2 from the Atmosphere. *Joule* **2018**, *2*, 1–22. https://doi.org/10.1016/j.joule.2018.05.006.

(63) Yeo, I.-H.; Johnson, D. C. Electrocatalysis of Anodic Oxygen-Transfer Reactions. Effect of Groups IIIA and VA Metal Oxides in Electrodeposited β-Lead Dioxide Electrodes in Acidic Media. *J. Electrochem. Soc.* **1987**, *134* (8). https://doi.org/10.1002/chin.198747023.

(64) Yeo, I.-H. Electrocatalysis of Anodic Oxygen Transfer Reactions: Comparison of Structural Data with Electrocatalytic Phenomena for Bismuth-Doped Lead Dioxide. *J. Electrochem. Soc.* **1989**, *136* (5), 1395. https://doi.org/10.1149/1.2096929.

(65) Hsiao, Y.-L. Electrocatalysis of Anodic Oxygen-Transfer Reactions: Chloride-Doped Lead Dioxide Electrodes. *J. Electrochem. Soc.* **1989**, *136* (12), 3704. https://doi.org/10.1149/1.2096534.

(66) Feng, J.; Johnson, D. C. Electrocatalysis of Anodic Oxygen-Transfer Reactions: Fe-Doped Beta-Lead Dioxide Electrodeposited on Noble Metals. *J. Electrochem. Soc.* **1990**, *137* (2), 507–510. https://doi.org/10.1149/1.2086488.

(67) Hsiao, Y.-L. Electrocatalysis of Anodic Oxygen-Transfer Reactions: Acetate-Doped Lead Dioxide Electrodes in Sulfuric Acid Media. *J. Electrochem. Soc.* **1992**, *139* (2), 377. https://doi.org/10.1149/1.2069226.

(68) Kawagoe, K. T.; Johnson, D. C. Electrocatalysis of Anodic Oxygen-Transfer Reactions: Oxidation of Phenol and Benzene at Bismuth-Doped Lead Dioxide Electrodes in Acidic Solutions. *J. Electrochem. Soc.* **1994**, *141* (12), 3404–3409.

https://doi.org/10.1149/1.2059345.

(69) Ge, J.; Johnson, D. C. Electrocatalysis of Anodic Oxygen-Transfer Reactions: Temperature Effects on Oxidation of Ethylamine, Alanine, and Ammonia at Anodized Ag-Pb Eutectic Alloy Electrodes. *J. Electrochem. Soc.* **1996**, *143* (8), 2543–2548. https://doi.org/10.1149/1.1837045.

(70) Holm, R. H. Metal-Centered Oxygen Atom Transfer Reactions. *Chem. Rev.* **1987**, *87* (6), 1401–1449. https://doi.org/10.1021/cr00082a005.

(71) Jin, K.; Maalouf, J.; Lazouski, N.; Corbin, N.; Yang, D.; Manthiram, K. Epoxidation of Cyclooctene Using Water as Oxygen-Atom Source at Manganese Oxide Electrocatalysts. *J. Am. Chem. Soc.* **2019**, *141* (15), 6413–6418. https://doi.org/10.1021/jacs.9b02345.

(72) Maalouf, J.; Jin, K.; Yang, D.; Limaye, A.; Manthiram, K. Kinetic Analysis of Electrochemical Lactonization of Ketones Using Water as the Oxygen Atom Source. *ACS Catal.*

(73) Sauermann, N.; Meyer, T. H.; Qiu, Y.; Ackermann, L. Electrocatalytic C-H Activation. *ACS Catal.* **2018**, *8* (8), 7086–7103. https://doi.org/10.1021/acscatal.8b01682.

(74) Meyer, T. H.; Finger, L. H.; Gandeepan, P.; Ackermann, L. Resource Economy by Metallaelectrocatalysis: Merging Electrochemistry and C H Activation. *Trends Chem.* **2019**, *1* (1), 63–76. https://doi.org/10.1016/j.trechm.2019.01.011.

(75) Newhouse, T.; Baran, P. S. If C-H Bonds Could Talk: Selective C-H Bond Oxidation. *Angew. Chemie - Int. Ed.* **2011**, *50* (15), 3362–3374. https://doi.org/10.1002/anie.201006368.

(76) Horn, E. J.; Rosen, B. R.; Chen, Y.; Tang, J.; Chen, K.; Eastgate, M. D.; Baran, P. S. Scalable and Sustainable Electrochemical Allylic C-H Oxidation. *Nature* **2016**, *533* (7601), 77–81. https://doi.org/10.1038/nature17431.

(77) Kawamata, Y.; Yan, M.; Liu, Z.; Bao, D. H.; Chen, J.; Starr, J. T.; Baran, P. S. Scalable, Electrochemical Oxidation of Unactivated C-H Bonds. *J. Am. Chem. Soc.* **2017**, *139* (22), 7448–7451. https://doi.org/10.1021/jacs.7b03539.

(78) Yan, M.; Kawamata, Y.; Baran, P. S. Synthetic Organic Electrochemical Methods since 2000: On the Verge of a Renaissance. *Chem. Rev.* **2017**, *117* (21), 13230–13319. https://doi.org/10.1021/acs.chemrev.7b00397.

(79) Kingston, C.; Palkowitz, M. D.; Takahira, Y.; Vantourout, J. C.; Peters, B. K.; Kawamata, Y.; Baran, P. S. A Survival Guide for the " Electro-Curious ." **2019**. https://doi.org/10.1021/acs.accounts.9b00539.

(80) Carneiro, J.; Nikolla, E. Electrochemical Conversion of Biomass-Based Oxygenated Compounds. *Annu. Rev. Chem. Biomol. Eng.* **2019**, *10*, 85–104. https://doi.org/10.1146/annurev-chembioeng-060718-030148.

(81) Williams, K.; Corbin, N.; Zeng, J.; Lazouski, N.; Yang, D.-T.; Manthiram, K. Protecting Effect of Mass Transport during Electrochemical Reduction of Oxygenated Carbon Dioxide Feedstocks. *Sustain. Energy Fuels* **2019**, *3* (5), 1225–1232. https://doi.org/10.1039/c9se00024k.

(82) Commission, I. E. *Electrical Energy Storage*; 2011.

(83) Kuhl, K. P.; Cave, E. R.; Abram, D. N.; Jaramillo, T. F. New Insights into the Electrochemical Reduction of Carbon Dioxide on Metallic Copper Surfaces. *Energy*

Environ. Sci. **2012**, *5* (5), 7050–7059. https://doi.org/10.1039/c2ee21234j.

(84) Kuhl, K. P.; Hatsukade, T.; Cave, E. R.; Abram, D. N.; Kibsgaard, J.; Jaramillo, T. F. Electrocatalytic Conversion of Carbon Dioxide to Methane and Methanol on Transition Metal Surfaces. *J. Am. Chem. Soc.* **2014**, *136* (40), 14107–14113. https://doi.org/10.1021/ja505791r.

(85) US Department of Commerce, NOAA, E. S. R. L. ESRL Global Monitoring Division - Global Greenhouse Gas Reference Network https://www.esrl.noaa.gov/gmd/ccgg/trends/ (accessed Nov 7, 2018).

(86) Wakerley, D. W.; Reisner, E. Oxygen-Tolerant Proton Reduction Catalysis: Much O2 about Nothing? *Energy Environ. Sci.* **2015**, *8* (8), 2283–2295. https://doi.org/10.1039/C5EE01167A.

(87) Cave, E. R.; Montoya, J. H.; Kuhl, K. P.; Abram, D. N.; Hatsukade, T.; Shi, C.; Hahn, C.; Nørskov, J. K.; Jaramillo, T. F. Electrochemical CO_2 Reduction on Au Surfaces: Mechanistic Aspects Regarding the Formation of Major and Minor Products. *Phys. Chem. Chem. Phys.* **2017**, *19* (24), 15856–15863. https://doi.org/10.1039/C7CP02855E.

(88) Chen, Y.; Li, C. W.; Kanan, M. W. Aqueous CO_2 Reduction at Very Low Overpotential on Oxide-Derived Au Nanoparticles. *J. Am. Chem. Soc.* **2012**, *134*, 19969–19972. https://doi.org/10.1021/ja309317u.

(89) Wuttig, A.; Yaguchi, M.; Motobayashi, K.; Osawa, M.; Surendranath, Y. Inhibited Proton Transfer Enhances Au-Catalyzed CO_2-to-Fuels Selectivity. *Proc. Natl. Acad. Sci.* **2016**, *113* (32), E4585–E4593. https://doi.org/10.1073/pnas.1602984113.

(90) Wuttig, A.; Yoon, Y.; Ryu, J.; Surendranath, Y. Bicarbonate Is Not a General Acid in Au-Catalyzed CO_2 Electroreduction. *J. Am. Chem. Soc.* **2017**, *139* (47), 17109–17113. https://doi.org/10.1021/jacs.7b08345.

(91) Dunwell, M.; Lu, Q.; Heyes, J. M.; Rosen, J.; Chen, J. G.; Yan, Y.; Jiao, F.; Xu, B. The Central Role of Bicarbonate in the Electrochemical Reduction of Carbon Dioxide on Gold. *J. Am. Chem. Soc.* **2017**, *139* (10), 3774–3783. https://doi.org/10.1021/jacs.6b13287.

(92) Lobaccaro, P.; Singh, M. R.; Clark, E. L.; Kwon, Y.; Bell, A. T.; Ager, J. W. Effects of Temperature and Gas-Liquid Mass Transfer on the Operation of Small Electrochemical Cells for the Quantitative Evaluation of CO_2 Reduction Electrocatalysts. *Phys. Chem. Chem. Phys.* **2016**, *18* (38), 26777–26785. https://doi.org/10.1039/C6CP05287H.

(93) Hatsukade, T.; Kuhl, K. P.; Cave, E. R.; Abram, D. N.; Jaramillo, T. F. Insight into the Electrocatalytic Reduction of CO_2 on Metallic Silver Surfaces. *Phys. Chem. Chem. Phys.* **2014**, *16*, 13814–13819. https://doi.org/10.1039/c4cp00692e.

(94) Wuttig, A.; Surendranath, Y. Impurity Ion Complexation Enhances Carbon Dioxide Reduction Catalysis. *ACS Catal.* **2015**, *5* (7), 4479–4484. https://doi.org/10.1021/acscatal.5b00808.

(95) Standard Reduction Potentials at 25 C; McGraw-Hill, 2009.

(96) Deen, W. M. *Analysis of Transport Phenomena*, 2nd ed.; Oxford University Press, 2011.

(97) Commerce, U. S. D. of. NIST Chemistry WebBook https://webbook.nist.gov/chemistry/ (accessed Dec 11, 2018).

(98) Clark, E. L.; Resasco, J.; Landers, A.; Lin, J.; Chung, L.-T.; Walton, A.; Hahn, C.; Jaramillo, T. F.; Bell, A. T. Data Acquisition Protocols and Reporting Standards for

Studies of the Electrochemical Reduction of Carbon Dioxide. *ACS Catal.* **2018**, acscatal.8b01340. https://doi.org/10.1021/acscatal.8b01340.

(99) Cussler, E. L. *Diffusion: Mass Transfer in Fluid Systems (2nd Ed.)*; 1997.

(100) Koper, M. T. M. Theory of Multiple Proton–Electron Transfer Reactions and Its Implications for Electrocatalysis. *Chem. Sci.* **2013**, *4*, 2710–2723. https://doi.org/10.1039/c3sc50205h.

(101) Srejić, I. Oxygen Reduction on Au(100)-like Polycrystalline Gold Electrode in Alkaline Solution. *Int. J. Electrochem. Sci.* **2016**, *11*, 10436–10448. https://doi.org/10.20964/2016.12.51.

(102) Ge, X.; Sumboja, A.; Wuu, D.; An, T.; Li, B.; Goh, F. W. T.; Hor, T. S. A.; Zong, Y.; Liu, Z. Oxygen Reduction in Alkaline Media: From Mechanisms to Recent Advances of Catalysts. *ACS Catal.* **2015**, *5* (8), 4643–4667. https://doi.org/10.1021/acscatal.5b00524.

(103) Gupta, N.; Gattrell, M.; Macdougall, B. Calculation for the Cathode Surface Concentrations in the Electrochemical Reduction of CO 2 in KHCO 3 Solutions. **2006**, 161–172. https://doi.org/10.1007/s10800-005-9058-y.

(104) Lee, C. W.; Cho, N. H.; Im, S. W.; Jee, M. S.; Hwang, Y. J.; Min, B. K.; Nam, K. T. New Challenges of Electrokinetic Study in Investigating the Reaction Mechanism of Electrochemical CO2 Reduction. *J. Mater. Chem. A* **2018**, *6*, 14043–14057. https://doi.org/10.1039/C8TA03480J.

(105) National Center for Biotechnology Information. Sodium bicarbonate | NaHCO3 - PubChem https://pubchem.ncbi.nlm.nih.gov/compound/sodium_bicarbonate#section=Solubility (accessed Dec 12, 2018).

(106) Huynh, M. T.; Mora, S. J.; Villalba, M.; Tejeda-Ferrari, M. E.; Liddell, P. A.; Cherry, B. R.; Teillout, A. L.; MacHan, C. W.; Kubiak, C. P.; Gust, D.; et al. Concerted One-Electron Two-Proton Transfer Processes in Models Inspired by the Tyr-His Couple of Photosystem II. *ACS Cent. Sci.* **2017**, *3* (5), 372–380. https://doi.org/10.1021/acscentsci.7b00125.

(107) Goldman, A. S.; Krogh-Jespersen, K. Why Do Cationic Carbon Monoxide Complexes Have High C-O Stretching Force Constants and Short C-O Bonds? Electrostatic Effects, Not σ-Bonding. *J. Am. Chem. Soc.* **1996**, *118* (48), 12159–12166. https://doi.org/10.1021/ja960876z.

(108) Xu, Q. Metal Carbonyl Cations: Generation, Characterization and Catalytic Application. *Coord. Chem. Rev.* **2002**, *231* (1–2), 83–108. https://doi.org/10.1016/S0010-8545(02)00115-7.

(109) Xu, X.; Song, C.; Wincek, R.; Andresen, J. M.; Miller, B. G.; Scaroni, A. W. Separation of CO_2 from Power Plant Flue Gas Using a Novel CO_2 "Molecular Basket" Adsorbent. *Fuel Chem. Div. Prepr.* **2003**, *48* (1), 162–163.

(110) Yang, Hong; Kuhn, Andrew; Chen, Zhitao; Lu, Y. Sequential Oxygen Reduction and Adsorption for Carbon Dioxide Purification for Flue Gas Applications. *Energy Technol.* **2018**. https://doi.org/10.1002/ente.201800917.

(111) Williams, K.; Limaye, A.; Weiss, T.; Chung, M.; Manthiram, K. Accounting for Species' Thermodynamic Activities Changes Mechanistic Interpretations of

Electrochemical Kinetic Data. *ChemRxiv* **2022**.

(112) Sasaki, K.; Kashimura, T.; Ohura, M.; Ohsaki, Y.; Ohta, N. Solvent Effect in the Electrochemical Reduction of P-Quinones in Several Aprotic Solvents. *J. Electrochem. Soc.* **1990**, *137* (8), 2437–2443. https://doi.org/10.1149/1.2086957.

(113) Park, J. W.; Yamauchi, K.; Takashima, E.; Tachikawa, N.; Ueno, K.; Dokko, K.; Watanabe, M. Solvent Effect of Room Temperature Ionic Liquids on Electrochemical Reactions in Lithium-Sulfur Batteries. *J. Phys. Chem. C* **2013**, *117* (9), 4431–4440. https://doi.org/10.1021/jp400153m.

(114) Barrette, W. C.; Sawyer, D. T. Determination of Dissolved Hydrogen and Effects of Media and Electrode Materials on the Electrochemical Oxidation of Molecular Hydrogen. *Anal. Chem.* **1984**, *56* (4), 653–657. https://doi.org/10.1021/ac00268a015.

(115) Monteiro, M. C. O.; Goyal, A.; Moerland, P.; Koper, M. T. M. Understanding Cation Trends for Hydrogen Evolution on Platinum and Gold Electrodes in Alkaline Media. *ACS Catal.* **2021**, 14328–14335. https://doi.org/10.1021/acscatal.1c04268.

(116) Goyal, A.; Koper, M. T. M. The Interrelated Effect of Cations and Electrolyte PH on the Hydrogen Evolution Reaction on Gold Electrodes in Alkaline Media. *Angew. Chemie - Int. Ed.* **2021**, *60* (24), 13452–13462. https://doi.org/10.1002/anie.202102803.

(117) Hatay, I.; Su, B.; Li, F.; Partovi-Nia, R.; Vrubel, H.; Hu, X.; Ersoz, M.; Girault, H. H. Hydrogen Evolution at Liquid-Liquid Interfaces. *Angew. Chemie - Int. Ed.* **2009**, *48* (28), 5139–5142. https://doi.org/10.1002/anie.200901757.

(118) Terry Weatherly, C. K.; Ren, H.; Edwards, M. A.; Wang, L.; White, H. S. Coupled Electron- and Phase-Transfer Reactions at a Three-Phase Interface. *J. Am. Chem. Soc.* **2019**, *141* (45), 18091–18098. https://doi.org/10.1021/jacs.9b07283.

(119) Dong, F.; Chen, H.; Malapit, C. A.; Prater, M. B.; Li, M.; Yuan, M.; Lim, K.; Minteer, S. D. Biphasic Bioelectrocatalytic Synthesis of Chiral β-Hydroxy Nitriles. *J. Am. Chem. Soc.* **2020**, *142* (18), 8374–8382. https://doi.org/10.1021/jacs.0c01890.

(120) Noël, T.; Cao, Y.; Laudadio, G. The Fundamentals behind the Use of Flow Reactors in Electrochemistry. *Acc. Chem. Res.* **2019**, *52* (10), 2858–2869. https://doi.org/10.1021/acs.accounts.9b00412.

(121) Chen, H.; Cong, G.; Lu, Y.-C. Recent Progress in Organic Redox Flow Batteries: Active Materials, Electrolytes and Membranes. *J. Energy Chem.* **2018**, *27* (5), 1304–1325. https://doi.org/10.1016/j.jechem.2018.02.009.

(122) Stace, A. J. Preferential Solvation of Hydrogen Ions in Mixed Water-Amine Ion Clusters. *J. Am. Chem. Soc.* **1984**, *106* (8), 2306–2315. https://doi.org/10.1021/ja00320a016.

(123) Mestdagh, J. M.; Binet, A.; Sublemontier, O. Solvation Shells of the Proton Surrounded by Acetonitrile, Ethanol, and Water Molecules. *J. Phys. Chem.* **1989**, *93* (26), 8300–8303. https://doi.org/10.1021/j100363a006.

(124) Jamroz, D.; Stangret, J.; Lindgren, J.; Jamroz, D.; Stangret, J. An Infrared Spectroscopic Study of the Preferential Solvation in Water-Acetonitrile Mixtures. *J. Am. Chem. Soc.* **1993**, *115* (14), 6165–6168. https://doi.org/10.1021/ja00067a036.

(125) Kovacs, H.; Laaksonen, A. Molecular Dynamics Simulation and NMR Study of Water-Acetonitrile Mixtures. *J. Am. Chem. Soc.* **1991**, *113* (15), 5596–5605. https://doi.org/10.1021/ja00015a013.

(126) Guo, J.-H.; Luo, Y.; Augustsson, A.; Kashtanov, S.; Rubensson, J.-E. E.; Shuh, D. K. D.; Agren, H.; Nordgren, J.; Ågren, H.; Nordgren, J. Molecular Structure of Alcohol-Water Mixtures. *Phys. Rev. Lett.* **2003**, *91* (15), 1–4. https://doi.org/10.1103/PhysRevLett.91.157401.

(127) Kashtanov, S.; Augustson, A.; Rubensson, J.-E.; Nordgren, J.; Ågren, H.; Guo, J.-H.; Luo, Y. Chemical and Electronic Structures of Liquid Methanol from X-Ray Emission Spectroscopy and Density Functional Theory. *Phys. Rev. B* **2005**, *71*, 104205. https://doi.org/10.1103/PhysRevB.71.104205.

(128) Verma, A.; Stoppelman, J. P.; McDaniel, J. G. Tuning Water Networks via Ionic Liquid/Water Mixtures. *Int. J. Mol. Sci.* **2020**, *21* (2). https://doi.org/10.3390/ijms21020403.

(129) Suo, L.; Borodin, O.; Gao, T.; Olguin, M.; Ho, J.; Fan, X.; Luo, C.; Wang, C.; Xu, K. "Water-in-Salt" Electrolyte Enables High-Voltage Aqueous Lithium-Ion Chemistries. *Science (80-.).* **2015**, *350* (6263), 938–943. https://doi.org/10.1126/science.aab1595.

(130) Shuai, L.; Luterbacher, J. Organic Solvent Effects in Biomass Conversion Reactions. *ChemSusChem* **2016**, *9* (2), 133–155. https://doi.org/10.1002/cssc.201501148.

(131) Mellmer, M. A.; Sanpitakseree, C.; Demir, B.; Bai, P.; Ma, K.; Neurock, M.; Dumesic, J. A. Solvent-Enabled Control of Reactivity for Liquid-Phase Reactions of Biomass-Derived Compounds. *Nat. Catal.* **2018**, *1* (3), 199–207. https://doi.org/10.1038/s41929-018-0027-3.

(132) Chew, A. K.; Walker, T. W.; Shen, Z.; Demir, B.; Witteman, L.; Euclide, J.; Huber, G. W.; Dumesic, J. A.; Van Lehn, R. C. Effect of Mixed-Solvent Environments on the Selectivity of Acid-Catalyzed Dehydration Reactions. *ACS Catal.* **2020**, *10* (3), 1679–1691. https://doi.org/10.1021/acscatal.9b03460.

(133) Angamuthu, R.; Bouwman, E. Reduction of Protons Assisted by a Hexanuclear Nickel Thiolate Metallacrown: Protonation and Electrocatalytic Dihydrogen Evolution. *Phys. Chem. Chem. Phys.* **2009**, *11* (27), 5578–5583. https://doi.org/10.1039/b904932k.

(134) Lee, C. H.; Dogutan, D. K.; Nocera, D. G. Hydrogen Generation by Hangman Metalloporphyrins. *J. Am. Chem. Soc.* **2011**, *133* (23), 8775–8777. https://doi.org/10.1021/ja202136y.

(135) Zeradjanin, A. R.; Vimalanandan, A.; Polymeros, G.; Topalov, A. A.; Mayrhofer, K. J. J.; Rohwerder, M. Balanced Work Function as a Driver for Facile Hydrogen Evolution Reaction - Comprehension and Experimental Assessment of Interfacial Catalytic Descriptor. *Phys. Chem. Chem. Phys.* **2017**, *19* (26), 17019–17027. https://doi.org/10.1039/c7cp03081a.

(136) Rebollar, L.; Intikhab, S.; Oliveira, N. J.; Yan, Y.; Xu, B.; McCrum, I. T.; Snyder, J. D.; Tang, M. H. "Beyond Adsorption" Descriptors in Hydrogen Electrocatalysis. *ACS Catal.* **2020**, *10* (24), 14747–14762. https://doi.org/10.1021/acscatal.0c03801.

(137) Ledezma-Yanez, I.; Díaz-Morales, O.; Figueiredo, M. C.; Koper, M. T. M. Hydrogen Oxidation and Hydrogen Evolution on a Platinum Electrode in Acetonitrile. *ChemElectroChem* **2015**, *2* (10), 1612–1622. https://doi.org/10.1002/celc.201500341.

(138) Lanning, J. A.; Chambers, J. Q. Voltammetric Study of the Hydrogen Ion/Hydrogen Couple in Acetonitrile/Water Mixtures. *Anal. Chem.* **1973**, *45* (7), 1010–1016. https://doi.org/10.1021/ac60329a002.

(139) Harlow, G. S.; Aldous, I. M.; Thompson, P.; Gründer, Y.; Hardwick, L. J.; Lucas, C. A. Adsorption, Surface Relaxation and Electrolyte Structure at Pt(111) Electrodes in Non-Aqueous and Aqueous Acetonitrile Electrolytes. *Phys. Chem. Chem. Phys.* **2019**, *21* (17), 8654–8662. https://doi.org/10.1039/c9cp00499h.

(140) Suárez-Herrera, M. F.; Costa-Figueiredo, M.; Feliu, J. M. Voltammetry of Basal Plane Platinum Electrodes in Acetonitrile Electrolytes: Effect of the Presence of Water. *Langmuir* **2012**, *28* (11), 5286–5294. https://doi.org/10.1021/la205097p.

(141) Roberts, J. A. S. S.; Bullock, R. M. Direct Determination of Equilibrium Potentials for Hydrogen Oxidation/Production by Open Circuit Potential Measurements in Acetonitrile. *Inorg. Chem.* **2013**, *52* (7), 3823–3835. https://doi.org/10.1021/ic302461q.

(142) Bautista-Martinez, J. A.; Tang, L.; Zeller, R.; Angell, C. A.; Friesen, C. Hydrogen Redox in Protic Ionic Liquids and a Direct Measurement of Proton Thermodynamics. *J. Phys. Chem. C* **2009**, *113*, 12586–12593. https://doi.org/10.1021/jp902762c.

(143) O'Reilly, N. J.; Magner, E. Electrochemistry of Cytochrome c in Aqueous and Mixed Solvent Solutions: Thermodynamics, Kinetics, and the Effect of Solvent Dielectric Constant. *Langmuir* **2005**, *21* (3), 1009–1014. https://doi.org/10.1021/la048796t.

(144) Matsubara, Y. Unified Benchmarking of Electrocatalysts in Noninnocent Second Coordination Spheres for CO2 Reduction. *ACS Energy Lett.* **2019**, *4* (8), 1999–2004. https://doi.org/10.1021/acsenergylett.9b01180.

(145) Briega-Martos, V.; Costa-Figueiredo, M.; Orts, J. M.; Rodes, A.; Koper, M. T. M.; Herrero, E.; Feliu, J. M. Acetonitrile Adsorption on Pt Single-Crystal Electrodes and Its Effect on Oxygen Reduction Reaction in Acidic and Alkaline Aqueous Solutions. *J. Phys. Chem. C* **2019**, *123* (4), 2300–2313. https://doi.org/10.1021/acs.jpcc.8b10690.

(146) Briega-Martos, V.; Solla-Gullón, J.; Koper, M. T. M.; Herrero, E.; Feliu, J. M. Electrocatalytic Enhancement of Formic Acid Oxidation Reaction by Acetonitrile on Well-Defined Platinum Surfaces. *Electrochim. Acta* **2019**, *295*, 835–845. https://doi.org/10.1016/j.electacta.2018.11.016.

(147) D'Elia, L. F.; Ortiz, R. L. Electrochemical Oxidation of Toluene on Glassy Carbon in Organic-Aqueous Acid Solution. *J. Electrochem. Soc.* **2006**, *153* (12), D187. https://doi.org/10.1149/1.2358120.

(148) Madon, R. J.; Iglesia, E. Catalytic Reaction Rates in Thermodynamically Non-Ideal Systems. *J. Mol. Catal. A Chem.* **2000**, *163* (1–2), 189–204. https://doi.org/10.1016/S1381-1169(00)00386-1.

(149) Treiner, C.; Tzias, P.; Chemla, M. Solvation of Tetrabutylammonium Bromide in Water Acetonitrile Mixtures at 298.15 K from Vapour Pressure Measurements of Dilute Solutions. *J. Chem. Soc. Faraday Trans. 1* **1976**, *72*, 2007–2015. https://doi.org/10.1039/F19767202007.

(150) Sirotkin, V. A.; Solomonov, B. N.; Faizullin, D. A.; Fedotov, V. D. IR Spectroscopic Study of the State of Water in Dioxane and Acetonitrile: Relationship with the Thermodynamic Activity of Water at 278-318 K. *J. Struct. Chem.* **2000**, *41* (6), 997–1003.

(151) Gonella, G.; Backus, E. H. G.; Nagata, Y.; Bonthuis, D. J.; Loche, P.; Schlaich, A.; Netz, R. R.; Kühnle, A.; McCrum, I. T.; Koper, M. T. M.; et al. Water at Charged Interfaces. *Nat. Rev. Chem.* **2021**, *5* (7), 466–485. https://doi.org/10.1038/s41570-021-00293-2.

(152) Noviandri, I.; Brown, K. N.; Fleming, D. S.; Gulyas, P. T.; Lay, P. A.; Masters, A. F.; Phillips, L. The Decamethylferrocenium/Decamethylferrocene Redox Couple: A Superior Redox Standard to the Ferrocenium/Ferrocene Redox Couple for Studying Solvent Effects on the Thermodynamics of Electron Transfer. *J. Phys. Chem. B* **1999**, *103* (32), 6713–6722. https://doi.org/10.1021/jp991381+.

(153) Agarwal, R. G.; Coste, S. C.; Groff, B. D.; Heuer, A. M.; Noh, H.; Parada, G. A.; Wise, C. F.; Nichols, E. M.; Warren, J. J.; Mayer, J. M. Free Energies of Proton-Coupled Electron Transfer Reagents and Their Applications. *Chem. Rev.* **2021**. https://doi.org/10.1021/acs.chemrev.1c00521.

(154) Wise, C. F.; Agarwal, R. G.; Mayer, J. M. Determining Proton-Coupled Standard Potentials and X-H Bond Dissociation Free Energies in Nonaqueous Solvents Using Open-Circuit Potential Measurements. *J. Am. Chem. Soc.* **2020**, *142* (24), 10681–10691. https://doi.org/10.1021/jacs.0c01032.

(155) Shinagawa, T.; Garcia-Esparza, A. T.; Takanabe, K. Insight on Tafel Slopes from a Microkinetic Analysis of Aqueous Electrocatalysis for Energy Conversion. *Sci. Rep.* **2015**, *5* (September), 1–21. https://doi.org/10.1038/srep13801.

(156) Kahyarian, A.; Brown, B.; Nesic, S. Mechanism of the Hydrogen Evolution Reaction in Mildly Acidic Environments on Gold. *J. Electrochem. Soc.* **2017**, *164* (6), H365–H374. https://doi.org/10.1149/2.1061706jes.

(157) Goyal, A.; Koper, M. T. M. Understanding the Role of Mass Transport in Tuning the Hydrogen Evolution Kinetics on Gold in Alkaline Media. *J. Chem. Phys.* **2021**, *155* (13). https://doi.org/10.1063/5.0064330.

(158) Limaye, A. M.; Zeng, J. S.; Willard, A. P.; Manthiram, K. Bayesian Data Analysis Reveals No Preference for Cardinal Tafel Slopes in CO2 Reduction Electrocatalysis. *Nat. Commun.* **2021**, *12* (1), 1–10. https://doi.org/10.1038/s41467-021-20924-y.

(159) de Grotthuß, C. J. D. T. Sur La Décomposition de l'eau et Des Corps Qu'elle Tient En Dissolution à l'aide de l'électricité Galvanique. *Ann. di Chim. (Rome, Italy)* **1805**, *58*, 54–73.

(160) Rasaiah, J. C.; Garde, S.; Hummer, G. Water in Nonpolar Confinement: From Nanotubes to Proteins and Beyond. *Annu. Rev. Phys. Chem.* **2008**, *59* (1), 713–740. https://doi.org/10.1146/annurev.physchem.59.032607.093815.

(161) Bates, J. S.; Bukowski, B. C.; Greeley, J.; Gounder, R. Structure and Solvation of Confined Water and Water-Ethanol Clusters within Microporous Brønsted Acids and Their Effects on Ethanol Dehydration Catalysis. *Chem. Sci.* **2020**, *11* (27), 7102–7122. https://doi.org/10.1039/d0sc02589e.

(162) Rudnev, A. V.; Molodkina, E. B.; Danilov, A. I.; Polukarov, Y. M.; Berna, A.; Feliu, J. M. Adsorption Behavior of Acetonitrile on Platinum and Gold Electrodes of Various Structures in Solution of 0.5 M H2SO4. *Electrochim. Acta* **2009**, *54* (14), 3692–3699. https://doi.org/10.1016/j.electacta.2009.01.047.

(163) Wu, X.; Liu, Z.; Huang, S.; Wang, W. Molecular Dynamics Simulation of Room-Temperature Ionic Liquid Mixture of [Bmim][BF4] and Acetonitrile by a Refined Force Field. *Phys. Chem. Chem. Phys.* **2005**, *7* (14), 2771–2779. https://doi.org/10.1039/b504681p.

(164) Bhowmik, D.; Malikova, N.; Mériguet, G.; Bernard, O.; Teixeira, J.; Turq, P. Aqueous Solutions of Tetraalkylammonium Halides: Ion Hydration, Dynamics and Ion-Ion

Interactions in Light of Steric Effects. *Phys. Chem. Chem. Phys.* **2014**, *16* (26), 13447–13457. https://doi.org/10.1039/c4cp01164c.

(165) Liu, Z.; Huang, S.; Wang, W. A Refined Force Field for Molecular Simulation of Imidazolium-Based Ionic Liquids. *J. Phys. Chem. B* **2004**, *108* (34), 12978–12989. https://doi.org/10.1021/jp048369o.

(166) Jorgensen, W. L.; Chandrasekhar, J.; Madura, J. D.; Impey, R. W.; Klein, M. L. Comparison of Simple Potential Functions for Simulating Liquid Water. *J. Chem. Phys.* **1983**, *79* (2), 926–935. https://doi.org/10.1063/1.445869.

(167) Martínez, L.; Andrade, R.; Birgin, E. G.; Martínez, J. M. PACKMOL: A Package for Building Initial Configurations for Molecular Dynamics Simulations. *J. Comput. Chem.* **2009**, *30* (13), 2157–2164. https://doi.org/10.1002/jcc.

(168) Goyal, A.; Marcandalli, G.; Mints, V. A.; Koper, M. T. M. Competition between CO2 Reduction and Hydrogen Evolution on a Gold Electrode under Well-Defined Mass Transport Conditions. *J. Am. Chem. Soc.* **2020**, *142* (9), 4154–4161. https://doi.org/10.1021/jacs.9b10061.

(169) Rogge, T.; Kaplaneris, N.; Chatani, N.; Kim, J.; Chang, S.; Punji, B.; Schafer, L. L.; Musaev, D. G.; Wencel-Delord, J.; Roberts, C. A.; et al. C-H Activation. *Nat. Rev. Methods Prim.* **2021**, *1*, 43.

(170) Zhang, H.; Li, C.; Lu, Q.; Cheng, M. J.; Goddard, W. A. Selective Activation of Propane Using Intermediates Generated during Water Oxidation. *J. Am. Chem. Soc.* **2021**, *143* (10), 3967–3974. https://doi.org/10.1021/jacs.1c00377.

(171) Tomás, R. A. F.; Bordado, J. C. M.; Gomes, J. F. P. P-Xylene Oxidation to Terephthalic Acid: A Literature Review Oriented toward Process Optimization and Development. *Chem. Rev.* **2013**, *113* (10), 7421–7469. https://doi.org/10.1021/cr300298j.

(172) Karakhanov, E. A.; Maksimov, A. L.; Zolotukhina, A. V.; Vinokurov, V. A. Oxidation of P-Xylene. *Russ. J. Appl. Chem.* **2018**, *91* (5), 707–727. https://doi.org/10.1134/s1070427218050014.

(173) Torii, S.; Tanaka, H.; Inokuchi, T.; Nakane, S.; Akada, M.; Saito, N.; Sirakawa, T. Indirect Electrooxidation (an Ex-Cell Method) of Alkylbenzenes by Recycle Use of (NH4)2Ce(NO3)6 in Various Solvent Systems. *J. Org. Chem.* **1982**, *47* (9), 1647–1652. https://doi.org/10.1021/jo00348a007.

(174) Kramer, K.; Robertson, P. M.; Ibl, N. Indirect Electrolytic Oxidation of Some Aromatic Derivatives. *J. Appl. Electrochem.* **1980**, *10* (1), 29–36. https://doi.org/10.1007/BF00937334.

(175) Kreysa, G.; Medin, H. Indirect Electrosynthesis of P-Methoxybenzaldehyde. *J. Appl. Electrochem.* **1986**, *16*, 757–767.

(176) Tomat, R.; Rigo, A. Electrochemical Oxidation of Toluene Promoted by OH Radicals. *J. Appl. Electrochem.* **1984**, *14* (1), 1–8. https://doi.org/10.1007/BF00611252.

(177) Shen, D.; Miao, C.; Wang, S.; Xia, C.; Sun, W. Efficient Benzylic and Aliphatic C-H Oxidation with Selectivity for Methylenic Sites Catalyzed by a Bioinspired Manganese Complex. *Org. Lett.* **2014**, *16* (4), 1108–1111. https://doi.org/10.1021/ol4037083.

(178) Zhao, J.; Wang, B.; Ma, H. Z.; Zhang, J. T. Electrochemical Oxidation of P-Xylene in Methanol Solvent Catalyzed by the Monometal and Multimetal Compounds. *Ind. Eng. Chem. Res.* **2006**, *45* (13), 4530–4536. https://doi.org/10.1021/ie060272w.

(179) Zhang, J. T.; Bai, Z. Q.; Feng, Y. R.; Yen, C. X.; Zhao, J.; Tian, W. Using Isopropanol as Solvent in Favor of P-Xylene Electrochemical Oxidation. *Russ. J. Electrochem.* **2009**, *45* (8), 913–921. https://doi.org/10.1134/s1023193509080126.

(180) Catino, A. J.; Nichols, J. M.; Choi, H.; Gottipamula, S.; Doyle, M. P. Benzylic Oxidation Catalyzed by Dirhodium(II,III) Caprolactamate. *Org. Lett.* **2005**, *7* (23), 5167–5170. https://doi.org/10.1021/ol0520020.

(181) Bonvin, Y.; Callens, E.; Larrosa, I.; Henderson, D. A.; Oldham, J.; Burton, A. J.; Barrett, A. G. M. Bismuth-Catalyzed Benzylic Oxidations with Tert-Butyl Hydroperoxide. *Org. Lett.* **2005**, *7* (21), 4549–4552. https://doi.org/10.1021/ol051765k.

(182) Młochowski, J.; Wójtowicz-Młochowska, H. Developments in Synthetic Application of Selenium(IV) Oxide and Organoselenium Compounds as Oxygen Donors and Oxygen-Transfer Agents. *Molecules* **2015**, *20* (6), 10205–10243. https://doi.org/10.3390/molecules200610205.

(183) Marko, J. A.; Durgham, A.; Bretz, S. L.; Liu, W. Electrochemical Benzylic Oxidation of C-H Bonds. *Chem. Commun.* **2019**, *55* (7), 937–940. https://doi.org/10.1039/c8cc08768g.

(184) Wentzel, B. B.; Donners, M. P. J.; Alsters, P. L.; Feiters, M. C.; Nolte, R. J. M. N-Hydroxyphthalimide/Cobalt(II) Catalyzed Low Temperature Benzylic Oxidation Using Molecular Oxygen. *Tetrahedron* **2000**, *56* (39), 7797–7803. https://doi.org/10.1016/S0040-4020(00)00679-7.

(185) Hruszkewycz, D. P.; Miles, K. C.; Thiel, O. R.; Stahl, S. S. Co/NHPI-Mediated Aerobic Oxygenation of Benzylic C-H Bonds in Pharmaceutically Relevant Molecules. *Chem. Sci.* **2017**, *8* (2), 1282–1287. https://doi.org/10.1039/c6sc03831j.

(186) Wendt, H.; Bitterlich, S.; Lodowicks, E.; Liu, Z. Anodic Synthesis of Benzaldehydes - II. Optimization of the Direct Anodic Oxidation of Toluenes in Methanol and Ethanol. *Electrochim. Acta* **1992**, *37* (11), 1959–1969.

(187) Loyson, P.; Gouws, S.; Barton, B.; Ackermann, M. Kinetic Aspects of the Direct Electrochemical Oxidation of P-Xylene in Methanol Using Graphite Electrodes. *South African J. Chem.* **2004**, *57*, 53–56.

(188) Otsuka, K.; Ishizuka, K.; Yamanaka, I.; Hatano, M. The Selective Oxidation of Toluene to Benzaldehyde Applying a Fuel Cell System in the Gas Phase. *J. Electrochem. Soc.* **1991**, *138* (11), 3176–3182. https://doi.org/10.1149/1.2085388.

(189) Meng, L.; Su, J.; Zha, Z.; Zhang, L.; Zhang, Z.; Wang, Z. Direct Electrosynthesis of Ketones from Benzylic Methylenes by Electrooxidative C-H Activation. *Chem. - A Eur. J.* **2013**, *19* (18), 5542–5545. https://doi.org/10.1002/chem.201204207.

(190) Roznyatovskaya, N.; Noack, J.; Pinkwart, K.; Tübke, J. Aspects of Electron Transfer Processes in Vanadium Redox-Flow Batteries. *Curr. Opin. Electrochem.* **2020**, *19*, 42–48. https://doi.org/10.1016/j.coelec.2019.10.003.

(191) Yang, D.-T.; Zhu, M.; Schiffer, Z. J.; Williams, K.; Song, X.; Liu, X.; Manthiram, K. Direct Electrochemical Carboxylation of Benzylic C–N Bonds with Carbon Dioxide. *ACS Catal.* **2019**, *9* (5), 4699–4705. https://doi.org/10.1021/acscatal.9b00818.

(192) Dresselhaus, M. S.; Dresselhaus, G.; Saito, R.; Jorio, A. Raman Spectroscopy of Carbon Nanotubes. *Phys. Rep.* **2005**, *409* (2), 47–99. https://doi.org/10.1016/j.physrep.2004.10.006.

(193) Greco, K. V.; Forner-Cuenca, A.; Mularczyk, A.; Eller, J.; Brushett, F. R. Elucidating the Nuanced Effects of Thermal Pretreatment on Carbon Paper Electrodes for Vanadium Redox Flow Batteries. *ACS Appl. Mater. Interfaces* **2018**, *10* (51), 44430–44442. https://doi.org/10.1021/acsami.8b15793.

(194) Hansch, C.; Leo, A.; Taft, R. W. A Survey of Hammett Substituent Constants and Resonance and Field Parameters. *Chem. Rev.* **1991**, *91* (2), 165–195. https://doi.org/10.1021/cr00002a004.

(195) Lu, X.; Jiang, Z.; Yuan, X.; Wu, Y.; Malpass-Evans, R.; Zhong, Y.; Liang, Y.; McKeown, N. B.; Wang, H. A Bio-Inspired O2-Tolerant Catalytic CO2 Reduction Electrode. *Sci. Bull.* **2019**, *64* (24), 1890–1895. https://doi.org/10.1016/j.scib.2019.04.008.

(196) Li, P.; Lu, X.; Wu, Z.; Wu, Y.; Malpass-Evans, R.; McKeown, N. B.; Sun, X.; Wang, H. Acid–Base Interaction Enhancing Oxygen Tolerance in Electrocatalytic Carbon Dioxide Reduction. *Angew. Chemie - Int. Ed.* **2020**, *59* (27), 10918–10923. https://doi.org/10.1002/anie.202003093.

(197) Xu, Y.; Edwards, J. P.; Zhong, J.; O'Brien, C. P.; Gabardo, C. M.; McCallum, C.; Li, J.; Dinh, C.-T.; Sargent, E. H.; Sinton, D. Oxygen-Tolerant Electroproduction of C2 Products Form Simulated Flue Gas. *Energy Environ. Sci.* **2020**. https://doi.org/10.1039/C9EE03077H.

(198) Ko, B. H.; Hasa, B.; Shin, H.; Jeng, E.; Overa, S.; Chen, W.; Jiao, F. The Impact of Nitrogen Oxides on Electrochemical Carbon Dioxide Reduction. *Nat. Commun.* **2020**, *11* (1), 1–9. https://doi.org/10.1038/s41467-020-19731-8.

(199) Song, H.; Song, J. T.; Kim, B.; Tan, Y. C.; Oh, J. Activation of C2H4 Reaction Pathways in Electrochemical CO2 Reduction under Low CO2 Partial Pressure. *Appl. Catal. B Environ.* **2020**, *272*, 119049. https://doi.org/10.1016/j.apcatb.2020.119049.

(200) Corson, E. R.; Creel, E. B.; Kostecki, R.; Urban, J. J.; McCloskey, B. D. Effect of Pressure and Temperature on Carbon Dioxide Reduction at a Plasmonically Active Silver Cathode. *Electrochim. Acta* **2021**, *374*, 137820. https://doi.org/10.1016/j.electacta.2021.137820.

(201) Zeng, J. S.; Corbin, N.; Williams, K.; Manthiram, K. Kinetic Analysis of the Role of Bicarbonate in Carbon Dioxide Electroreduction at Immobilized Cobalt Phthalocyanine. *ACS Catal.* **2020**, *10* (7), 4326–4336. https://doi.org/10.1021/acscatal.9b05272.

(202) Leonard, M. E.; Clarke, L. E.; Forner-Cuenca, A.; Brown, S. M.; Brushett, F. R. Investigating Electrode Flooding in a Flowing Electrolyte, Gas-Fed Carbon Dioxide Electrolyzer. *ChemSusChem* **2020**, *13* (2), 400–411. https://doi.org/10.1002/cssc.201902547.

(203) Li, Y. C.; Yan, Z.; Hitt, J.; Wycisk, R.; Pintauro, P. N.; Mallouk, T. E. Bipolar Membranes Inhibit Product Crossover in CO2 Electrolysis Cells. *Adv. Sustain. Syst.* **2018**, *2*, 1700187. https://doi.org/10.1002/adsu.201700187.

(204) Corbin, N.; Yang, D. T.; Lazouski, N.; Steinberg, K.; Manthiram, K. Suppressing Carboxylate Nucleophilicity with Inorganic Salts Enables Selective Electrocarboxylation without Sacrificial Anodes. *Chem. Sci.* **2021**, *12* (37), 12365–12376. https://doi.org/10.1039/d1sc02413b.

(205) Dunwell, M.; Wang, J.; Yan, Y.; Xu, B. Surface Enhanced Spectroscopic Investigations of Adsorption of Cations on Electrochemical Interfaces. *Phys. Chem. Chem. Phys.* **2017**,

19 (2), 971–975. https://doi.org/10.1039/c6cp07207k.

(206) Velasco-Velez, J. J.; Wu, C. H.; Pascal, T. A.; Wan, L. F.; Guo, J.; Prendergast, D.; Salmeron, M. The Structure of Interfacial Water on Gold Electrodes Studied by X-Ray Absorption Spectroscopy. *Science (80-.).* **2014**, *346* (6211), 831–834. https://doi.org/10.1126/science.1259437.

(207) Schiffer, Z. J.; Chung, M.; Steinberg, K.; Manthiram, K. Electrochemical Reductive Amination of Benzaldehyde at Heterogeneous Metal Surfaces. *Submitted*.

(208) Bard, A. J.; Faulkner, L. R. *Electrochemical Methods*, 2nd ed.; Wiley, 2001.

(209) Yoshida, H.; Okuno, K.; Naruse, Y. Gas Chromatographic Measurements of Hydrogen Isotopes Mixture by Using Catalytic Oxidation Type Detector. *J. Nucl. Sci. Technol.* **1982**, *19* (7), 578–586. https://doi.org/10.1080/18811248.1982.9734185.

(210) Konopka, S. J.; Mcduffie, B. Diffusion Coefficients of Ferri- and Ferrocyanide Ions in Aqueous Media, Using Twin-Electrode Thin-Layer Electrochemistry. *Anal. Chem.* **1970**, *42* (14), 1741–1746.

(211) Silva, F. L.; Reis, R. M.; Barros, W. R. P.; Rocha, R. S.; Lanza, M. R. V. Electrogeneration of Hydrogen Peroxide in Gas Diffusion Electrodes : Application of Iron (II) Phthalocyanine as a Modifier of Carbon Black. **2014**, *723*, 32–37. https://doi.org/10.1016/j.jelechem.2014.03.007.

(212) Truong, T. N.; Truhlar, D. G. Surface Diffusion of H, D, and T on a Metal Surface: The Role of Metal Motions in the Kinetic Isotope Effects. *J. Chem. Phys.* **1988**, *88* (10), 6611. https://doi.org/10.1063/1.454449.

(213) Ojeda, M.; Li, A.; Nabar, R.; Nilekar, A. U.; Mavrikakis, M.; Iglesia, E. Kinetically Relevant Steps and H2/D2 Isotope Effects in Fischer-Tropsch Synthesis on Fe and Co Catalysts. *J. Phys. Chem. C* **2010**, *114* (46), 19761–19770. https://doi.org/10.1021/jp1073076.

(214) Shvets, V. A.; Kazansky, V. B. Oxygen Anion-Radicals Adsorbed on Supported Oxide Catalysts Containing Ti, V and Mo Ions. *J. Catal.* **1972**, *130*, 123–130.

(215) Trushin, E. V.; Zilberberg, I. L. Anion-Radical Oxygen Centers in Small (AgO)n Clusters: Density Functional Theory Predictions. *Chem. Phys. Lett.* **2013**, *560*, 37–41. https://doi.org/10.1016/j.cplett.2012.12.059.

(216) Pourbaix, M. *Atlas of Electrochemical Equilibria in Aqueous Solutions*; National Association of Corrosion Engineers, 1974.

(217) Mariano, R. G.; McKelvey, K.; White, H. S.; Kanan, M. W. Selective Increase in CO2 Electroreduction Activity at Grain-Boundary Surface Terminations. *Science (80-.).* **2017**, *358* (6367), 1187–1192. https://doi.org/10.1126/science.aao3691.

(218) Li, Q.; Batchelor-McAuley, C.; Lawrence, N. S.; Hartshorne, R. S.; Compton, R. G. Anomalous Solubility of Oxygen in Acetonitrile/Water Mixture Containing Tetra-n-Butylammonium Perchlorate Supporting Electrolyte; the Solubility and Diffusion Coefficient of Oxygen in Anhydrous Acetonitrile and Aqueous Mixtures. *J. Electroanal. Chem.* **2013**, *688*, 328–335. https://doi.org/10.1016/j.jelechem.2012.07.039.

(219) York, D.; Evensen, N. M.; Martínez, M. L.; De Basabe Delgado, J. Unified Equations for the Slope, Intercept, and Standard Errors of the Best Straight Line. *Am. J. Phys.* **2004**, *72* (3), 367–375. https://doi.org/10.1119/1.1632486.

(220) Wiens, T. Linear Regression with Errors in X and Y

https://www.mathworks.com/matlabcentral/fileexchange/26586-linear-regression-with-errors-in-x-and-y (accessed Jan 12, 2022).

(221) Lowe, B. M.; Skylaris, C. K.; Green, N. G. Acid-Base Dissociation Mechanisms and Energetics at the Silica-Water Interface: An Activationless Process. *J. Colloid Interface Sci.* **2015**, *451*, 231–244. https://doi.org/10.1016/j.jcis.2015.01.094.

(222) Harris, J.; Kasemo, B. On Precursor Mechanisms for Surface Reactions. *Surf. Sci.* **1981**, *105*, L281–L287.

(223) Durst, J.; Simon, C.; Hasché, F.; Gasteiger, H. A. Hydrogen Oxidation and Evolution Reaction Kinetics on Carbon Supported Pt, Ir, Rh, and Pd Electrocatalysts in Acidic Media. *J. Electrochem. Soc.* **2015**, *162* (1), F190–F203. https://doi.org/10.1149/2.0981501jes.

(224) Haghighat, S.; Dawlaty, J. M. PH Dependence of the Electron-Transfer Coefficient: Comparing a Model to Experiment for Hydrogen Evolution Reaction. *J. Phys. Chem. C* **2016**, *120* (50), 28489–28496. https://doi.org/10.1021/acs.jpcc.6b10602.

(225) Zheng, J.; Yan, Y.; Xu, B. Correcting the Hydrogen Diffusion Limitation in Rotating Disk Electrode Measurements of Hydrogen Evolution Reaction Kinetics. *J. Electrochem. Soc.* **2015**, *162* (14), F1470–F1481. https://doi.org/10.1149/2.0501514jes.

7 APPENDICES

APPENDIX A: ADDITIONAL CONSIDERATIONS FOR CO_2R WITH BLENDED GAS FEEDS

A.1 Cell Design

A two-compartment cell was used for all electrochemical experiments discussed in this text.[92] This cell was manufactured out of polycarbonate by Lab Machinist Solutions. Plugs and connections that served as the cell parts were made of polypropylene, while ferrules were made of ETFE (Tefzel™); these parts were purchased from IDEX Health & Science. O-rings to seal the compartments upon assembly were made of FEP-Encapsulated Silicone (9319K15 & 9319K142) and were purchased from McMaster-Carr. The design of the openings for the catalysts in the cell was such that 1 cm^2 would be exposed to electrolyte. In this way, partial currents obtained in electrochemical experiments were converted directly to partial current densities.

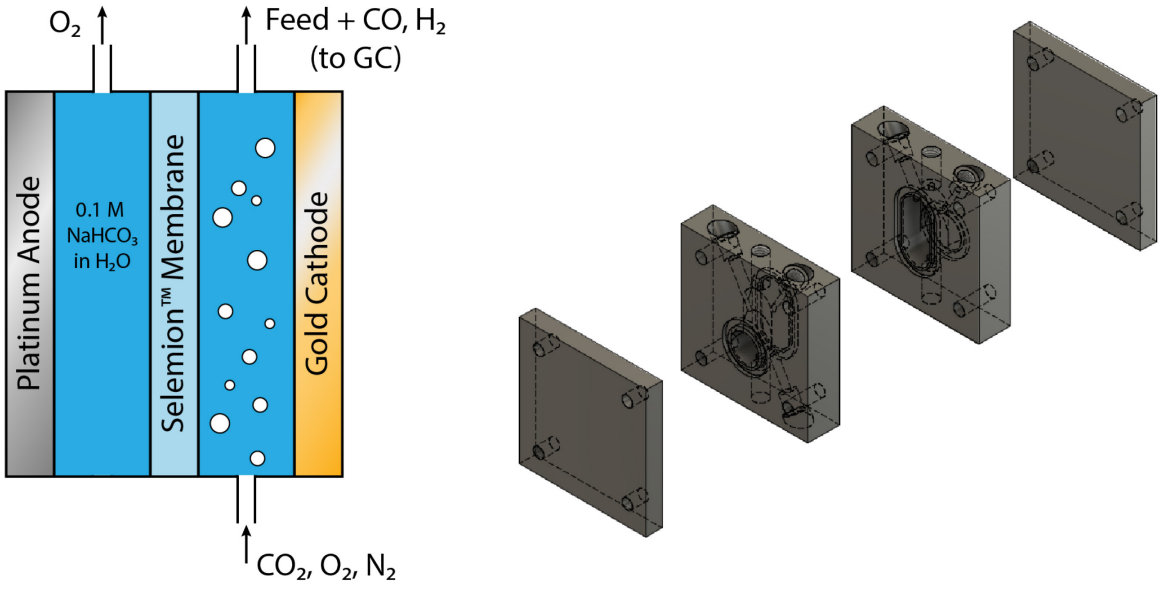

Figure A-A1. Schematic of the electrochemical cell and flow scheme used in CO_2 reduction experiments.[92]

A.2 Electrolyte preparation

Sodium bicarbonate electrolyte was prepared by dissolving enough sodium carbonate in Milli-Q® to yield sodium carbonate of half of the desired final bicarbonate molarity. For example, in preparing 200 mL of 0.1 M sodium bicarbonate, 1.06 g of Na_2CO_3 was dissolved in 200 mL of water to yield 0.05 M sodium carbonate. This solution was then bubbled overnight (using 1/16" tubing submerged in the electrolyte solution) to convert the carbonate to bicarbonate

using Instrument grade CO_2. Electrolyte solutions were stored in colorless polypropylene containers (VWR). They were bubbled periodically as used, with a bubbling time of 30-60 minutes sometime within the day before use in an experiment.

A.3 Foil preparation

Au foils were prepared by placing the 25x25 mm catalyst foil on a clean aluminum foil polishing surface, then covering the face of the Au foil with roughly 1 mL Milli-Q® water, and subsequently hand-polishing (while wearing fresh nitrile gloves) with 400 grit sandpaper for 3 minutes. Foils were scrubbed gently but thoroughly, moving in a circular pattern and rotating the foil throughout the polish. A few mL of fresh Milli-Q® were used to gently rinse the surface of the foil. The foil was then submerged in Milli-Q® within a 50 mL centrifuge tube and sonicated for 3-5 minutes. VEVOR PS-10A (2 L; 60 W, 40 kHz) Ultrasonic Cleaners were used interchangeably with a VWR Symphony™ (97043-992; 90 W, 35 kHz) Ultrasonic Cleaner for this purpose. The Milli-Q® was then decanted, and the foil dried off by passing it under a stream of house-supplied compressed air.

Foils were designated as having a "back" and a "front," so that only one side of the foil was polished and used in catalysis throughout the foil lifetime.

A.4 Reference Electrode Calibration

3.4 M Ag/AgCl reference electrodes used in the experiments were calibrated in the morning before each experiment in order to prevent reference potential drift. These leak-free references were stored with their frits submerged in vials of Milli-Q® water. The reference electrode to be calibrated was placed in a solution of saturated KCl (i.e. a solution of Milli-Q® at equilibrium with solid KCl in the bottom of the vial) along with a saturated master electrode. The master electrode was purchased with 1.0 M KCl filling, but was stored in an insulation-wrapped vial of saturated KCl in Milli-Q® and not used in any electrochemical experiments. Because the master electrode had a porous frit which allowed ion transport, storing the electrode in saturated KCl caused it to take on the characteristics of a saturated KCl reference. The Ag/AgCl in saturated KCl master reference was then taken to be +0.197 V vs. SHE.[208] By hooking up the master as the counter/reference electrode and the experimental reference as the working electrode using a BioLogic VMP3 potentiostat, it was possible to monitor (either through observation or data-recorded OCV experiments) the potential difference between the two references in the same saturated KCl solution. In this way, the reference electrode values

were adjusted daily. For instance, a morning reading indicating the experimental reference was +0.016 V vs. the master was interpreted to mean the experimental reference was +0.213 V vs. SHE on that day. Long-term data collection suggests that the reference most used in this work drifted upwards by less than 1 mV (0.001 V) per day – roughly 25 mV per month – through constant storage in Milli-Q® water.

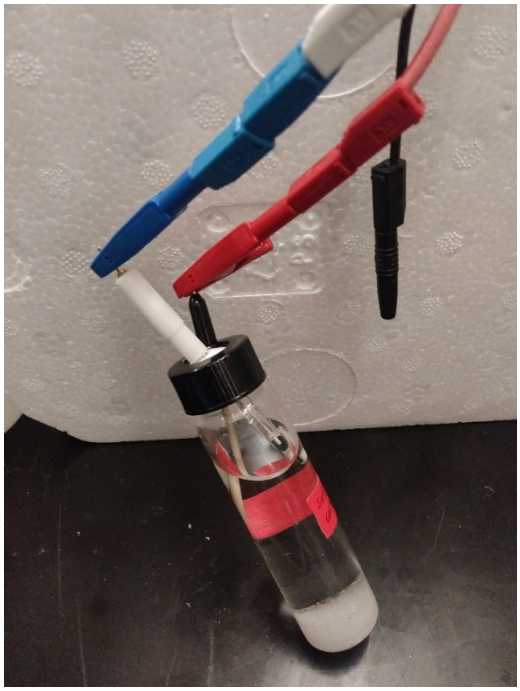

Figure A-A2. Calbrating the LF-2 Ag/AgCl reference electrode used in experiments to a master saturated Ag/AgCl reference.

Conversion between voltages applied on an SHE scale and an RHE scale:

$$U_{RHE} = U_{SHE} + 0.059pH$$

The bulk pH value of 0.1 M bicarbonate is taken to be 6.8 at 1 atm CO_2 and 7.1 at 0.5 atm CO_2, and the broadly-used conversion in this work is that 0 V vs. RHE corresponds to -0.41 V vs. SHE.

A.5 Gas Mixing and Flow Scheme

A three-gas mixing setup was constructed using three flow controllers (MC-50SCCM-D/5M, 5IN, GAS: Air; accurate to two decimal places in sccm) purchased from Alicat Scientific. One was hooked up to CO_2 via lab manifold dropdown lines and 1/8" FEP tubing (Cole-Parmer, EW-06406). Another controller was connected to house N_2 through 1/8" FEP tubing. These two gases were mixed using an ETFE (Tefzel™) tee from IDEX Health & Science. The

resulting stream was carried off the center connection of the tee and through an additional 1/8" FEP tubing section, then united with a gas line coming off of a free-standing oxygen tank through 1/8" FEP. This combined stream from all three gas sources was conveyed by another section of 1/8" FEP and then bubbled through a 20-mL hydration bubbler (maintained between 1/3 and 2/3 full with Milli-Q® water). This stream was sent into the electrochemical setup using a 1/16" FEP tubing. A 1/16" tubing section exiting the electrochemical setup then conveyed gas to a mostly-empty 20 mL vial where it was mixed in order to average out any bubbles of evolved gas leaving the electrochemical cell. 1/8" FEP tubing connected the outlet of this mixing vial to an Alicat flow meter (MS-100SCCM-D/5M, GAS: Air; accurate to 1 decimal place in sccm). This flow meter helped to ensure there were no gas leaks anywhere in the flow configuration. The outlet of this flow meter was sent to a gas chromatograph (SRI Instruments, Inc., Model 8610C) where gas products were detected in-line. The sample loop vented to local exhaust when samples were not being loaded onto the GC columns; when samples were injected, the analyzed products were vented to the ambient environment in an intrinsically safe fashion (the last analytical device in the gas line was an FID, which converted all hydrocarbons and hydrogen to CO_2 and water). Disjointed tubing sections throughout the gas flow setup were connected by ETFE (Tefzel™) unions (IDEX Health & Science).

Custom gas mixes were programmed into the Alicat flow controllers and meter to ensure proper flow rates and closures. An example of such a mixture includes 50% CO_2, 37.5% N_2, 12.5% O_2.

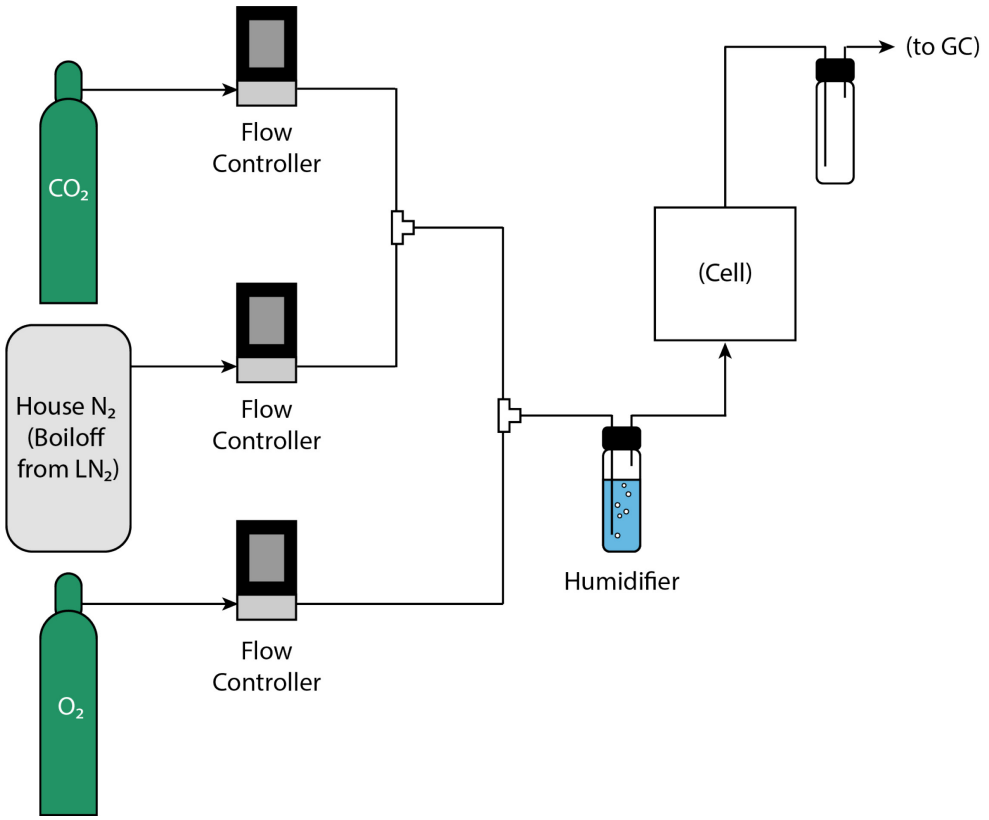

Figure A-A3. Schematic for gas flow through the CO_2 reduction system.

A.6 Electrochemical Experiments

In preparation for an electrochemical experiment, the polycarbonate cell and all cell parts in immediate contact with the electrolyte (plugs for working compartment; reference electrode connector & ferrule; plug for counter compartment) were submerged in 20% v/v nitric acid. The polycarbonate (PC) was removed from nitric acid after less than one minute so as to avoid PC dissolution or etching (as PC is not compatible with nitric acid over long exposure times). The PC cell (with o-rings assembled) was then rinsed with Milli-Q® and allowed to air-dry. The 20% nitric acid was decanted off of the cell parts after roughly five minutes, and the parts were triple-rinsed with Milli-Q®. These parts were placed onto a clean absorbent towel (WypAll Cleaning Wipes) and allowed to air-dry. The Au foil was then polished and prepared according to the procedure described above. The Pt counter-electrode was placed on the aluminum current collector for the anode side, then the counter compartment was used to sandwich the foil in place. A new piece of Selemion™ (stored in Milli-Q®; roughly 2 cm by 4 cm; enough to cover the window between the two cell compartments) was then cut using scissors which were reserved for cutting membranes and dried after each use. The Selemion™ was rinsed with fresh Milli-Q® and assembled into the cell, followed by the working

compartment, then the gold foil. Once the second backplate of the cell was in place, the pieces were bolted together with wing nuts and tightened with a hex key. A calibrated reference electrode was then inserted into the reference port of the working electrode compartment of the cell using an extra-long IDEX connector and a 2.0 mm ferrule. The bottom port of the working side of the cell was then connected to the gas mixing setup, with the desired flow of each component already set; meanwhile, the bottom port of the counter compartment was plugged with a polypropylene plug. Flow rates for the gases were modulated depending on the type of experiment being conducted. Unless otherwise indicated, all experiments were conducted with a total inlet gas flow rate of 10 sccm. (So a normal gas flow consisting of 0.5 atm CO_2 and 0.5 atm O_2 would be fed as 5 sccm CO_2, 5 sccm O_2.)

The prepared electrolyte was loaded into the cell using the same plastic pipette tip for each test. 1.75 mL was used to fill each side of the cell. After filling, the working compartment of the cell was then closed from the atmosphere by plugging the top ports on the cell diagonals, and the center port was hooked up to the gas flow system as described above. The cell was then allowed to sit while bubbling for roughly 15 minutes to allow air to flush out of the gas flow lines. Meanwhile, the reference and anode/cathode current collectors were hooked up to a BioLogic VMP3 potentiostat. Upon beginning an experiment, a blank GC sample was initiated; GC samples were taken every 10 minutes thereafter, with the results at t = 10 minutes thrown out due to lack of complete mixing. To compute faradaic efficiencies and partial current densities, the data points at t = 20, 30, and 40 minutes were averaged. Long-time experiments were avoided due to persistent current decay over time during electrochemical reduction on gold (consistent with previous literature observations; see A.9. Discussion – CO_2RR Current Decay on Gold).

IR compensation was handled in each experiment by performing potentiostatic electrochemical impedance spectroscopy (PEIS – frequency range 10 kHz-1 Hz) and visually extrapolating the EIS curve to the x-intercept (estimating to the nearest Ohm). 85% IR compensation was then applied. Typical 100% IR compensation values obtained from PEIS were 70 Ohms for 0.1 M $NaHCO_3$ and 5-15 Ohms for 1.0 M sodium electrolytes.

All data points were gathered independently of one another and in a randomized order to ensure no bias by variables drifting in time. That is, a new cell was prepared as described above for each data point reported herein.

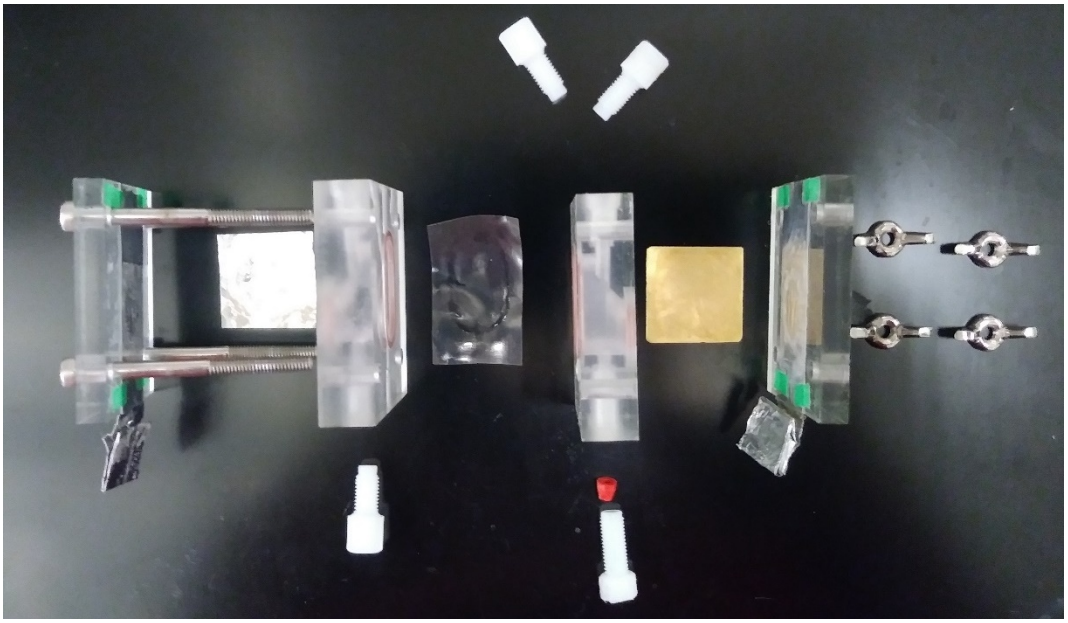

Figure A-A4. Image of disassembled electrochemical cell, including (L-R): Backplate with bolts and Al foil current collector, Pt counter electrode, counter electrode compartment, plug, Selemion membrane, working electrode compartment, plugs and reference electrode adapter, Au working electrode, backplate with Al foil current collector, and wing nuts.

Steps in cell construction:

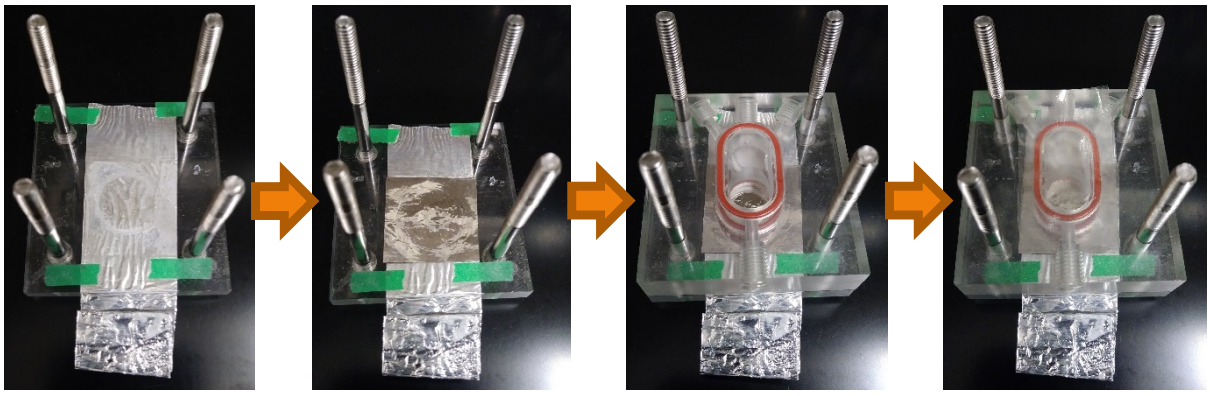

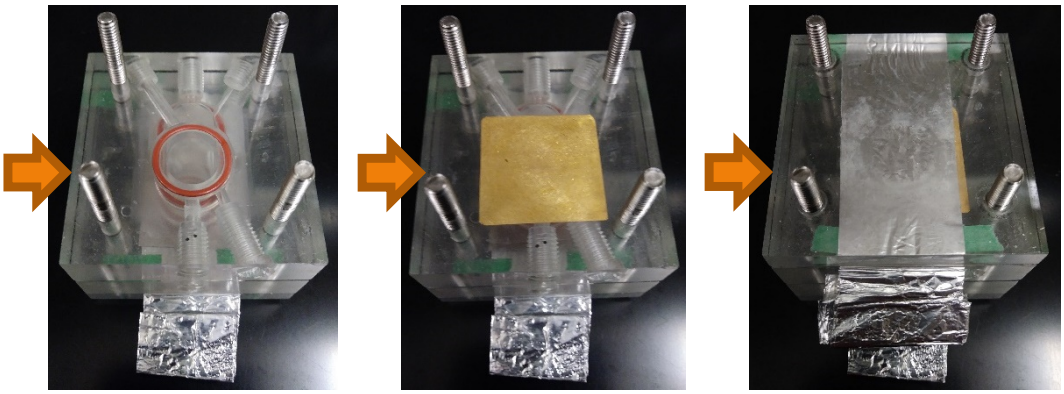

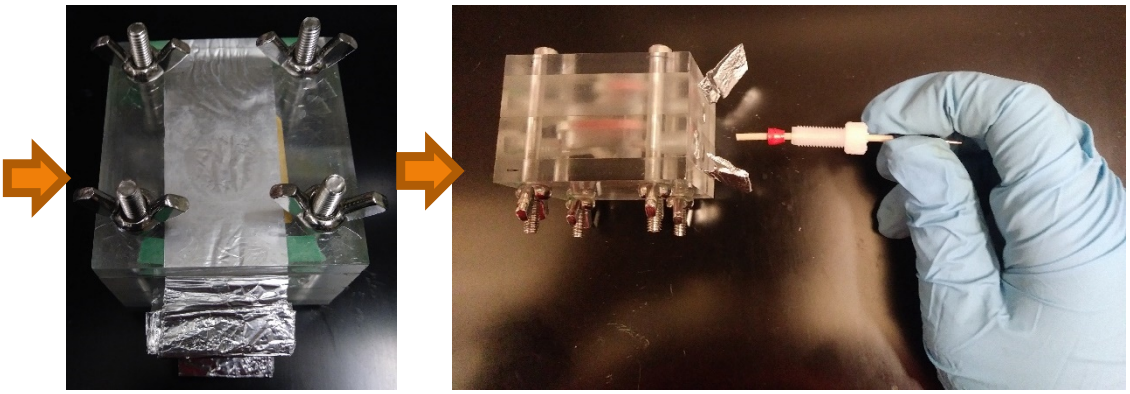

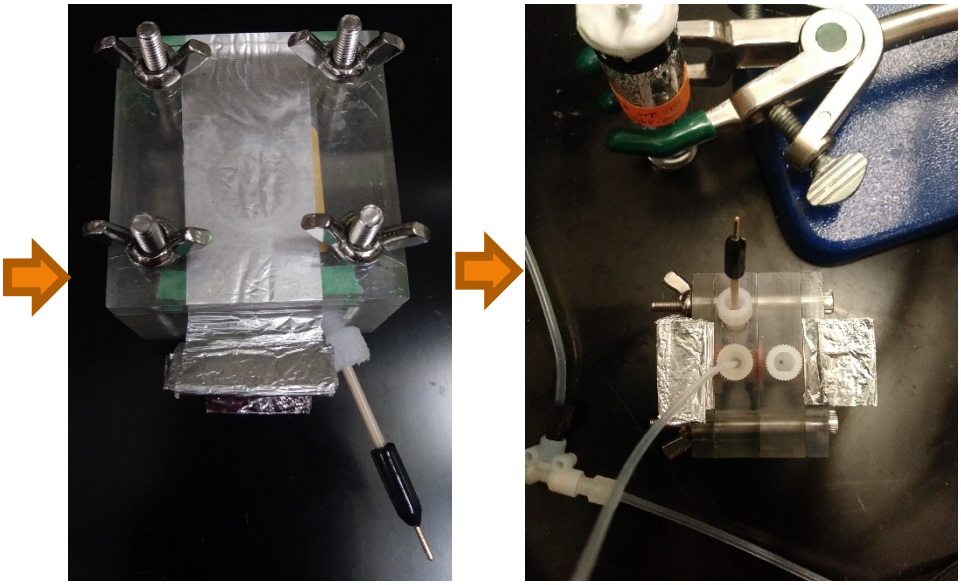

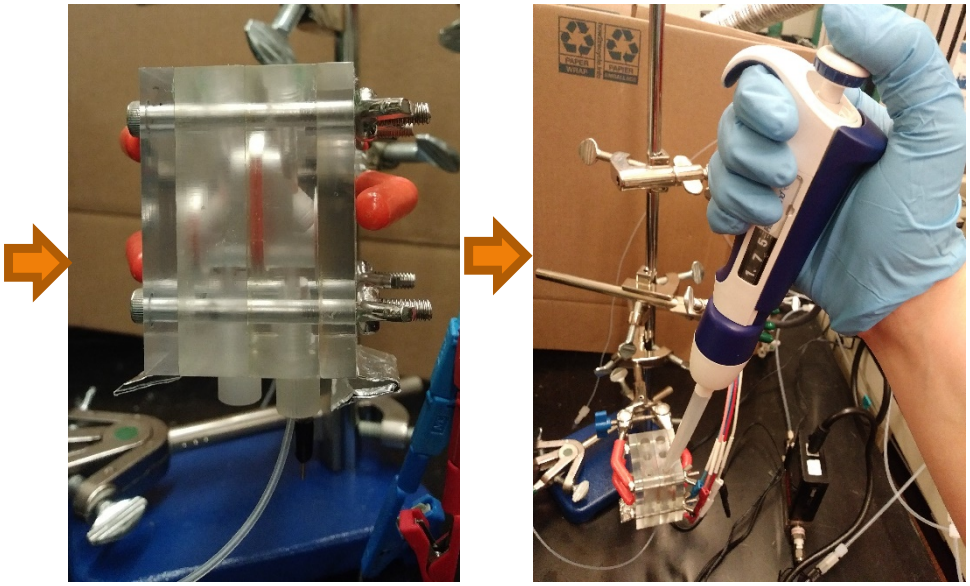

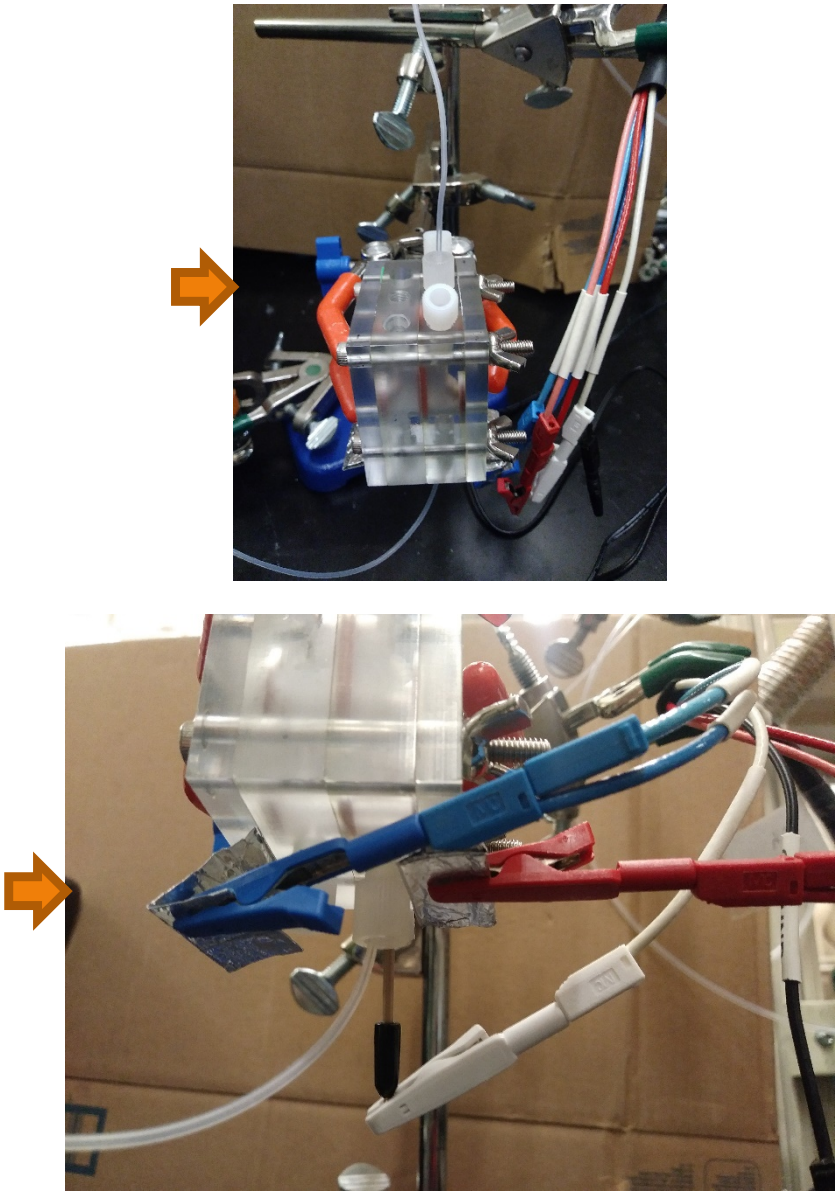

Figure A-A5. Steps in cell construction, from laying down the Pt electrode to connecting the closed cell to potentiostat cables.

A.6.1 P_{O2} Effect, Tafel Analysis, and CO_2 Order Dependence Studies

P_{O2} effect and Tafel analysis data points were gathered as described above. P_{O2} effect was determined by holding CO_2 flow rate constant at 5.00 sccm and varying O_2 pressure (through flow rate), while using N_2 to balance the total flow to 10.00 sccm. Tafel analysis was conducted with either 5.00 sccm CO_2/5.00 sccm N_2 or 5.00 sccm CO_2/5.00 sccm O_2 and varying the applied potential. CO_2 order dependence was determined by holding oxygen flow rate constant at either 0.00 sccm or 5.00 sccm and varying CO_2 pressure (through flow rate), while using N_2 to balance the total flow to 10.00 sccm.

A.6.2 Bicarbonate Order Dependence Studies

Bicarbonate dependence was probed by holding absolute potential constant (vs. SHE) – not potential vs. RHE. This is for reasons discussed below. Bicarbonate concentration was varied while holding total solution ionic strength constant. This was done using sodium perchlorate as the supporting electrolyte. In most cases, the electrolyte was made by mixing prepared 1.0 M sodium bicarbonate (made using ≥99.0% pure untreated sodium carbonate, Sigma-Aldrich S7795, Lot SLBT0414) with 1.0 M sodium perchlorate in the desired ratio. For instance, 0.4 M bicarbonate solution was made by mixing 4 mL of 1.0 M bicarbonate with 6 mL of 1.0 M perchlorate. For the potassium bicarbonate order dependence experiments detailed in the SI, it was not possible to balance the electrolyte with perchlorate, as potassium perchlorate is not soluble up to 1.0 M. Thus, these experiments were conducted at different total ionic strengths.

In interpreting these experiments, in contrast to what is reported in our 2019 publication, we have not normalized the data by the concentration of CO_2 in solution. This is because while the concentration of dissolved CO_2 may change with alterations to the electrolyte, the activity of CO_2 is set by the partial pressure of CO_2 in the gas phase and does not change. As long as the lower solubility does not lead to transport limitations, there should be no effect of salting-out on rate. Note that the magnitude of the reported correction is very small and does not fundamentally change the interpretation of the data.

Sodium Bicarbonate Experiments at High Bicarbonate Concentration

Sodium bicarbonate experiments were carried out at up to 1.0 M $NaHCO_3$, but at very high concentrations, extremely low currents to both CO_2RR and HER were observed (Figure A-A6). It is estimated that this is due to a secondary effect such as metal impurity plating or being close to the solubility limit of bicarbonate.

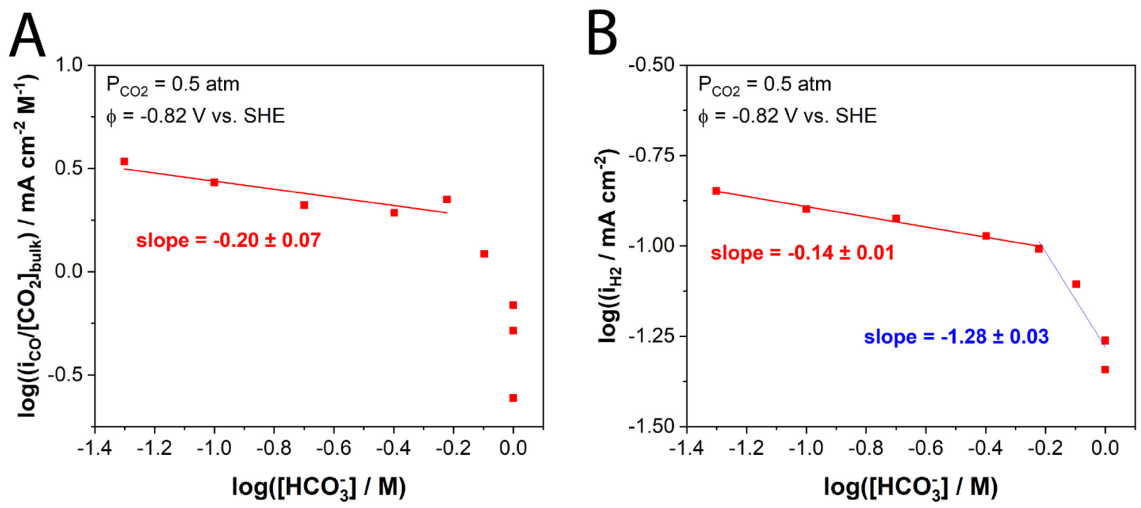

Figure A-A6. Bicarbonate dependence of both (A) CO_2RR and (B) HER at a wide range of bicarbonate concentrations.

Potassium Bicarbonate Experiments

Bicarbonate order dependence was studied with unbalanced potassium bicarbonate electrolyte, resulting in the conclusion that the negative dependence of CO_2RR on sodium bicarbonate was due to some secondary effect. Note in the case of $KHCO_3$ that there appears to be a region in which there is a positive dependence upon bicarbonate, but that this is below the concentrations at which the experiments employed in this work operate.

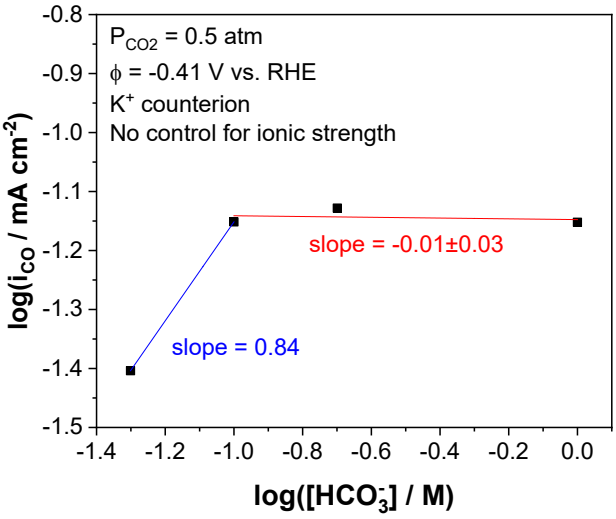

Figure A-A7. Bicarbonate order dependence using potassium bicarbonate as the electrolyte.

A.6.3 KIE Experiments

The kinetic isotope effect was elucidated by preparing electrolyte in the same way as other experiments, but this time using D_2O. D_2O was removed from its sealed container with a syringe. Special care was taken when bubbling the D_2O-based electrolyte to cover the top of the container it was in, in order to prevent absorption of H_2O in the air. Other changes to procedure relative to the standard CO_2 reduction were:

- Cell drying: rather than allowing cell and cell parts to dry in air, all parts were dried in an 80 °C oven for at least 15-20 minutes to evaporate as much residual water as possible.
- Selemion™ soaking: prior to use in the experiment, the Selemion™ membrane to be used in the experiment was shaken dry, placed in a nitric-acid-cleaned petri dish (no more than 5 cm in diameter), and covered in a thin layer (~4 mL) of D_2O. The dish was covered to prevent atmospheric water uptake, and the membrane was allowed to soak for roughly half an hour. After this time had elapsed, two more 4 mL soaks were provided, each with soak times on the order of 10 minutes. This helped to prevent adventitious water sources that may have convoluted the results of the experiment.
- Hydration bubbler: switched out the normal water hydration bubbler to a D_2O-based bubbler.

For HER quantification in the deuterated solvent case, it was necessary to perform normalizations on the raw H_2 data, as the thermal conductivity detector used in product detection was less sensitive to D_2 than to H_2. It was gathered from existing literature that the sensitivity factor (ratio of D_2 peak to H_2 peak area of identical concentration) should be roughly 0.75,[209] but this was tested for our instrument by preparing a conductive electrolyte without CO_2 (0.1 M $NaClO_4$ in D_2O) and bubbling N_2 through the solution at 10 sccm to remove any dissolved O_2 and/or CO_2, then applying a constant current of -0.5 mA to the system and quantifying the hydrogen signal as a result of HER. From this, it was found that the appropriate sensitivity factor was 0.7031, so a conversion factor corresponding to the reciprocal of this value – 1.4223 – was applied to all hydrogen signals for experiments with deuterated electrolyte.

A.6.4 Modified Cyclic Voltammetry

Cyclic voltammetry, modified to study characteristics of the non-quiescent cell, was used as evidence that the onset of ORR occurred at a much less reductive potential than required for

CO_2RR or HER in the system in question – and, moreover, that ORR was transport-limited at the tested voltages. CVs were conducted in 0.1 M $NaHCO_3$, and were IR-corrected just as constant-potential experiments were. The CV blank was obtained by bubbling N_2 at 10 sccm and scanning from +1.00 V vs. SHE to -0.40 V vs. SHE and back, while the CV with O_2 and CO_2 was obtained by scanning from +1.00 V vs. SHE to -0.80 V vs. SHE and back (this extends the first test to within the Tafel regime and after CO_2RR/HER onset).

While the main-text scan (Figure 2A) does not highlight this feature, a persistent observation during these experiments was an initial reductive wave around 0.2 V vs. SHE, followed by another reduction which quickly became transport-limited around -0.2 V vs. SHE. This is highlighted more clearly in the figure below. We hypothesize that the initial reductive wave is the more kinetically facile ORR to peroxide, while ORR to water takes over when overpotentials and current densities are higher.

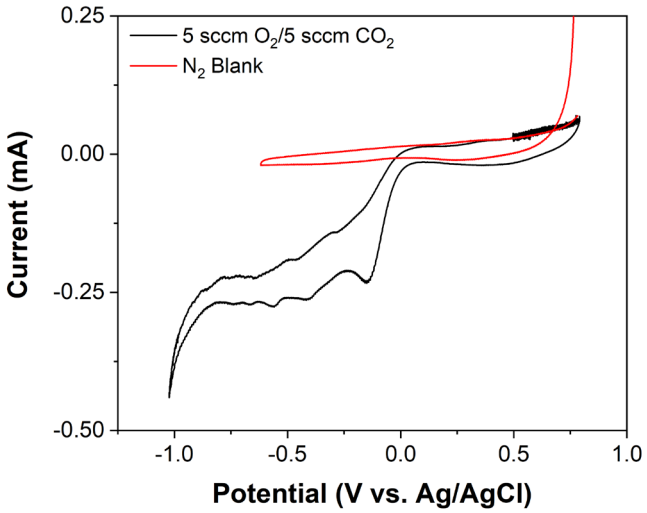

Figure A-A8. Modified cyclic voltammogram better highlighting the different reductive waves observed during ORR onset.

A.6.5 Measuring Boundary Layer Thickness

Because transport is so integral to dictating oxygen's effect on the CO_2RR system, it was useful to quantify the boundary layer thickness at the surface of the cathode in the cell. This was done using a procedure from Clark et al.[98] A full description may be found in the cited work's Supporting Information, section SI-4.

In short, mass transport boundary layer thickness was quantified by measuring the diffusion-limited current of a known reaction – ferricyanide reduction to ferrocyanide:

$$Fe(CN)_6^{3-} + e^- \rightarrow Fe(CN)_6^{4-}$$

Two bicarbonate solutions were made – one 0.1 M in $NaHCO_3$, and the other 1.0 M in $NaHCO_3$ – and both of these were made to be 0.01 M in $K_3Fe(CN)_6$ by addition of 32.9 mg ferricyanide salt per 10 mL electrolyte solution. By performing a CV extending from roughly +1.1 V vs. RHE (+0.69 V vs. SHE) to -0.4 V vs. RHE (-0.81 V vs. SHE) in the 0.1 M solution, it was possible to extract the mass transport boundary layer thickness from the steady-state current density at the plateau of the CV. This plateau occurs from roughly +0.5 V vs. RHE to -0.2 V vs. RHE. Taking the value at around +0.1 V vs. RHE to be a good middle point, the steady-state current density can be related to boundary layer thickness by:

$$\delta_{BL} = \frac{F \cdot D_{Fe(CN)_6^{3-}} \cdot C^*_{Fe(CN)_6^{3-}}}{i_{SS}}$$

where F is Faraday's constant, $D_{Fe(CN)_6^{3-}}$ is the diffusivity of the ferricyanide ion (this is taken to be 0.720×10^{-5} cm^2 s^{-1}),[210] $C^*_{Fe(CN)_6^{3-}}$ is the concentration of ferricyanide ion in the bulk of the electrolyte, and i_{SS} is the steady-state current.

It should be noted that the accuracy of the boundary layer thickness when determined this way is contingent upon migration being negligible. The ferricyanide ion in these tests is dilute enough in the supporting salt that migration effects can be ignored; and moreover, experimental evidence suggests no substantial difference between reduction currents under the above protocol for 0.1 M and 1.0 M bicarbonate electrolytes. Using this method, the δ for ferricyanide mass transport was found to be 140 μm, as the steady-state reduction current density was around 0.497 mA cm^{-2}.

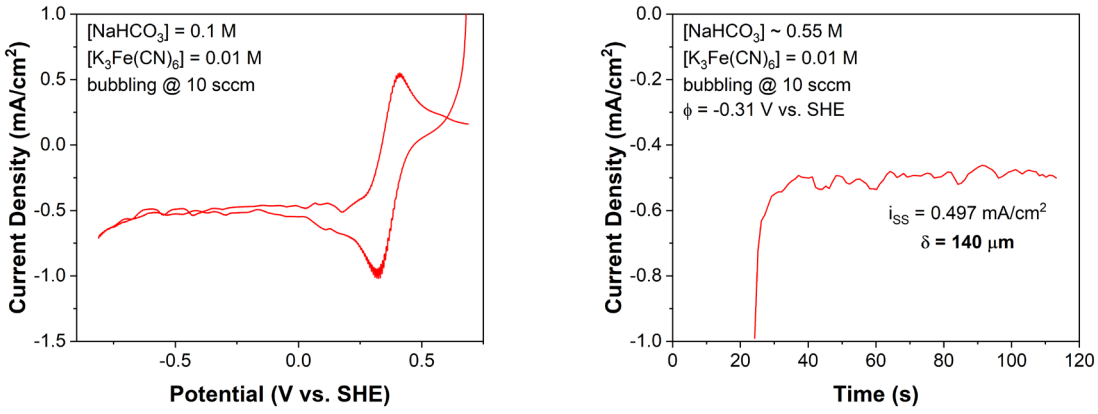

Figure A-A9. CV to identify the proper potential for testing boundary layer thickness, and CA to determine limiting current density of ferricyanide reduction.

Conversion of ferricyanide boundary layer to relevant species' boundary layer

The delta obtained above is the accurate value for the transport of the ferricyanide ion; however, an adjustment must be applied in order to obtain δ_j for the dissolved gas species.

It can be (and has been) derived that the concentration boundary layer δ_C and momentum boundary layer δ_M scale as such:[96]

$$\delta_C \sim Re^{-1/2} Sc^{-1/3}$$

$$\delta_M \sim Re^{-1/2}$$

So that, for reference,

$$\frac{\delta_M}{\delta_C} \sim Sc^{1/3} = \left(\frac{\nu}{D}\right)^{1/3} \gg 1$$

Or, because the Schmidt number *Sc* to the 1/3 power is much greater than 1 for almost all liquids, including water, the concentration (or mass-transport) boundary layer δ_C is embedded within the momentum boundary layer δ_M. To understand the nature of how different species' mass transport boundary layers scale with one another, we expand the expression for δ_C, where below the δs correspond to the concentration boundary layers for the subscripted species:

$$\delta_j \sim Re^{-1/2} Sc^{-1/3} = \left(\frac{uL}{\nu}\right)^{-\frac{1}{2}} \left(\frac{\nu}{D_j}\right)^{-1/3}$$

So that the following is true:

$$\frac{\delta_{Fe(CN)_6^{3-}}}{D_{Fe(CN)_6^{3-}}^{1/3}} = \frac{\delta_{CO_2}}{D_{CO_2}^{1/3}} = \frac{\delta_{O_2}}{D_{O_2}^{1/3}}$$

Rearranging to find the boundary layer thickness for either of the gas-phase species, we obtain:

$$\delta_{gas} = \delta_{Fe(CN)_6^{3-}} \left(\frac{D_{gas}}{D_{Fe(CN)_6^{3-}}}\right)^{1/3}$$

The diffusion coefficient of ferricyanide is as above taken to be 0.720×10^{-5} cm^2 s^{-1}.[210] Diffusion coefficients for CO_2 and O_2 are taken as 1.92×10^{-5} cm^2 s^{-1} and 2.10×10^{-5} cm^2 s^{-1} respectively.[99] Therefore, the conversion factor from the above ferricyanide boundary layer of 140 μm is 1.387 in the case of CO_2 and 1.429 in the case of O_2, making the values of boundary layer thickness:

$$\boldsymbol{\delta_{CO_2} = 194\ \mu m, \quad \delta_{O_2} = 200\ \mu m}$$

Further, noise in the current signal during the chronoamperometric experiment in S.7.5 can be used to put errors on these values; in the case of the signal pictured above, the final value for the boundary layer thickness for O_2 is 200±7 μm.

This value is larger than the reported ferricyanide boundary layer thickness for similar cells in the literature, which report $\delta_{Fe(CN)_6^{3-}} \approx 50$ μm at gas bubbling = 10 sccm;[98] however, differences in gas bubbling techniques in the cells may account for this difference.

A.7 Product Detection

The product of CO_2 reduction on gold is typically CO. CO_2 can, however, be reduced further to methane, ethylene, and even liquid products such as short-chain alcohols. The competing reaction, HER, generates H_2. Oxygen reduction on gold generates water or peroxide, depending on the pH and other cell conditions. It was necessary to quantify the various reactions occurring during the electrochemical reduction experiments. This was done primarily through in-line gas chromatography, but the results are also supported by negative results of product detection through both liquid ^{1}H-NMR and a UV-visible quantification method for determining peroxide concentration.

It should be noted that, for all experiments implementing O_2, the ORR current was interpreted from the lack of Faradaic closure, as water produced during ORR could not be quantified.

A.7.1 Gas Chromatography

An in-line gas chromatograph (SRI Instruments, Inc., MG #5, Model 8610C) with auto-sampling capabilities was used for gas-phase product detection. N_2 gas available in-house was used as the GC carrier gas, and was adjusted to roughly 16.5 psig on the instrument. Data sample rate was 5 Hz. The GC was calibrated to detect CO and H_2, although representative tests on other instruments also allowed for confirmation that the products CH_4, C_2H_4, and C_2H_6 were not produced during CO_2 reduction on gold.

Gas flow into the GC was normally vented out through a 1-mL sample loop. The GC configuration was modified so that upon sample injection, gas flow was sent onto a 6’ HayesepD pre-column. After this pre-column, gas flowed onto a 6’ MS-5A column. Finally, gas was analyzed with both a thermal conductivity detector (TCD) and a flame ionization detector (FID; coupled with a methanizer to detect products such as CO). Burnt sample gas was vented to ambient air as CO_2 and water.

The long pre-column allowed for adequate column elution times so that hydrogen and oxygen could be resolved, while at the same time excluding components from the MS-5A such as CO_2, water, and hydrocarbons heavier than methane. These heavier components cannot be separated on an MS-5A column, and therefore were excluded from loading by backflushing the pre-column around the pre-column elution time for methane. The order of elution from the pre-column was: Hydrogen – Oxygen – CO – Methane – CO_2 – Ethylene – Ethane – Water. The order of elution out of the entire system was: Hydrogen – Oxygen – Methane – CO. Note that while CO emerges from a HayesepD column before methane, it elutes later than methane on an MS-5A. The species spend a longer time on the MS-5A, so the elution of CO and CH_4 out of the entire system is swapped relative to coming out of the pre-column.

Table A-A1. GC event sequence for quantifying CO_2 reduction products.

Time (min)	Event
0.000	Zero baseline
0.050	G valve on (Flow forward through HayesepD pre-column)
2.600	G valve off (Flow backward through HayesepD pre-column)
5.250-6.600	Integration-based baseline adjustments
8.000	Program ends; wait at least 2 minutes to cool all the way back down to 50 °C before loading next sample

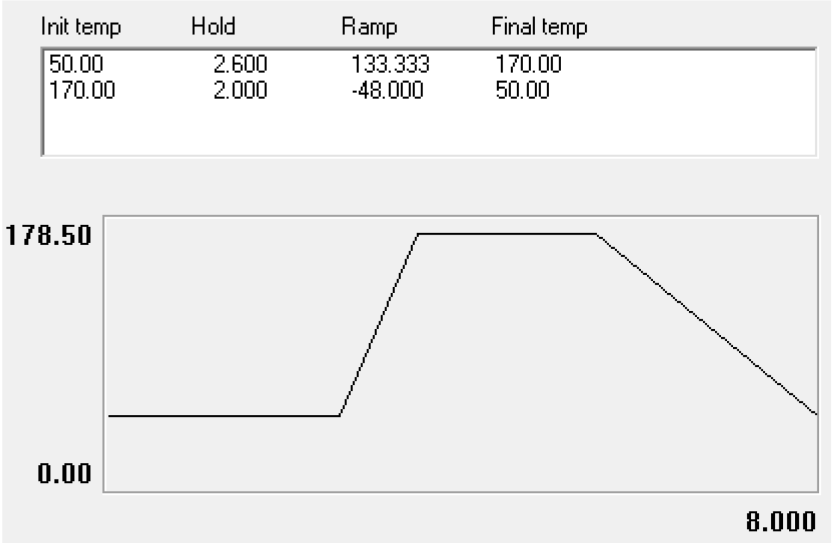

Figure A-A10. GC temperature profile for quantifying CO_2 reduction products. 50 °C for 2.6 minutes, 0.9 minute ramp to 170 °C, 2 minute hold at 170 °C, 2.9 minute ramp down to 50 °C.

The GC was calibrated using two standard gas solutions, representing low- and high-concentration samples.

Table A-A2. Concentrations in ppm of gases in the calibration gas tanks.

Gas	H_2	O_2	CO	CH_4	C_2H_4	C_2H_6
1,000 ppm Cal. Gas	980	990	990	990	980	980
10,000 ppm Cal. Gas	10,000	0	10,000	10,200	0	0

The pure CO_2 tank contained < 0.554 ppm of CO (per Airgas specifications) and negligible amounts of other gases, so it was assumed to be pure CO_2. Calibration gases both had CO_2 as the balance.

To calibrate, GC samples were taken every 10 minutes (8-minute program, 2 minutes to purge sample loop of carrier gas and cool down). One 20 mL hydration mixing vial (half filled) and one 20 mL empty vial were used prior to insertion into the GC. No baseline subtraction was used.

An Alicat FlowVision script was written to automatically change gas flow rate set points every 4 samples (40 minutes), starting 60 seconds after the last sample at a given concentration was injected. See the table below for flow controller settings.

Table A-A3. GC calibration sequence for CO_2 reduction work.

1,000 ppm Cal. Gas (sccm)	Pure CO_2 (sccm)	Nominal ppm Value	File Numbers
High FID Sensitivity			
20	0	1000	1-5
18	2	900	6-9
10	10	500	10-13
6	14	300	14-17
2	18	100	18-21
1	19	50	22-25
0.5	19.5	25	26-29
0.5	30	16.4	30-33
0.5	40	12.3	34-37
0.3	40	7.4	38-41
Medium FID Sensitivity			
2	18	100	42-46
10	10	500	47-50
20	0	1000	51-54
10,000 ppm Cal. Gas (sccm)	Pure CO_2 (sccm)	Nominal ppm value	File Numbers
High FID Sensitivity			
0.5	19.5	250	55-59
2	18	1000	60-63
3	17	1500	64-67
3.8	16.2	1900	68-71
Medium FID Sensitivity			
0.5	19.5	250	72-76

2	18	1000	77-80
6	14	3000	81-84
10	10	5000	85-88
14	6	7000	89-92

Chromatogram processing: no baseline subtraction or smoothing was conducted, nor were the windows of integration around the components shifted. Data are given as-collected from the above experiments.

Calibration Curve Results:

Table A-A4. Area calibration parameters for FID high signal.

Gas	Retention Time (min)	m	b	σ_m^2	σ_b^2	σ_{mb}^2	RMSE (ppm)	R^2	LQA (ppm)	MQA (ppm)
H_2	2.4	37.192	-15.906					0.9999	12-16	--
CO	6.2	0.1474	-5.7033					1.0000	<7.3	~1400

Both fits are for low cal gas, and as a result are only valid up to 1,000 ppm.

Table A-A5. Area calibration parameters for FID medium signal

Gas	Retention Time (min)	a	m	b	σ_m^2	σ_b^2	σ_{mb}^2	RMSE (ppm)	R^2	LQA (ppm)	MQA (ppm)
H_2	2.4	--	36.825	2.6655					1.0000		
CO	6.2	0.0019	2.2834	62.405					0.9984		

These are taken from the combined H_2 and high-cal gas CO fits.

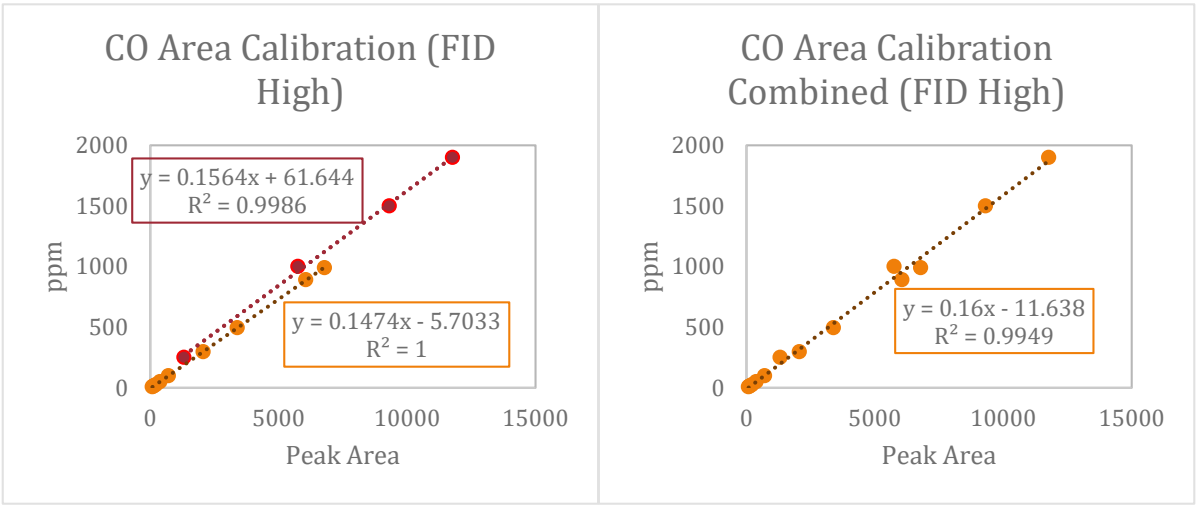

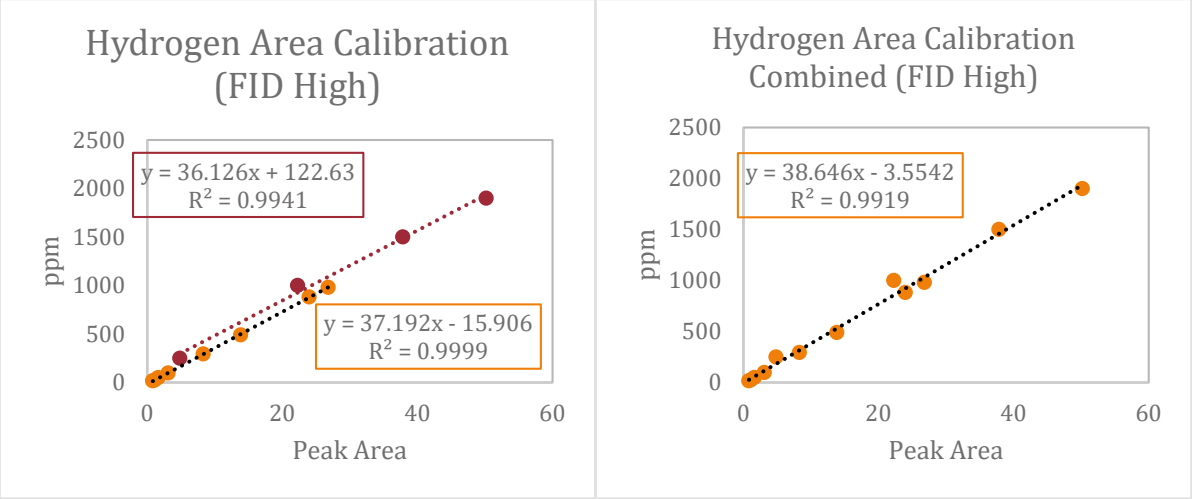

Figure A-A11. Calibration graphs for high FID sensitivity.

Fit for data points below 50 ppm CO: [CO] (ppm) = 0.13903×Peak Area – 4.12485

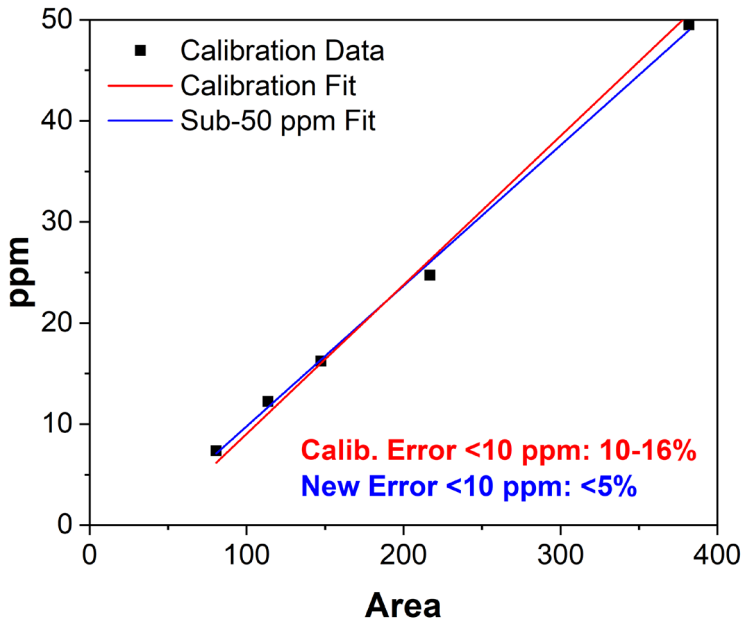

Figure A-A12. GC fit for data points below 50 ppm CO.

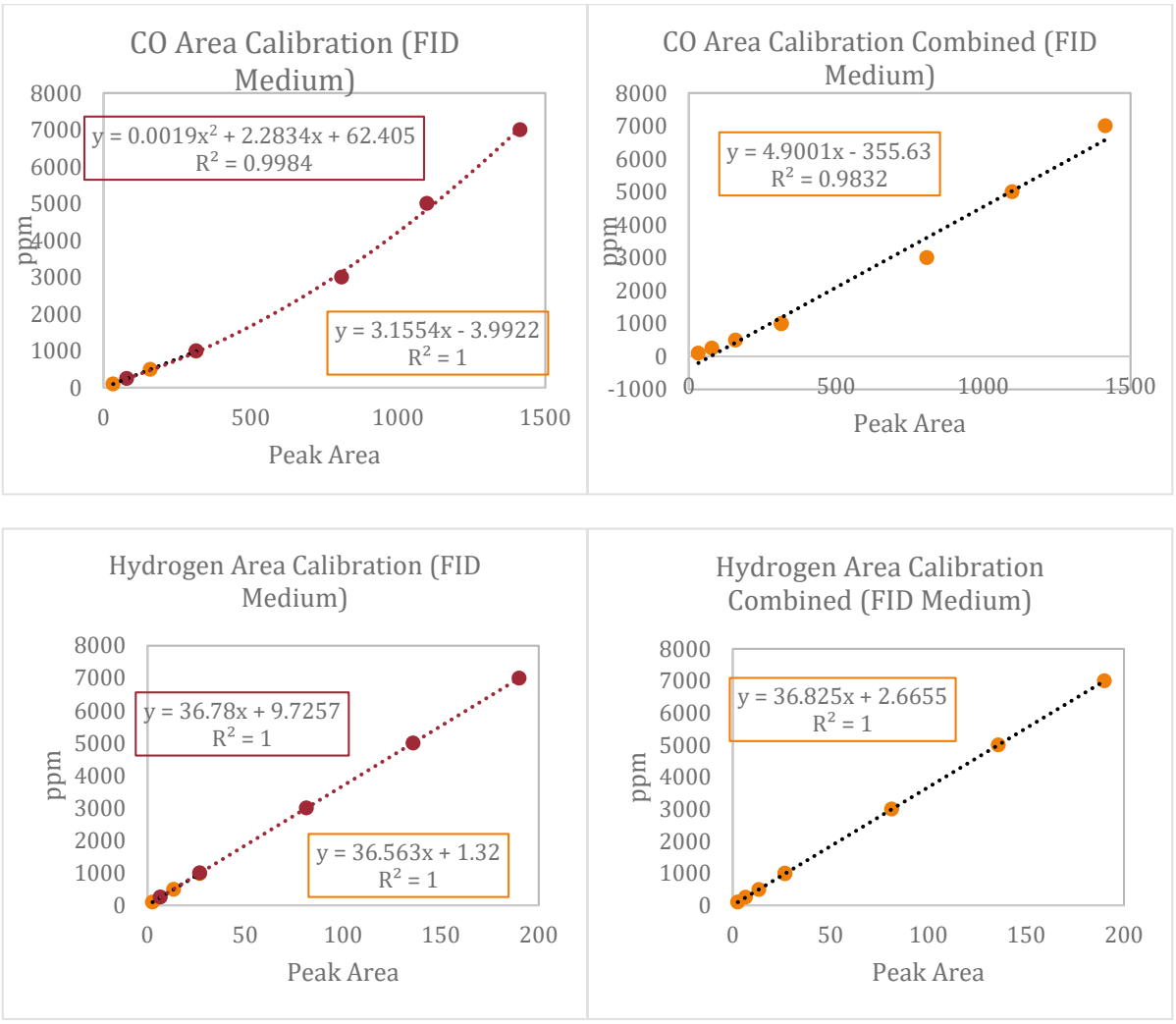

Figure A-A13. Calibration graphs for medium FID sensitivity.

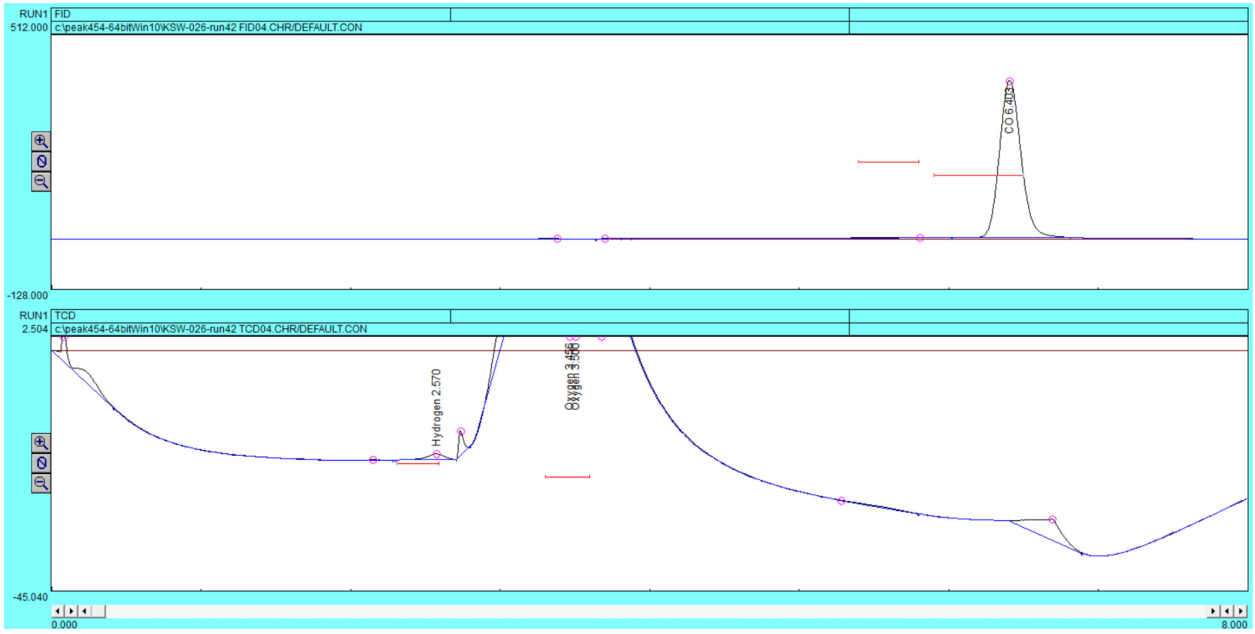

Figure A-A14. Typical gas chromatogram for CO_2 reduction experiments.

Calculating Partial Current from GC Data

GC peak areas were converted to parts-per-million (ppm) according to the procedure above. Once these values were known, they could be converted to partial current by:

$$ppm \times \frac{moles\ product/total\ moles}{1{,}000{,}000\ ppm} \times \frac{1\ total\ mol}{22.4\ std.L} \times \frac{1\ std.L}{1000\ scc} \times (flowrate)\ sccm \times \frac{1\ minute}{60\ sec} \times \frac{n\ moles\ e^-}{1\ mole\ product} \times \frac{96485.3\ C}{1\ mol\ e^-} \times \frac{1\ A}{1\ C/s} \times \frac{1000\ mA}{1\ A} = Partial\ Current\ (mA)$$

For example, for n = 2 (CO) and flowrate = 10 sccm, the conversion is 1 ppm = 1.436×10^{-3} mA.

A.7.2 Proton NMR for Liquid CO_2RR Products

^{1}H NMR was used to interrogate the formation of liquid-phase CO_2 reduction products such as methanol, ethanol, and formate. The procedure used to do this was taken from Kuhl et al.[83]

In short, samples were prepared by combining 700 μL of the bicarbonate catholyte with 35 μL standard solution containing 10 mM DMSO, 50 mM phenol in D_2O. Samples were then analyzed using a Varian 501 MHz NMR. Solvent suppression was conducted to dampen the water peak. (PreSat RF = 50, number of peaks = 1). The ^{1}H probe was manually tuned, lock was achieved on the D_2O in the sample, and gradient shimming was performed. Auto-gain was used, but phasing was performed manually. 36 transients were collected per sample.

Quantification was achieved by comparing the areas of the peaks of interest to those of the internal standards (phenol and DMSO – one standard on each side of the water peak to avoid issues due to phasing). To ensure that relaxation times did not convolute results, calibration curves were made for typically observed CO_2RR products such as formate and methanol (examples below). Detection limits for these methods were about 0.1 mM.

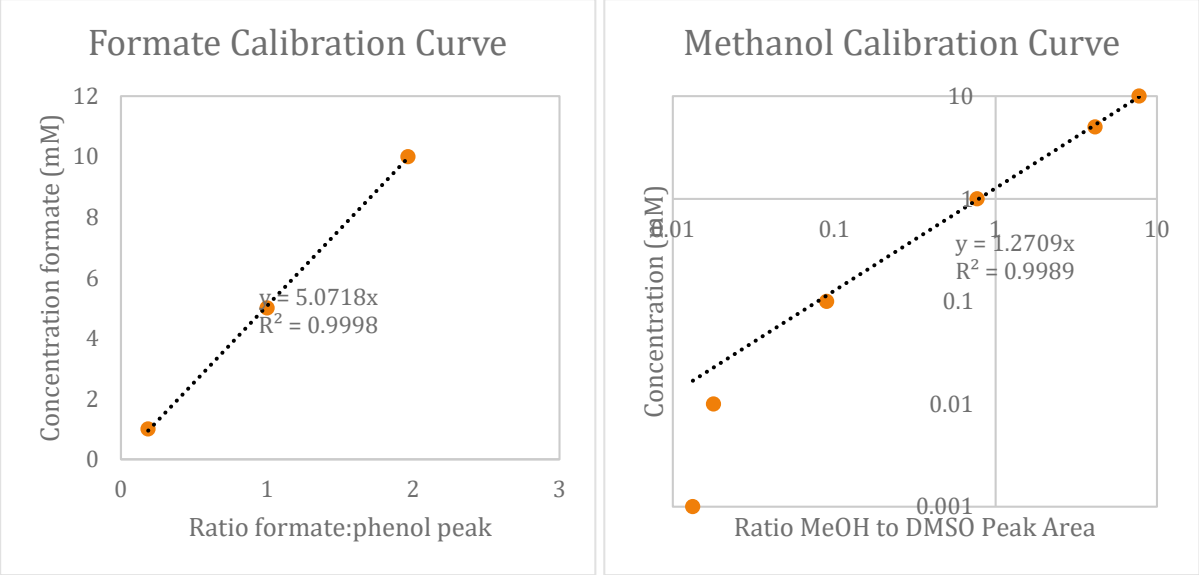

Figure A-A15. NMR calibration curves for formate and methanol.

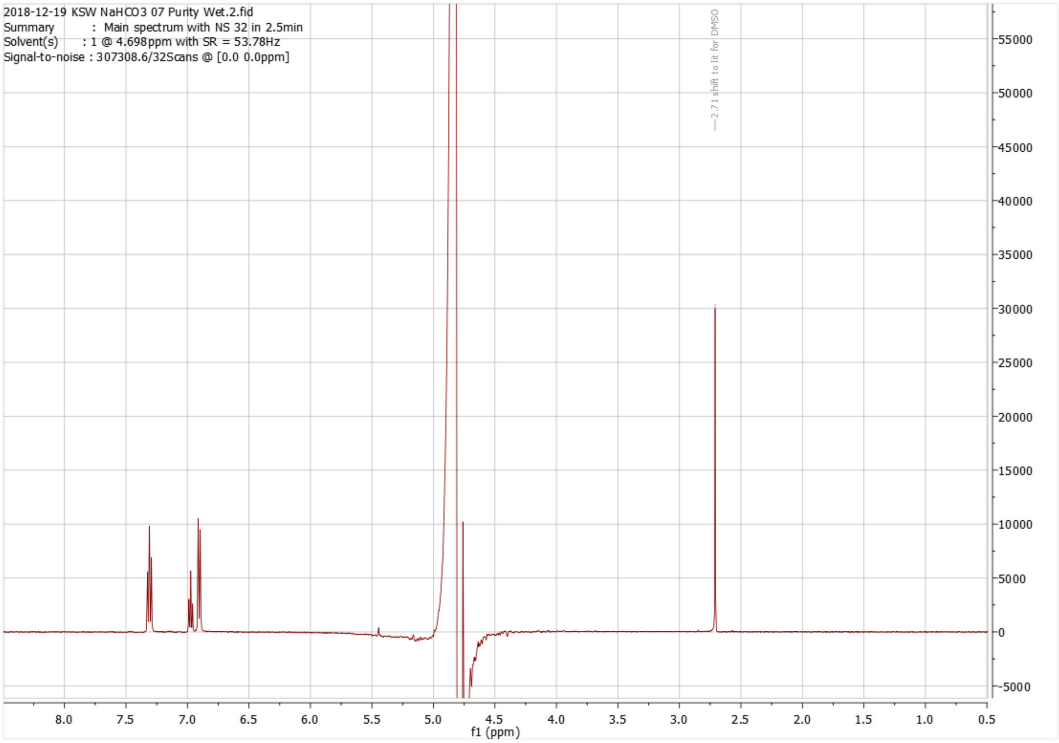

Figure A-A16. Blank NMR spectrum for CO_2 reduction experiments.

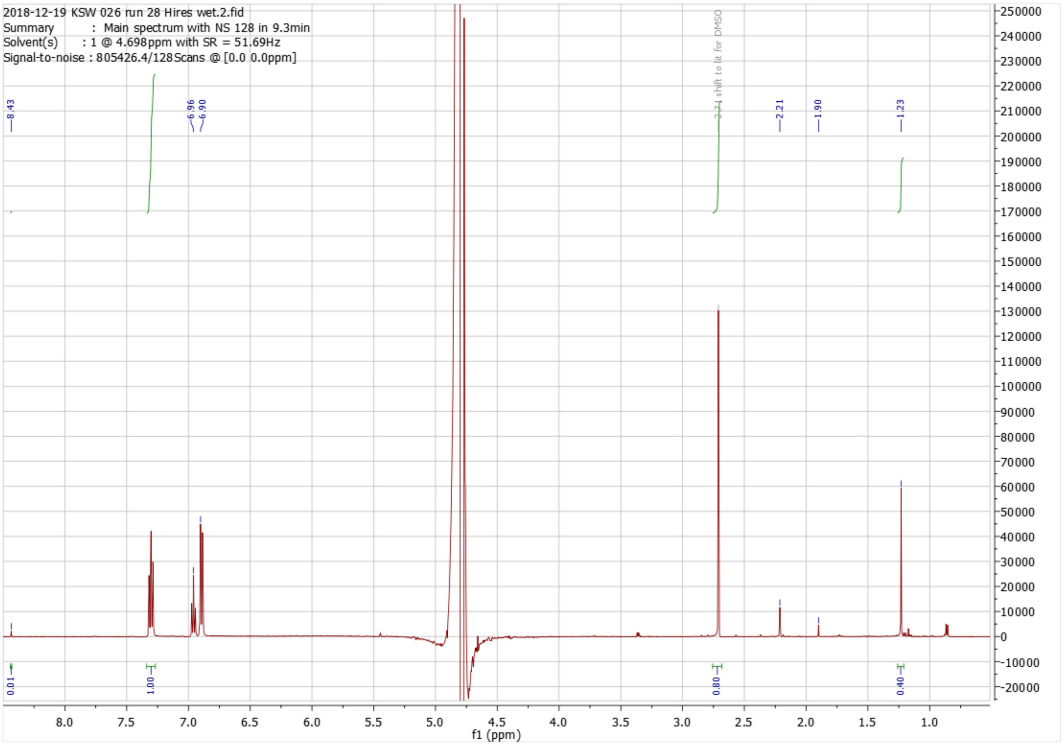

Figure A-A17. NMR spectrum post-electrolysis.

Note that a very small amount of formate (8.43 ppm above) was generated from Au, but not enough to contribute significantly to accounting for Faradaic efficiency. In addition, a negligible peak in the alcohols portion of the spectrum was present. The remaining peaks are likely acetone and hydrocarbon residues from the electrochemical cell itself.

A.7.3 UV-visible Quantification of Hydrogen Peroxide

Electrolytes were tested for hydrogen peroxide using a colorimetric assay.[211] 1 mL of electrolyte from a test having passed over 50 C of charge (16 hour test on gold around -0.7 V vs. RHE, flowing 5.0 sccm CO_2 and 5 sccm O_2 through 0.1 M $NaHCO_3$; charge toward ORR roughly 15 C) was combined with 1 mL of a stock solution containing 2.4 mM ammonium molybdate tetrahydrate and 0.5 M H_2SO_4 in Milli-Q®. The resulting solution appeared yellow in the presence of hydrogen peroxide. This solution was analyzed using an Ocean Optics spectrophotometer with a Flame-S-UV-Vis detector and a DH-mini-UV-Vis-NIR light source. The absorbance was scanned at wavelengths from 200 to 800 nm, and the absorbance at 370 nm was used to quantify peroxide. A blank bicarbonate solution spiked with the ammonium molybdate standard was used to zero the instrument prior to every acquisition. The calibration curve provided here has been constructed by JHM. A single data point with a known concentration of 5 mM H_2O_2 was used to check if this calibration curve, which is valid for

detecting peroxide in water, was also valid for bicarbonate solutions. The data point deviated less than 50% from the given curve, so a similar quantification limit is expected. No peroxide was observed.

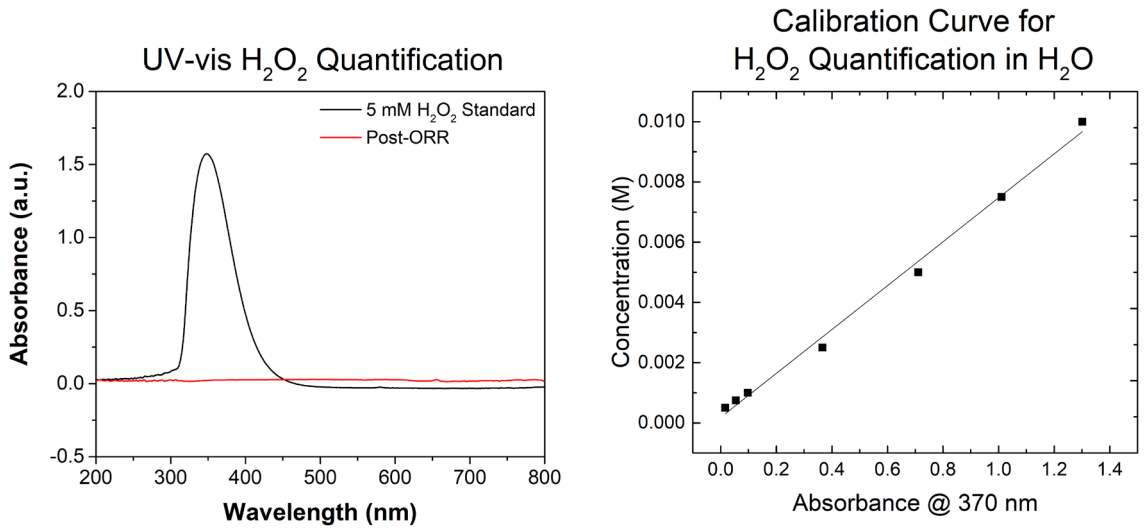

Figure A-A18. Peroxide quantification calibration curve and test confirming lack of peroxide generation.

Calibration equation: $(7.284\times10^{-3}) \times Abs_{370} + 0.190\times10^{-3}$ = concentration (M)

A.8 Discussion – Effect of O_2 at Lower Overpotentials

It should be noted that at potentials closer to the linear Tafel regime, a small but consistent downward trend in HER and CO_2RR was observed as more oxygen was added to the cell. This small downward trend is reflected in the consistently lower CO_2RR current densities obtained for all mechanistic tests in the main text. It is possible that this small downward trend is caused by the fact that ORR contributes a much higher percentage of the overall current density achieved at lower overpotentials, leading to a number of effects including an increase in pH in the vicinity of the electrode with large amounts of ORR taking place.

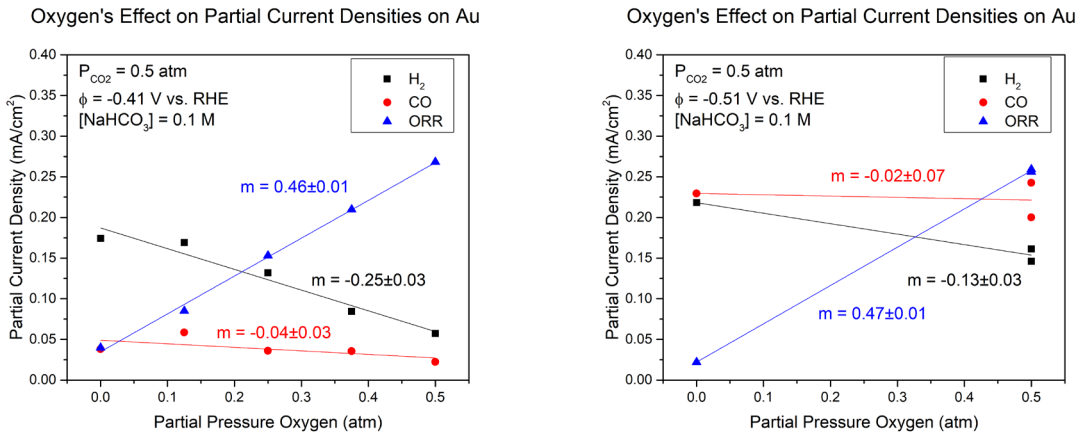

Figure A-A19. Effect of P_{O2} in gas feed on CO_2 reduction and HER at less reductive potentials than those discussed in the main text: -0.82 V vs. SHE and -0.92 V vs. SHE.

A.9 Discussion – CO_2RR Current Decay on Gold

It should be noted that a persistent observation during tests on gold was that CO_2RR currents decreased over time. This is consistent with observations from the literature regarding time-variance in currents and selectivities on polycrystalline Au.[88] A full treatment has been given to what we believe to be the cause this phenomenon: trace impurities in carbonate sources (Zn, Cu).[94] For this reason, only early-time-averaged data points (t = 20, 30, and 40 min) were used to construct all correlations described herein. Each data point taken in this work was from a newly assembled electrochemical cell and newly polished gold foil. A sample of data points taken after 1 hour of electroreduction indicates that this does not affect conclusions drawn (e.g. with regard to the values of Tafel slopes), so long as the procedure for calculating the current densities toward particular reactions is consistent across all data points on a single plot.

A.10 Discussion – Kinetic Rate Laws for CO_2RR

Under typical CO_2RR conditions in this study – namely, ambient temperature and pressure – the form of the Tafel slope should be:

$$Tafel\ slope = \frac{59\ mV/dec}{n + q\beta}$$

where n is the number of pre-RDS electron transfers, q is the number of electron transfers in the RDS (either 0 or 1 in almost all cases), and β is the symmetry factor – typically 0.5. A Tafel slope of 59 mV/dec implies that n = 1 and q = 0, or in other words that there is one electron transfer step prior to the RDS, and the RDS itself does not involve an electron transfer. This

means that we need to write out a number of possibilities for what such a chemical step might be, as in the main text.

After collecting kinetic data and narrowing down the list of possible RDSs, the remaining candidates include: (D.2) a vacant surface site could accept an $O^{\bullet-}$ atom, leaving a cationic CO adsorbate; (E.2) CO_2 could accept an $O^{\bullet-}$ atom, leaving a cationic CO adsorbate; (G.3) CO desorption under certain circumstances may be consistent with the given data; or (H.2) θ_{CO2}•- could rearrange in a distinct chemical step on the surface before undergoing subsequent chemistry. Note that step G.2 has been excluded on the grounds of lack of observable KIE. While surface metal motions may be implicated in the vibrational modes of adsorbed protons – which may in turn dampen any observed KIE – it has been shown both theoretically[212] and experimentally[213] that KIEs from adsorbed species may be observed. Therefore, it is likely from KIE data that step G.2 is not the RDS.

D.2 and E.2 are regarded as unlikely mechanisms. In the case of D.2, the presence of $O^{\bullet-}$ adsorbate on gold has not to the authors' knowledge been described (although it has been seen on earlier transition metals and predicted for oxides of silver),[214,215] and may imply that gold is acting as the cation for $O^{\bullet-}$ – in other words, that a gold oxide is forming. Gold is not a very oxophilic metal, and at such reductive potentials as studied here, we are well within the stability window of Au^0.[216] In the case of E.2, the sudden formation of opposite charges without a concurrent electron transfer likely has quite a low probability; and, once again, this mechanism invokes an intermediate (θ_{CO+}) which seems only to have been described in metal complexes rather than on surfaces.[107,108]

In the case of CO desorption (G.3), such a step mathematically remains a candidate for the RDS if the two electrons involved in CO_2 reduction occur in parallel. However, such a mechanism also requires invoking the unlikely intermediate θ_{COOH-}, which can in principle exist, but only if drawn with a carbon radical. Further, the electron pushing required to finally achieve CO and OH^- evolution from this adsorbate is also dubious. Unfortunately, testing such an unlikely mechanistic step is also difficult – we do not believe that P_{CO} dependence studies necessarily probe the possibility that such a step is the RDS, as adding CO to the feed of a CO_2RR cell may modulate the bulk concentration of CO, but will likely not affect the concentration of CO at the electrode surface. This is because the activity of CO is already quite high (although not unity) in the vicinity of CO-containing bubbles at the surface.

It is of course possible, however, that the chemical step is merely a surface rearrangement of the $CO_2^{\bullet-}$ adsorbate (H.2). Because it has been shown that grain boundary sites are more active for CO_2 reduction,[217] it seems reasonable to suggest that certain sites are required for further chemistry to proceed on gold surfaces, and consequently that the diffusion of $CO_2^{\bullet-}$ to such sites could be the bottleneck in CO production. This hypothesis would require spectroscopic investigation.

Below we derive many of the kinetic rate laws which give rise to the kinetic parameters tabulated in Table 1 of the main text.

A.10.1 – Step A.2 as RDS

The first possibility considered in the text is that bicarbonate in solution, with a pK_a of 10.3 (therefore a better proton donor than water, with pK_a of 14.0), is donating a proton to adsorbed $CO_2^{-\cdot}$. We can write out the following elementary steps in such a mechanism, describing all steps other than the RDS as being in equilibrium:

A.1 $$CO_2 + \theta + e^- \rightleftharpoons \theta_{CO_2^-}$$

A.2 $$\theta_{CO_2^-} + HCO_3^- \rightarrow \theta_{COOH} + CO_3^{2-}$$

A.3 $$\theta_{COOH} + e^- \rightleftharpoons \theta + CO + OH^-$$

From A.2 being rate-limiting, we can assert that the following is true about the rate:

$$rate = k_{A2}\theta_{CO_2^-}[HCO_3^-]$$

Note that the rate constant k_{A2} is an agglomerate variable standing in for the Arrhenius kinetics of the reaction absent any potential driving force, i.e.:

$$k_{A2} = k_{A2,0}\exp\left(-\frac{E^0_{a,A2}}{RT}\right)$$

Note also that in the derivation of Butler-Volmer from basic kinetics principles, we are left with an expression that is exponentially dependent on φ, the absolute potential – not on overpotential.

While bicarbonate concentration is known in principle, the expression for the surface coverage of $CO_2^{-\cdot}$ must be calculated using the equilibrium expressions for steps A.1 and A.3:

$$K_{A1} = \frac{\theta_{CO_2^-}}{\theta[CO_2]\exp\left(\frac{-F\Phi}{RT}\right)} \quad \rightarrow \quad \theta_{CO_2^-} = K_{A1}\theta[CO_2]\exp\left(\frac{-F\Phi}{RT}\right)$$

$$K_{A3} = \frac{\theta[CO][OH^-]}{\theta_{COOH}\exp\left(\frac{-F\Phi}{RT}\right)} \quad \rightarrow \quad \theta_{COOH} = \frac{\theta[CO][OH^-]}{K_{A3}\exp\left(\frac{-F\Phi}{RT}\right)}$$

Henceforth, for simplicity, we will make a change of variables, substituting lowercase φ for the quantity –FΦ/RT.

We also have the site balance relationship:

$$\theta + \theta_{CO_2^{-\cdot}} + \theta_{COOH} = 1$$

Substituting,

$$\theta + K_{A1}\theta[CO_2]\exp(\phi) + \frac{\theta[CO][OH^-]}{K_{A3}\exp(\phi)} = 1$$

Isolating θ,

$$\theta = \frac{1}{1 + K_{A1}[CO_2]\exp(\phi) + \frac{[CO][OH^-]}{K_{A3}\exp(\phi)}}$$

Substituting back into the expression for the CO_2^- radical:

$$\theta_{CO_2^-} = \frac{K_{A1}[CO_2]\exp(\phi)}{1 + K_{A1}[CO_2]\exp(\phi) + \frac{[CO][OH^-]}{K_{A3}\exp(\phi)}}$$

Therefore the rate expression becomes:

$$rate = \frac{k_{A2}[HCO_3^-]K_{A1}[CO_2]\exp(\phi)}{1 + K_{A1}[CO_2]\exp(\phi) + \frac{[CO][OH^-]}{K_{A3}\exp(\phi)}}$$

In order to retain the exp(φ) term in the numerator and remain in line with the experimentally obtained Tafel slope, we must be in the limit of low adsorbate coverage (i.e. the dominant term in the denominator should be 1). Therefore,

$$rate = k_{A2}K_{A1}[HCO_3^-][CO_2]\exp(\phi)$$

This expression is 1st order in bicarbonate concentration as well as CO_2 concentration. Thus we can directly test this mechanism by assessing the order dependence of the rate with respect to bicarbonate and CO_2. Notably, if we instead wrote step A.3 as generating a θ_{CO} rather than CO directly, there would be one surface coverage term not containing exp(φ), meaning this limit of coverage could also hold true. This would result in a rate expression of

$$rate = \frac{k_{A2}K_{A1}K_{A4}[HCO_3^-][CO_2]\exp(\phi)}{[CO]}$$

which would additionally be inversely dependent upon CO concentration in solution. This argument holds true for many of the other dissociative steps to follow, but will not be discussed in depth.

Regarding the feasibility of the main-text conclusions – upon much thought regarding the mechanism, it seems fairly reasonable that bicarbonate, as a negatively charged species, would not be able to easily approach the negatively polarized electrode to conduct chemistry there. Electrostatic repulsion may in fact dictate that while there is a 3.7-order-of-magnitude driving force for bicarbonate to act as a proton donor (over water) in this context (partially negated by a 2.7-order-of-magnitude greater abundance of water than bicarbonate), still bicarbonate may have a difficult time participating in cathodic surface reactions. We investigate the possibility of water as the proton donor in S.11.3 below.

A.10.2 – Step B.2 as RDS

For mechanism B, the elementary steps are:

B.1 $$CO_2 + \theta + e^- \rightleftharpoons \theta_{CO_2^-}$$

B.2 $$\theta_{CO_2^-} + H_2O \rightarrow \theta_{COOH} + OH^-$$

B.3 $$\theta_{COOH} + e^- \rightleftharpoons \theta + CO + OH^-$$

The rate law is then:

$$rate = k_{B2}\theta_{CO_2^-}[H_2O]$$

Equilibria B.1 and B.3 give us:

$$K_{B1} = \frac{\theta_{CO_2^-}}{\theta[CO_2]\exp(\phi)} \quad \rightarrow \quad \theta_{CO_2^-} = K_{B1}\theta[CO_2]\exp(\phi)$$

$$K_{B3} = \frac{\theta[CO][OH^-]}{\theta_{COOH}\exp(\phi)} \quad \rightarrow \quad \theta_{CO^+} = \frac{\theta[CO][OH^-]}{K_{B3}\exp(\phi)}$$

We also have the site balance relationship:

$$\theta + \theta_{CO_2^-} + \theta_{COOH} = 1$$

Substituting,

$$\theta + K_{B1}\theta[CO_2]\exp(\phi) + \frac{\theta[CO][OH^-]}{K_{B3}\exp(\phi)} = 1$$

Isolating θ,

$$\theta = \frac{1}{1 + K_{B1}[CO_2]\exp(\phi) + \frac{[CO][OH^-]}{K_{B3}\exp(\phi)}}$$

Substituting back into the expression for the CO_2^- radical:

$$\theta_{CO_2^-} = \frac{K_{B1}[CO_2]\exp(\phi)}{1 + K_{B1}[CO_2]\exp(\phi) + \frac{[CO][OH^-]}{K_{B3}\exp(\phi)}}$$

Therefore the rate expression becomes:

$$rate = \frac{k_{B2}K_{B1}[CO_2][H_2O]\exp(\phi)}{1 + K_{B1}[CO_2]\exp(\phi) + \frac{[CO][OH^-]}{K_{B3}\exp(\phi)}}$$

In the low-coverage limit:

$$rate = k_{B2}K_{B1}[CO_2][H_2O]\exp(\phi)$$

This expression is 1st order in CO_2 concentration, and also in water. Because water is the solvent, there is no easy way to test the mechanism by varying the availability of the reactants. Therefore we are left to test this possibility with the kinetic isotope effect, as described previously.

A.10.3 – Step C.3 as RDS

For mechanism C derivation, we will assume water to be the proton donor; thus, the elementary steps are:

C.1 $$CO_2 + \theta + e^- \rightleftharpoons \theta_{CO_2^-}$$

C.2 $$\theta_{CO_2^-} + H_2O \rightarrow \theta_{COOH} + OH^-$$

C.3 $$\theta_{COOH} + \theta \rightleftharpoons \theta_{CO} + \theta_{OH}$$

C.4 $$\theta_{CO} \rightleftharpoons \theta + CO$$

C.5 $$\theta_{OH} + e^- \rightleftharpoons \theta + OH^-$$

The rate law is then:

$$rate = k_{C3}\theta_{COOH}\theta$$

Equilibria C.1, C.2, C.4, and C.5 give us:

$$K_{C1} = \frac{\theta_{CO_2^-}}{\theta[CO_2]\exp(\phi)} \quad \rightarrow \quad \theta_{CO_2^-} = K_{C1}\theta[CO_2]\exp(\phi)$$

$$K_{C2} = \frac{\theta_{COOH}[OH^-]}{\theta_{CO_2^-}[H_2O]} \quad \rightarrow \quad \theta_{COOH} = \frac{K_{C1}K_{C2}\theta[CO_2][H_2O]\exp(\phi)}{[OH^-]}$$

$$K_{C4} = \frac{\theta[CO]}{\theta_{CO}} \quad \rightarrow \quad \theta_{CO} = \frac{\theta[CO]}{K_{C4}}$$

$$K_{C5} = \frac{\theta[OH^-]}{\theta_{OH}\exp(\phi)} \quad \rightarrow \quad \theta_{OH} = \frac{\theta[OH^-]}{K_{C5}\exp(\phi)}$$

We also have the site balance relationship:

$$\theta + \theta_{CO_2^-} + \theta_{COOH} + \theta_{CO} + \theta_{OH} = 1$$

Substituting,

$$\theta + K_{C1}\theta[CO_2]\exp(\phi) + \frac{K_{C1}K_{C2}\theta[CO_2][H_2O]\exp(\phi)}{[OH^-]} + \frac{\theta[CO]}{K_{C4}} + \frac{\theta[OH^-]}{K_{C5}\exp(\phi)} = 1$$

Isolating θ,

$$\theta = \frac{1}{1 + K_{C1}[CO_2]\exp(\phi) + \frac{K_{C1}K_{C2}[CO_2][H_2O]\exp(\phi)}{[OH^-]} + \frac{[CO]}{K_{C4}} + \frac{[OH^-]}{K_{C5}\exp(\phi)}}$$

Substituting back into the expression for COOH:

$$\theta_{COOH} = \frac{K_{C1}K_{C2}[CO_2][H_2O]\exp(\phi)}{[OH^-]\left(1 + K_{C1}[CO_2]\exp(\phi) + \frac{K_{C1}K_{C2}[CO_2][H_2O]\exp(\phi)}{[OH^-]} + \frac{[CO]}{K_{C4}} + \frac{[OH^-]}{K_{C5}\exp(\phi)}\right)}$$

Therefore the rate expression becomes:

$$rate = \frac{k_{C3}K_{C1}K_{C2}[CO_2][H_2O]\exp(\phi)}{[OH^-]\left(1 + K_{C1}[CO_2]\exp(\phi) + \frac{K_{C1}K_{C2}[CO_2][H_2O]\exp(\phi)}{[OH^-]} + \frac{[CO]}{K_{C4}} + \frac{[OH^-]}{K_{C5}\exp(\phi)}\right)^2}$$

In the low-coverage limit:

$$rate = \frac{k_{C3}K_{C1}K_{C2}[CO_2][H_2O]\exp(\phi)}{[OH^-]}$$

This may in a sense be interpreted as an expression at least first-order in protons, in which case the mechanism can be eliminated as a possibility. Certainly surface pH should affect the rate of a reaction under such control; however, tests to probe pH effects are inextricably convoluted with other aspects of the solution chemistry, and would have to be confirmed with efforts to model surface pH under reaction conditions.

A.10.4 – Step D.2 as RDS

For mechanism D, the elementary steps are:

D.1 $$CO_2 + \theta + e^- \rightleftharpoons \theta_{CO_2^-}$$

D.2 $$\theta_{CO_2^-} + \theta \rightarrow \theta_{CO} + \theta_{O^-}$$

D.3 $$\theta_{CO} \rightleftharpoons \theta + CO$$

To complete the mechanism, O-atom anion adsorbates would have to undergo the following final step, or something adjacent:

D.4 $$\theta_{O^-} + HCO_3^- + e^- \rightleftharpoons \theta + OH^- + CO_3^{2-}$$

We have the following rate expression in the case of D.2 as the RDS:

$$rate = k_{D2}\theta_{CO_2^-}\theta$$

Equilibria D.1, D.3, and D.4 give us:

$$K_{D1} = \frac{\theta_{CO_2^-}}{\theta[CO_2]\exp(\phi)} \quad \rightarrow \quad \theta_{CO_2^-} = K_{D1}\theta[CO_2]\exp(\phi)$$

$$K_{D3} = \frac{\theta[CO]}{\theta_{CO}} \quad \rightarrow \quad \theta_{CO} = \frac{\theta[CO]}{K_{D3}}$$

$$K_{D4} = \frac{\theta[OH^-][CO_3^{2-}]}{\theta_{O^-}[HCO_3^-]\exp(\phi)} \quad \rightarrow \quad \theta_{O^-} = \frac{\theta[OH^-][CO_3^{2-}]}{K_{D4}[HCO_3^-]\exp(\phi)}$$

We also have the site balance relationship:

$$\theta + \theta_{CO_2^-} + \theta_{CO} + \theta_{O^-} = 1$$

Substituting,

$$\theta + K_{D1}\theta[CO_2]\exp(\phi) + \frac{\theta[CO]}{K_{D3}} + \frac{\theta[OH^-][CO_3^{2-}]}{K_{D4}[HCO_3^-]\exp(\phi)} = 1$$

Isolating θ,

$$\theta = \frac{1}{1 + K_{D1}[CO_2]\exp(\phi) + \frac{[CO]}{K_{D3}} + \frac{[OH^-][CO_3^{2-}]}{K_{D4}[HCO_3^-]\exp(\phi)}}$$

Substituting back into the expression for the CO_2^- radical:

$$\theta_{CO_2^-} = \frac{K_{D1}[CO_2]\exp(\phi)}{1 + K_{D1}[CO_2]\exp(\phi) + \frac{[CO]}{K_{D3}} + \frac{[OH^-][CO_3^{2-}]}{K_{D4}[HCO_3^-]\exp(\phi)}}$$

Therefore the rate expression becomes:

$$rate = \frac{k_{D2}K_{D1}[CO_2]\exp(\phi)}{\left(1 + K_{D1}[CO_2]\exp(\phi) + \frac{[CO]}{K_{D3}} + \frac{[OH^-][CO_3^{2-}]}{K_{D4}[HCO_3^-]\exp(\phi)}\right)^2}$$

In the low-coverage limit:

$$rate = k_{D2}K_{D1}[CO_2]\exp(\phi)$$

Also, in the limit of high CO coverage, the same Tafel slope holds, while there is a $[CO]^{-2}$ dependence of the rate.

A.10.5 – Step E.2 as RDS

We apply analysis in much the same form for subsequent mechanistic possibilities. For mechanism E, the RDS possibility is step E.2, so that the elementary steps are:

E.1 $$CO_2 + \theta + e^- \rightleftharpoons \theta_{CO_2^-}$$

E.2 $$\theta_{CO_2^-} + CO_2 \rightarrow \theta_{CO^+} + CO_3^{2-}$$

E.3 $$\theta_{CO^+} + e^- \rightleftharpoons \theta + CO$$

The rate law is then:

$$rate = k_{E2}\theta_{CO_2^-}[CO_2]$$

Equilibria E.1 and E.3 give us:

$$K_{E1} = \frac{\theta_{CO_2^-}}{\theta[CO_2]\exp(\phi)} \quad \rightarrow \quad \theta_{CO_2^-} = K_{E1}\theta[CO_2]\exp(\phi)$$

$$K_{E3} = \frac{\theta[CO]}{\theta_{CO^+}\exp(\phi)} \quad \rightarrow \quad \theta_{CO^+} = \frac{\theta[CO]}{K_{E3}\exp(\phi)}$$

We also have the site balance relationship:

$$\theta + \theta_{CO_2^{-\cdot}} + \theta_{CO^+} = 1$$

Substituting,

$$\theta + K_{E1}\theta[CO_2]\exp(\phi) + \frac{\theta[CO]}{K_{E3}\exp(\phi)} = 1$$

Isolating θ,

$$\theta = \frac{1}{1 + K_{E1}[CO_2]\exp(\phi) + \frac{[CO]}{K_{E3}\exp(\phi)}}$$

Substituting back into the expression for the CO_2^- radical:

$$\theta_{CO_2^{-\cdot}} = \frac{K_{E1}[CO_2]\exp(\phi)}{1 + K_{E1}[CO_2]\exp(\phi) + \frac{[CO]}{K_{E3}\exp(\phi)}}$$

Therefore the rate expression becomes:

$$rate = \frac{k_{E2}K_{E1}[CO_2]^2\exp(\phi)}{1 + K_{E1}[CO_2]\exp(\phi) + \frac{[CO]}{K_{E3}\exp(\phi)}}$$

In the low-coverage limit:

$$rate = k_{E2}K_{E1}[CO_2]^2\exp(\phi)$$

This expression is 2nd order in CO_2 concentration. Thus we can directly test this mechanism by assessing the order dependence of the rate with respect to CO_2.

A.10.6 – Step F.3 as RDS

For mechanism F, the elementary steps are:

F.1 $$CO_2 + \theta + e^- \rightleftharpoons \theta_{CO_2^{-\cdot}}$$

F.2 $$\theta_{CO_2^{-\cdot}} + H_2O \rightarrow \theta_{COOH} + OH^-$$

F.3 $$\theta_{COOH} \rightleftharpoons \theta_{CO^+} + OH^-$$

F.4 $$\theta_{CO^+} + e^- \rightleftharpoons \theta + CO$$

The rate law is then:

$$rate = k_{F3}\theta_{COOH^-}$$

Equilibria F.1, F.2, and F.4 give us:

$$K_{F1} = \frac{\theta_{CO_2^{\cdot-}}}{\theta[CO_2]\exp(\phi)} \quad \rightarrow \quad \theta_{CO_2^{\cdot-}} = K_{F1}\theta[CO_2]\exp(\phi)$$

$$K_{F2} = \frac{\theta_{COOH}[OH^-]}{\theta_{CO_2^{\cdot-}}[H_2O]} \quad \rightarrow \quad \theta_{COOH} = \frac{K_{F2}K_{F1}\theta[CO_2][H_2O]\exp(\phi)}{[OH^-]}$$

$$K_{F4} = \frac{\theta[CO]}{\theta_{CO^+}\exp(\phi)} \quad \rightarrow \quad \theta_{CO^+} = \frac{\theta[CO]}{K_{F4}\exp(\phi)}$$

We also have the site balance relationship:

$$\theta + \theta_{CO_2^{\cdot-}} + \theta_{COOH} + \theta_{CO^+} = 1$$

Substituting,

$$\theta + K_{F1}\theta[CO_2]\exp(\phi) + \frac{K_{F2}K_{F1}\theta[CO_2][H_2O]\exp(\phi)}{[OH^-]} + \frac{\theta[CO]}{K_{F4}\exp(\phi)} = 1$$

Isolating θ,

$$\theta = \frac{1}{1 + K_{F1}[CO_2]\exp(\phi) + \frac{K_{F2}K_{F1}[CO_2][H_2O]\exp(\phi)}{[OH^-]} + \frac{[CO]}{K_{F4}\exp(\phi)}}$$

Substituting back into the expression for $COOH^-$:

$$\theta_{COOH} = \frac{K_{F2}K_{F1}[CO_2][H_2O]\exp(\phi)}{[OH^-] + K_{F1}[CO_2][OH^-]\exp(\phi) + K_{F2}K_{F1}[CO_2][H_2O]\exp(\phi) + \frac{[CO][OH^-]}{K_{F4}\exp(\phi)}}$$

Therefore the rate expression becomes:

$$rate = \frac{k_{F3}K_{F2}K_{F1}[CO_2][H_2O]\exp(\phi)}{[OH^-] + K_{F1}[CO_2][OH^-]\exp(\phi) + K_{F2}K_{F1}[CO_2][H_2O]\exp(\phi) + \frac{[CO][OH^-]}{K_{F4}\exp(\phi)}}$$

In the low-coverage limit:

$$rate = \frac{k_{F3}K_{F2}K_{F1}[CO_2][H_2O]\exp(\phi)}{[OH^-]}$$

This may in a sense be interpreted as an expression at least first-order in protons, in which case the mechanism can be eliminated as a possibility. Certainly surface pH should affect the rate

of a reaction under such control; however, tests to probe pH effects are inextricably convoluted with other aspects of the solution chemistry, and would have to be confirmed with efforts to model surface pH under reaction conditions.

A.10.7 – Step G.2/G.3 as RDS

For mechanism G, the elementary steps are:

G.1 $$CO_2 + \theta + e^- \rightleftharpoons \theta_{CO_2^-}$$

$$HCO_3^- + \theta + e^- \rightleftharpoons \theta_H + CO_3^{2-}$$

G.2 $$\theta_{CO_2^-} + \theta_H \rightarrow \theta_{COOH^-} + \theta$$

G.3 $$\theta_{COOH^-} \rightleftharpoons \theta + CO + OH^-$$

Here there is necessary adsorption of H to the surface prior to the CO_2RR RDS. In principle, the donor for this proton could also be water, and the adsorbed H could also divert toward HER. Depending on the HER mechanism, the subsequent step may either be the Tafel or Heyrovsky generation of H_2:

Tafel $$2\theta_H \rightleftharpoons 2\theta + H_2$$

Heyrovsky $$\theta_H + HCO_3^- + e^- \rightleftharpoons \theta + H_2 + CO_3^{2-}$$

It has been shown in other works' Supporting Information that using the initial H adsorption as the equilibrium expression for the coverage θ_H leads to Tafel slopes not consistent with our experimental data (30 mV/dec).[90] If, however, the Volmer step (H adsorption) is the RDS of HER, and not truly in equilibrium, then the equilibrium expression that holds true is either the Tafel or Heyrovsky relation. We will derive here the case in which the equilibrium expression for θ_H is obtained through the Tafel step equilibrium.

$$rate = k_{D2}\theta_{CO_2^-}\theta_H$$

Equilibria G.1, G.3, and the Tafel step give us:

$$K_{G1} = \frac{\theta_{CO_2^-}}{\theta[CO_2]\exp(\phi)} \quad \rightarrow \quad \theta_{CO_2^-} = K_{G1}\theta[CO_2]\exp(\phi)$$

$$K_{G3} = \frac{\theta[CO][OH^-]}{\theta_{COOH^-}} \quad \rightarrow \quad \theta_{COOH^-} = \frac{\theta[CO][OH^-]}{K_{G3}}$$

$$K_{GT} = \frac{\theta^2[H_2]}{\theta_H^2} \quad \rightarrow \quad \theta_H = \sqrt{\frac{[H_2]}{K_{GT}}}\,\theta$$

We also have the site balance relationship:

$$\theta + \theta_{CO_2^{-\cdot}} + \theta_{COOH^-} + \theta_H = 1$$

Substituting,

$$\theta + K_{G1}\theta[CO_2]\exp(\phi) + \frac{\theta[CO][OH^-]}{K_{G3}} + \sqrt{\frac{[H_2]}{K_{GT}}}\,\theta = 1$$

Isolating θ,

$$\theta = \frac{1}{1 + K_{G1}[CO_2]\exp(\phi) + \frac{[CO][OH^-]}{K_{G3}} + \sqrt{\frac{[H_2]}{K_{GT}}}}$$

Substituting back into the expressions for the CO_2^- radical and H sites:

$$\theta_{CO_2^-} = \frac{K_{G1}[CO_2]\exp(\phi)}{1 + K_{G1}[CO_2]\exp(\phi) + \frac{[CO][OH^-]}{K_{G3}} + \sqrt{\frac{[H_2]}{K_{GT}}}}$$

$$\theta_H = \frac{\sqrt{\frac{[H_2]}{K_{GT}}}}{1 + K_{G1}[CO_2]\exp(\phi) + \frac{[CO][OH^-]}{K_{G3}} + \sqrt{\frac{[H_2]}{K_{GT}}}}$$

Therefore the rate expression becomes:

$$rate = \frac{k_{G2}K_{G1}[CO_2]\sqrt{\frac{[H_2]}{K_{GT}}}\exp(\phi)}{\left(1 + K_{G1}[CO_2]\exp(\phi) + \frac{[CO][OH^-]}{K_{G3}} + \sqrt{\frac{[H_2]}{K_{GT}}}\right)^2}$$

In the low-coverage limit:

$$rate = k_{G2}K_{G1}[CO_2]\sqrt{\frac{[H_2]}{K_{GT}}}\exp(\phi)$$

The unique thing about this mechanism is that it is 0.5-order in the concentration of H_2 gas. However, due to H_2's low solubility in water and relative abundance at the surface of the cathode, this mechanism is rather difficult to test by modulating P_{H2}.

It should also be noted that such a mechanism is additionally plausible by assuming separate types of adsorption sites for protons on the surface, in which case the following expression is obtained (γ = H adsorption site):

$$rate = \frac{k_{G2}K_{G1}[CO_2]\sqrt{\frac{[H_2]}{K_{GT}}}\exp(\phi)}{\left(1 + K_{G1}[CO_2]\exp(\phi) + \frac{[CO][OH^-]}{K_{G3}}\right)\left(1 + \sqrt{\frac{[H_2]}{K_{GT}}}\right)}$$

Moreover, Tafel slopes are still consistent with experiment even if the coverages of $COOH^-$ or H dominate in either case. However, this mechanism was excluded in the main text because it likely involves an observable KIE.

In the case of G.3 as the RDS, we have the rate:

$$rate = k_{G3}\theta_{COOH^-}$$

Equilibria G.1, G.2, and the Tafel step give us:

$$K_{G1} = \frac{\theta_{CO_2^{\cdot-}}}{\theta[CO_2]\exp(\phi)} \quad \rightarrow \quad \theta_{CO_2^{\cdot-}} = K_{G1}\theta[CO_2]\exp(\phi)$$

$$K_{GT} = \frac{\theta^2[H_2]}{\theta_H^2} \quad \rightarrow \quad \theta_H = \sqrt{\frac{[H_2]}{K_{GT}}}\,\theta$$

$$K_{G2} = \frac{\theta\theta_{COOH^-}}{\theta_{CO_2^{\cdot-}}\theta_H} \quad \rightarrow \quad \theta_{COOH^-} = K_{G1}K_{G2}\theta[CO_2]\sqrt{\frac{[H_2]}{K_{GT}}}\exp(\phi)$$

We also have the site balance relationship:

$$\theta + \theta_{CO_2^{\cdot-}} + \theta_{COOH^-} + \theta_H = 1$$

Substituting,

$$\theta + K_{G1}\theta[CO_2]\exp(\phi) + K_{G1}K_{G2}\theta[CO_2]\sqrt{\frac{[H_2]}{K_{GT}}}\exp(\phi) + \sqrt{\frac{[H_2]}{K_{GT}}}\,\theta = 1$$

Isolating θ,

$$\theta = \frac{1}{1 + K_{G1}[CO_2]\exp(\phi) + K_{G1}K_{G2}[CO_2]\sqrt{\frac{[H_2]}{K_{GT}}}\exp(\phi) + \sqrt{\frac{[H_2]}{K_{GT}}}}$$

Substituting back into the expressions for the $COOH^-$ sites:

$$\theta_{COOH^-} = \frac{K_{G1}K_{G2}[CO_2]\sqrt{\frac{[H_2]}{K_{GT}}}\exp(\phi)}{1 + K_{G1}[CO_2]\exp(\phi) + K_{G1}K_{G2}[CO_2]\sqrt{\frac{[H_2]}{K_{GT}}}\exp(\phi) + \sqrt{\frac{[H_2]}{K_{GT}}}}$$

Therefore the rate expression becomes:

$$rate = \frac{k_{G3}K_{G1}K_{G2}[CO_2]\sqrt{\frac{[H_2]}{K_{GT}}}\exp(\phi)}{1 + K_{G1}[CO_2]\exp(\phi) + K_{G1}K_{G2}[CO_2]\sqrt{\frac{[H_2]}{K_{GT}}}\exp(\phi) + \sqrt{\frac{[H_2]}{K_{GT}}}}$$

In the low-coverage limit:

$$rate = k_{G3}K_{G1}K_{G2}[CO_2]\sqrt{\frac{[H_2]}{K_{GT}}}\exp(\phi)$$

A.10.8 – Step H.2 as RDS

There are a number of post-RDS paths in mechanism H, so these have not been specified in the table, nor will they be specified here. However, it should follow from very similar math as applied above that the rearrangement of adsorbed $CO_2^{\bullet-}$ on the surface is a chemical step with a Tafel slope of 59 mV/dec, first-order dependence on CO_2, and no dependence on protons.

APPENDIX B: ADDITIONAL CONSIDERATIONS FOR BLENDED ELECTROLYTES

B.1 Methods: Electrolyte preparation

Electrolytes for electrochemical experiments as well as headspace experiments were prepared from a combination of the following stock solutions:

1. Acetonitrile, dried over 3Å Molecular Sieves
    - Anhydrous acetonitrile direct from the supplier was removed and pipetted into a 250 mL polypropylene stock bottle, where it was stored over 3Å molecular sieves at a ratio of about 10% molecular sieves by volume.
    - Molecular sieves were regenerated periodically to maintain low moisture content by:
        i. Pouring off any residual acetonitrile
        ii. Rinsing sieves in acetone to remove organic contaminants
        iii. Rapidly evaporating residual acetone on the sieves by leaving sieves in a negative-pressure location such as in a hood or under a snorkel, until sieves returned to original light tan color
        iv. Transferring sieves to a ceramic crucible
        v. Heating sieves in a general-use muffle furnace with the following temperature program:
            1. Ramp: Room Temperature -> 350 °C at rate of 15 °C/min (20 min ramp)
            2. Hold at 350 °C for 4 hours
            3. Shut off program at 4 hours and allow to cool naturally
        vi. Retrieving the sieves after ~30 minutes and returning them to a dry, solvent-free 250 mL polypropylene stock bottle
        vii. Adding fresh acetonitrile
        viii. Stirring/shaking bottle gently
        ix. Allowing solvent to sit like this overnight prior to using
    - Water content of stock acetonitrile was tested periodically by Karl Fischer titration. Sieves consistently kept water content undetectable (<100 ppm water given a ~0.5 mL sample of acetonitrile).
2. Milli-Q water

- Obtained directly from the lab Milli-Q unit; stored temporarily in a 50 mL polypropylene falcon tube.

3. 1.0 M $TBABF_4$ in acetonitrile
    - Because of the bulkiness of the tetrabutylammonium cation in solution, 1.0 M $TBABF_4$ was prepared by adding enough $TBABF_4$ powder to produce the desired molarity, then dissolving it in enough acetonitrile to lead to the desired solution volume. For 100 mL of 1.0 M $TBABF_4$, the formulation was found to be:
        i. 32.93 grams $TBABF_4$ (= 0.1 mol)
        ii. 67.5 mL acetonitrile (= 53.055 g = 1.292 mol at room temperature)
    - It may be noted that this implies $TBABF_4$ in acetonitrile takes up space in such a manner that it adds ~1 mL/gram $TBABF_4$.
    - The stock solution is 7.18 mol% $TBABF_4$ and 92.82 mol% acetonitrile.
4. 100 mM ferrocene in acetonitrile
    - 372.1 mg ferrocene in 20 mL acetonitrile
5. 5 mM decamethyl ferrocene in acetonitrile
    - Added 21.2 mg decamethyl ferrocene to 13 mL of sieve-dried acetonitrile. Vortexed/sonicated to dissolve. This is right at / slightly above the solubility limit of decamethyl ferrocene in acetonitrile, so some decamethyl ferrocene powder may persist in solution.

Note that, while volume changes were accounted for in solution (3), volume changes due to mixing were ignored for the combination of any of these stock solutions with one another. Visually, volumes were observed to be consistent, suggesting this approximation contributed very little error (certainly <5%) to reported molarities. See below for solution formulations.

B.2 Methods: Electrochemical cells

The electrochemical cell used in RDE experiments was a custom 2-compartment glass H-cell by JamesGlass. The two compartments were separated by a glass frit, and each compartment was equipped at the top with a female 24/25 ground glass joint. Total electrolyte volume used in experiments, in order to fully cover the glass frit, was 30 mL. A horizontal glass threaded fitting on the working compartment allowed for the use of a reference electrode. A leak-free Ag/AgCl in 3.5 M KCl reference was inserted into this fitting and sealed using a compression O-ring (Markez, size 201, shaved down to non-standard size allowing full seal on the reference

electrode). The O-ring fitting was finger-tightened as much as possible to maintain a seal against the electrolyte. The cell was cleaned prior to all experiments by a dip in 20% nitric acid, and between experiments was cleaned with Milli-Q water & acetone rinses.

Figure A-B1. Photo of H-cell used in electrochemical experiments. Custom cell by JamesGlass.

B.3 Methods: RDE experiments

Prior to every RDE experiment, the reference electrode was calibrated (see *Methods: Calibrating Reference Electrode – 1. Calibrating vs. Master Ag/AgCl*) and the working electrode was cleaned and prepared according to literature-based procedures (see *Methods: Preparation of RDE Working Electrodes*). In addition, the custom 2-compartment glass H-cell with reference port – cleaned from any prior experiments – was removed from an 80 °C oven where it had been drying. After the glass electrochemical cell had cooled close to room temperature and the calibrated leak-free Ag/AgCl had been inserted, the relevant electrolyte was added to each compartment to entirely cover the glass frit. See table below for formulation of basic electrolytes.

Table A-B1. Electrolyte formulations for RDE experiments in H-cell.

Solution	0.5 M H_2O	1 M H_2O	2.5 M H_2O	5 M H_2O	6.6 M H_2O
Volume Water	--	270 µL	1.08 mL	2.43 mL	3.28 mL
Volume TBAOH	451 µL	451 µL	451 µL	451 µL	451 µL
Volume Fresh ACN	6.22 mL	5.95 mL	5.14 mL	3.79 mL	2.93 mL
Volume 1.0 M TBA/ACN	23.32 mL	23.32 mL	23.32 mL	23.32 mL	23.32 mL

After adding the electrolyte to the cell, 1/16” FEP tubing was used to bubble Argon gas into the working electrolyte at a rate of 20 sccm for at least 10 minutes to purge the electrolyte of dissolved oxygen gas. A brief purge of the counter electrolyte was also sometimes conducted. Immediately after the electrolyte purge, the rotator shaft with working electrode was lowered into the working compartment of the H-cell, and a Pine Gas-Purged Bearing was used to seal the working compartment. The Ar line was reconnected to direct 20 sccm Ar through this bearing, maintaining an inert Ar atmosphere in the working compartment headspace. The three-electrode setup was completed by inserting a Pt wire into the counter compartment and attaching it to the potentiostat cables. At this point the enclosure was lowered, the rotator set to spin at 1600 rpm, and the local exhaust ventilation put in place. The setup was then ready for electrolysis.

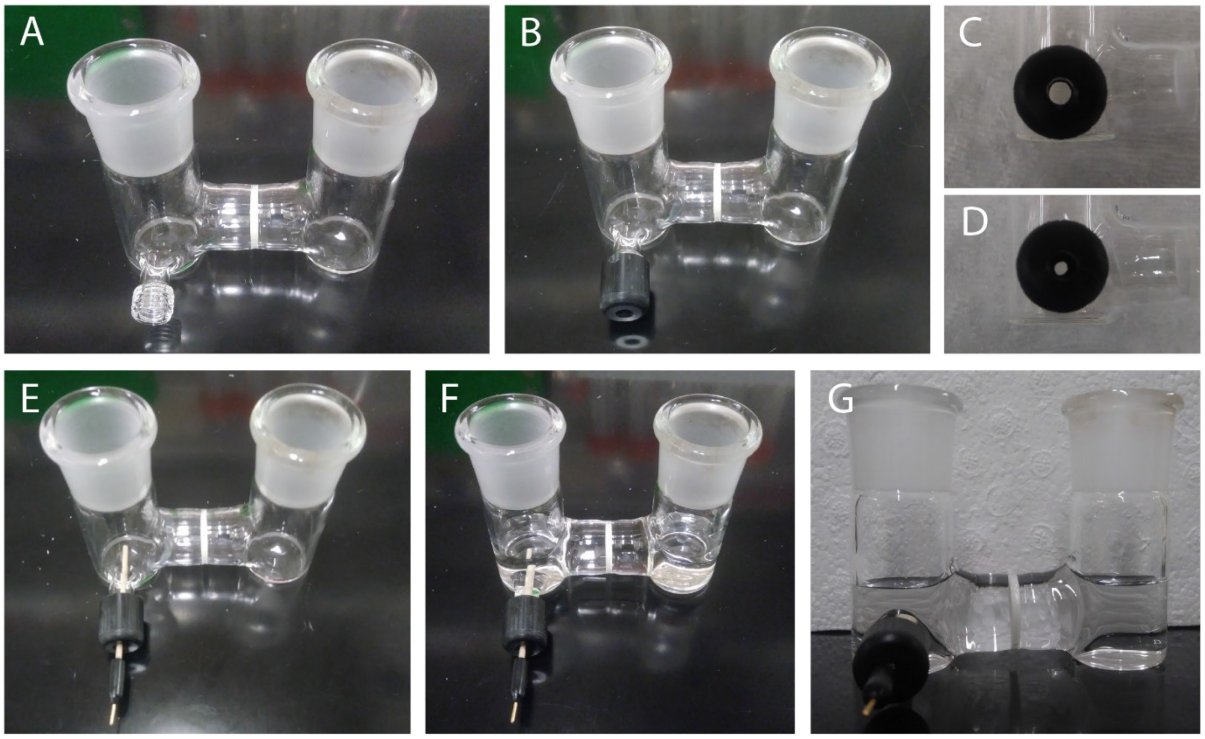

Figure A-B2. Assembly and loading of H-Cell. A) H-Cell taken directly from drying oven. B) H-Cell with addition of compression O-ring and compression fitting on reference port. C) O-ring/reference port prior to tightening fitting. D) O-ring/reference port after slightly tightening fitting – note O-ring compression. E) Full cell with reference inserted into port. F) Full cell after loading with 30 mL electrolyte. G) Front-on image of full cell after loading with 30 mL electrolyte.

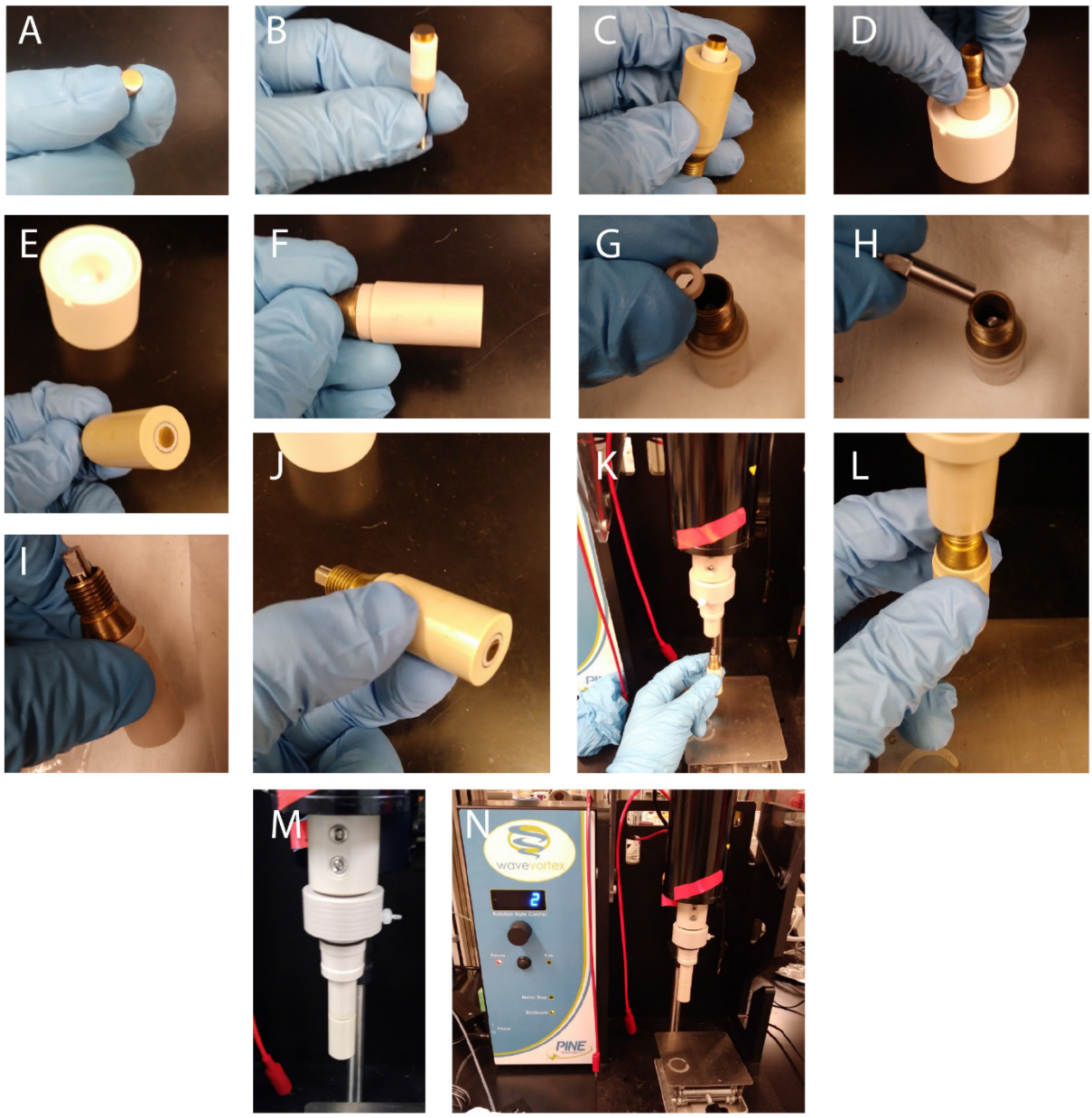

Figure A-B3. Insertion of prepared disk into RDE assembly.A) Polished Au disk. B) Disk in PTFE casing at the rotator shaft tip. C) Assembly in (B) inserted into the outer PEEK shroud. D) Pushing down the assembly in (C) to properly seat the Au disk into the PEEK shroud. E) Image of the result of proper seating. F) Side-profile image of the same. G) Dropping a plastic spacer into the back of the assembly. H) Screwing in the disk contact stud to enable electrical connection to the working electrode. I) The electrode tip assembly, ready to insert onto the rotator shaft. J) The electrode tip assembly from a different angle. K) Preparing to insert the electrode tip into the rotator shaft. L) Seating the electrode assembly into the rotator & screwing in. M) Final assembly, including gas-purged bearing attached to rotator shaft. N) Wider view of final assembly, now ready to use.

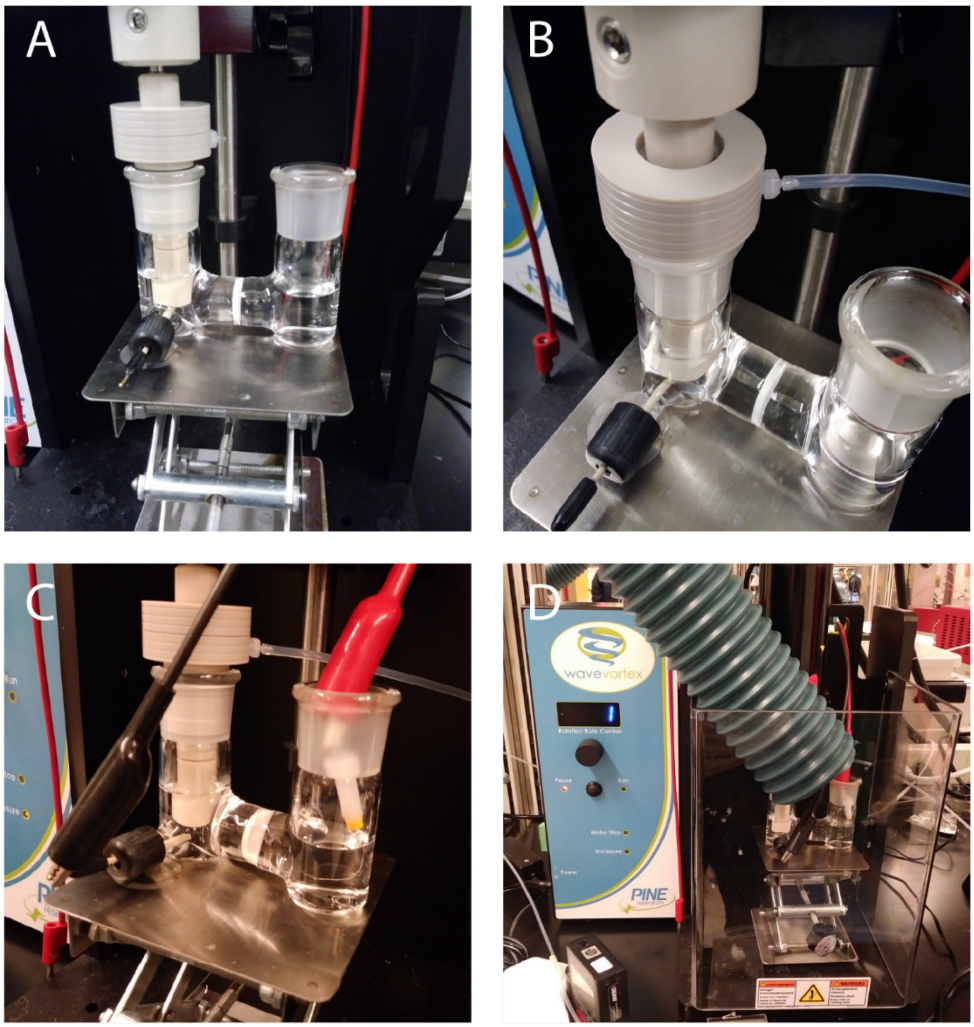

Figure A-B4. Combining the prepared H-cell with the prepared electrode to finalize setup. A) RDE inserted into working compartment of filled H-cell. B) Argon gas line connected to gas-purged bearing. C) Counter electrode inserted into counter compartment, and electrodes hooked up to potentiostat. D) Final setup complete with local exhaust ventilation.

For a typical HER experiment, the following EC-Lab sequence was run:

1. PEIS: 200 kHz – 1 Hz
2. Pause
3. MIR: Correct for [$R_{measured}$] at 85%
    - Resistance was measured as the x-intercept of EIS data, to the nearest Ohm. Usually ~15 Ohm total.
4. LSV: -0.5 V to -2.0 V vs. Ag/AgCl
    - 10 mV/sec scan rate

- Initial LSV gave a sense for the required sweep windows and hold potentials in subsequent steps.

5. CA: hold at [V_{ORR}] for 30 minutes
    - To remove any residual oxygen from the system, the working electrode was held at a potential at which only the oxygen reduction reaction (ORR) was taking place. A typical value was -1.5 V vs. Ag/AgCl. Over the course of the half-hour hold, the remaining oxygen in the cell was depleted through reaction. Water produced by ORR during the experiment was considered to be negligible in comparison to the amount of water explicitly added to the system, due to the low solubility of oxygen gas in acetonitrile.[218]
6. LSV: -0.5 V to -2.0 V vs. Ag/AgCl
    - 2 mV/sec scan rate – nearly steady-state measurements at every potential, with very little contribution due to capacitance
7. CA: hold at -1.9 V vs. Ag/AgCl for 30 minutes
    - To assess stability of current at any given potential
8. OCV for 1 min
9. PEIS: 200 kHz – 1 Hz
    - Confirm no change in resistance
10. LSV: -0.5 V to -2.0 V vs. Ag/AgCl
    - 10 mV/sec scan rate
    - Duplicate fast LSV with no oxygen
11. CA: hold at [V_{ORR}] for 5-10 minutes
    - Confirm no increase in ORR background
12. LSV: -0.5 V to -2.0 V vs. Ag/AgCl
    - 2 mV/sec scan rate
    - Duplicate slow LSV
13. CA: hold at -1.9 V vs. Ag/AgCl for 30 minutes
    - To assess recovery of current at any given potential

Data from these experiments was processed in order to:

- Manually correct for the remaining 15% IR drop that was uncompensated during the experiment
- Plot as log (i) vs. V, a.k.a. as a Tafel plot

- Make a cut at constant V vs. Me_{10}-Fc across all values of water content, using the calibration of the Ag/AgCl reference versus Me_{10}-Fc.

B.4 Methods: Preparation of RDE working electrodes

B.4.1 Gold disk[168]

The Au disk (Pine Research #AFED050P040AU) was prepared by first removing any visible residue from prior experiments by rinsing with acetone and water. The Au was then placed in a PTFE disk polishing holder and hand-polished, in some cases with 0.3 μm alumina on a vinyl pad reserved for use with Au (30 sec – 2 min), and in all cases finishing with a fine 0.05 μm alumina MicroPolish on a microfiber pad reserved for use with Au (2 min). Following the 0.05 μm polish, the Au disk was removed from the holder and placed in a 15 mL Falcon tube, to which was added ~2 mL of 50:50 Milli-Q water:acetone by volume. The disk was sonicated using a VWR Symphony™ (97043-992; 90 W, 35 kHz) Ultrasonic Cleaner in the water/acetone mixture for at least 2 minutes, then the water/acetone mixture was decanted, more 50:50 water:acetone was added, and one more sonication cycle of 2+ minutes was initiated. At this point the Au disk was retrieved and inserted into the RDE assembly with Kimwipes and relatively clean gloves.

Finally, the Au disk was electro-polished by inserting the RDE into a beaker cell (10 mL beaker volume) containing ~1 mL of 0.1 M H_2SO_4 and running a 200x cycled oxidative CV between 0 and +1.800 V vs. the counter electrode at a scan rate of 1 V/sec. In this case the counter electrode was a Pt wire. The chosen voltage window was selected to correspond to roughly 0 to +1.700 V vs. SHE. The rotator was spun at a rotation rate of 600 rpm during these oxidative cycles. Following the completion of this 200x oxidative cycling in 0.1 M H_2SO_4, the working electrode was rinsed twice with Milli-Q water and any residual water remaining on the electrode was gently wicked away using a Kimwipe. At this point the disk was ready for use in an electrochemical experiment.

B.4.2 Platinum disk[41]

Pt disks were handled in a similar manner to Au disks, with the differences being:

- During sonication, a 50:50 v/v mixture of Milli-Q and ethanol was used, rather than 50:50 water:acetone.
- During electro-polishing, the H_2SO_4 electrolyte was 0.5 M H_2SO_4 rather than 0.1 M.

- Also during electro-polishing, the oxidation was split out into two steps, with replacement of the 0.5 M H_2SO_4 electrolyte in-between:
    1. 2-minute hold at +2.1 V vs. counter (est. +2.0 V vs. SHE)
    2. 10x CV from 0 to 1.40 V vs. counter (est. +1.35 V vs. SHE) at 50 mV/sec

B.5 Methods: Calibrating reference electrode

B.5.1 Calibrating vs. Master Ag/AgCl

Prior to most experiments, reference stability and drift were assessed by calibration versus a "Master" Ag/AgCl reference in saturated KCl. This Master was not used in electrochemical experiments, and was stored in saturated KCl in Milli-Q water. To calibrate, the Master reference and the leak-free Ag/AgCl reference being calibrated were placed in the same vial filled with saturated KCl. The reference being calibrated was hooked up as the Working Electrode, and the Master was hooked up as the Counter/Reference Electrode. OCV was then measured until drift over time had decreased substantially below 1 mV – often for around an hour. The final "plateau" OCV was recorded and used to gauge reference drift between experiments, correcting for small changes from run to run. For example: if a leak-free reference had been calibrated as +0.100 V vs. Master Ag/AgCl, and simultaneously +0.020 V vs. Me_{10}-Fc in the relevant solvent being tested, and then on a subsequent experiment the reference was measured to be +0.105 V vs. Master, then that reference was interpreted as representing +0.025 V vs. Me_{10}-Fc. Historical calibration data – with two or more ferrocene calibrations separated by multiple measurements of drift vs. a Master – corroborate the accuracy of this approach to drift correction.

B.5.2 Calibrating vs. ferrocene, decamethylferrocene

Reference electrodes were calibrated simultaneously versus both Fc and Me_{10}-Fc by preparing solutions that were roughly 2.5 mM in both redox standard species. Other than Fc/Me_{10}-Fc content, solutions were prepared to reflect the conditions (water content) of each HER water dependence test. The following table reflects the compositions of the 4-mL electrolytes used for calibration:

Table A-B2. Formulations of solutions used in Fc/Me_{10}-Fc calibrations.

Solution	0 M H_2O	0.5 M H_2O	1 M H_2O	2.5 M H_2O	5 M H_2O	6.6 M H_2O
$TBABF_4$ powder	1.0527 g (1.0537 g)	1.0214 g (1.0248 g)	1.0242 g (1.0248 g)	1.0252 g (1.0248 g)	1.0258 g (1.0248 g)	1.0253 g (1.0248 g)

100 mM Fc Stock	100 µL	100 µL	100 µL	100 µL	100 µL	100 µL
5 mM Me_{10}-Fc Stock	2 mL	2 mL	2 mL	2 mL	2 mL	2 mL
Milli-Q Water	--	--	36 µL	144 µL	324 µL	438 µL
Fresh ACN	846 µL	815 µL	779 µL	671 µL	491 µL	377 µL
40% (1.5 M) TBAOH	--	60.1 µL	60.1 µL	60.1 µL	60.1 µL	60.1 µL

Solutions were tested in a randomized order (achieved via an online random number generator). For each solution, ~2 mL was added to a 10 mL beaker containing a Pt wire that served as the counter electrode. The working electrode was a Pt RDE disk on the WaveVortex 10 rotator. This electrode had been rinsed with water and acetone prior to the experiment, and dried of all solvent prior to insertion into the electrolyte being tested. During the experiment, the rotator was spun at a rotation rate of 900 rpm.

To ascertain the potential of the reference electrode versus the redox of Fc and Me_{10}-Fc species in solution, square wave voltammetry (SWV) was used. The SWV started with an initial oxidative pre-hold on the working electrode at 0 V vs. Ag/AgCl for 20 seconds, followed by a scan down to roughly -0.300 V vs. Ag/AgCl, and then a return to the initial potential of 0 V vs. Ag/AgCl. This was repeated twice, once with an initial hold at the reductive potential (-0.300 V vs. Ag/AgCl), and again with an initial hold at the oxidative potential (0 V vs. Ag/AgCl). Because the cleanest data was obtained for the first scan, only results from the first SWV for each composition is reported here. In these tests, the pulse height was 50 mV; pulse width was 100 ms; step height was (+/-)1 mV; and *I* was averaged over the last 20% of the step. The potentiostat Erange was -1 – 1 V, Irange 10 mA, and bandwidth medium. Note the SWV voltage window was shifted as necessary to contain peaks for both the Fc and Me_{10}-Fc redox events in any given electrolyte. In addition, 85% software IR correction was implemented during the experiment.

Potentials were determined by identifying the peak potential on a plot of I_{delta} vs. E_{step}, and averaging the peaks in the oxidative and reductive directions.

It should be noted that for lower water content (0 - 1 M water), stable measurements past the initial SWV were difficult, so for each experiment (including those at higher water content, for consistency) only the first SWV was used for peak-potential-averaging.

Following each electrolyte measurement, the electrolyte was removed and discarded, and the working electrode and rotator were rinsed with acetone and Milli-Q water, while the beaker cell and counter electrode were rinsed with dry acetonitrile. Trace acetonitrile was removed from the beaker cell, and then the next electrolyte in the sequence was inserted and tested.

The following figures show results of this calibration.

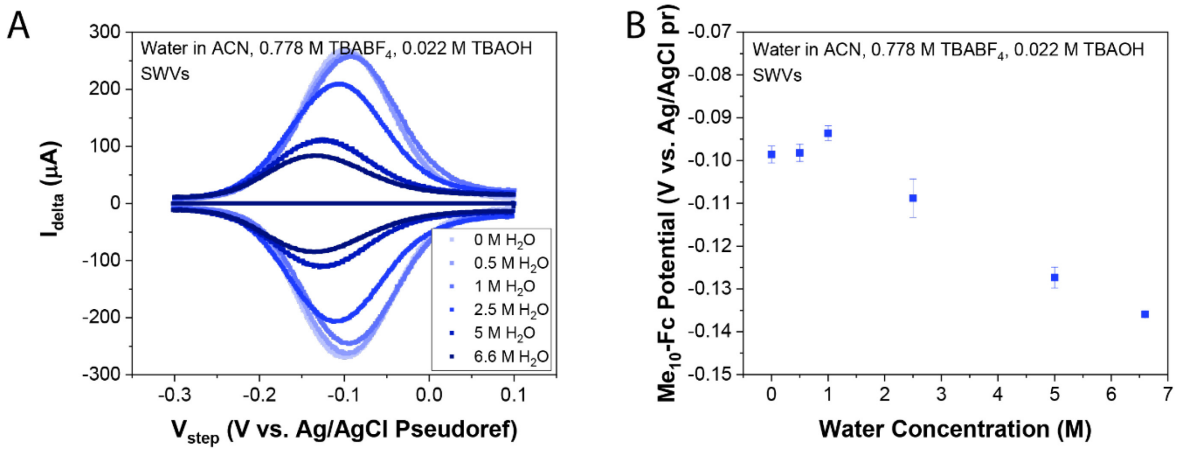

Figure A-B5. Me_{10}-Fc calibration in alkaline ACN electrolyte. Note that Fc was more difficult to calibrate in base due to overlapping OER / other pH-sensitive oxidative chemistries. A) Raw data from Me_{10}-Fc calibrations across water content. Darker lines correspond to higher water content. Note the decreasing solubility of Me_{10}-Fc is reflected by the decrease in SWV peak height with increasing water content. B) Me_{10}-Fc calibration data.

In addition, calibrations were also conducted in neutral electrolytes consisting of ACN, water, and 0.8 M $TBABF_4$ in the absence of TBAOH. Slightly different SWV settings were used for these scans (voltage window +0.700 V vs. Ref – -0.300 V vs. Ref, pulse height 25 mV, pulse width 50 ms, step height (+/-)2 mV, E range -2 – 2 V). These neutral calibrations yielded similar results to those in base. Note the shifting of the leak-free Ag/AgCl pseudoreference electrode over time led to a shift in the y-axis that is not reflective of thermodynamic shifts between the alkaline and neutral conditions, but rather of changes in the pseudoreference itself in the weeks/months between the neutral and alkaline tests.

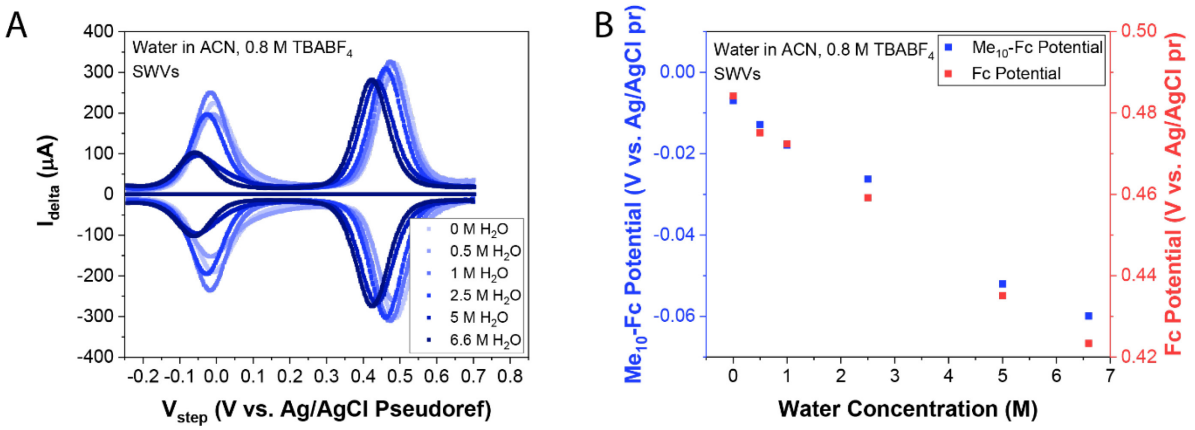

Figure A-B6. Simultaneous Me_{10}-Fc and Fc calibration in neutral ACN electrolyte. A) Raw data from Fc/Me_{10}-Fc calibrations across water content. Darker lines correspond to higher water content. B) Fc/Me_{10}-Fc calibration data. Note that there is a similar shift in both Fc and Me_{10}-Fc vs. the Ag/AgCl pseudoreference.

B.6 Methods: Headspace-GC-TCD

Species thermodynamic activities were measured by sampling from the headspace of vials containing electrolyte with a specified water content. This was achieved using an Agilent 7890B GC with 7890A Thermal Conductivity Detector and attached 12-vial 7697A Headspace Sampler. These experiments can be broken down into two components: 1) sample preparation and equilibration, and 2) sampling and detection.

B.6.1 Sample preparation & equilibration

Electrolyte samples were prepared in 20 mL headspace vials, with liquid sample volumes of 4 mL. Sample formulation was according to the following table:

Table A-B3. Formulations of 4-mL basic electrolytes for headspace sampling.

Solution	0 M H_2O	0.5 M H_2O	1 M H_2O	2.5 M H_2O	5 M H_2O	6.6 M H_2O	Sat'd H_2O
Volume Water	--	--	36 µL	144 µL	324 µL	438 µL	600 µL
Volume TBAOH	--	60.1 µL	60.1 µL	60.1 µL	60.1 µL	60.1 µL	60.1 µL
Volume Fresh ACN	800 µL	829 µL	793 µL	685 µL	505 µL	391 µL	229 µL
Volume 1.0 M TBA/ACN	3.2 mL	3.11 mL	3.11 mL	3.11 mL	3.11 mL	3.11 mL	3.11 mL

It should be noted that these samples included two conditions – 0 M and saturated (~8.3 M) water – which did not represent electrolysis conditions, but rather served as the endpoints on the concentration-activity relationship, including a "blank" measurement.

For each sample, the vial for the sample was first stored overnight in an 80 °C oven to fully dry the glass and remove any adventitious water. The vial was then rapidly cooled to room temperature by air-cooling in a snorkel vent, and the sample components were added to the vial via pipette. The vial was then sealed with a Silver Aluminum 20 mm headspace crimp cap with PTFE/silicone stopper. Sealing was done using an Agilent manual crimper for 20 mm caps. The seal was such that the cap did not easily rotate on the vial when twisted, but the cap was also not visibly deformed around the stopper due to over-tightening. 3 sets of samples were prepared in this manner. Within each set, samples were prepared in a randomized order, specified by an online random number generator.

In addition to all electrolyte samples, a pure-water reference sample was prepared for each sample – with the intention being that a reference could be gathered before and after each electrolyte sample, providing a standard for water activity = 1 at every time point, i.e. at every value of room temperature.

After sealing, each sample was equilibrated at room temperature (~23 °C) for at least 12 hours. This threshold is supported by equilibration tests on electrolytes containing only water (see below). Water peak area reached its equilibrium value by roughly t = 8 hours.

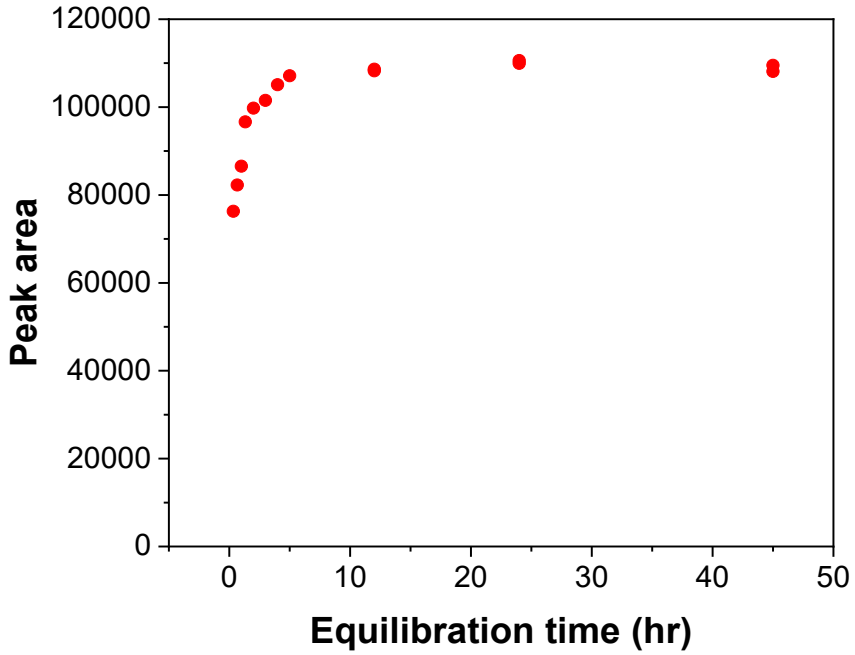

Figure A-B7. Time-dependence of vapor-liquid equilibrium for electrolyte headspace tests. Samples are pure water.

B.6.2 Sampling & detection

After samples were sufficiently equilibrated, they were submitted to the Agilent 7697A headspace unit carousel for auto-sampling. A pure water sample was included prior to every electrolyte sample (i.e. pure water vial 1 → sample 1 → pure water vial 2 → sample 2 → pure water vial 3 → …), and electrolyte vials within each set were sampled in a randomized order, specified by an online random number generator. Once a vial cap was pierced, the sample was considered no longer usable (i.e., no vials were double-sampled).

The trajectory of each sample, including temperatures of components, was as follows:

1. On its turn, the sample vial was inserted into the oven of the headspace sampling unit, which did not have an active setpoint and measured T ~ 24-26 °C during tests. Vial remained in the oven for 9 seconds prior to sampling.
2. The headspace autosampler needle punctured the vial cap and began pressurizing the sample with helium, the carrier gas. The injection duration was set to 30 seconds.
3. The He-carried sample was withdrawn into a sample loop, which was kept at the lowest possible set point of 35 °C.

4. The sample was sent through a heated transfer line leading from the headspace unit to the GC. The transfer line was heated at 50 °C.
5. The sample entered the GC at the Front Inlet, which was held at 280 °C.
6. The sample passed through an Agilent DB-624UI column (30 m length, 0.32 mm diameter, 1.80 u) with the following temperature profile:
    - 1-minute hold at 35 °C
    - 4-minute ramp at 20 °C/min to final temp of 115 °C
    - 1-minute hold at 115 °C
7. The sample was finally detected at an Agilent 7890A Thermal Conductivity Detector (TCD).

Following sample processing, TCD results were plotted and water peaks integrated. The peak area of the pure water reference prior to each sample was used as the standard for activity = 1. That is, this area was the denominator in the calculation:

$$a_{water,sample} = \frac{A_{water\ peak.sample}}{A_{water\ peak,reference}}$$

where a represents species activity and A represents peak area. The following is a representative TCD spectrum for a blended electrolyte sample.

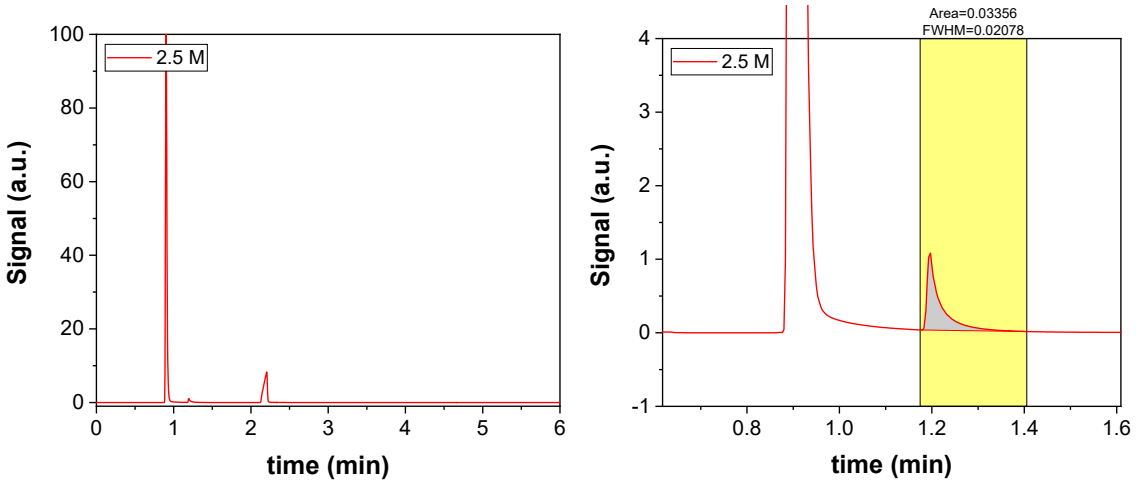

Figure A-B8. Full and zoomed-in TCD spectra for a representative headspace sample of 2.5 M water in ACN with 0.778 M $TBABF_4$ and 0.022 M TBAOH. The first peak (~0.9 min) is air; the second, small peak (~1.2 min) is water; and the final peak (~2.1 min) is acetonitrile.

This method for determining activities was validated using a binary ethanol (EtOH) / isopropanol (IPA) system of varying compositions. The activity coefficient of each species in this mixture is predicted to deviate minimally from unity – up to about $\gamma_{IPA} = 1.015$ for dilute

IPA and γ_{EtOH} = 1.013 for dilute EtOH (using PSRK). That is, the relationship between mole fraction and activity should be roughly a straight line for each species, exhibiting ideality in the Raoult's Law sense. This was observed experimentally, suggesting the quantification method itself does not interfere with the activity measurements. (Figure A-B9)

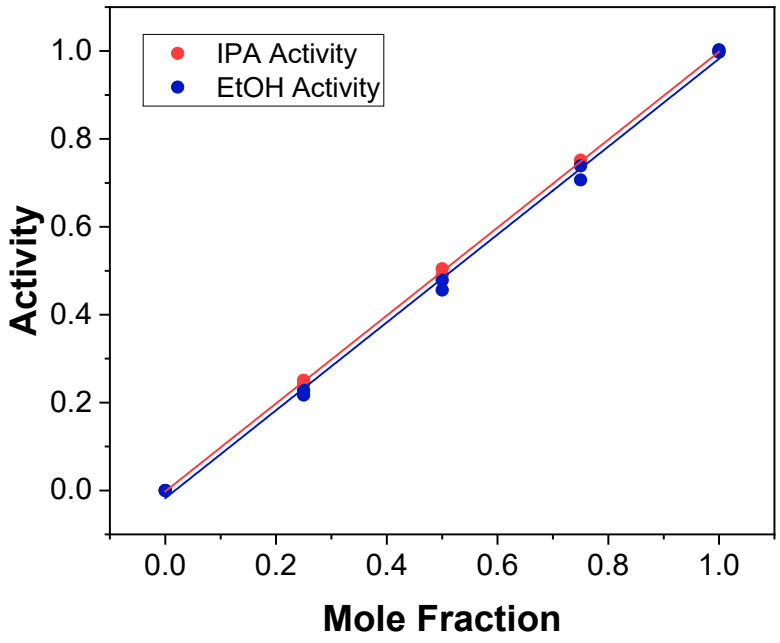

Figure A-B9. Measured activity-concentration relationship for a binary mixture of ethanol (blue) and isopropanol (red).

B.7 Methods: Linear regression

Most of the linear regression performed in this work was carried out in Origin 2018b. Y-errors were incorporated into the fits in this software where applicable. Instrumental weighting was used for errors, and error was scaled with sqrt(reduced chi-squared). Fit parameters are reported with 95% confidence intervals.

Specifically for data containing both x- and y-errors, namely the water dependence data from main text Figure 2C, a Matlab script by Wiens employing the methods of York et al. was utilized.[219,220]

B.8 Raw data from main-text figures

Fig 2A: Water concentration-activity relationship for HER electrolyte

Water Concentration (M)	Activity 1	Activity 2	Activity 3	Avg Activity
0	0	0	0	0
0.5	0.12622	0.12193	0.09097	0.11304 ± 0.01570
1	0.26031	0.18365	0.27076	0.23824 ± 0.03884
2.5	0.61005	0.42509	0.57317	0.53610 ± 0.07993
5	0.77496	0.5697	0.64987	0.66484 ± 0.08446
6.6	0.86044	0.87173	0.72846	0.82021 ± 0.06504
8.2	0.99346	0.94075	0.99195	0.97539 ± 0.02450
55.5	1	1	1	1

Fig 2C: Water dependence of HER at -1.875 V vs. Me_{10}-Fc

Concen-tration H_2O (M)	log (c_{H2O} / M)	Activity H_2O	log (a_{H2O})	Error in log (a_{H2O})	Current density / mA cm^{-2}	log (Current density / mA cm^{-2})	Error in log (i / mA cm^{-2})
0.5	-0.30103	0.11304	-0.94677	-: -0.065 +: 0.056	-3.60E-01	-0.44399	-: -0.009 +: 0.009
1	0	0.23824	-0.62299	-: -0.077 +: 0.066	-2.32E+00	0.36495	-: -0.011 +: 0.010
2.5	0.39794	0.5361	-0.27075	-: -0.07 +: 0.060	-1.77E+01	1.24868	-: -0.023 +: 0.014
5	0.69897	0.66484	-0.17728	-: -0.059 +: 0.052	-5.06E+01	1.70408	-: -0.009 +: 0.007
6.6	0.819544	0.82021	-0.08607	-: -0.036 +: 0.033	-6.43E+01	1.80819	-: 0.001 +: 0.005

Note: the 0.5 M data point of this data set was not fit in Figure 2C because the measured partial current was determined to be too low to yield a reliable measure for HER.

See below for more details on error estimation.

Fig 4A: Water concentration-activity relationship for epoxidation electrolyte

Water Concentration (M)	Activity 1	Activity 2	Activity 3	Avg Activity
0	0	0	0	0
0.5	0.18532	0.18596	0.1971	0.18946 ± 0.00541
1	0.28558	0.31913	0.31963	0.30811 ± 0.01593
2	0.49606	0.54726	0.52185	0.52172 ± 0.02090
5	0.79107	0.85994	0.86597	0.83899 ± 0.03398
10	0.92543	0.9786	0.97072	0.95825 ± 0.02343
12.5	0.91607	0.95618	0.95348	0.94191 ± 0.01830
15	0.94637	0.99434	1.02212	0.98761 ± 0.03129
55.5	1	1	1	1

Fig 4B: Water concentration-activity relationship for lactonization electrolyte

Water Concentration (M)	Activity 1	Activity 2	Activity 3	Avg Activity
0	0	0	0	0
0.5	0.15441	0.15101	0.15518	0.15353 ± 0.00181
0.7	0.19631	0.20098	0.20607	0.20112 ± 0.00399
1	0.25538	0.3077	0.25893	0.27400 ± 0.02387
1.5	0.35674	0.3458	0.42429	0.37561 ± 0.03471
2	0.41419	0.41277	0.53932	0.45543 ± 0.05932
5	0.61013	0.78799	0.58197	0.66003 ± 0.09121
10	0.88726	1.01342	0.99859	0.96642 ± 0.05630
55.5	1	1	1	1

Fig 4C: Water dependence of cyclooctene epoxidation at 1.45 V vs. Fc

Concentration H_2O (M)	log (c_{H2O} / M)	Activity H_2O	log (a_{H2O})	log (Current density / A cm^{-2})	Error in log (i / A cm^{-2})
0.5	-0.30103	0.18946	-0.72248	-3.30549	0.16001
1	0	0.30811	-0.51129	-3.00145	0.01172
2	0.30103	0.52172	-0.28256	-2.70984	0.05482
5	0.69897	0.83899	-0.07624	-2.50142	0.0334
10	1	0.95825	-0.01852	-2.62897	0.04864
12.5	1.09691	0.94191	-0.02599	-2.64739	0.03956
15	1.17609	0.98761	-0.00541	-2.73304	0.08898

Fig 4D: Water dependence of cyclohexanone lactonization

Concentration H_2O (M)	log (c_{H2O} / M)	Activity H_2O	log (a_{H2O})	log (Current density / A cm^{-2})
0.5	-0.30103	0.15353	-0.8138	-3.50516
0.7	-0.1549	0.20112	-0.69654	-3.27263
1	0	0.27400	-0.56224	-3.0002
1.5	0.17609	0.37561	-0.42526	-2.85696
2	0.30103	0.45543	-0.34158	-2.59061
2	0.30103	0.45543	-0.34158	-2.69673
5	0.69897	0.66003	-0.18044	-2.49055
10	1	0.96642	-0.01483	-2.45865
10	1	0.96642	-0.01483	-2.45347

B.9 Discussion: Measured activity curves overlaid on one another

In order to compare the behavior of water in the blended electrolyte at varying $TBABF_4$ contents, activity measurements from the various electrolytes reported here – 800 mM $TBABF_4$, 350 mM $TBABF_4$ + 400 mM cyclohexanone, ~100 mM $TBABF_4$ + 200 mM cyclooctene, as well as the binary water/acetonitrile mixture (0 mM $TBABF_4$) – were overlaid on the same plot. (Figure A-B10) Note that for the purposes of this analysis, we will ignore the small amount of organic substrate in the 350 mM and 100 mM $TBABF_4$ samples; however, a more complete comparison could be drawn by removing these substrates.

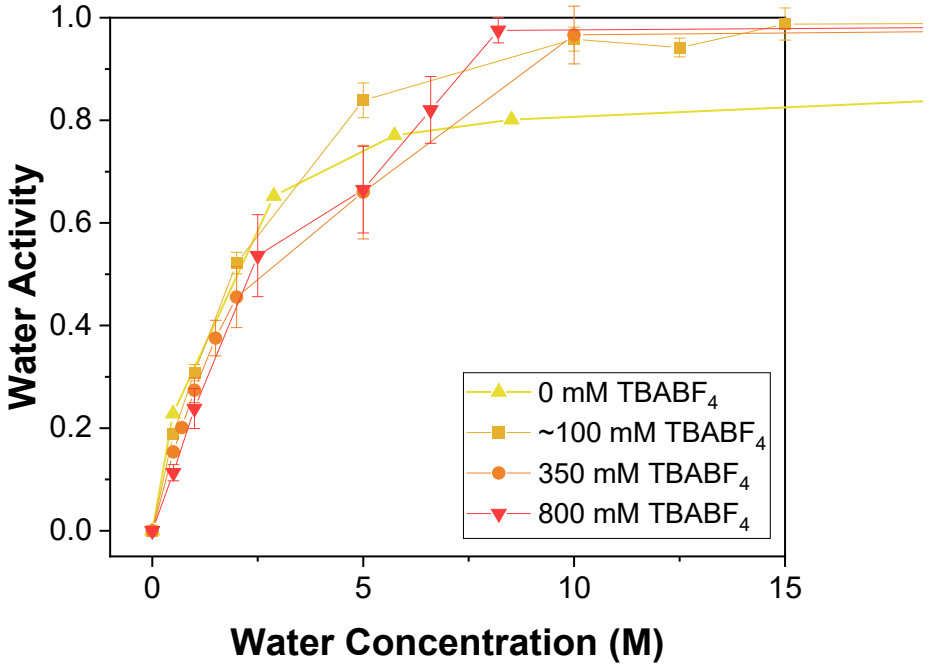

Figure A-B10. Overlay of four activity-concentration data sets: binary water/acetonitrile as reported in literature[149,150] (yellow), acetonitrile/water + ~100 mM $TBABF_4$ + 200 mM cyclooctene (light orange), acetonitrile/water + 350 mM $TBABF_4$ + 400 mM cyclohexanone (dark orange), and acetonitrile/water + 800 mM $TBABF_4$ (red).

As mentioned in the main text, the activity of water reaches unity at much lower concentrations for higher $TBABF_4$ content. This is because unfavorable interactions with the highly hydrophobic TBA^+ cation increase water activity, leading to phase separation at lower water concentrations with increasing TBA^+ content. However, there is a markedly different trend at lower water concentrations. Zooming in… (Figure A-B11)

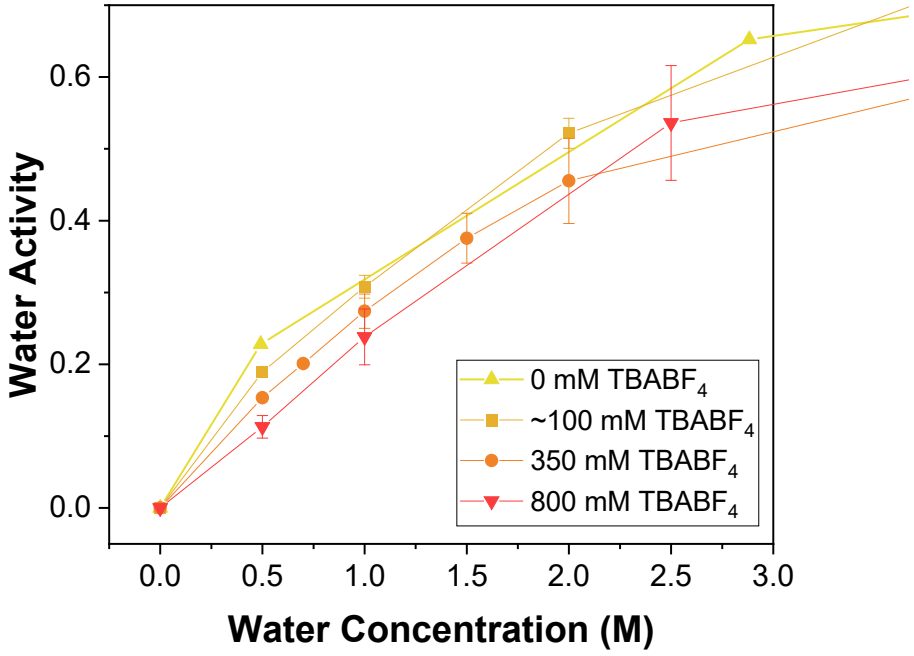

Figure A-B11. Zoomed-in water concentration-activity relationships in acetonitrile with varying $TBABF_4$ content.

We can observe that at low water concentrations, the trend reverses: water activity at a given concentration of water is measured to be higher at lower concentrations of $TBABF_4$. This could be due to a number of factors: for instance, perhaps favorable interactions with the BF_4^- ion stabilize water at these low concentrations. Perhaps trace halogens or other salt impurities in the $TBABF_4$ play a larger role in coordinating water at these low concentrations. These are hypotheses we will seek to test in future work.

B.10 Discussion: Faradaic efficiency of HER

Due to the incomplete sealing of the H-cell setup used in experiments, it was not possible to quantify HER during most of the electrochemical tests reported here. However, constant-potential holds in sandwich cell setups connected to a gas chromatograph confirm 100% Faradaic efficiency (FE) for HER at moderate currents (~0.1 – 10 mA). This is corroborated by results detailed in previous O-atom transfer works.[71,72]

The primary difference between the system used for FE closure analysis and the system used for kinetic analysis in this work, in terms of variables that may affect FE, is that the kinetic analysis setup cannot be fully sealed. Because the tests are not conducted in a glovebox,

glovebag, or other rigorously controlled atmosphere outside of the cell, it is necessary to purge an inert gas through the working compartment in order to remove dissolved O_2. When O_2 is present, background ORR current artificially inflates the measured current by a small amount (~0.2 mA). Further discussion on how this current was controlled and eliminated can be found below. (See Discussion: Experimental troubleshooting & minimizing background current.)

B.11 Reference: Volmer, Tafel, and Heyrovsky steps

The most common named microkinetic reaction steps in the HER/HOR couple reaction pathway are as follows (shown here in the alkaline case):

Volmer step: $$H_2O + * + e^- \rightleftharpoons H^* + OH^-$$

Heyrovsky step: $$H^* + H_2O + e^- \rightleftharpoons H_2 + OH^- + *$$

Tafel step: $$2H^* \rightleftharpoons H_2 + 2*$$

B.12 Discussion: TST reaction rate expression formulation

Here we will explain the derivation of the rate expression for a reaction based on Transition State Theory – motivating our use of the term "activity" in the discussion, rather than "chemical potential," despite the fact that these two quantities are directly related. Many thanks to Thejas Wesley for contributing the following distinction.

To begin, we write classical transition state theory rate expressions for an arbitrary elementary surface reaction – noting of course that this would also apply to reactions not taking place at surfaces, just with different notation:

$$\alpha A + \beta B + \cdots \rightarrow [TS]$$

$$r = \frac{k_B T}{h}\theta_{\ddagger} \qquad \text{(Eq. 1)}$$

$$K_{eq}^{\ddagger} = \exp\left(\frac{-\Delta G^{0\ddagger}}{RT}\right) = \frac{\gamma_{\ddagger}\theta_{\ddagger}}{\prod_j a_j^{\nu_j}}$$

$$\Rightarrow \theta_{\ddagger}(\{a_j\}) = \exp\left(\frac{-\Delta G^{0\ddagger}}{RT}\right)\frac{1}{\gamma_{\ddagger}}\prod_j a_j^{\nu_j} \qquad \text{(Eq. 2)}$$

where $\{\nu_j\} = \{\alpha, \beta, \ldots\} > 0$ are (absolute value) stoichiometric coefficients of reactants {A,B,…} moving into the transition state, a_j is the thermodynamic activity of species *j*, $\gamma_{\ddagger}$ is the activity coefficient of the adsorbed transition state, and $\Delta G^{0\ddagger}$ is the *standard state* activation free energy:

$$\Delta G^{0\ddagger} = \mu_{\ddagger}^{0} - \sum_{j} \nu_j \mu_j^{0}$$

where μ_j^0 is the standard state chemical potential of species j.

Bringing the product into the exponential,

$$\Rightarrow \theta_{\ddagger}(\{a_j\}) = \exp\left(\frac{-\Delta G^{0\ddagger} + RT\sum_j \nu_j \ln a_j}{RT}\right)\frac{1}{\gamma_{\ddagger}}$$

we can then substitute for $\Delta G^{0\ddagger}$ using the expression above,

$$\theta_{\ddagger}(\{a_j\}) = \exp\left(\frac{-\left(\mu_{\ddagger}^{0} - \sum_j \nu_j \mu_j^{0}\right) + RT\sum_j \nu_j \ln a_j}{RT}\right)\frac{1}{\gamma_{\ddagger}}$$

and from here we can combine the sums,

$$\theta_{\ddagger}(\{a_j\}) = \exp\left(\frac{-[\mu_{\ddagger}^{0} - \sum_j \nu_j (\mu_j^{0} + RT\ln a_j)]}{RT}\right)\frac{1}{\gamma_{\ddagger}}$$

at which point we recognize a common definition for chemical potential: $\mu_j = \mu_j^0 + RT\ln a_j$. Substituting this in the expression, we get

$$\theta_{\ddagger}(\{\mu_j\}) = \exp\left(\frac{-[\mu_{\ddagger}^{0} - \sum_j \nu_j \mu_j]}{RT}\right)\frac{1}{\gamma_{\ddagger}}$$

And finally, we combine the numerator in the exponential into $\Delta G^{\ddagger} = \mu_{\ddagger}^{0} - \sum_j \nu_j \mu_j$, which is the free energy change going from the actual solution species to the (standard state of the) transition state:

$$\theta_{\ddagger}(\{\mu_j\}) = \exp\left(\frac{-\Delta G^{\ddagger}}{RT}\right)\frac{1}{\gamma_{\ddagger}} \qquad \text{(Eq. 3)}$$

Combining Eq. 1 and 2, the rate may be written as:

$$r = \frac{k_B T}{h}\theta_{\ddagger} = \frac{k_B T}{h}\exp\left(\frac{-\Delta G^{0\ddagger}}{RT}\right)\frac{1}{\gamma_{\ddagger}}\prod_j a_j^{\nu_j} = r(\{a_j\}) \qquad \text{(Eq. 4)}$$

But instead combining Eq. 1 and 3, it may instead be equivalently written as

$$r = \frac{k_B T}{h}\theta_{\ddagger} = \frac{k_B T}{h}\exp\left(\frac{-\Delta G^{\ddagger}}{RT}\right)\frac{1}{\gamma_{\ddagger}} = r(\{\mu_j\}) \qquad \text{(Eq. 5)}$$

Eq. 4 and 5 are identical, but simply in different notation: using the activity form (Eq. 4) implies that the free energy used in the rate constant is based on the chemical potential of the fluid species at the standard state; however, using (Eq. 5) implies that the free energy used in the

rate constant is based on the chemical potential of the fluid species at the real concentrations/partial pressures in the reactor.

Eq. 4 is the more familiar formalism, common throughout thermal catalysis literature, and which we employ in the context of this work. This is why we use the term “activity” rather than “chemical potential” throughout the main text.

B.12.1 A note on “hot” reactants and other thermodynamic exceptions

While in this instance we hold activity to be the best descriptor of reaction rate, there are cases in which reacting species’ thermodynamic activities are not always the best descriptors of reaction rate. An example discussed in the main text is the previously-reported “fortuitous cancellation” of activity coefficients of the reactant and transition state species.[148] In this case the best variable for describing reaction rate comes out to be reactant concentration rather than activity. Similarly, reactions which are “activationless” or “barrierless”[221] – in certain cases, involving species so reactive that they instantly react upon collision with essentially 100% probability – may be limited by collisions and therefore also dependent upon reactant concentration. Another example of activity not being the best descriptor is in the literature of “hot” reactants – that is to say, species which react while they are not yet at thermodynamic equilibrium with the surface.[222] Reactants impinging upon a surface or entering from the subsurface carry with them energy – in many cases, translational energy – that has not yet been dissipated as the species come into equilibrium with the surface at hand. This extra energy can be used to overcome activation barriers, thereby yielding different reaction rates than might be expected from the thermodynamics of the reactants and surface alone. In these senses, reactant activity is not always a good descriptor of rate.

B.13 Discussion: HER on Pt cathode

In addition to the HER experiments reported in the main text, we also conducted HER on a Pt cathode, in accordance with the methods reported above (see Methods: Preparation of RDE working electrodes: 2. Platinum disk[41]). The results of these experiments are shown below. (Figure A-B12)

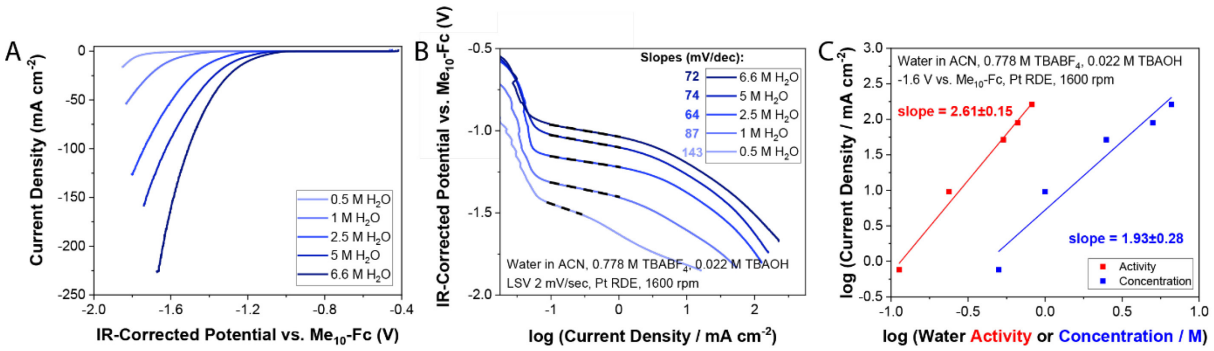

Figure A-B12. HER on Pt at various concentrations of water in acetonitrile + 0.778 M $TBABF_4$ + 0.022 M TBAOH. A) Raw LSV data plotted vs. Me_{10}-Fc. B) The same data visualized on a Tafel plot. C) Water dependence of HER on Pt at a -1.6 V vs. Me_{10}-Fc.

As expected, Pt catalyzes HER in the blended electrolyte at much less reductive potentials than required by Au for similar rates. In addition, once onset occurs, the Tafel slope is lower for Pt than for Au, meaning the current responds more strongly to applied voltage. It may be noted that the reported Tafel slopes increase with decreasing concentrations of water, similar to what was noted in the main text. From 6.6 M water down to 2.5 M water, the measured Tafel slope is between 64-74 mV/dec, which is consistent with a RDS in which no ET is involved, but rather there is a pre-equilibrated ET step. (see Reference: Tafel slopes) At 1 M water, the Tafel slope increases to 87, and at 0.5 M water, the slope increases further to 143 mV/dec. There could be a variety of factors leading to an increase in Tafel slope across this range, similar to the increase reported in the main text – however, because the swing in slopes is so large that it could be partially attributed to a changing mechanism (i.e. cardinal "60 mV/dec" slope -> cardinal "120 mV/dec" slope), we elected to focus instead on results obtained on Au, where the direct mechanism is less likely to be changing as conditions are altered.

It is notable, however, that water dependences in the case of both Au and Pt (with potentials referenced to Me_{10}-Fc) are measured to be between 2.5-3. This may suggest that the measured water order in fact has little to do with surface catalytic phenomena at all.

B.14 Reference: Tafel slopes

As a reminder, the general form taken by a Tafel slope at standard conditions is:

$$m_T = \frac{59\ mV/dec}{n + \beta q}$$

where m_T is the Tafel slope, n is the number of electrons transferred prior to the RDS, q is the number of electrons transferred during the RDS, and β is the symmetry factor, often assumed to be 0.5. This latter assumption is supported by historical measurements of acidic HER kinetics on Pt,[223] although the symmetry factor (or at least the transfer coefficient α as the experimentally measurable parameter) can change with electrolyte composition,[224] and apparent β from literature measurements on Au[157] can be calculated to be anywhere between 0.37-0.57. Assuming β is 0.5, some examples of cardinal values of Tafel slopes would be:

- 120 mV/dec: $n = 0$, $q = 1$, $\beta = 0.5$ (initial electron transfer RDS)
    - e.g., the Volmer step
- 60 mV/dec: $n = 1$, $q = 0$ (subsequent chemical step RDS)
- 40 mV/dec: $n = 1$, $q = 1$, $\beta = 0.5$ (second electron transfer RDS)
    - e.g., the Heyrovsky step
- 30 mV/dec: $n = 2$, $q = 0$ (subsequent chemical step RDS)
    - e.g., the Tafel step

As previously reported, these cardinal values can be altered by a wide variety of phenomena in an electrocatalytic system, and are not necessarily expected to be observed in actual measurements.[158]

B.15 Discussion: Confirming lack of transport limitations in RDE measurements

The lack of limitations due to diffusional mass transport through the electrolyte was confirmed by varying the rotation rate of the RDE during LSV experiments. The Tafel plots for these experiments are shown below. Note that in general there is no monotonic trend in Tafel slope as rotation rate is increased/decreased, and in fact experiments conducted at 900 RPM, 1600 RPM, and 2500 RPM all yield similar Tafel slopes within the same fit region and similar currents at the same potential. These results serve to quell concerns that slow H_2 transport away from the electrode surface in particular leads to lower HER rates.[225]

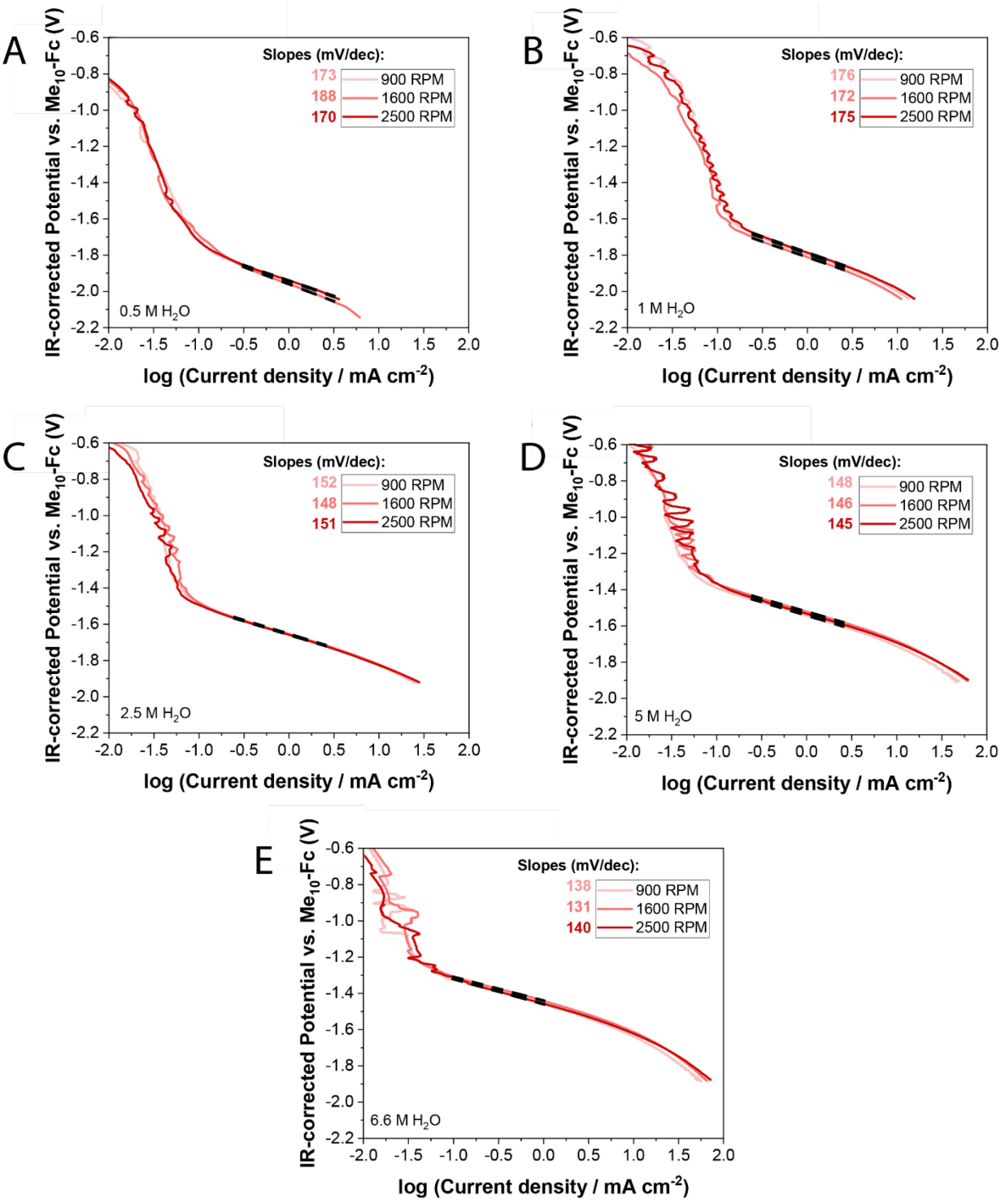

Figure A-B13. Rotation rate dependences for HER shown via Tafel plots taken at 900, 1600, and 2500 RPM. (Order: 1600 – 900 – 2500.) Electrolytes contained acetonitrile, 0.778 M $TBABF_4$, 0.022 M TBAOH, and: A) 0.5 M water, B) 1 M water, C) 2.5 M water, D) 5 M water, and F) 6.6 M water.

B.16 Discussion: ET potential scales versus CPET potential scales (Measurement of RHE in blended electrolyte)

As mentioned in the main text, the reference potential for reported data is the redox potential of Me_{10}-Fc, the oxidation and reduction of which involves only the transfer of electrons to the Fe center. However, because the rate-determining step of HER involves a proton transfer, the energetics of the proton in solution will also impact the reversible potential for HER, which is definitionally the reversible hydrogen electrode, RHE. The thermodynamics of protons in the blended electrolyte are subject to change alongside alterations in water composition. Here we detail our accounting for the changing thermodynamics of proton transfer with blended electrolyte composition through the direct measurement of RHE in those electrolytes.

A method to measure RHE in any electrolyte has been reported in the literature[141] and has also been extended to apply to the determination of the potential of H-atom transfer reactions.[153,154] In short, the method involves measuring the OCV of a clean Pt electrode in the electrolyte of interest versus a pseudoreference electrode while simultaneously flowing H_2 gas to saturate the electrolyte. As long as the electrolyte contains some reasonably labile proton, HER/HOR is the most facile reaction on a clean Pt surface, having the largest exchange current density i_0. Because of this, the potential of the Pt electrode is defined by that equilibrium. By subsequently measuring the potential of the pseudoreference electrode versus Fc or Me_{10}-Fc, it is then possible to define RHE vs. that ET reference, which can in turn be referenced in electrochemical experiments.

We employed this OCV measurement for the determination of RHE in the blended electrolytes of interest, with some notable changes to procedure. The main difference was in the preparation of the Pt electrode. Rather than H_2 flame-annealing a Pt wire that was then handled under H_2 and/or N_2 atmospheres prior to the experiment, we elected to use the same Pt disk employed in HER experiments and apply the same preparation procedures as for those tests. (see Methods: Preparation of RDE working electrodes: 2. Platinum disk[41]) The reasoning behind this was that it should be much more likely for condensed-phase species such as acetonitrile and tetrabutylammonium to poison the Pt surface than for gas-phase species such as O_2 or trace contaminants in the air to do so – and the Pt must be exposed to the condensed-phase species regardless. Moreover, we have evidence that the preparation procedures employed in this work have been sufficient to observe H_{UPD} peaks on cyclic voltammograms of Pt in aqueous electrolytes, and to our understanding, these are more sensitive measurements than the OCV measurements we are attempting here. In order to test this hypothesis that micropolishing +

sonication + electro-oxidative treatment in H_2SO_4 was sufficient to clean the Pt for OCV measurements, we used this preparation procedure and measured the OCV of the Pt versus our pseudoreference in two aqueous solutions: one at pH 1 (0.09167 M H_2SO_4), and one at pH 13 (0.1 M KOH). Note the molarity of H_2SO_4 required for a solution of pH = 1 was calculated by assuming full dissociation of the first proton and a $pK_{a,2}$ of 2. The results of two representative OCV measurements are shown here.

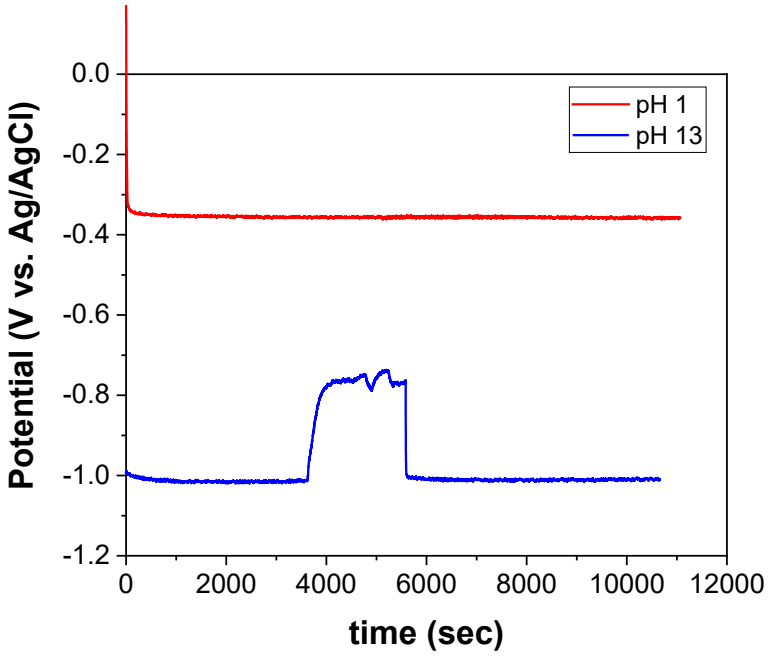

Figure A-B14. OCV measurements of Pt electrodes versus Ag/AgCl pseudoreference in a pH 1 electrolyte (red) and a pH 13 electrolyte (blue). The bump from t = 3600 sec to t = 5580 sec corresponds to when the working electrode was rotated at 1600 RPM.

During the OCV measurements of the aqueous solutions, we monitored the OCV over the course of about 3 hours. For a majority of this time, the RDE setup was allowed to sit still, not rotating, with a direct H_2 purge of 20 sccm into the working electrolyte and a parafilm seal around the top of the H-cell used for the measurements. However, the effect of rotation was also tested. The RDE was rotated at a rate of 1600 RPM from t = 5100 sec (1.42 hr) to t = 7620 (2.12 hr) in the pH 1 case, and from t = 3600 sec (1 hr) to t = 5580 sec (1.55 hr) in the pH 13 case. From Figure A-B14, we can see that there was minimal effect of rotation on the measured OCV in the pH 1 case, whereas the measured potential in the pH 13 case increased markedly with working electrode rotation.

The fact that stirring impacted the OCV measurement was at first a bit concerning to us. However, upon closer examination, we noted that other changes to the system could also induce

increases in the measured OCV, such as the removal of the loose parafilm seal or the adjustment of the position of the H_2 purge line. We hypothesize that these adjustments actually led to an increase in the dissolved O_2 content, which in turn led the OCV to be defined by a mixed potential involving both HER/HOR and OER/ORR. This effect was only observed in alkaline conditions because HER/HOR is kinetically more difficult in base than in acid, whereas OER/ORR is relatively more favored kinetically in base than in acid – essentially, the exchange current densities for the two couples became comparable in the alkaline condition. The key, then, was to ensure these measurements fully excluded O_2 to the best of our ability. By running the same OCV measurements in a sandwich cell setup where it was easier to seal against air while purging H_2, (Figure A-B15) we determined that the non-stirred condition in the H-cell setup was sufficient for excluding O_2, as the ΔOCV between pH 1 and pH 13 conditions was nearly identical. ($[OCV_{pH1} - OCV_{pH13}]_{sandwich}$ = 657.7 mV, while $[OCV_{pH1} - OCV_{pH13}]_{Hcell}$ = 658.7 mV. Note the theoretical value for this difference is roughly (12 pH)*(293 K/298 K)*(59 mV/pH) = 696 mV, implying a reasonable difference in junction potentials ΔV_{junct} of about 34-35 mV between acidic and alkaline conditions.

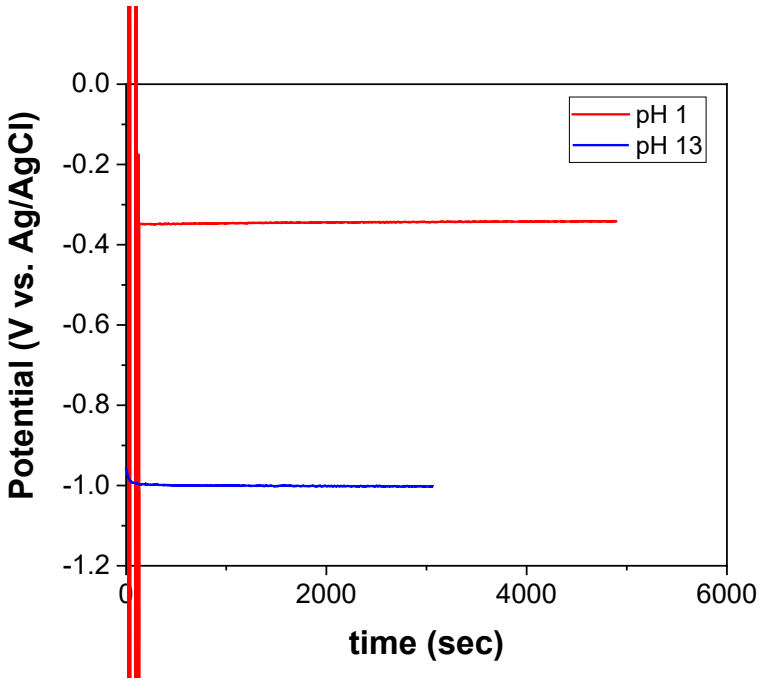

Figure A-B15. OCV measurements of Pt foil electrode versus Ag/AgCl pseudoreference for the aqueous pH 1 (red) and pH 13 (blue) electrolytes, conducted in a sandwich cell.

With our experimental conditions validated by the aqueous electrolytes, we used this procedure (Pt prep as above for RDE disk, no stirring, H_2 purge) to measure OCVs for the blended electrolytes. For each experiment, the OCV was first measured for at least 4 hours. This was

followed by a CV between 0 – -1.5 V vs. the pseudoreference, a short CA at -0.8 V, an LSV from +0.1 V vs. OCV to roughly -2 V vs. the pseudoreference, and a final OCV, in order to glean information on the overpotentials required for HER on the Pt working electrode and the OCV following a reductive hold. Steps after the first OCV were not strictly necessary. Following this final OCV, the pseudoreference was removed from the cell, quickly rinsed with acetone and water, transferred to a new sandwich cell, and immediately calibrated versus Fc in an electrolyte of composition corresponding to that of the OCV measurement. Results are shown below.

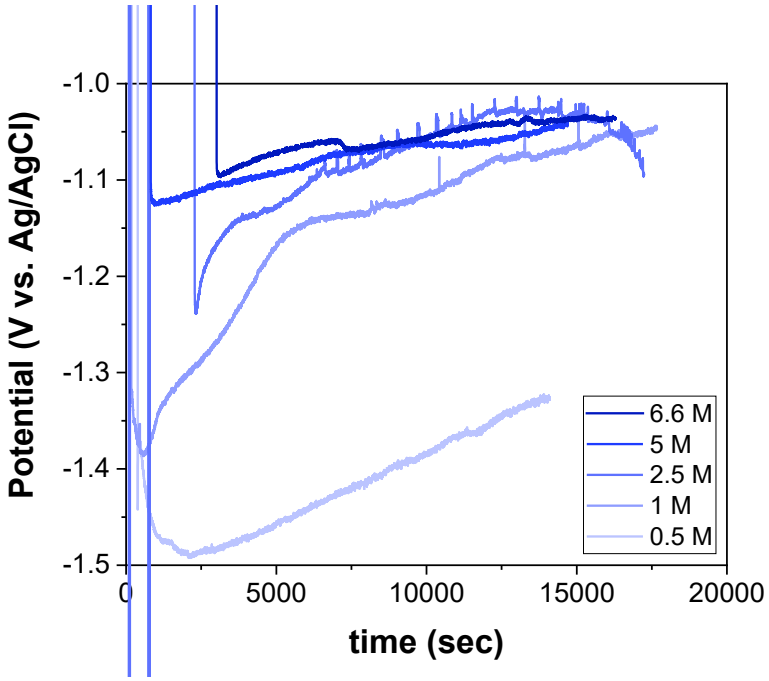

Figure A-B16. OCV measurements in the various blended electrolyte compositions reported in this work. Darker blue corresponds to higher water content.

Figure A-B16 displays the OCV measurements in each electrolyte composition over time. It can be seen that the measurement drifts, without an obvious plateau of steady potential, over the course of the 4+ hours. Moreover, the drift happens at different rates for different water content.

Following the voltammograms, which did not yield substantially more information beyond the relatively low overpotentials required for HER/HOR on the Pt electrode, final OCV measurements of various durations were conducted. These results are shown below.

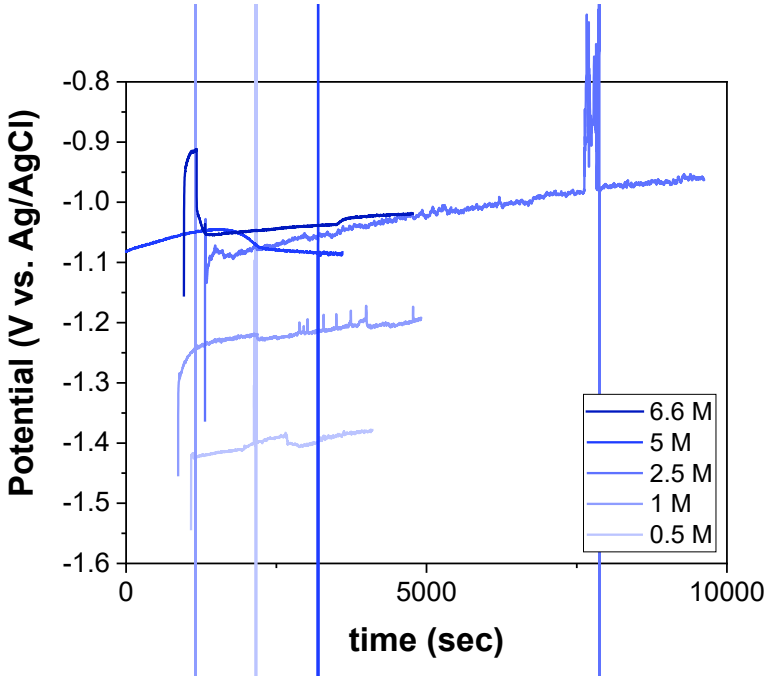

Figure A-B17. The final OCV measurements prior to calibration of the pseudo-reference. During the final OCVs, potentials continued to drift at similar rates as in the initial OCV measurements.

Following the OCV measurement procedure, the pseudoreference electrode was calibrated versus Fc, which was added to a few mL of the electrolyte that had previously been set aside. Fc calibrations are shown below.

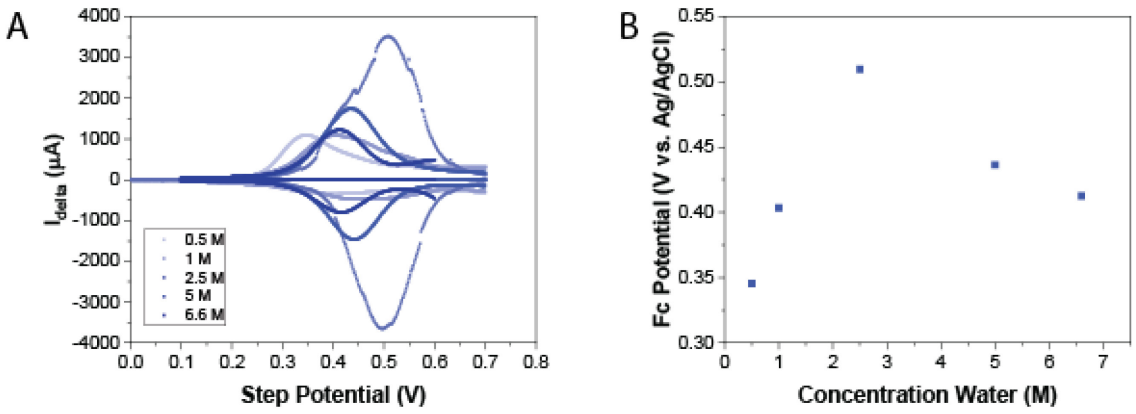

Figure A-B18. Fc calibrations of the pseudo-reference electrode following OCV measurements. A) Raw SWV data. B) Resulting averages of oxidative and reductive peak potentials. Only the first SWV was used in every case.

It should be noted that in contrast to the Fc calibrations used for HER experiments, these calibrations were conducted after the pseudoreference had been allowed to equilibrate in the

electrolyte of interest for many hours. It is perhaps for this reason that there was not an overall trend to the measured potential of the pseudoreference versus Fc. In fact, it seems that there is more of a correlation between duration of the OCV procedure and potential of the pseudoreference versus Fc than anything else, with the longest-duration experiment being the one at 2.5 M water, and the shortest being 0.5 M water. That is, longer equilibration with the blended electrolyte leads to a decreasing potential of the pseudoreference. This would be observed as both an increase in the measured OCV over time, as well as an increase in the measured potential of Fc over time.

B.16.1 Water dependence at a constant V vs. RHE

Because there is no plateau in the OCV data – no clear stopping point for the experiment – we are left with a variety of reasonable approaches we could take in order to process the data. A non-comprehensive list of these approaches, as well as reasoning behind each approach, follows here:

1. Compare all OCVs at a consistent time point within the respective measurement

   In this approach, we treat all data at a consistent time point in the experiment as being equivalent. This might be justified by the fact that for each experiment, the pseudoreference electrode starts in roughly the same condition. In addition, in the LSV data set, comparable data is taken at comparable time points in the experiment, lending another reason in favor of this approach. However, taking this approach requires that we further ask: at what point is it reasonable to compare data? This added layer of choice is consequential, as the rate of OCV drift is inconsistent between tests.

2. Compare OCVs once drift rate over time becomes comparable

   Because this drift rate in OCVs does change over time and is not consistent, we could also elect to take each trace's OCV once the drift rate has become more internally consistent. Put another way, this approach would be to wait until the derivative of the OCV with respect to time becomes roughly constant, and measure the OCV at this point. There is not a strong physical basis for such an approach, however.

3. Measure OCVs from the initial "dip"

   An interesting feature of each of these data sets is the initial OCV "dip" that occurs sometime within the first hour of the experiment. Because we do not saturate the electrolyte with H_2 prior to the start of the experiment, we hypothesize that this dip is

attributable to the point at which H_2 has displaced enough O_2 from the air that the dominant reaction defining the potential of the electrode switches from OER/ORR to HER/HOR. We could elect to take the approach of measuring OCVs from this initial dip, perhaps with the motivation that changes in the potential over time are due to changes in the electrolyte; however, we do not believe this is the case, and there is nothing particularly special about the point in time where the dip occurs from the perspective of the pseudoreference electrode.

4. Extrapolate long-time data back to the origin

   If we wished to capture the behavior of the reference at the beginning of the experiment, one approach might be to extrapolate the data from the constant-drift-rate region of the OCV profile back to the origin. This approach assumes both that the reference behavior at the beginning of the experiment is most relevant, and also that deviations from the constant-drift-rate changes in the electrolyte should be ignored, neither of which are based on convincing physical arguments.

5. Take only the OCV value measured at the very end of the run

   Finally, we could also assume that all transient changes observed in the OCV data are entirely attributable to changes in the pseudoreference over time, and that the point at which the measured OCV most closely reflects the potential which can be related to the Fc calibration is the OCV measured immediately prior to that calibration. We find this to be a reasonable hypothesis, and likely the closest to the truth. The only issue is that we do not know how the behavior of the reference changes as it is moved from one cell to another and rinsed with water and acetone. It is possible that this part of the procedure "resets" the pseudoreference electrode in some way, in which case the data collected here may not mean much. We have yet to perform experiments without washing the pseudoreference.

In truth, it is difficult to know which of these approaches will yield the most accurate results. We visualize below how each approach leads to a different interpretation of the water dependence data.

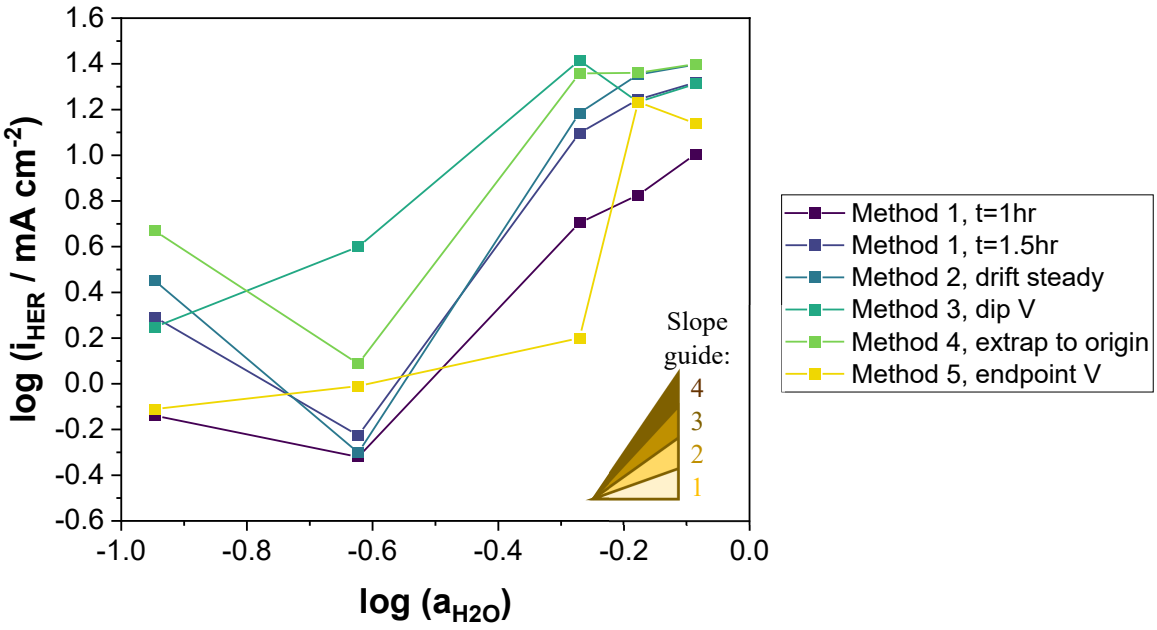

Figure A-B19. Water dependence data at a constant potential vs. RHE, using various approaches to quantify RHE. Slope inset is provided as a visual reference.

From these various approaches, it seems that there is still a strong dependence of HER rate on water content. However, the sign and magnitude of that dependence is particularly unclear at low water activity. Between the 0.5 M water and 1 M water samples, the various methods for determining RHE yield water dependences ranging from 1.1-order all the way down to -2.3-order. On the other hand, between the 1 M and 2.5 M water samples, point-to-point slopes range from 0.6 to 4.2. In general, the various approaches seem to indicate a low dependence on water in the low-activity limit, and a dependence on water that is on-par with the dependence reported in the main text for all other data points (1.4-3.4). In the specific case of approach #5, the endpoint OCV method which we find the most compelling, the water dependence appears to exhibit more of a step-change behavior: low dependence between 0.5 M – 2.5 M, low dependence between 5 M – 6.6 M, but an increase of about an order of magnitude in HER current between 2.5 M and 5 M water.

It is partly due to a combination of the many uncertainties in this RHE measurement that we elected to instead analyze water dependence at a constant potential versus an ET reference. In addition, knowing potentials versus the ET reference in the case of HER in the blended electrolyte is also practically useful in the sense that the full cell voltage may be better understood in this frame of reference – assuming the counter reaction is also understood w.r.t. an ET potential scale.

B.17 Discussion: pH effect on HER

Experiments were carried out in order to assess the impact of adding explicit base to the electrolyte in the form of TBAOH. Because the experiment with no TBAOH was unbuffered, it was subject to unmitigated pH changes during the LSV. These tests served to very roughly probe whether the interfacial pH in neutral tests was substantially different from a bulk alkaline experiment. This is of relevance since some electrochemical systems operate with no buffer, but only water in acetonitrile with $TBABF_4$ and similar aprotic salts.

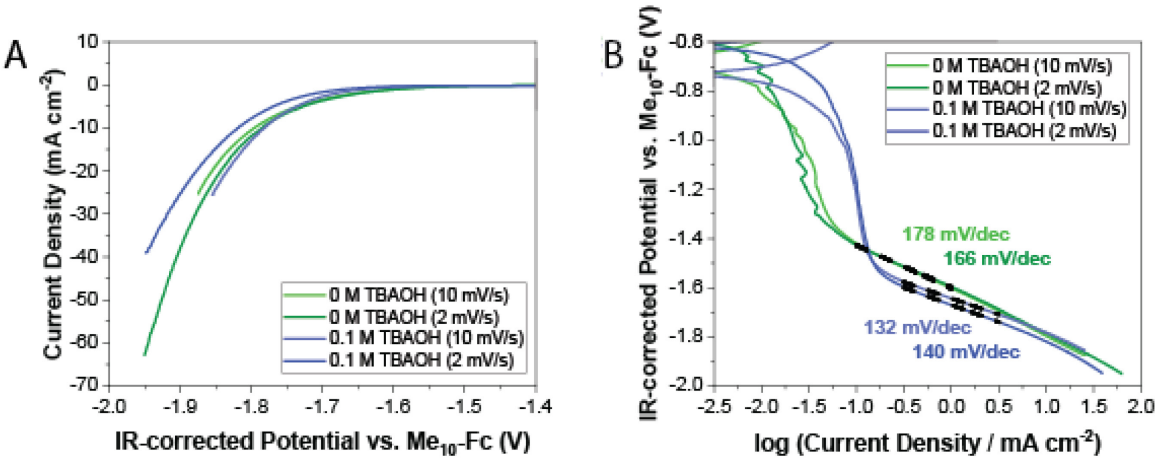

Figure A-B20. LSVs of electrolyte solutions containing 2.5 M water with either 0 M TBAOH/0.8 M $TBABF_4$ (green) or 0.1 M TBAOH/0.7 M $TBABF_4$ (blue). A) Raw LSV data and B) the same data presented as a Tafel plot.

Note that while the scan rates were different between the light and dark blue data points, as well as between the light and dark green data, the main point being illustrated is that run-to-run differences are comparable to differences brought about due to explicit base, especially at higher currents (>10 mA/cm^2). From these results we can see that the initial takeoff of HER may be slightly delayed in the alkaline case relative to the neutral case, which may be expected from a thermodynamic perspective – in fact, a pH shift of this magnitude should theoretically yield a larger potential gap than observed, ~350 mV. However, these differences roughly cancel out once currents reach >10 mA/cm^2. Under these conditions HER is producing enough base at the electrode surface that the reaction environment in the neutral case is essentially similar to that in the alkaline case. Note that the Tafel slope, however, is fit at lower current densities and is therefore sensitive to the bulk pH value – with lower Tafel slopes attainable under more alkaline conditions.

B.18 Discussion: Experimental troubleshooting & minimizing background current

As this project was taking shape, we progressed through several stages of experimental setups. These are detailed here for the benefit of any researchers who may be interested in pitfalls we encountered along the way. A rough scheme of the progression of the system is shown below.

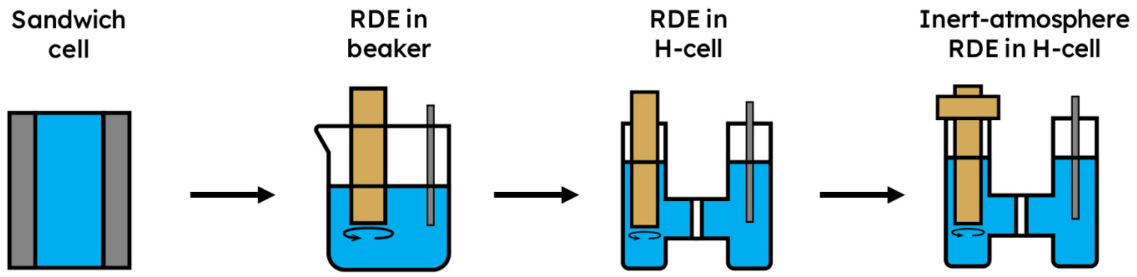

Figure A-B21. Experimental setup progression during troubleshooting phase.

At the outset, we started with a symmetric cell setup in sandwich configuration, with Pt foils as both anode and cathode. While this setup was conducive to online H_2 quantification, it also yielded high values of HER Tafel slopes (>300 mV/dec), even on Pt. We concluded that there were substantial transport limitations at play, and switched to an RDE configuration in a glass beaker cell.

While using the beaker cell, we were able to obtain higher current densities, as the rotation of the electrode allowed for more facile transport of reactants to the surface and products away from the surface. It was at this time that we noticed, however, that current would decrease substantially over time at a constant potential. Hypothesizing that this might be due to interference from the counter reaction, we returned to the sandwich cell and attempted to quantify gas-phase products from the oxidative reaction on the Pt wire counter-electrode. We found that at the various potentials tested, the counter electrode consistently produced a very small amount of carbon monoxide from the oxidative breakdown of acetonitrile in the presence of water. We hypothesize that this CO poisoned the surface of the Pt working electrode, leading to a decrease in HER current over time. This issue was solved by the separation of the working electrode and counter electrode by a glass frit in an H-cell configuration.

Once in the H-cell configuration, currents were steadier over time and Tafel slopes for HER were much lower. However, at this point it became apparent from LSV experiments that some amount of background current existed. The current was reductive, with current densities on the order of -1 mA/cm^2 when the electrode was spun at 1600 RPM with no gas purge through the

working compartment. By experimenting with purging inert gas into the working electrolyte, we were able to observe substantial decreases in background current when O_2 was excluded from the electrolyte. As a result, a gas-purged bearing compatible with the RDE was purchased, and a custom H-cell was ordered to provide the proper seal. At this point we arrived at the final set of methods reported in this work. With this setup, a background of only ~0.05 mA/cm^2 ORR persisted. Decreasing the background current in this way was necessary in order to observe reasonable Tafel slopes for HER.

It should be noted that, in addition to purging N_2 and Ar, we also attempted to purge H_2 through the system. The reasoning for this is similar to the reasoning behind the purging H_2 during the OCV measurement experiments; having the product of the reaction present at a defined activity makes the reaction better thermodynamically defined. Because H_2 is such a light gas, however, the H_2 purge in general took longer to achieve the same effectiveness as Ar at excluding O_2, especially when H_2 was not introduced directly through the electrolyte but rather through the headspace. We were unable to remove O_2 to acceptably low levels using the H_2 purge alone. For this reason, the experiments reported in this work rely on Ar, a heavier gas, to remove the O_2 from solution and eliminate background ORR current.

B.19 Discussion: Local Tafel slopes & sensitivity of Tafel slope to fit range

By taking a point-to-point instantaneous slope in the HER LSV data set and smoothing it using a 41-point moving average, we were able to plot the approximate local Tafel slope at each potential. (Figure A-B22) Note: there is no inherent significance to the 41-point average; this value was chosen for visual smoothness.

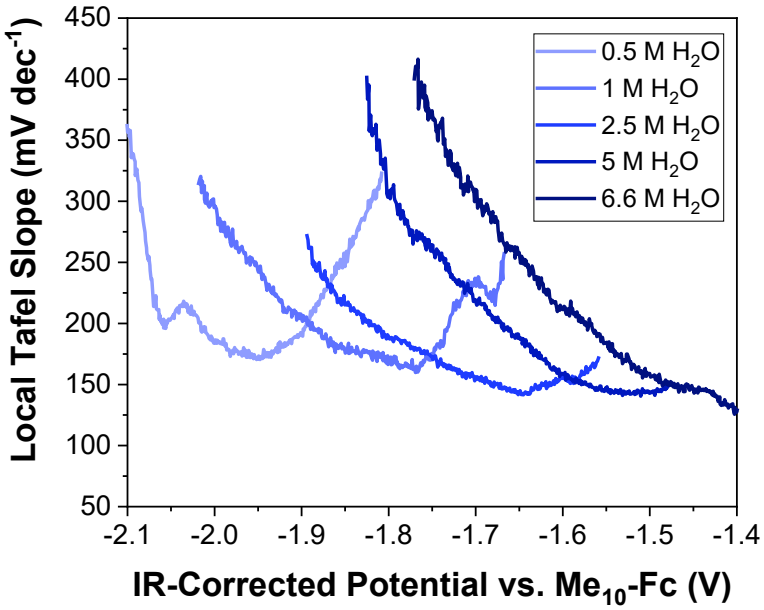

Figure A-B22. Local Tafel slope for HER on Au in the potential range studied. Note: Tafel data at higher currents were noisy; therefore, the local data reported here are cut off prior to the end of the data set, for clarity.

In each trace, as the Au electrode is negatively polarized, the measured current comes off of the small ORR plateau and potential has an increasing effect on rate (i.e. a lower Tafel slope). This is followed by a minimum in measured Tafel slope and an ensuing steady increase as a variety of factors (transport, Marcus-like kinetics, etc.) begin to play a larger role.

Because of the density of data points used in collecting the Tafel data, it was unreasonable to report errors in Tafel slope estimated from fitting that data, as they are artificially deflated by an abundance of data points. However, we were also unable to use the Bayesian data analysis approach developed previously[158] to fit the full data set, as this approach has difficulty dealing with phenomena such as background current. Instead, we have opted to tabulate here how the reported Tafel slope would change with slight changes in the fit region. Note that we have not altered the width of the fit region, which is 1 decade of current in all cases.

Table A-B4. Sensitivity of Tafel slope to fit range

Concen-tration H_2O (M)	Reported TS fit start (log (i / mA cm^{-2}))	Reported TS fit end (log (i / mA cm^{-2}))	Reported TS (mV/dec)	TS 0.1 decade earlier	TS 0.1 decade later
0.5	-0.5	0.5	183.4	186.1	184
1	-0.6	0.4	172.1	176.4	172.4
2.5	-0.6	0.4	148	148.9	148.4
5	-0.6	0.4	144.5	145.1	144.8
6	-1	0	130.4	132.2	130.6

The Tafel slope is relatively insensitive to fit range within this window, changing by less than 5 mV/dec with a shift of 0.1 dec in either direction.

B.20 Discussion: Water dependences of HER in blended electrolyte at different potentials

There was a small window in which we could make comparisons of HER rate across most water activities. The following plots represent constant-potential cuts (w.r.t. Me_{10}-Fc) through the same data set, made at different potentials than the one reported in the main text. Data for which total current density was lower than ~0.75 mA/cm^2 was discarded as there was likely too much interference from the ORR background.

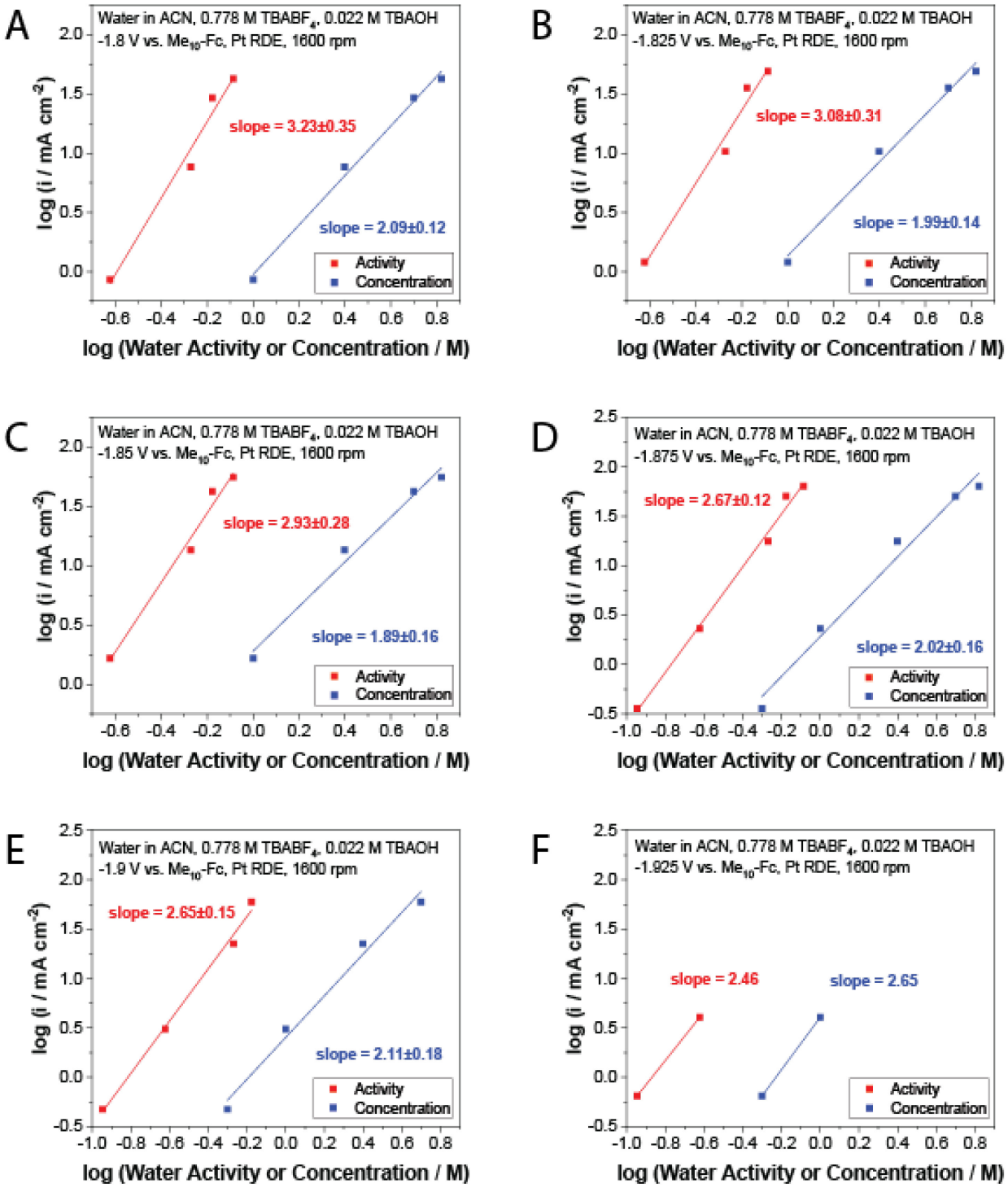

Figure A-B23. Water dependences of HER on Au at multiple potentials: A) -1.8 V vs. Me_{10}-Fc, B) -1.825 V vs. Me_{10}-Fc, C) -1.85 V vs. Me_{10}-Fc, D) -1.875 V vs. Me_{10}-Fc, E) -1.9 V vs. Me_{10}-Fc, F) -1.925 V vs. Me_{10}-Fc.

Data shown in the main text – the plot at -1.875, here also shown with an additional lower-concentration data point (Figure A-B23D) – was selected so that the broadest range of water concentrations could be compared at a single potential. Because the water dependence across this range of potentials is similar, we can say that the data selected for inclusion in the main text is fairly representative of the full data set, and that the analysis would not change drastically if we had selected a slightly different potential.

In all cases, the linear fits to the activity data are fairly strong. In addition, we can observe an interesting trend: there is an apparent decrease in water dependence with decreasing potential (increasing overpotential). At the same time, the discrepancy between measured water dependence with respect to concentration versus activity decreases as potential becomes more reductive – although this is at least partially due to the concentration range being compared.

B.21 Discussion: Sources of errors (accounted and unaccounted) in HER water dependence data

The errors accounted for in main text Figure 3-2C, the water dependence of HER in the acetonitrile-water blended electrolyte, are the following:

- X-error: error from triplicate activity measurements (no x-error reported for concentration data)
    - This is the same as error shown in Figure 3-2A, shifted into the log space.
- Y-error: error estimated from the process of averaging the oxidative and reductive peaks during Me_{10}-Fc calibration
    - This potential error from calibration was propagated through to the LSV data to yield errors in measured current. Note that it is relatively small compared to X-error on activity data set.

Known errors that are *not* accounted for, either because they are difficult to accurately quantify or because they likely contribute little to the results, include:

- Temporal changes in electrolyte composition throughout the HER run due to evaporation
    - Because the system was open, some amount of electrolyte was able to evaporate during the run. Since acetonitrile is the most volatile system component, followed by water, it stands to reason that the electrolyte left to evaporate would increase both in water concentration and in ionic strength over time. However, typical volume losses for recovered electrolyte over the course of a ~4-hour

experiment were roughly 3 mL, about 10% of the total electrolyte volume and no more than 20% of the working electrolyte volume. Actual electrolyte losses at the time of the reported LSV were likely substantially less than this.

- Temporal changes in the reference throughout the HER run, and corresponding differences in potential
    - From the measured OCV data, we know that the junction behavior of the "leak-free" Ag/AgCl pseudoreference changes over time. Depending on the electrolyte and the state of the reference, it appears that potential behavior can shift at different rates as well. (Figure A-B16) This is why, despite the LSV experiments being shorter than the reported OCV measurement experiments, and despite the LSVs for all compositions taking place at nearly identical time points after the start of the corresponding experiment (1.5 hours), there is still considerable uncertainty in how the behavior of the pseudoreference contributed to errors in water dependence measurements. However, looking at LSVs immediately following those reported in Figure 2B (see Figure A-B13, as the rotation rate dependence experiments were conducted in the following 2 hours, in the order 1600 RPM – 900 RPM – 2500 RPM), we can see that HER takeoff occurs around the same potential at each time point, suggesting that the reference is reasonably stable in the working electrolyte, and therefore this source of error is relatively small. Perhaps coincidentally, the largest change over time is observed in the 1 M water experiment, for both the sequential LSVs (Figure A-B13) as well as for the OCV measurements. (Figure A-B16)
- Any run-to-run differences for a given electrolyte composition
    - Because only one data set for each electrolyte is used to draw the conclusions here, we did not account for error between runs. However, replication experiments completed within the lab using different pseudoreference electrodes yielded similar Tafel slopes and water dependences as those reported here.
- Instrumental errors from electrolyte formulation
    - This can be calculated from reported errors for pipettes used in making electrolytes, but such errors tend to cancel and should be negligibly small.

B.22 Discussion: On curvature in order-dependence data

We wish to stress once again that linearity should absolutely not be expected from order-dependence data *a priori*. It is interesting to note, however, that at essentially every ET-referenced potential shown here, the activity correction does serve to make water dependence data more linear. One way to show this mathematically is to look at the residuals of the linear fits for the concentration-based and activity-based data. If a data set is fairly linear, the residuals will scatter around the fit without a trend. On the other hand, if there is curvature in the data, the residuals will exhibit obvious curvature, with a parabolic shape. We show a representative visualization for the HER water dependence data here.

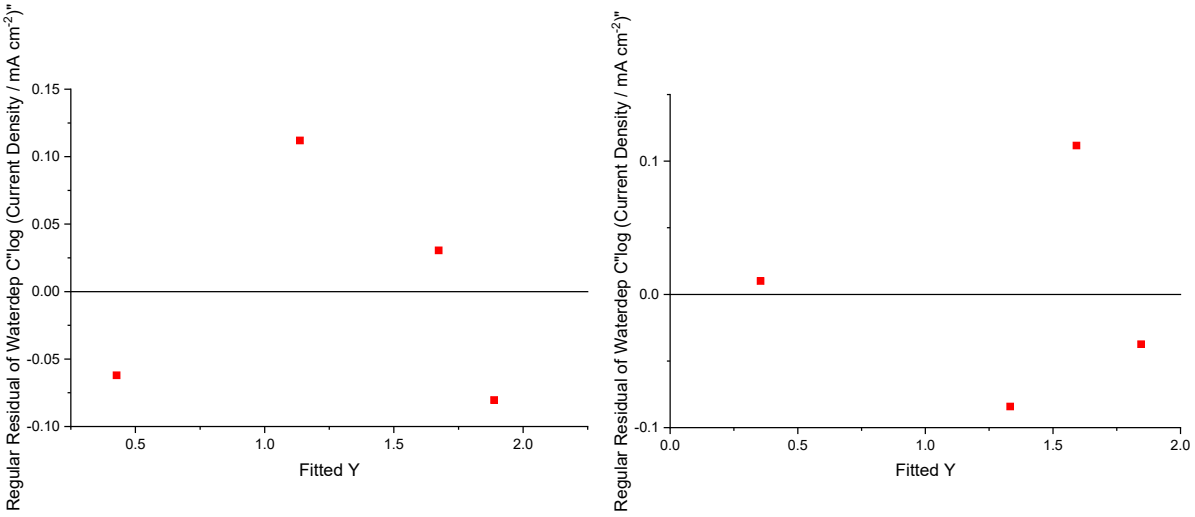

Figure A-B24. Residuals of fit for HER water dependence data in the case where the x-axis is log(concentration) (left) and log(activity) (right).

B.23 Discussion: Water movement across the glass frit

It was noted that during hydrogen evolution experiments on the RDE with electrolytes containing a high activity of water – i.e. the 6.6 M condition – the counter-electrolyte would cloud up and phase-separate as the experiment progressed, indicating that water activity exceeded unity in this compartment. We hypothesize that because the cell was operated under basic conditions, the primary ionic charge carrier was OH^- – and as this OH^- diffused/migrated toward the anode during operation, it brought with it a solvation shell containing mostly water. For this reason, there is some transiency to the electrochemical measurements – water activity may be slightly decreasing in the working electrolyte over time. (This balances with electrolyte evaporation, however, which favors vaporization of acetonitrile – therefore, it is hard to predict

the nature of the transient change in water activity. This could of course be directly measured through HS-GC-TCD.)

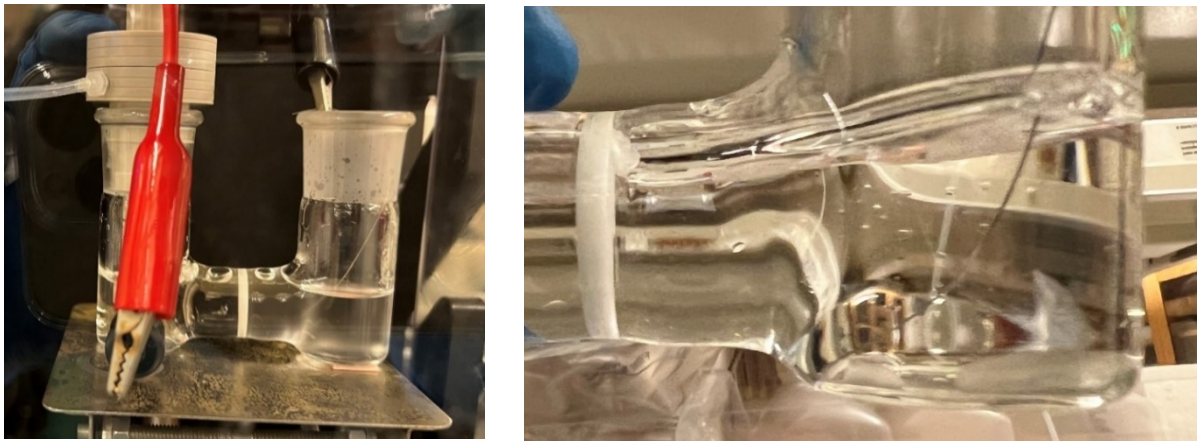

Figure A-B25. Phase separation observed in anolyte of H-cell during HER at high-a_{H2O} conditions.

B.24 Discussion: Effect of water content on organic substrate activity for OAT reactions

While quantifying water activity for the OAT electrolytes, we were also able to quantify activity for the OAT substrates (cyclooctene, cyclohexanone) with changing water content. A plot of cyclohexanone peak area vs. electrolyte water content is shown here.

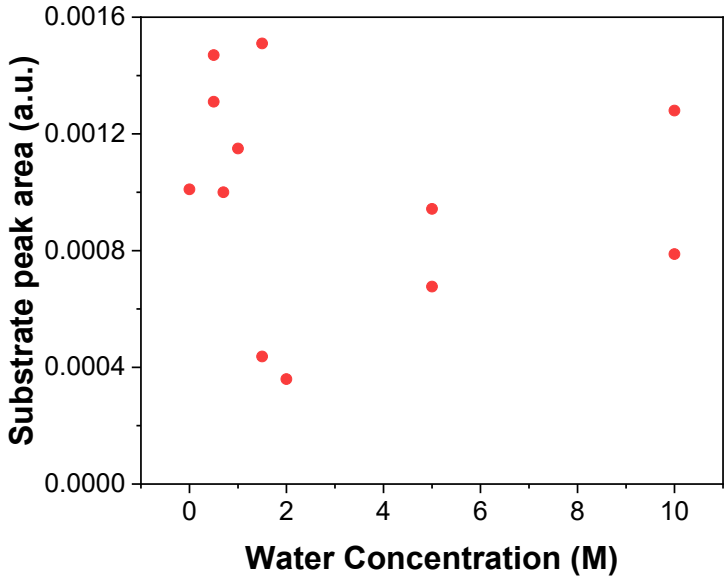

Figure A-B26. Cyclohexanone substrate HS-GC-TCD peak area versus lactonization electrolyte water content.

Unfortunately, likely due to the low volatility of the organic substrates, the spread on these measurements was fairly large. It was difficult to assess whether there was a trend in cyclohexanone activity with water content from this data set alone.

In the case of cyclooctene, only two data points were collected: one at low water content and one at 12.5 M water. In line with our intuition that increasing water content should increase the activity of hydrophobic cyclooctene, the peak area for the 12.5 M water case was 3.4 times larger than the substrate peak area in a 0 M water electrolyte. However, this difference is on the same order as the spread in the cyclohexanone data, so results here too are inconclusive.

APPENDIX C: ADDITIONAL CONSIDERATIONS FOR DIRECT ELECTROCHEMICAL BENZYLIC C-H ACTIVATION

C.1 Methods

C.1.1 Experimental

Prior to each xylene oxidation experiment, PEEK electrochemical cell parts (described in Appendices A & B) were washed using acetone, water, and 10% nitric acid. For the working electrode, circular AvCarb P50 working electrodes were punched out of a stock sheet with a 12 mm hole punch. Sigracet BC electrodes, which served as the backer to prevent electrolyte leakage, were punched slightly larger (~14 mm). An aluminum foil current collector was placed behind this Sigracet paper, and discarded after every experiment. A leak-free pseudo-reference electrode was calibrated versus a Master Ag/AgCl reference as described in Appendices A & B. A Pt foil washed with acetone, water, and 10% nitric acid between experiments was used as the counter electrode. The PEEK cell was assembled with an acetone/water/nitric-washed stir bar in the working compartment, and a similarly washed Daramic separator between the working and counter compartments.

After insertion of the electrolyte, the stir bar was set to stir at 80 rpm. For a typical chronoamperometric experiment, the following EC-Lab sequence was then initiated on the potentiostat:

- PEIS: 200 kHz – 1 Hz (measure Ohmic resistance)
- Pause (enter measured R value into MIR)
- MIR: 85% (manual IR compensation of ~15 Ohm for experiments in 0.885 M $TBABF_4$)
- CV: between OCV and ~1.7 V vs. Ag/AgCl (roughly 1.3-1.4 V vs. Fc)
- OCV: 10 seconds (relax)
- CA: at desired potential, passing 50 C

All tests were conducted in a fume hood or under local exhaust ventilation to prevent exposure to xylene, which is carcinogenic.

Following each experiment, electrolyte was removed from the cell into a 5-mL volumetric flask where it was diluted to 5 mL total volume before being returned to a vial for sampling. This was to ensure the total volume of the sample was known, and therefore the concentrations measured during product quantification could be converted to total number of moles.

NMR samples were then prepared using:

- 300 μL electrolyte sample
- 270 μL d3-ACN (for locking)
- 30 μL 1,3,5-trimethoxybenzene internal standard in d3-ACN

Each sample was then measured using a Varian 501 MHz NMR. Solvent suppression was conducted to dampen the ACN and water peaks ('wet' method). Quantification was achieved by comparing the areas of the peaks of interest to those of the internal standard (1,3,5-trimethoxybenzene). To ensure that relaxation times did not convolute results, standards were collected with known concentrations of products (examples below).

C.1.2 Data processing

In processing NMR spectra, the following steps were taken:

- PH1 phasing around the solvent peak
    - If needed, PH0 phasing around xylene peak
- Baseline correction
    - Whittaker smoother with custom filter
- 1,3,5-trimethoxybenzene aryl peak shifted to 6.1 ppm
- Peaks integrated manually

C.2 NMR standards

Solutions were prepared with known amounts of the following xylene oxidation products:

- Terephthalic acid
- 4-carboxybenzoic acid
- Terephthalaldehyde
- P-toluic acid
- P-tolualdehyde
- 4-methylbenzyl alcohol
- None (xylene blank)

Solutions were made using 1,3,5-trimethoxybenzene as an internal standard. ^{1}H NMR of the solutions is shown below, with color scheme matching that of Figure 4-1.

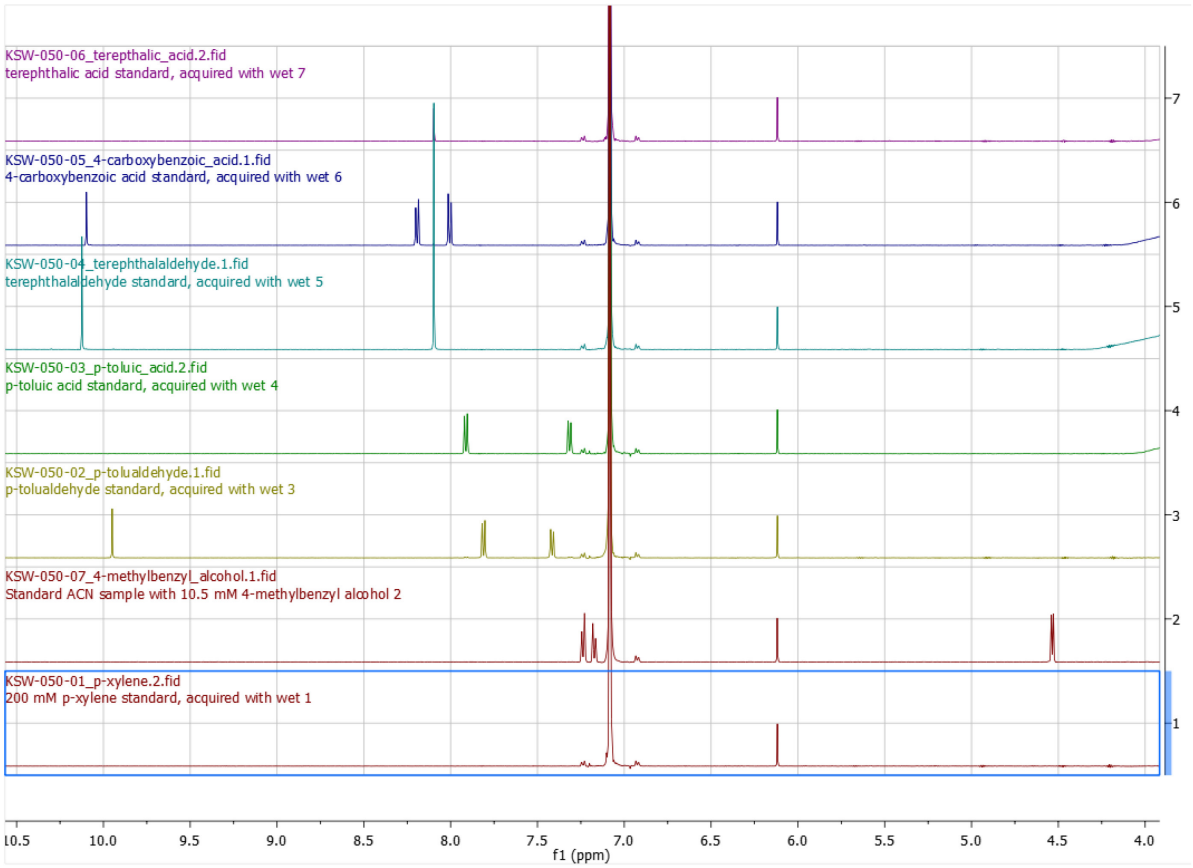

Figure A-C1. NMR standards for selected xylene oxidation products.

C.3 Confirming overall reaction: HER Faradaic Efficiency

To verify the overall reaction, an experiment was conducted at standard conditions (ACN with 0.885 M $TBABF_4$, 5 M H_2O, 200 mM xylene; ~1.3 V vs. Fc) while N_2 was purged through the counter electrolyte (catholyte) to an in-line gas chromatograph. H_2 was detected at this chromatograph with essentially 100% cathodic FE following a lag time during which the experiment was starting up. This confirms that the overall reaction is largely:

$$C_8H_{10}(xylene) + H_2O \rightarrow C_8H_8O(tolualdehyde) + 2H_2$$

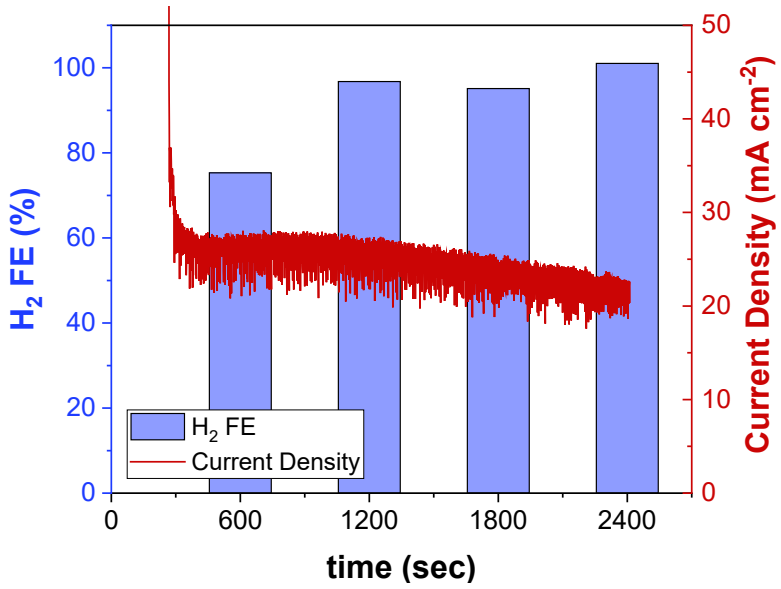

Figure A-C2. Hydrogen from the cathodic half-reaction detected using in-line gas chromatography.

C.4 Mass closure

A series of potential-dependence experiments was further examined to calculate the percentage of xylene mass accounted for, between known (calibrated) oxidation products and the remaining xylene substrate. Total mass closure percentages ranged from ~60-90%, with one outlier at 120% mass closure. Note that this low mass closure may be partly due to the fact that xylene as the substrate has not been calibrated on ^{1}H NMR. Additional experiments are required in order to fully account for the initial substrate mass.

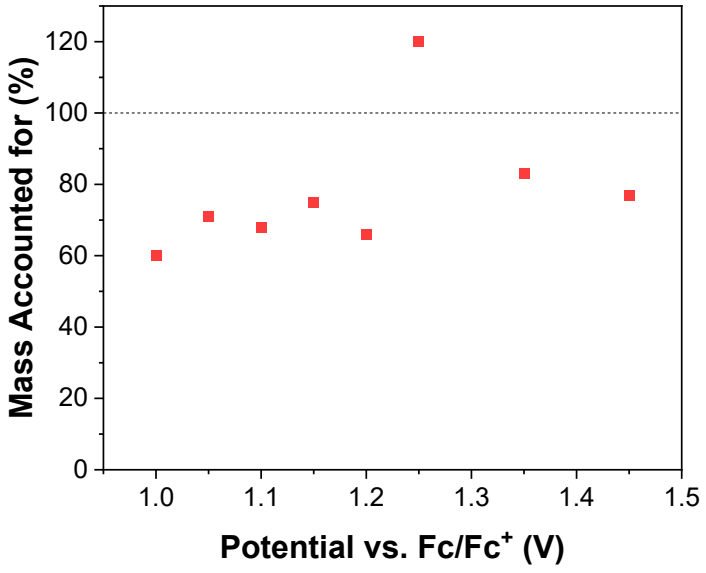

Figure A-C3. Mass closure on initial xylene substrate, based on ^{1}H NMR.

C.5 Bayesian method Tafel slope distribution

In order to better estimate uncertainty around the collected Tafel data, a Bayesian estimation framework was employed to yield a Tafel slope distribution.[158] The data submitted for analysis were a combination of aldehyde and alcohol FEs, in contrast to the data presented in Section 4.8.1. This should not greatly affect analysis, however, since the amount of alcohol generated in these experiments is relatively small.

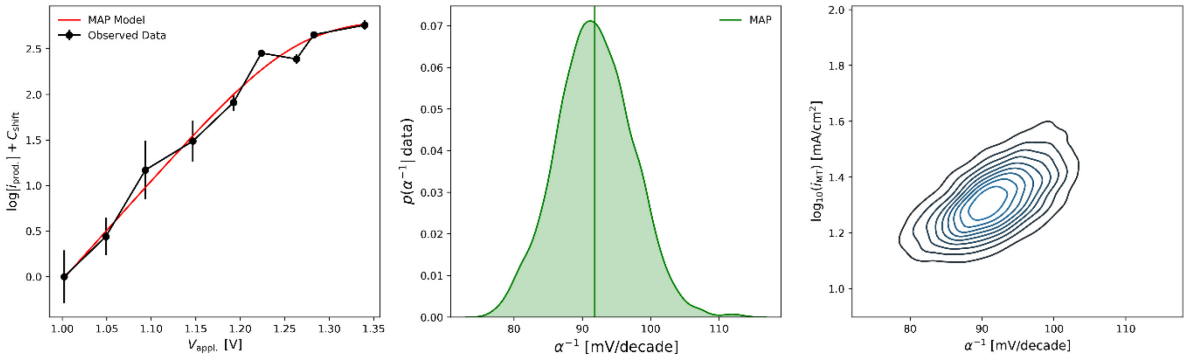

Figure A-C4. Tafel data for xylene oxidation fitted using Bayesian analysis approach.[158]

Results indicate that the Tafel slope exhibits a monomodal Tafel slope distribution around ~90 mV/dec. It is possible that the relatively small number of data points (18) used to achieve this fit have led to the intermediate, non-cardinal value.

C.6 Impact of water concentration on xylene activity

Using manual headspace injection techniques, the activity of xylene was measured as a function of electrolyte water content in order to assess whether the measured water order was in any way attributable to changes in the substrate thermodynamics.

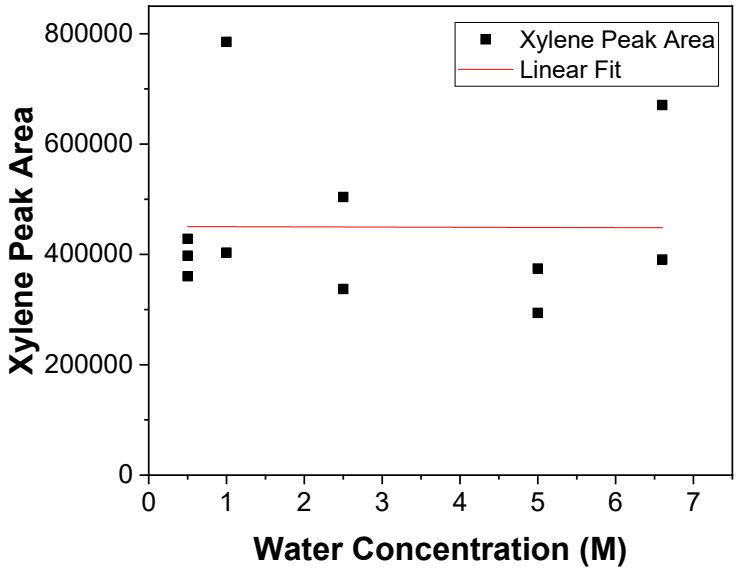

Figure A-C5. Rough measurement of xylene activity as a function of water concentration.

The resulting fit to xylene peak area is fairly flat, exhibiting no trend with respect to water concentration, although it should be noted that there is a large spread in the data, on the same order as the total peak signal. This is likely due to a combination of the relatively low volatility of xylene at room temperature (and therefore the low total peak area), as well as the fact that these were manual injections from poorly-sealed headspace vials. Additional automated headspace measurements are recommended.

C.7 A note on running constant-conversion experiments

During the xylene dependence experiments, the initial approach tested was to run at constant charge passed, rather than constant theoretical conversion. This resulted in as much as ~80% theoretical conversion at very low concentrations of substrate, which resulted in substantial depletion of substrate throughout the run, and corresponding decreases in reaction rate. This had the overall effect of increasing the apparent reaction order with respect to xylene, causing us to run many superfluous experiments in search of the cause of this dependence. This is all to say, we wish to reiterate the importance of running experiments to similar extents of conversion to avoid issues of substrate depletion in the course of a batch run.